

LA-UR-17-21054

Approved for public release; distribution is unlimited.

Title: Groundwater Pathway Model for the Los Alamos National Laboratory
Technical Area 21, Material Disposal Area T

Author(s): Stauffer, Philip H.
Levitt, Daniel G.
Miller, Terry Ann
Jordan, Amy
Chu, Shaoping
Dash, Zora

Intended for: Report

Issued: 2017-02-09

Disclaimer:

Los Alamos National Laboratory, an affirmative action/equal opportunity employer, is operated by the Los Alamos National Security, LLC for the National Nuclear Security Administration of the U.S. Department of Energy under contract DE-AC52-06NA25396. By approving this article, the publisher recognizes that the U.S. Government retains nonexclusive, royalty-free license to publish or reproduce the published form of this contribution, or to allow others to do so, for U.S. Government purposes. Los Alamos National Laboratory requests that the publisher identify this article as work performed under the auspices of the U.S. Department of Energy. Los Alamos National Laboratory strongly supports academic freedom and a researcher's right to publish; as an institution, however, the Laboratory does not endorse the viewpoint of a publication or guarantee its technical correctness.

***Groundwater Pathway Model
for the
Los Alamos National Laboratory Technical Area 21,
Material Disposal Area T***

Authors:

Philip H. Stauffer
Daniel G. Levitt
Terry A. Miller
Amy Jordan
Shaoping Chu
Zora Dash

October 13, 2011

Table of Contents

| | |
|--|-----|
| List of Figures | iii |
| List of Tables | v |
| List of Attachments | v |
| Acronyms and Abbreviations | vi |
| | |
| 1.0 Introduction | 1 |
| 2.0 Background..... | 2 |
| 2.1 Site Description | 2 |
| 2.2 Previous Investigations..... | 7 |
| 2.2.1 MDA T Investigations | 7 |
| 2.2.2 Area G Investigations | 10 |
| 2.3 Conceptual Model..... | 11 |
| 2.3.1 Hydrology and Contaminant Transport at DP Mesa | 11 |
| 2.3.2 Vadose Zone Moisture Field Observations..... | 13 |
| 2.3.3 Nature and Extent of Contamination..... | 19 |
| 3.0 Methods..... | 27 |
| 3.1 Three-Dimensional Model Development | 27 |
| 3.1.1 Development | 28 |
| 3.1.2 Model Configuration and Boundary Conditions | 33 |
| 3.1.2.1 Particle Release Locations..... | 33 |
| 3.1.2.2 Infiltration | 37 |
| 3.1.2.3 Wastewater Application to Beds..... | 38 |
| 3.1.2.4 Boundary Conditions..... | 40 |
| 3.1.3 Hydrogeologic Input Data | 40 |
| 3.1.4 Model Simulation Initial Steady State Set-up..... | 41 |
| 3.1.4.1 Conservative Breakthrough Curves | 43 |
| 4.0 Results..... | 44 |
| 4.1 Penetration of Bed Water: 1945 - 2010 | 44 |
| 4.1.1 Role of Fractures on Bed Infiltration | 48 |
| 4.1.2 Numerical diffusion of the wetting front: Mesa-Scale Versus Local-Scale Meshes... | 50 |
| 4.2 Particle Breakthrough at the Water Table..... | 52 |
| 5.0 Discussion | 56 |
| 6.0 References | 58 |

List of Figures

| | | |
|------------|---|----|
| Figure 1 | Locations of Material Disposal Area T within the Laboratory (taken from LANL 2006a, Fig. 1.0-1)..... | 3 |
| Figure 2 | Map of TA-21 showing MDAs A, B, T, U, and V (adapted from LANL, 2011a, Figure 1)..... | 4 |
| Figure 3 | Aerial Photograph of TA-21 Facing WNW (MDA T located within red oval)..... | 4 |
| Figure 4 | Locations of absorption beds and shafts at MDA T (taken from LANL 2004, Figure B-6)..... | 5 |
| Figure 5 | Generalized stratigraphy of bedrock units at MDA T (adapted from LANL 2009, Figure 4.2-1)..... | 6 |
| Figure 6 | Locations of absorption beds and shafts at MDA T illustrating relative radionuclide inventory estimates | 12 |
| Figure 7 | Water-content data from boreholes at and near MDA T | 15 |
| Figure 8 | Water-content data from boreholes at and near MDA T (top 400 ft only)..... | 16 |
| Figure 9 | Locations of boreholes with water-content data at MDA T and in DP Canyon..... | 18 |
| Figure 10 | Depth profiles of gravimetric water content under bed #1 (left) and bed #2 (right) from 1978 (taken from LANL 2004, Figure B-24)..... | 19 |
| Figure 11 | Depth profiles of Pu-238 (top) and Pu-239 (bottom) detections above background values in MDA T boreholes..... | 20 |
| Figure 12 | Depth profiles of tritium (left) and Am-241 (right) detections above background values in MDA T boreholes..... | 21 |
| Figure 13 | Depth profiles of tritium concentrations from vapor monitoring wells 21-25262 and 21-607955 (taken from LANL 2011b, Fig. 5.2-2)..... | 22 |
| Figure 14 | Depth profiles of selected chemical concentrations from core from boreholes 21-25262 (left) and 21-607955 (right) | 23 |
| Figure 15 | Depth profiles of total VOC concentrations in 2009 from four MDA T vapor monitoring wells (taken from LANL 2009, Fig. 6.3-1)..... | 24 |
| Figure 16 | Depth profiles of TCE concentrations in vapor from boreholes 21-25262 and 21-607955 (taken from LANL 2011b, Fig. 5.1-5)..... | 24 |
| Figure 17 | Depth profiles of 1978 concentrations of plutonium (top) and americium (bottom) measured in core under bed #1 (left) and bed #2 (right) (taken from LANL 2004b, Figs. B-22 and B-23)..... | 25 |
| Figure 18 | Depth profiles of concentrations of plutonium measured in core under bed #1 in 1953, 1960, and 1978 (taken from LANL 2004b, Fig. B-25) | 26 |
| Figure 19 | MDA T Model Domain within the WC09 GFM..... | 28 |
| Figure 20 | Digital Elevation Model and drillhole locations used for the MDA T GFM | 30 |
| Figure 21 | Mesa-scale mesh of TA-21 | 31 |
| Figure 22a | Slice of the mesa-scale mesh with one half of the high-resolution, local-scale mesh centered on MDA T. Adsorption beds are plotted in bright pink on the surface. The local-scale mesh extrudes behind the slice. The bottom of the local-scale mesh extends to 7 m below the regional aquifer..... | 31 |
| Figure 22b | High-resolution, local-scale mesh. Bed one is green, two red, three purple and four yellow. Mesh spacing is 1 m (3.28 ft) in the z direction from the surface to 7 m below the water table..... | 32 |
| Figure 23 | Particle release location and saturation distribution for 1 mm/yr infiltration scenario at elevation 2106 m (230 ft bgs) | 35 |

| | | |
|------------|---|----|
| Figure 24a | Particle release locations and saturation distributions for various infiltration scenarios and elevations (from left to right: 10, 5, 1 and 0.1 mm/yr) and from top to bottom in 35 m depth intervals. Color bar for saturation is shown in Figure 23. | 36 |
| Figure 24b | Particle release locations and saturation distributions for various infiltration scenarios and elevations (from left to right: 10, 5, 1 and 0.1 mm/yr) and from top to bottom in 35 m depth intervals. Color bar for saturation is shown in Figure 23. | 37 |
| Figure 25 | MDA T wastewater disposal history (adapted from LANL, 2004, Table B-3) | 39 |
| Figure 26 | MDA T wastewater disposal history and application to absorption beds in FEHM. | 39 |
| Figure 27 | Steady-state water content profiles at four infiltration rates. | 42 |
| Figure 28a | Simulated gravimetric water content profiles in 2010 at four infiltration rates compared with measured GWC data from 2005-2009. | 45 |
| Figure 28b | Simulated gravimetric water content profiles in 2010 at two infiltration rates compared with measured GWC data from 2005-2009, Puye porosity in this case is 0.4. | 46 |
| Figure 28c | Simulated saturation distribution at 65 yrs for the 10 mm/yr case in the 3-D high resolution local-scale mesh. The slice is along A-A' of Figure 22b. | 47 |
| Figure 28d | Simulated saturation distribution at 65 yrs for the 10 mm/yr case in the 3-D high resolution local-scale mesh. The slice is along B-B' of Figure 22b. | 48 |
| Figure 28e | Difference in saturation between the unfractured (scm) and fractured (ecm) simulations for the 10 mm/yr case at 65 years. The slice is along A-A' from Figure 22b. | 49 |
| Figure 28f | Difference in saturation between the unfractured (scm) and fractured (ecm) simulations for the 10 mm/yr case at 65 years. The slice is along B-B' from Figure 22b. | 50 |
| Figure 28g | Saturation front penetration depth for both the high resolution local-scale mesh and the mesa-scale mesh. | 51 |
| Figure 29 | Particle breakthrough for the 10 mm/yr background flow field. | 52 |
| Figure 30 | Particle breakthrough for the 5 mm/yr background flow field. | 53 |
| Figure 31 | Particle breakthrough for the 1 mm/yr background flow field. Curves are normalized to 10,000 particles due to particle attrition in the low flow background area. | 54 |
| Figure 32 | Number of particles reaching the water table for the 1 mm/yr background flow field. | 54 |
| Figure 33 | Particle breakthrough for the 0.1 mm/yr background flow field. Curves are normalized to 10,000 particles due to particle attrition in the low flow background area. | 55 |
| Figure 34 | Number of particles reaching the water table for the 0.1 mm/yr background flow field. | 55 |

List of Tables

| | | |
|---------|--|----|
| Table 1 | History of MDA T Periodic Monitoring Events (taken from LANL 2011b, Table 2.0-1) | 9 |
| Table 2 | Summary of MDA T and Nearby Boreholes with Moisture Data | 14 |
| Table 3 | Particle Release Locations at MDA T | 34 |
| Table 4 | Hydrogeologic Properties Used for the Three-Dimensional Model | 40 |

List of Attachments

- Attachment I. Geologic Framework Models
- Attachment II. Computational Meshes
- Attachment III. Summary of Hydraulic Properties
- Attachment IV. Scoping Calculations for Transport Simulations

Acronyms and Abbreviations

| | |
|-------|--|
| 1-D | One-dimensional |
| 3-D | Three-dimensional |
| AOC | Areas of concern |
| bgs | Below ground surface |
| Ci | Curies |
| DEM | Digital elevation model |
| FEHM | Finite Element Heat and Mass (transfer code) |
| GFM | Geologic Framework Model |
| GWC | Gravimetric water content |
| LANL | Los Alamos National Laboratory |
| MDA | Material Disposal Area |
| msl | Mean sea level |
| OMR | Octree mesh refinement |
| PA/CA | Performance Assessment/Composite Analysis |
| PE | Plutonium-239 equivalent |
| PE-Ci | Plutonium-239 equivalent Curies |
| RTD | Residence time distribution functions |
| SWMU | Solid waste management unit |
| TA | Technical Area |
| VWC | Volumetric water content |

1.0 *Introduction*

This report describes the groundwater flow and transport modeling conducted in support of the Los Alamos National Laboratory (LANL or the Laboratory) Material Disposal Area (MDA) T radiological dose assessment. The MDA T dose assessment uses models created with GoldSim™ (Golder, 2005a and 2005b, 2007a and 2007b), a system-level modeling tool that allows the integration of numerous process-level models and provides the tools needed to conduct probabilistic assessments of long-term releases. The groundwater transport model detailed in this report is one of several process models incorporated into the dose assessment model.

The groundwater transport modeling effort builds on the knowledge gained through previous studies at both MDAs T and G and is augmented by the use of new data, modeling tools, and computer simulations. The approach combines geologic, hydrologic, and topographic data into a three-dimensional (3-D) site-scale model. Mathematical models are used to simulate the transport of radionuclides from the surface through a deep vadose (unsaturated) zone, into the saturated zone directly beneath MDA T.

This report consists of four major sections, including this introductory section. Section 2 provides an overview of previous investigations related to the development of the current site-scale model. The methods and data used to develop the 3-D groundwater model and the techniques used to distill that model into a form suitable for use in the GoldSim models are discussed in Section 3. Section 4 presents the results of the model development effort and discusses some of the uncertainties involved. Three attachments that provide details about the components and data used in this groundwater pathway model are also included with this report.

The approach documented in this report is similar to the approach conducted for the 2011 update (Stauffer et al., 2013) of the MDA G groundwater pathway analysis (Stauffer et al., 2005) conducted for the 2005 Performance Assessment/Composite Analysis (PA/CA) (French et al., 2008).

2.0 *Background*

Material Disposal Area (MDA) T is an inactive subsurface disposal facility. MDA T is a Hazard Category 2 Nuclear Environmental Site (NES) (LANL 2004) indicating that “the Hazard Analysis shows the potential for significant on-site consequences” (DOE-STD-1027-92, p.10). MDA T has a large, buried radioactive waste inventory of approximately 4,000 plutonium-239 equivalent (PE) Curies (Ci) (PE-Ci) which includes 37,400 Ci of Pu-241 (LANL 2010a, Table E-1). The location, topography, general description, general stratigraphy of MDA T, and radiologic inventory are described briefly in Section 2.1. Section 2.2 summarizes some of the details of previous environmental investigations and Section 2.3 describes the conceptual model of vadose zone flow and transport for MDA T.

2.1 *Site Description*

As shown in Figure 1, MDA T is located on the northern edge of the Laboratory in Technical Area (TA) 21, approximately 11 km (7 mi) west of the Rio Grande. The site lies on Delta Prime (DP) Mesa, which is bounded to the north by DP Canyon and to the south by Los Alamos Canyon (Figure 2). The surface of MDA T slopes downward from south to north. The elevation at the downslope (north) boundary of MDA T is approximately 7,130 m (2,173 ft) above mean sea level (msl). The site is slightly larger than 2 acres and is vegetated with grasses, chamisa bushes, and two young ponderosa pines (LANL 2006a, p.3). A photo of TA-21, showing the location of MDA T (taken in 1995) is shown in Figure 3.

Although MDA T consists of 25 solid waste management units (SWMUs) and areas of concern (AOCs) (LANL 2006a, p.3), the primary SWMUs of interest for this report include SWMU 21-016(a) (absorption beds) and 21-016(c) (disposal shafts). SWMU 21-016(a) is comprised of four inactive absorption beds; the beds measured approximately 120 ft long x 20 ft wide x 6 ft deep. Untreated liquid wastes from uranium- and plutonium-processing laboratories and the filter building (Building 21-12) were discharged into the absorption beds. An estimated 18.3 million gallons of wastewater were discharged into the absorption beds. SWMU 21-016(c) consists of sixty-four 8-ft-diameter and 4-ft-to-6-ft-diameter asphalt-lined disposal shafts located between absorption beds 2 and 4. The shafts are 15 ft to 69 ft deep and were installed between 1968 and 1974. The shafts received treated liquid wastes, some contaminated with americium-241, mixed with cement. Five of the shafts have bathyspheres that contain plutonium-239/240 and other mixed fission products. In addition, some shafts received unspecified volumes of wash water. Once the shafts were filled with the waste cement mixture, they were capped. A diagram of the MDA T absorption beds and disposal shafts are shown in Figure 4.

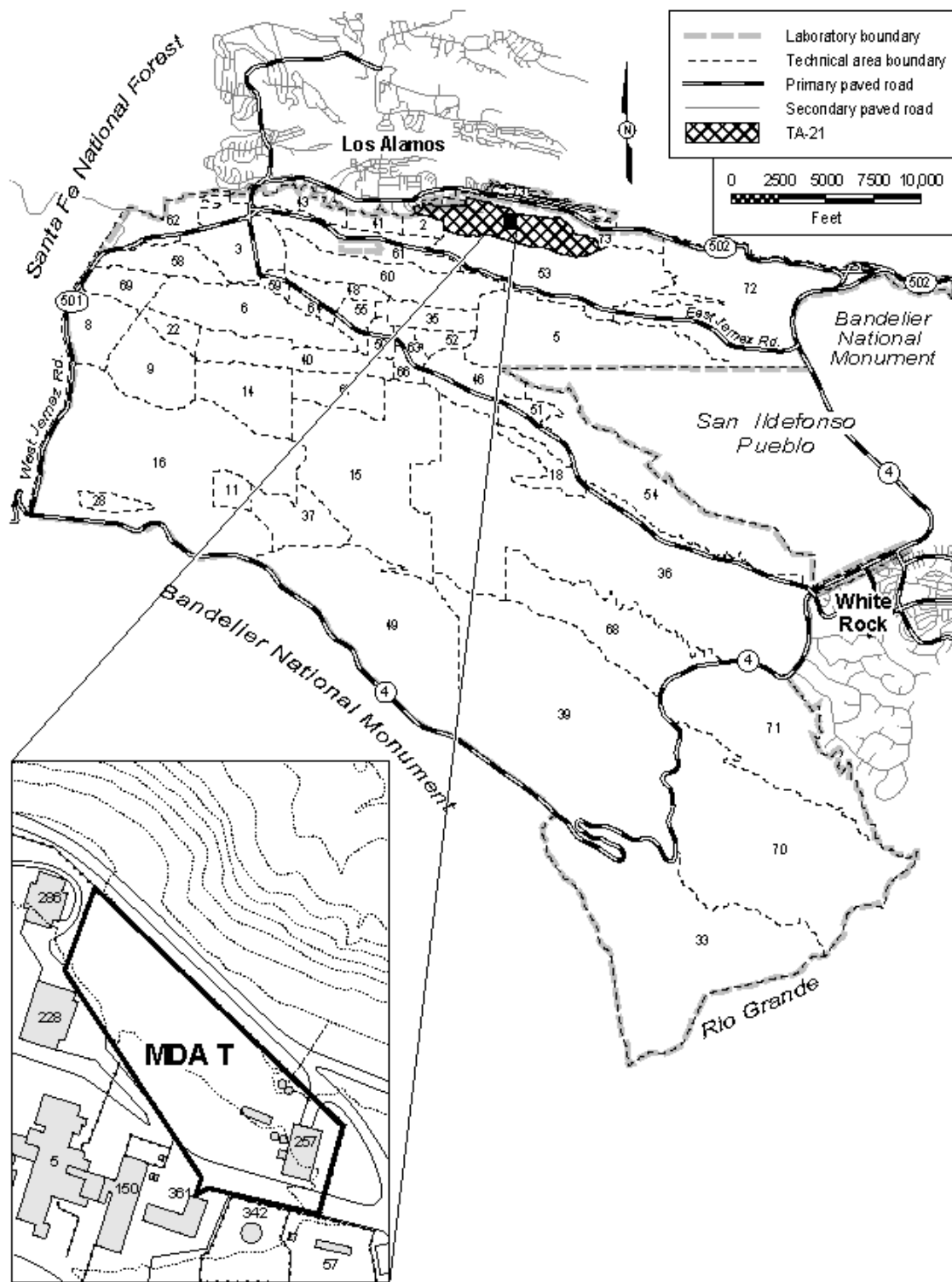


Figure 1
Locations of Material Disposal Area T within the Laboratory
(taken from LANL 2006a, Fig. 1.0-1).

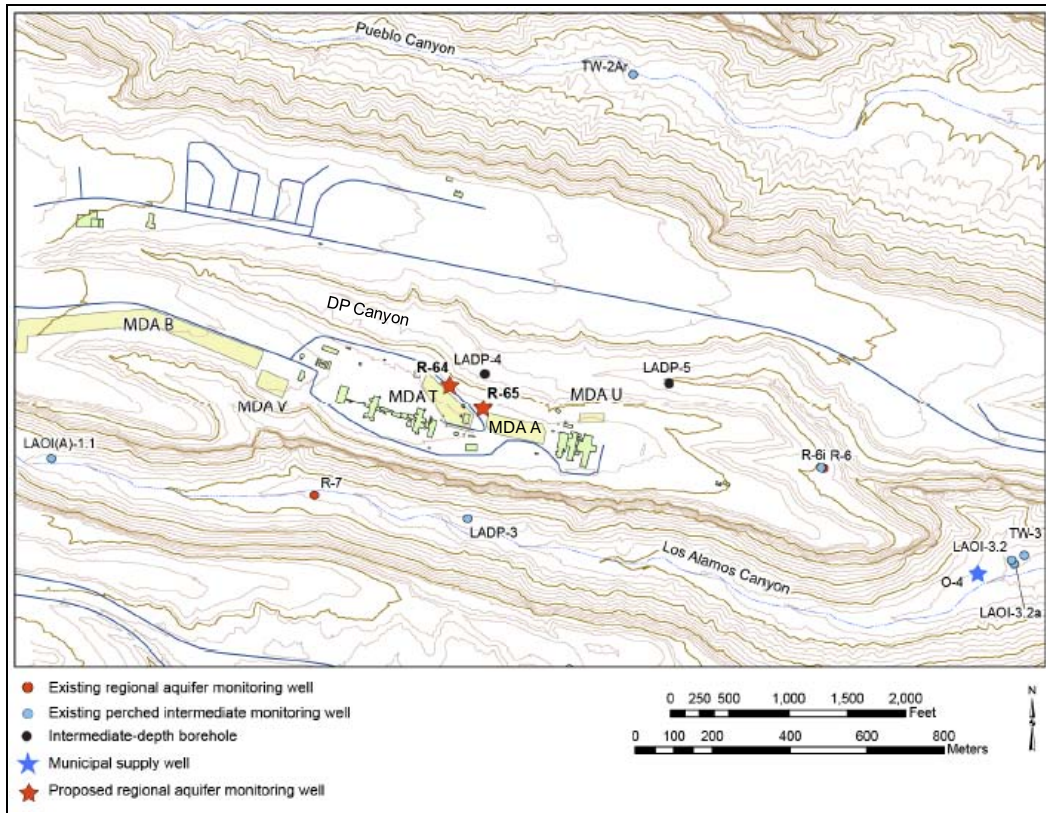


Figure 2

Map of TA-21 showing MDAs A, B, T, U, and V (adapted from LANL, 2011a, Figure 1).



Figure 3

Aerial Photograph of TA-21 Facing WNW (MDA T located within red oval).

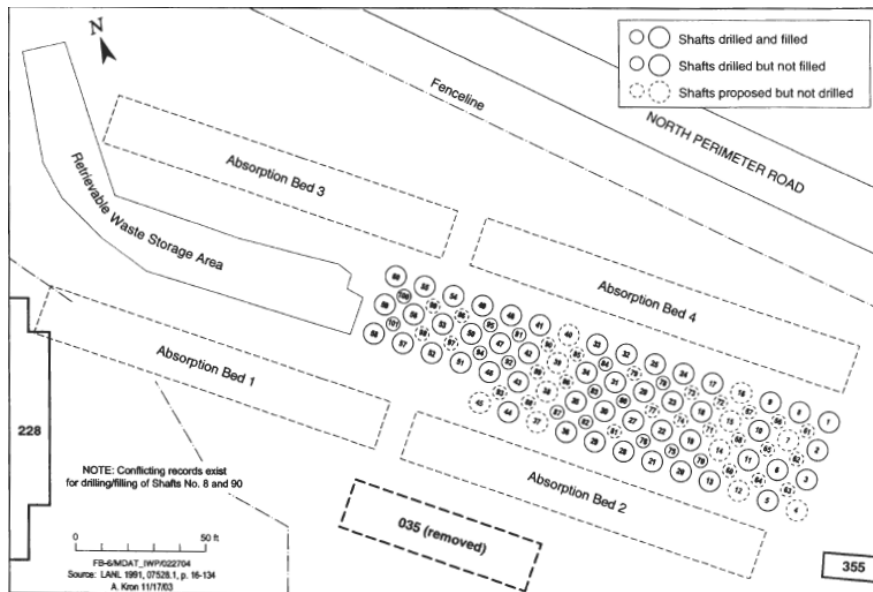


Figure 4
Locations of absorption beds and shafts at MDA T (taken from LANL 2004, Figure B-6)

Subsurface information about the basic stratigraphy beneath MDA T was obtained from borehole 21-607955 (LANL 2009, Fig. 4.2-1), and is shown in cross section in Figure 5. Although the stratigraphy at TA-21 does vary from borehole to borehole, in general the stratigraphy is fairly uniform. Given that MDA T has a small footprint and is close to borehole 21-607955, the stratigraphy from only this borehole is summarized here. The nomenclature for the Bandelier Tuff units discussed in this report (Figure 5) follows the usage of Broxton and Reneau (1995), who provide a detailed description of this formation. The absorption beds and disposal shafts at MDA T have been excavated into unit 3 of the Tshirege Member (Qbt) of the Bandelier Tuff. The Qbt extends below the ground surface to 94.5 m (310 ft) deep in borehole 21-607955. Between units 1v and 1g of the Qbt lies a feature known as the vapor phase notch (VPN) where elevated water contents are observed in most boreholes that penetrate this feature. Although quite thin, the VPN may be an important hydrologic feature for inducing lateral flow.

The Cerro Toledo interval (Qct) lies below the Tshirege Member and above the Otowi Member of the Bandelier Tuff and has a thickness of 12.2 m (40 ft) at borehole 21-607955. The Otowi Member lies below the Qct, which has a thickness of about 91 m (300 ft) at borehole 21-607955. The Guaje Pumice Bed lies at the base of the Otowi Member and has a thickness of about 10.4 m (34 ft) at borehole 21-607955. Beneath the Otowi Member lies the Puye Formation, a highly heterogeneous formation whose facies represents the deposits of the ancestral Rio Grande River that experienced periods of damming and diversions caused by eruptions of lavas (Broxton and Vaniman, 2005). At MDA T, the water table is at a depth of 386.8 m (1,269 ft) bgs as measured in regional groundwater monitoring well R-64 (LANL 2011a). Unlike the stratigraphy at Area G (LANL 2005), there is no known occurrence of the Cerros del Rio basalt beneath MDA T.

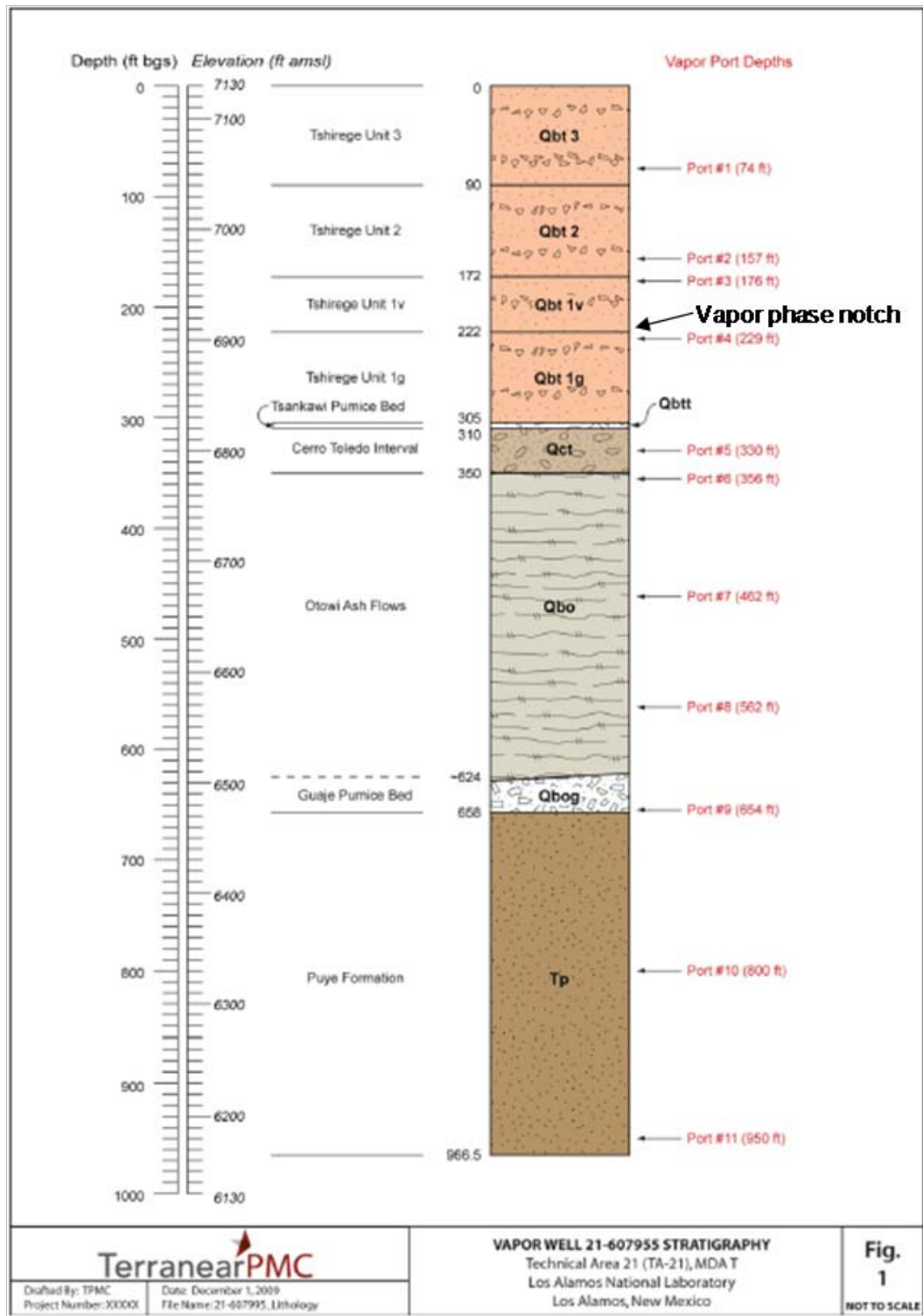


Figure 5
Generalized stratigraphy of bedrock units at MDA T
(adapted from LANL 2009, Figure 4.2-1).

The mass of TRU inventory at MDA T is reported to be about 5159 g (LANL 2004, Table B-9). DOE (2000, Table 3) reports a decay-corrected (to 2000) TRU inventory of 3,780 Ci in MDA T shafts. The 2010 “Documented Safety Analysis for the Nuclear Environmental Sites at Los Alamos National Laboratory reports a PE inventory at MDA T of 4,000 PE-Ci which includes 37,400 Ci of Pu-241 (LANL 2010a, Table E-1).

2.2 Previous Investigations

2.2.1 MDA T Investigations

Details of the MDA T disposal history and environmental investigations can be found in the following LANL documents:

- MDA T Investigation Work Plan (LANL 2004)
- MDA T Investigation Report (LANL 2006a)
- MDA T Investigation Report Phase II (LANL 2007)
- MDA T Investigation Report Phase III, Rev 1 (LANL 2009)
- MDA T Investigation Report Phase III, Rev 1, Replacement pages (LANL 2010b)

The MDA T Investigation Work Plan (LANL 2004) contains an Historical Investigation Report (included as an Appendix) that describes details of historical investigations. The MDA T Investigation Report (LANL 2006a) described details of the 2005-2006 field investigation. The primary purpose for the MDA T Phase II report (LANL 2007) was to report 2007 field activities that included borehole abandonment, installation and sampling of three permanent vapor-monitoring wells, and collection of soil samples from 11 locations on the DP Canyon slope. The primary purpose for the MDA T Phase III, Rev 1 report (LANL 2009) was to report 2009 field activities that included:

- Drilling and sampling of solid media in boreholes (BHs) 21-25262 and 21-607955 to total depths (TDs) of ~695 ft below ground surface (bgs) and ~966 ft bgs, respectively;
- Installing a 9-port permanent vapor-monitoring system in BH 21-25262;
- Installing an 11-port permanent vapor-monitoring system in BH 21-607955;
- Monthly sampling of MDA T vapor-monitoring well 21-25262 for six rounds, June–November 2009;
- Monthly sampling of MDA T vapor-monitoring well 21-607955 for one round in December 2009; and
- Sampling of MDA T vapor-monitoring wells 21-603058, 21-603059, and 21-25264 for an additional eight rounds (February–November 2009).

The primary purpose for the MDA T Phase III, Rev 1, Replacement pages (LANL 2010b) was to correct errors on pages 25-26 of LANL (2009) and report hydraulic properties from borehole 21-607955 that were not yet available during publication of LANL (2009).

Periodic vapor monitoring data are reported quarterly. Table 1 is taken from LANL (2011b, Table 2.0-1) and lists all the vapor monitoring reports associated with MDA T. The groundwater and vadose-zone monitoring strategy for TA-21 is described in LANL (2010c), and in LANL (2011c). Regional groundwater monitoring well R-64 has been completed and was sited for monitoring groundwater directly downgradient from MDA T (Figure 2). Proposed monitoring well R-65 is also shown in Figure 2, but this well has not yet been drilled (as of September 2011). Other nearby groundwater monitoring wells such as R-6 and R-7 are also shown in Figure 2.

Table 1
History of MDA T Periodic Monitoring Events
(taken from LANL 2011b, Table 2.0-1).

| Quarter | Sampling Event Date | Number of Vapor-Monitoring Wells ^a | Associated Report Title |
|---------------------------|---------------------|---|---|
| 13th Quarter | April 2011 | 5 | Periodic Monitoring Report for Vapor-Sampling Activities at Material Disposal Area T Consolidated Unit 21-016(a)-99, at Technical Area 21, Second Quarter FY2011 (current report) |
| 12th Quarter | December 2010 | 5 | Periodic Monitoring Report for Vapor-Sampling Activities at Material Disposal Area T Consolidated Unit 21-016(a)-99, at Technical Area 21, October to December 2010 (LANL 2011, 202272) |
| 11th Quarter | September 2010 | 5 | Periodic Monitoring Report for Vapor-Sampling Activities at Material Disposal Area T Consolidated Unit 21-016(a)-99, at Technical Area 21, July to September 2010 (LANL 2011, 111733) |
| 10th Quarter ^b | June 2010 | 5 | Periodic Monitoring Report for Vapor-Sampling Activities at Material Disposal Area T Consolidated Unit 21-016(a)-99, at Technical Area 21, April to June 2010 (LANL 2010, 111121) |
| | April 2010 | | |
| 9th Quarter | March 2010 | 5 | Periodic Monitoring Report for Vapor-Sampling Activities at Material Disposal Area T Consolidated Unit 21-016(a)-99, at Technical Area 21, January to March 2010 (LANL 2010, 110059) |
| | February 2010 | | |
| | January 2010 | | |
| 8th Quarter | December 2009 | 5 | Periodic Monitoring Report for Vapor-Sampling Activities at Material Disposal Area T Consolidated Unit 21-016(a)-99, at Technical Area 21, October to December 2009 (LANL 2010, 109254) |
| | November 2009 | | |
| | October 2009 | | |
| 7th Quarter | September 2009 | 4 | Periodic Monitoring Report for Vapor-Sampling Activities at Material Disposal Area T Consolidated Unit 21-016(a)-99, at Technical Area 21, September to November 2009 (LANL 2010, 108529) |
| | August 2009 | | |
| | July 2009 | | |
| 6th Quarter ^c | June 2009 | 3 | Periodic Monitoring Report for Vapor-Sampling Activities at Material Disposal Area T Consolidated Unit 21-016(a)-99, at Technical Area 21, June to August 2009 (LANL 2009, 107448) |
| | April 2009 | | |
| 5th Quarter | February 2009 | 3 | Periodic Monitoring Report for Vapor-Sampling Activities at Material Disposal Area T Consolidated Unit 21-016(a)-99, at Technical Area 21, February and April 2009 (LANL 2009, 106665) |
| 4th Quarter | September 2008 | 3 | Periodic Monitoring Report for Vapor-Sampling Activities at Material Disposal Area T Consolidated Unit 21-016(a)-99, at Technical Area 21, Fiscal Year 2008 (LANL 2009, 105187) |
| 3rd Quarter | May 2008 | 3 | |
| 2nd Quarter | February 2008 | 3 | |
| 1st Quarter | October 2007 | 3 | |

Note: Results from the shaded dates are not presented in the current monitoring report.

^a The number includes boreholes sampled and field screened.

^b Monthly sampling ended in April 2010 with resumption of quarterly sampling.

^c Sampling frequency increased from quarterly to monthly in June 2009.

2.2.2 Area G Investigations

The groundwater pathway modeling presented in this report builds upon the findings and information provided by a number of earlier investigations at Area G, a mesa-top site similar to MDA T. Stauffer et al. (2005, 2011) describe the groundwater pathway evaluations that were conducted for Area G. The 1997 performance assessment and composite analysis (Hollis et al., 1997) includes geologic information (Vaniman et al., 1996) and hydrologic parameters for MDA G (Krier et al., 1996; Rogers and Gallaher, 1995).

Previous groundwater transport investigations at MDA G (Birdsell et al., 1995, 1999, and 2000; Hollis et al., 1997; Soll, 1995) provide a wealth of insight into the local transport of radionuclides; these studies relied on the process-level, multidimensional, finite-element porous flow and transport simulator known as FEHM (Finite Element Heat and Mass) (Zyvoloski et al., 1995a and 1995b) to model the movement of water-soluble radionuclides from the disposal pits and shafts at MDA G to a drinking water compliance point. Summaries of pertinent aspects of these studies, which guided the current effort for MDA T, are provided below.

Birdsell et al. (1999) conducted investigations into specific flow processes that are relevant to the modeling approach adopted for this study. To determine the effect of transient pulses of moisture on radionuclide transport in the MDA G area, Birdsell et al. ran 1-D and 2-D models of liquid-phase C-14 transport through the Bandelier Tuff. Four scenarios were evaluated. These scenarios had nearly identical long-term infiltration rates of 5.5 mm/yr (0.22 in./yr); however, infiltration rates for individual years varied greatly (from zero to over 100 mm/yr [3.9 in./yr]), and the four selected scenarios had different temporal distributions. Simulations were run for 5,000 years, and the results of the C-14 transport modeling were compared to a simulation using the long-term average infiltration rate. This study showed that a steady-state flow assumption is valid within the range of likely infiltration rates for MDA G and the surrounding area because the transient pulses were damped out as they propagated downward through the system.

Other modeling examined the effect that fractures in the tuff may have on water flow by evaluating possible scenarios where significant fracture flow may occur (Birdsell et al., 1999; Soll and Birdsell, 1998). In this study, the effects of fracture coatings and fills, locations of fractures with respect to the waste, and interactions between fractures and the surrounding matrix were examined. High-infiltration rates were assigned to the top of the simulated fracture systems to ensure that “worst case” conditions were achieved. The results showed that limited fracture flow was activated only during extreme events such as surface ponding of water. The authors concluded that, in most cases, fractures in tuff at MDA G are not a major conduit for the movement of water from the surface to the water table. Because MDA T experienced large volumes of focused infiltration, the role of fractures is investigated in our analysis in this report.

Another parallel study conducted in 2011 concerns the variability of hydraulic properties of the rocks beneath MDA G. Results of this study show that at a fixed surface infiltration of 1 mm/yr, variability in hydraulic properties can lead to changes in predicted breakthrough times. The study uses 1000 random samples spanning the uncertainty in measured rock properties (van Genuchten α and n , porosity, permeability, and residual saturation) for the Qbt2, Qbt1v, Qbt1g, and Qbo units. The earliest breakthrough times are reduced by a factor of two with mean breakthrough time reduced by approximately the same factor. However, a significant portion of the breakthrough times are delayed, many to more than a factor of two times longer than the mean breakthrough time. Fortunately, the behavior of the system is such that the median breakthrough curve from 1000 realizations converges to the same breakthrough curve obtained using the mean hydrologic properties that are used for all simulations presented in this report. Interestingly, the mean breakthrough (time or curve?) of the 1000 realizations does not recreate the behavior of the mean property set, a fact that shows that analysis of the mean behavior of a set of realizations tends to smear the behavior of individual curves within the set.

2.3 *Conceptual Model*

2.3.1 *Hydrology and Contaminant Transport at DP Mesa*

Under natural conditions, DP Mesa fits the “dry and disturbed mesa conceptual model” for the Pajarito Plateau as defined by Birdsall et al. (2005). It is a dry finger mesa; the hydrologic conditions on the surface and within such dry mesas generally lead to slow unsaturated flow and transport. Dry mesas shed precipitation as surface runoff to the surrounding canyons such that most deep infiltration occurs episodically following snowmelt, and even then much of the water is lost through evapotranspiration. As a result, annual net infiltration rates for dry mesas are less than 10 mm/yr and are more often estimated to be on the order of 1 mm/yr or less (Kwicklis et al. 2005). Because dry mesas are generally composed of nonwelded to moderately welded unsaturated tuffs with low water content, water flow is matrix-dominated rather than fracture-dominated. Under natural or undisturbed conditions, travel times for contaminants migrating through dry mesas to the regional aquifer are expected to be several hundred to thousands of years (Nylander et al. 2003; Birdsall et al. 2005). However, beneath disturbed sites or those where liquid wastes were disposed of, travel times to groundwater may be shorter.

MDA T was used for disposal of liquid waste. Enhanced moisture migration and decreased contaminant travel times to groundwater are expected beneath liquid waste disposal sites where infiltration beneath absorption beds increased the moisture content, decreased matric potential, and increased downward driving forces in the underlying tuffs. Field observations indicate moisture migration may have included components of both fracture and matrix flow during periods of liquid discharge (Nyhan et al. 1984; LANL 2004). With discharges discontinued, the adsorption beds and underlying tuff are no longer saturated, and moisture migration is expected to occur as matrix flow under present-day and future conditions (Soll and Birdsall 1998; Birdsall

et al. 2005). Also, infiltration rates at the ground surface are expected to have returned to near-background levels. However, an extended period of greater than normal, downward water flow likely continues at depth under MDA T based upon elevated vadose zone moisture contents.

A reported total of approximately 18 million gallons of wastewater containing plutonium was disposed of in the MDA T absorption beds between 1945 and 1967, 14 million gallons of which was disposed of between 1945 and 1952 (Rogers 1977). During disposal operation, water movement from the beds was probably primarily downward. Water from the absorption beds may have moved rapidly through vertical fractures (primarily in units Qbt 3 and Qbt 2) and paleochannel soils during near-saturated conditions. Water may also have moved laterally at hydrologic contacts (e.g., at the VPN between Qbt 1v/1g, in Cerro Toledo interval and Tsankawi Pumice Bed, and in Guaje pumice layer).

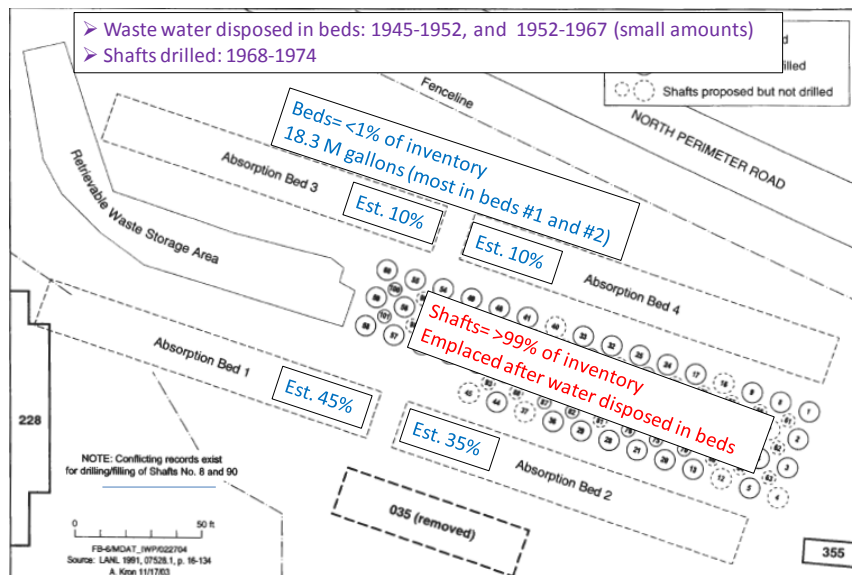


Figure 6
Locations of absorption beds and shafts at MDA T illustrating relative radionuclide inventory estimates

The disposal shafts were installed between 1968 and 1974, 16 to 22 yr after 14 million gallons of the 18 million gallons of wastewater had been disposed of (LANL 2006a). Over 99% of the radiologic inventory disposed of at MDA T was disposed of in the shafts, while less than 1% was disposed of in the beds with wastewater. Wastes disposed of in the shafts were primarily radiological waste mixed with cement for stabilization. This process is thought to immobilize the radiological constituents through a mineralization reaction with the cement. Therefore, if the shaft waste was immobilized by the curing cement, the vast majority of the radiologic inventory of MDA T should not be affected by the movement of waste water because 1) it is bound in a cement-based waste and 2) the bulk of the waste water migrated well below the shaft depth

before the shafts were emplaced. Figure 6 shows the percentages of radiologic inventory between the absorption beds and the shafts at MDA T.

There is no direct evidence of high residual moisture from wastewater disposed of in absorption beds being present in the shaft field during shaft installation, which began in 1968. In contrast, Purtymun et al. (1978) reported volumetric water contents (VWCs) of 7% to 10% in a borehole (TH-7) located 2 ft (to the north) from a shaft drilled in 1968, which correspond to gravimetric water contents (GWCs) of approximately 5% to 7%, consistent with the data shown in Figure 7. Purtymun et al. (1978) also reported that water contents in a separate borehole (TH-7A) drilled in 1969 and located 2 ft (to the east) from the same shaft had VWCs of 4% to 8% (GWCs of 3% to 5%), indicating apparent drying because of cement hydration. They concluded that disposing of wet cement wastes in the shafts at MDA T may not have increased the subsurface moisture content because the cement removed water from the surrounding formation as it cured. Also, these reported water contents are low and indicate that the area of boreholes TH-7 and TH-7A located 60 cm from an unidentified shaft were either unaffected by disposed wastewater in the absorption beds or else elevated water contents had decreased in the time since most of the approximately 18 million gallons had been disposed of in the absorption beds (Purtymun et al., 1978).

2.3.2 Vadose Zone Moisture Field Observations

Vadose zone moisture data from the vicinity of MDA T have been compiled in the form of gravimetric water content versus depth (Figure 7). Figure 8 shows the top 400 ft of data shown in Figure 7. Core samples from nine boreholes at or near MDA T are included. Water content data from deep boreholes at MDAs A, U, and V are included, along with data from boreholes LADP-3 and LADP-4 for comparison. These data are used to define the extent of moisture beneath MDA T. Information on these 13 boreholes is summarized in Table 2.

Table 2
Summary of MDA T and Nearby Boreholes with Moisture Data

| Borehole ID | Depth (ft) | Location | Conditions |
|-------------------|------------|-----------------|--|
| 21-25262 | 680 | S of bed #1 | Potentially affected by MDA T wastewater |
| 21-25263 | 345 | N of bed #3 | Potentially affected by MDA T wastewater |
| 21-25264 | 345 | N+E of bed #4 | Potentially affected by MDA T wastewater |
| 21-60755 | 953 | N of bed #4 | Potentially affected by MDA T wastewater |
| 21-25372 | 279 | N of bed #4 | Potentially affected by MDA T wastewater |
| 21-25373 | 279 | N+E of bed #4 | Potentially affected by MDA T wastewater |
| 21-26589 | 140 | E side of MDA T | Unlikely to be affected by MDA T |
| 21-26588 | 360 | MDA A | Dry; no known liquid disposed |
| 21-24772 | 358 | MDA U | 135,000 gallons disposed |
| 21-24524 | 716 | MDA V | Wet; 40 million gallons disposed |
| 21-02523 (MDAVDH) | 315 | MDA V | Wet; 40 million gallons disposed |
| 21-01682 (LADP-3) | 342 | LA Canyon | Wet |
| 21-01683 (LADP-4) | 800 | DP Canyon | Dry; especially in Otowi |

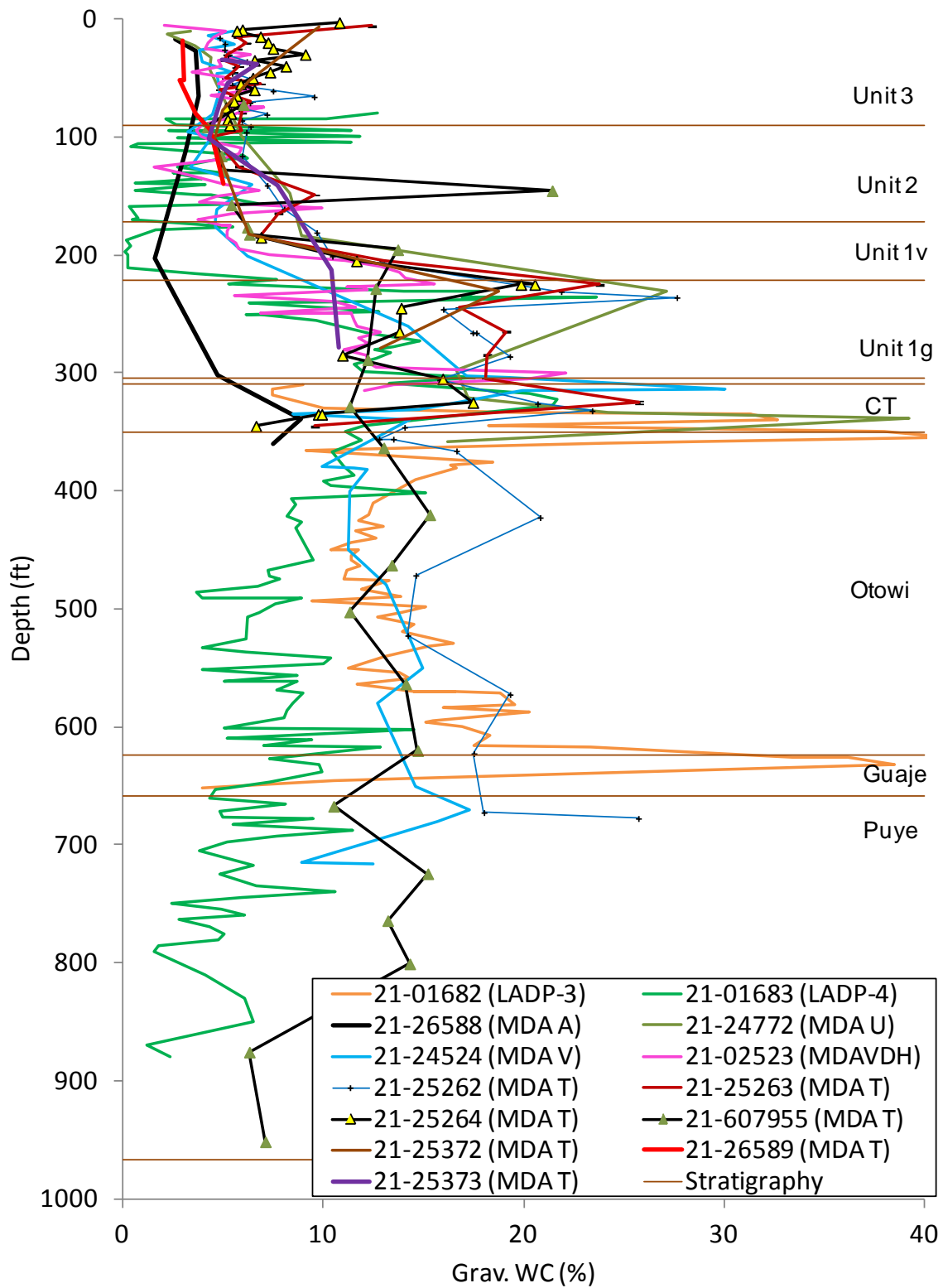


Figure 7
Water-content data from boreholes at and near MDA T

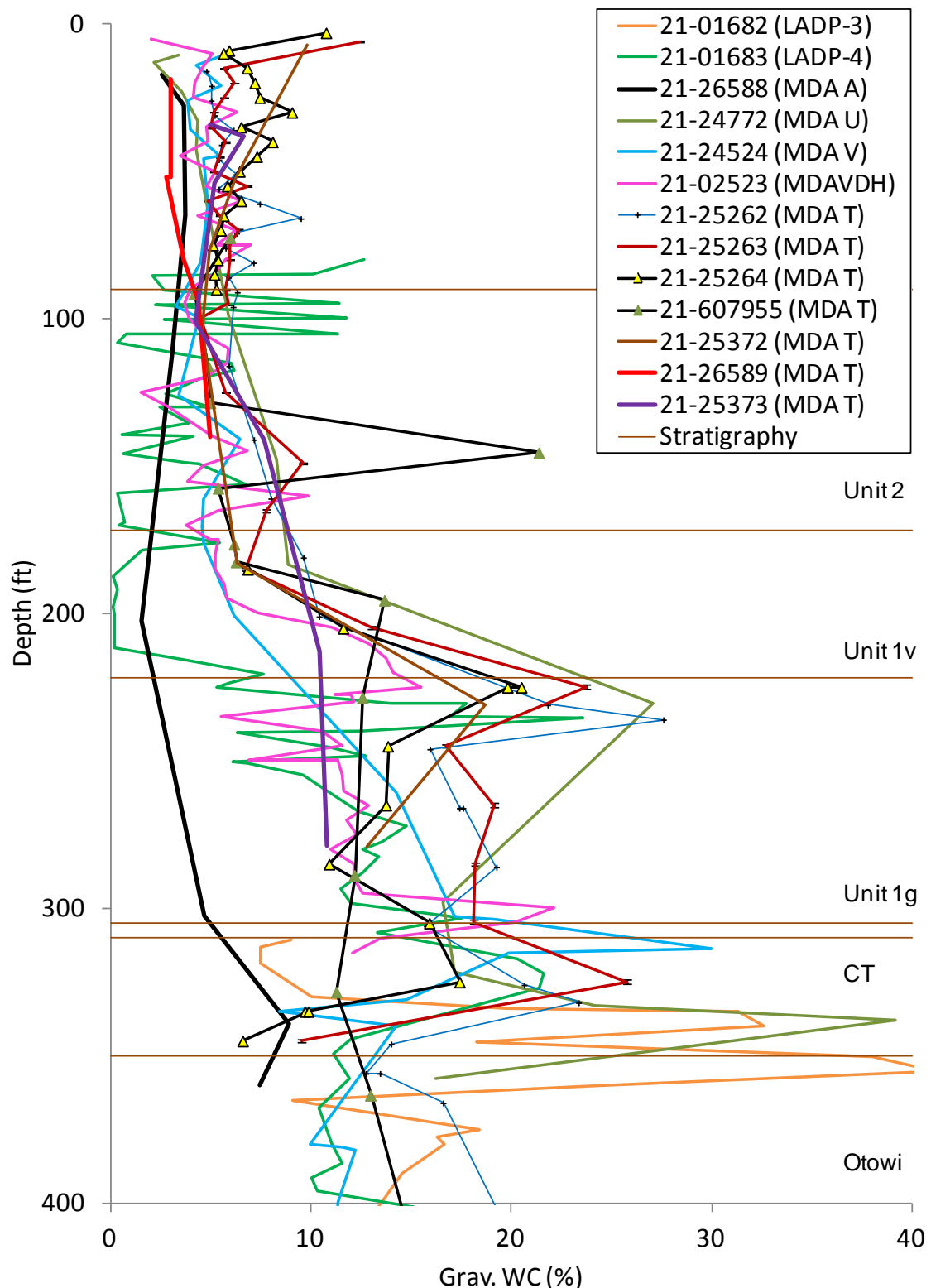


Figure 8
Water-content data from boreholes at and near MDA T (top 400 ft only)

The MDA A borehole is included because it was drilled in a dry site that was unaffected by liquid disposal activities and should represent near-ambient conditions. Unfortunately, this borehole is only 360 ft deep and does not penetrate into the Otowi Member. The MDA U borehole is included because it was drilled in the center of MDA U, which consists of two absorption beds where approximately 135,000 gallons of wastewater was disposed of between 1945 and 1968 (LANL 2006b), so these data should represent conditions that are not dry, ambient conditions. Like MDA U, the MDA V boreholes are included because they were drilled in the center of MDA V, which consists of three absorption beds where approximately 40 million gallons of wastewater was disposed of between 1945 and 1961 (LANL 2006c); these data should represent wet conditions, perhaps throughout the Otowi Member. The water contents in borehole LADP-3 represent wet conditions in Los Alamos Canyon where the canyon floor is subjected to large runoff and infiltration events, and the canyon has a shallow alluvial aquifer. The water contents in borehole LADP-4 represent drier conditions beneath DP Canyon compared with Los Alamos Canyon. Although borehole LADP-4 is located at the bottom of a canyon, DP Canyon is a small canyon that experiences smaller runoff events than occur in Los Alamos Canyon. Figure 9 shows the locations of the seven boreholes at MDA T plus borehole LADP-4 in DP Canyon.

Figures 7 and 8 show water content profiles from all 13 boreholes, with the profiles from boreholes LADP-3 and LADP-4 repositioned to align stratigraphic contacts to the approximate equivalent depths of the MDA T borehole data (since they are located within canyons below the ground surface [bgs] elevation of MDA T). The water content data are fairly consistent in the top 350 ft of the profile. The profile from MDA A appears to have lower water contents, but the data density from this borehole is lower than for the other boreholes for a direct comparison. The water contents in the Otowi Member (between about 350 and 625 ft deep) from boreholes 21-25262 and 21-607955 (both drilled near MDA T) are similar to the water contents from the MDA V borehole where 40 million gallons of wastewater was disposed of. In addition, these two MDA T boreholes have similar water contents to those measured in the Otowi Member in borehole LADP-3 located in wet Los Alamos Canyon. The water contents from borehole LADP-4 in dry DP Canyon are considerably lower than for all other borehole data from the Otowi Member. These data suggest that throughout the Otowi Member under MDA T, conditions are wetter than ambient dry mesa conditions. Since the water contents do not decline in borehole 21-607955 until a depth of between 800 and 875 ft, it is possible that the GWCs are elevated to this depth as a result of previous wastewater disposal in the MDA T absorption beds. Comparison to the GWCs in the Otowi Member from TA-49 (Stimac et al. 2002) and TA-54 (Krier et al. 1997) also suggests the water contents observed in the Otowi Member beneath MDA T are elevated relative to these other two TAs.

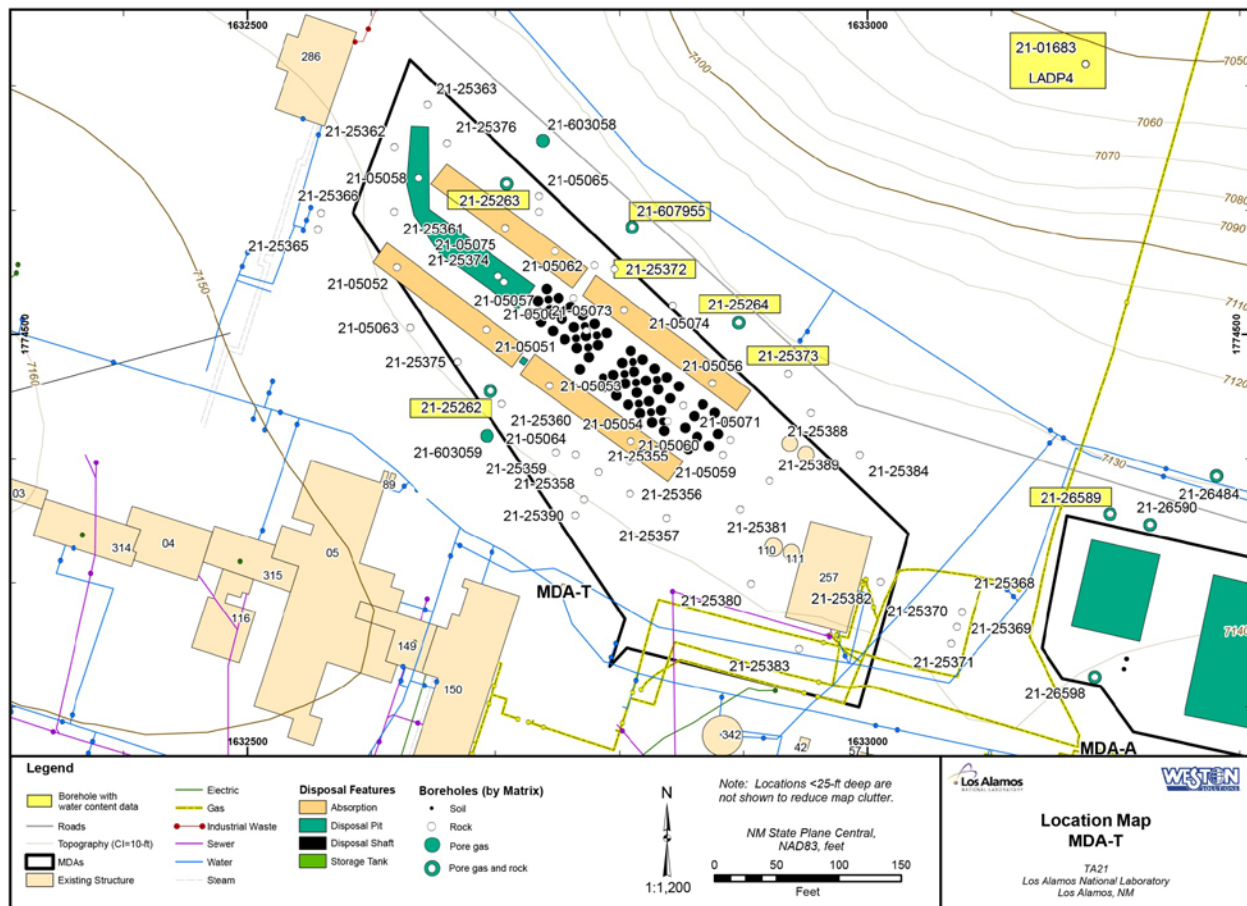


Figure 9
Locations of boreholes with water-content data at MDA T and in DP Canyon

Historical water content profiles from 1978 are shown in Figure 10. These profiles depict the water content conditions beneath beds #1 and #2 approximately 11 years after the end of wastewater disposal at MDA T. There are data from two boreholes for each absorption bed. The maximum values of about 30 percent (gravimetric) water content shown at depths of 7, 10, and 24 m under bed #1 are probably close to saturation based on porosity data for the Qbt3 unit.

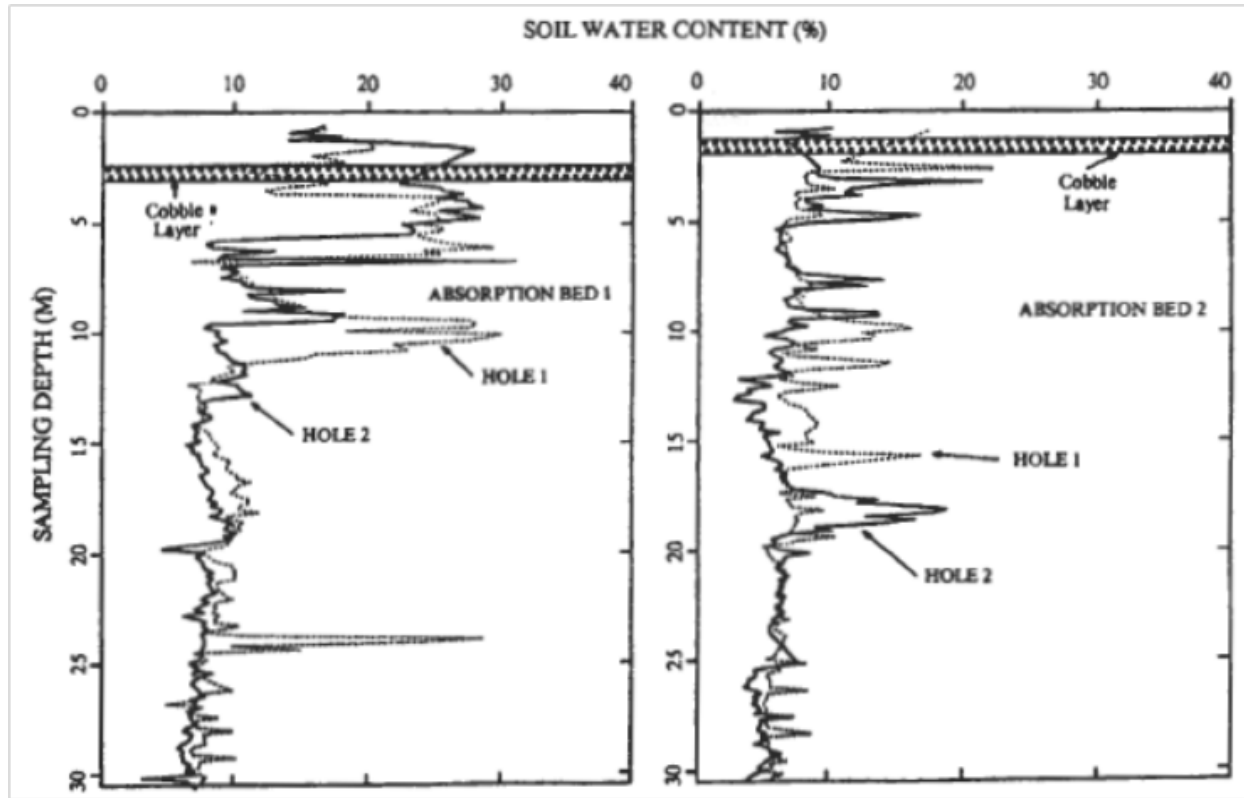


Figure 10
Depth profiles of gravimetric water content under bed #1 (left)
and bed #2 (right) from 1978 (taken from LANL 2004, Figure B-24)

2.3.3 *Nature and Extent of Contamination*

The nature and extent of contamination at MDA T are described in detail in the MDA T reports described above. To summarize some of the findings in those reports, the radionuclides plutonium and americium were detected to depths of 342 and 109.5 ft bgs, respectively, and tritium was detected to 425 ft bgs. Depth profiles of plutonium activities are shown in Figure 11. Depth profiles of americium and tritium activities from core samples are shown in Figure 12. Activities in Figures 11 and 12 are plotted in log scale because they drop off several orders of magnitude with depth. Depth profiles of tritium activities measured in vapor samples are shown in Figure 13, where elevated tritium is observed at a depth of 475 ft in monitoring well 21-25262. Strontium-90 was detected at an activity of 0.348 pCi/g at a depth interval of 800 to 802 ft bgs in borehole 21-607955. However, this detection is considered to be anomalous because strontium-90 was not detected between depths of 179 ft and 800 ft bgs.

Perchlorate, nitrate and fluoride were detected in core samples at depths of 695, 680, and 766 ft bgs, respectively (Figs 14). Metals have not migrated as deep as other hazardous constituents (LANL 2006a). No samples were collected beneath the shafts during the investigations at MDA T, so it is not known if radionuclides have migrated from the shafts.

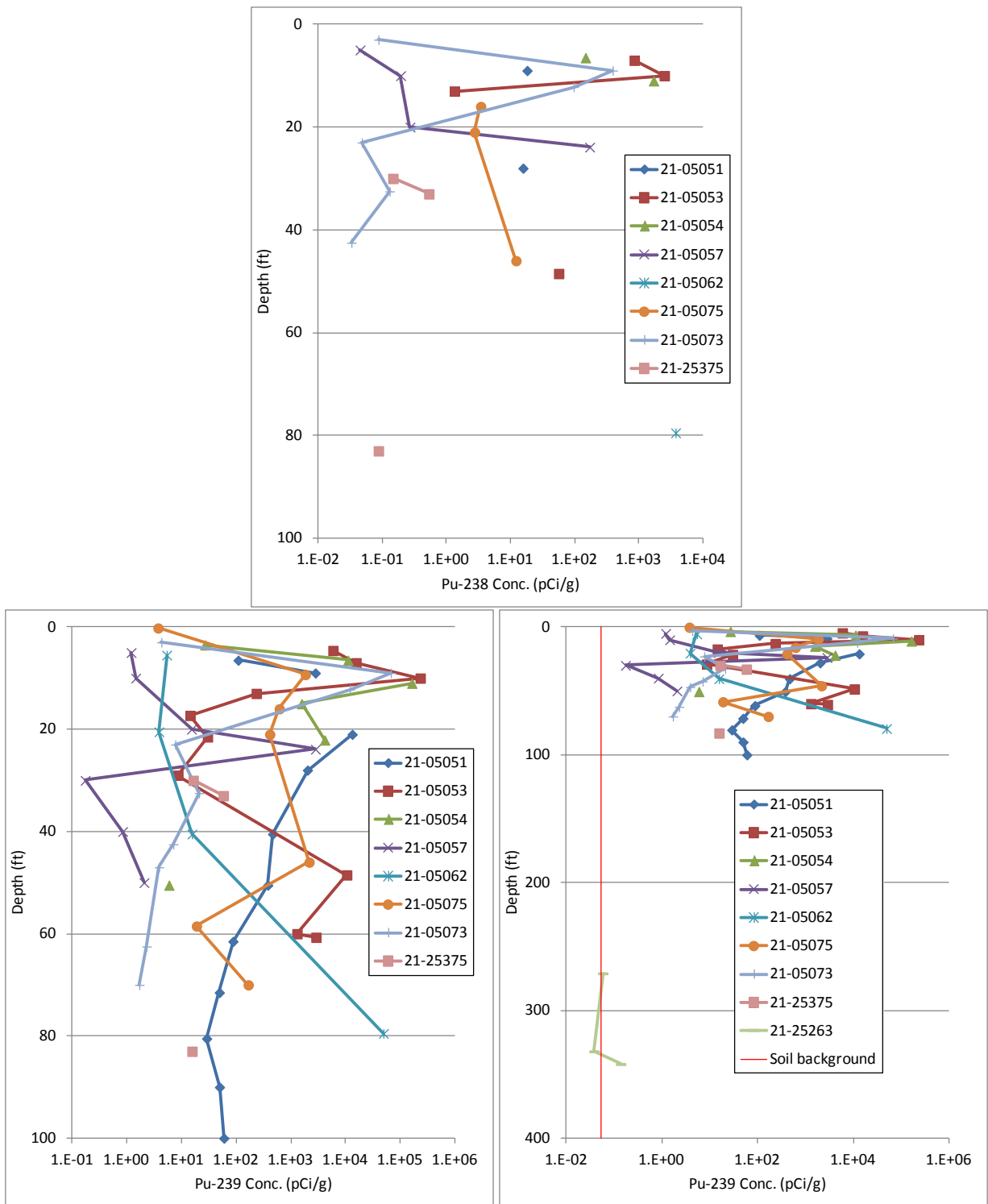


Figure 11
Depth profiles of Pu-238 (top) and Pu-239 (bottom) detections above background values in MDA T boreholes.

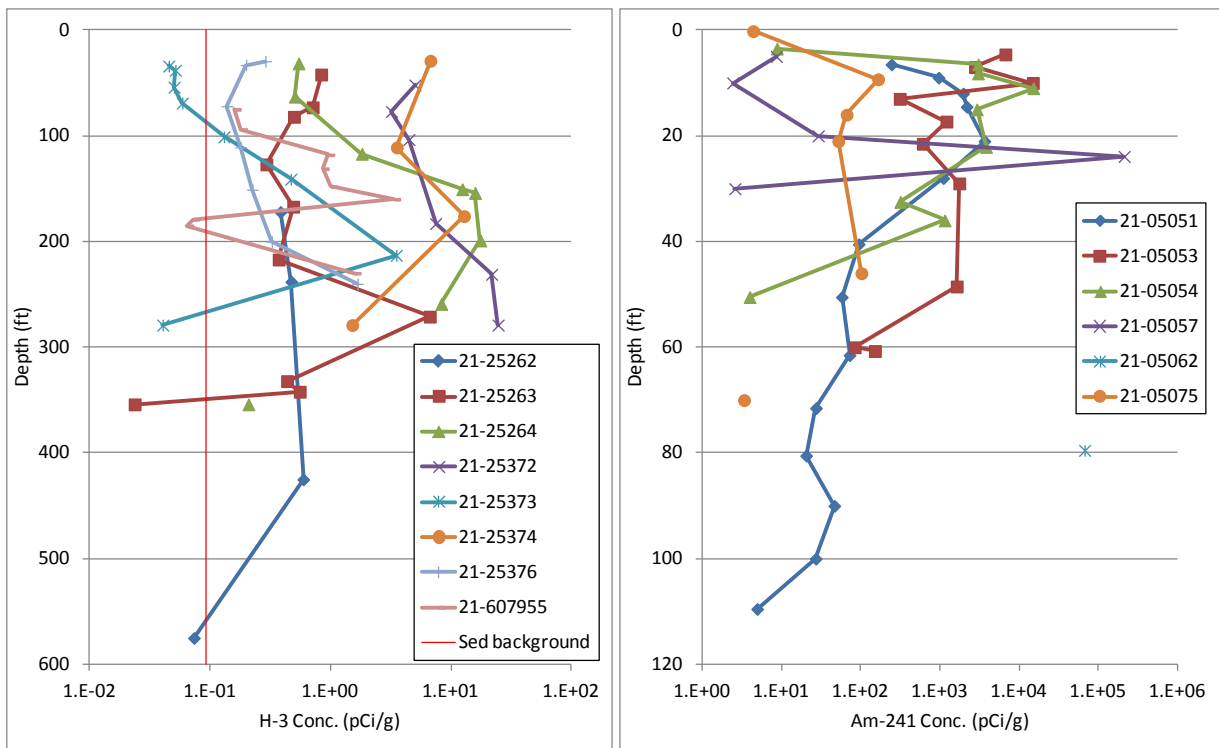


Figure 12
Depth profiles of tritium (left) and Am-241 (right) detections above background values in MDA T boreholes.

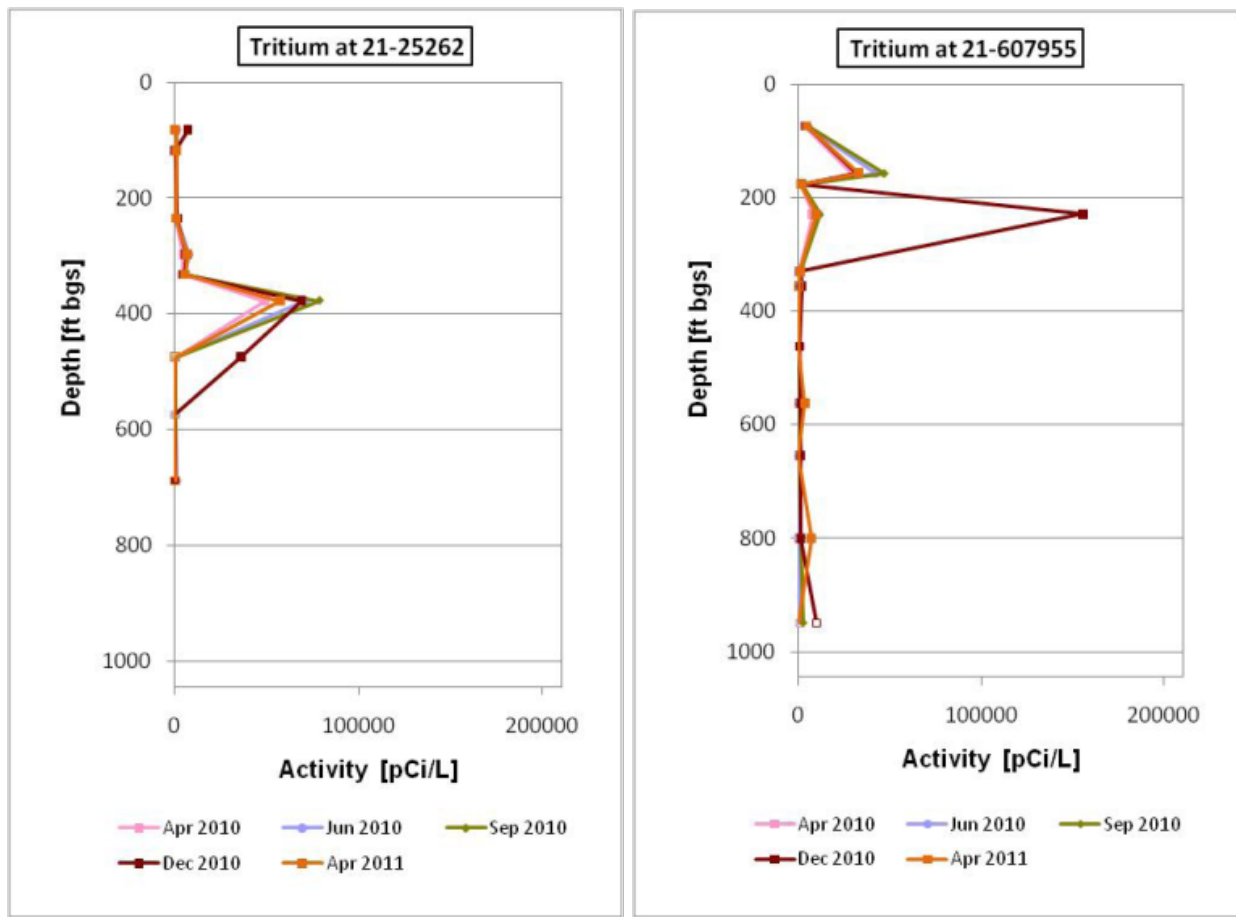


Figure 13
Depth profiles of tritium concentrations from vapor monitoring wells
21-25262 and 21-607955 (taken from LANL 2011b, Fig. 5.2-2)

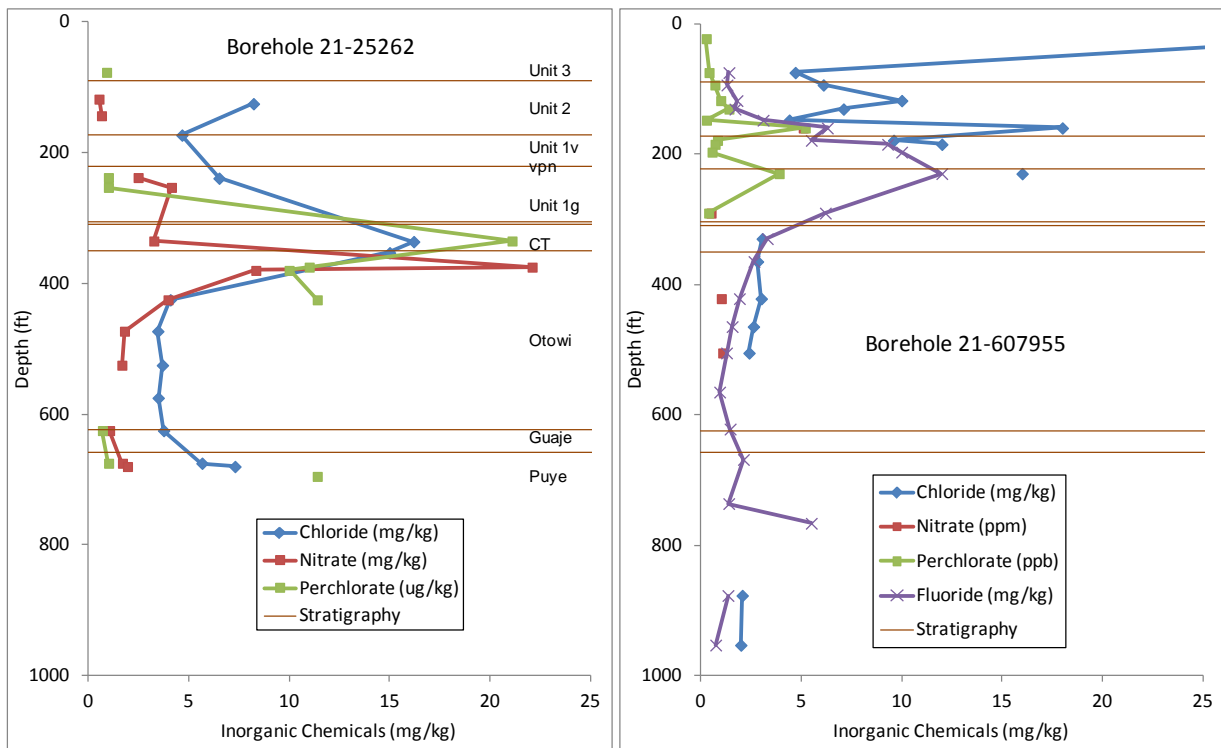


Figure 14
Depth profiles of selected chemical concentrations from core from boreholes 21-25262 (left) and 21-607955 (right)

Maximum concentrations of total VOCs measured in vapor samples appear to have reached depths of about 575 ft bgs (Figure 15). Depth profiles of trichlorethene (TCE) are shown in Figure 16, where elevated concentrations occur to a maximum depth of 654 ft bgs in vapor monitoring well 21-607955.

Historical plutonium data are also included to provide a snapshot of plutonium distributions with depth during and after wastewater disposal in the four absorption beds. Depth profiles of plutonium and americium measured in 1978 are shown in Figure 17 and depth profiles of plutonium measured in 1953, 1960, and 1978 are shown in Figure 18.

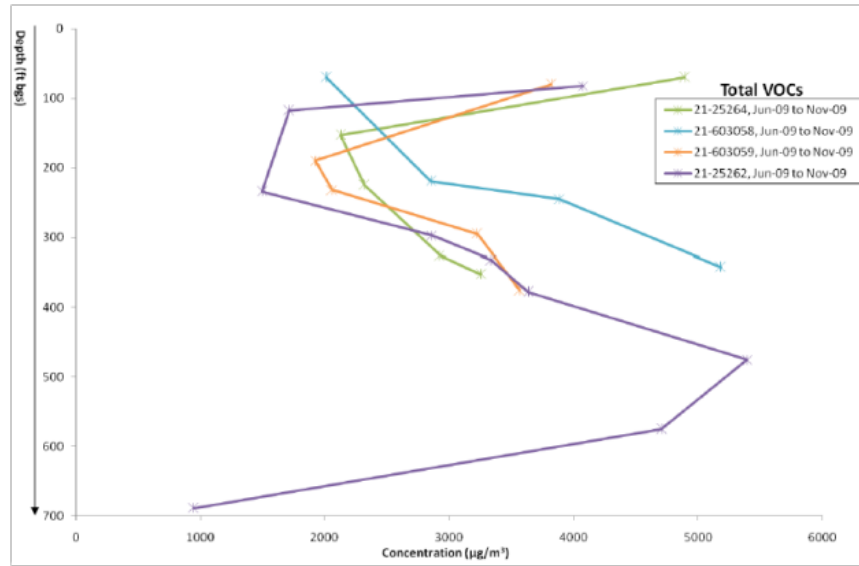


Figure 15
Depth profiles of total VOC concentrations in 2009 from four MDA T vapor monitoring wells (taken from LANL 2009, Fig. 6.3-1)

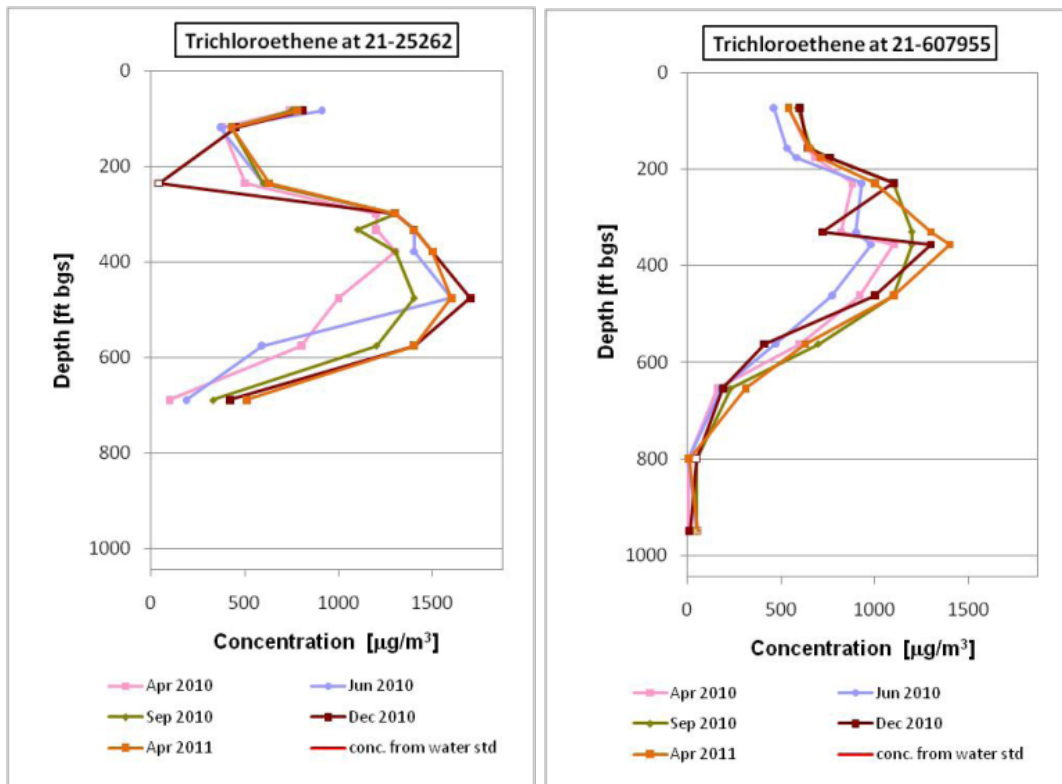


Figure 16
Depth profiles of TCE concentrations in vapor from boreholes 21-25262 and 21-607955 (taken from LANL 2011b, Fig. 5.1-5)

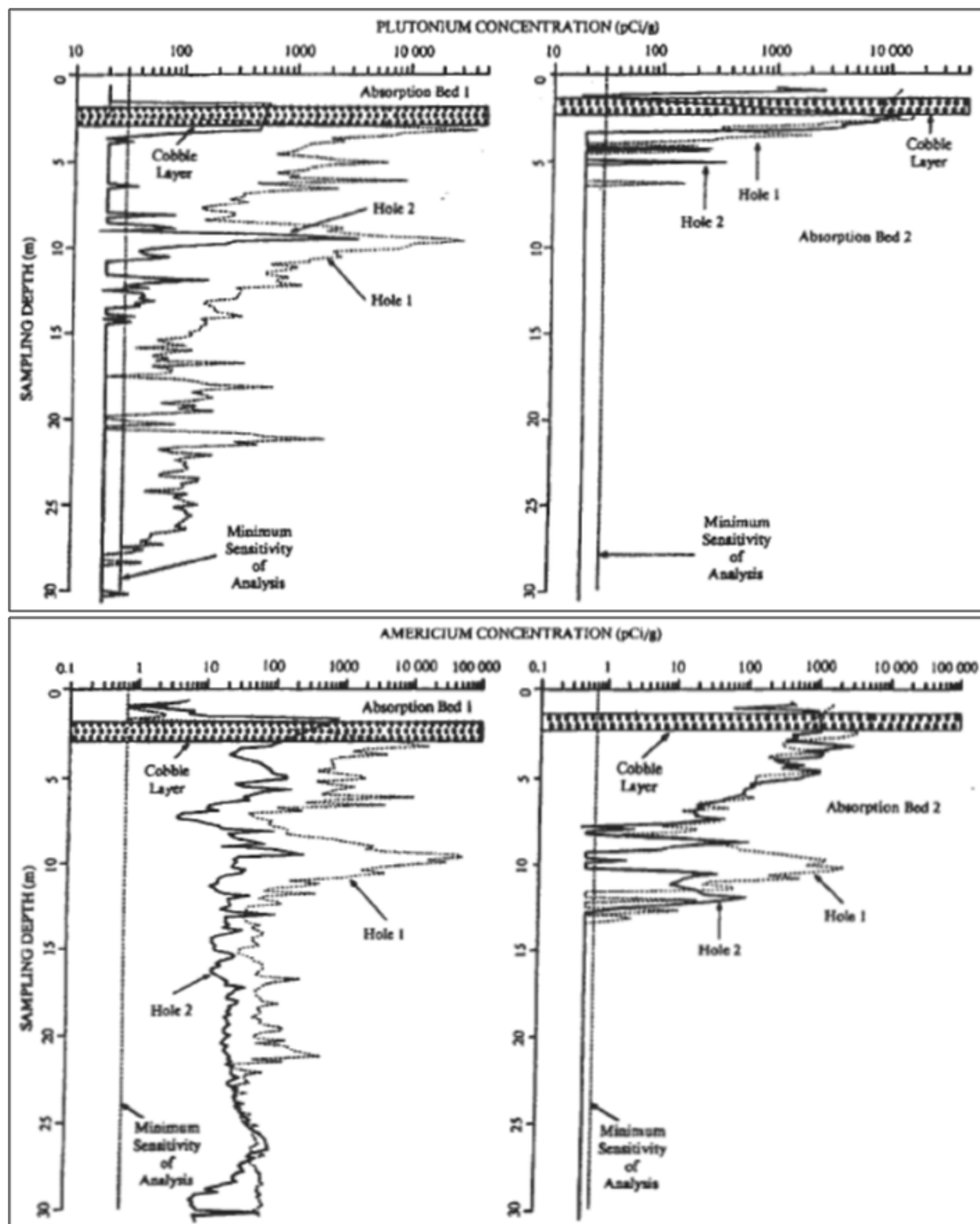


Figure 17
Depth profiles of 1978 concentrations of plutonium (top) and americium (bottom)
measured in core under bed #1 (left) and bed #2 (right) (taken from LANL 2004, Figs. B-22 and B-23)

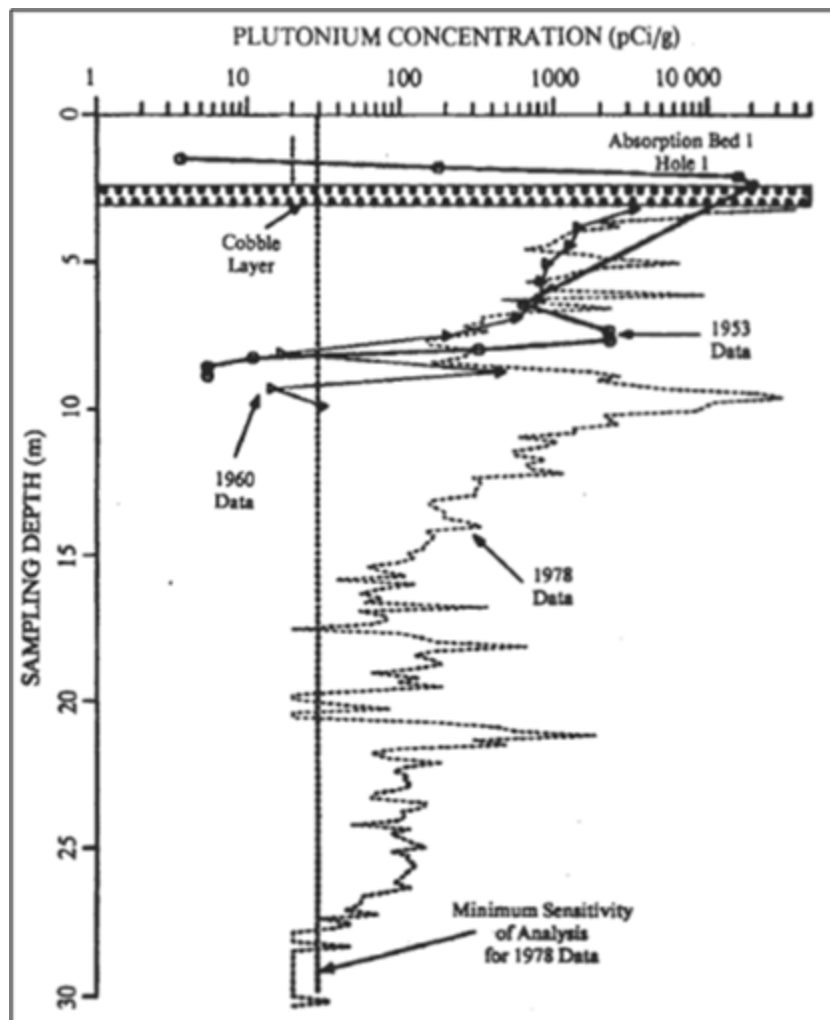


Figure 18
Depth profiles of concentrations of plutonium measured in core under bed #1 in 1953, 1960, and 1978 (taken from LANL 2004, Fig. B-25)

3.0 Methods

The MDA T groundwater pathway modeling effort included the development of two 3-D models capable of simulating the transport of water-soluble radionuclides released from the absorption beds and disposal shafts at MDA T and will ultimately include the abstraction of this complex model to a 1-D form suitable for implementation within GoldSim. As was the case for the 2011 groundwater pathway update for Area G (Stauffer et al., 2013) and the 2005 groundwater pathway model (Stauffer et al., 2005), the 3-D modeling was conducted using FEHM (Zyvoloski et al., 1995a, 1995b, and Zyvoloski, 2007). Stochastic modeling of groundwater transport can, potentially, require thousands of simulations. Given the computationally-intensive nature of FEHM simulations, 1-D abstractions of the 3-D model will be developed from the results of this study for use in the probabilistic analyses (see Section 3.2). The GoldSim model controls these 1-D model abstractions, allowing the bulk transport properties of the subsurface for all radionuclides undergoing groundwater transport to be modified as desired.

The 3-D modeling requires a numerical mesh that represents the topography and geology of MDA T and the surrounding area. Section 3.1 describes how the mesh was developed and the 3-D model configured to enable more realistic simulations of flow and transport.

3.1 *Three-Dimensional Model Development*

Two 3-D computational meshes were developed for flow and transport simulations from MDA T. The first mesh encompasses the entire area of TA-21 and has relatively large mesh cells (especially at depth); this is referred to as the mesa-scale (Mesa) mesh. The second 3-D mesh, which encompasses an area surrounding MDA T, is referred to as the local-scale (Beds) mesh. The local-scale mesh was developed after it became apparent that the coarse mesh resolution at depth in the mesa-scale mesh adversely affected water flow simulations.

The geometry of the GFM09 is defined with a 3-D geocellular model of the Pajarito study area and encompassing DP mesa, DP canyon, and Los Alamos Canyon. The framework stratigraphy is formed through a process that creates a 3D model from disparate input data. The process simplifies the available data near the model area and extrapolates from widely spaced data in other areas of the model domain. The Weston Solutions Inc. 2009 GFM (WC09) used for these studies is updated with information not previously available and includes 2009 updates that incorporate the geologic information contained in 330 wells and 25 cross sections that are available for the Pajarito Plateau and described in Cole et al. (2009). The WC09 series of the GFM is constructed using Earthvision by Dynamics Graphics Inc. The WC09 is evolving as new data are acquired and geologists view and evaluate the resulting GFM. The version used for this model is the December 2009 WC09 model and includes a paleochannel subset that gives special

attention to the paleochannel and overburden around the MDA T site. The area used for the MDA T model is shown in Figure 19 (red box). Details on the development of the WC09 are included in this report as *Attachment I*.

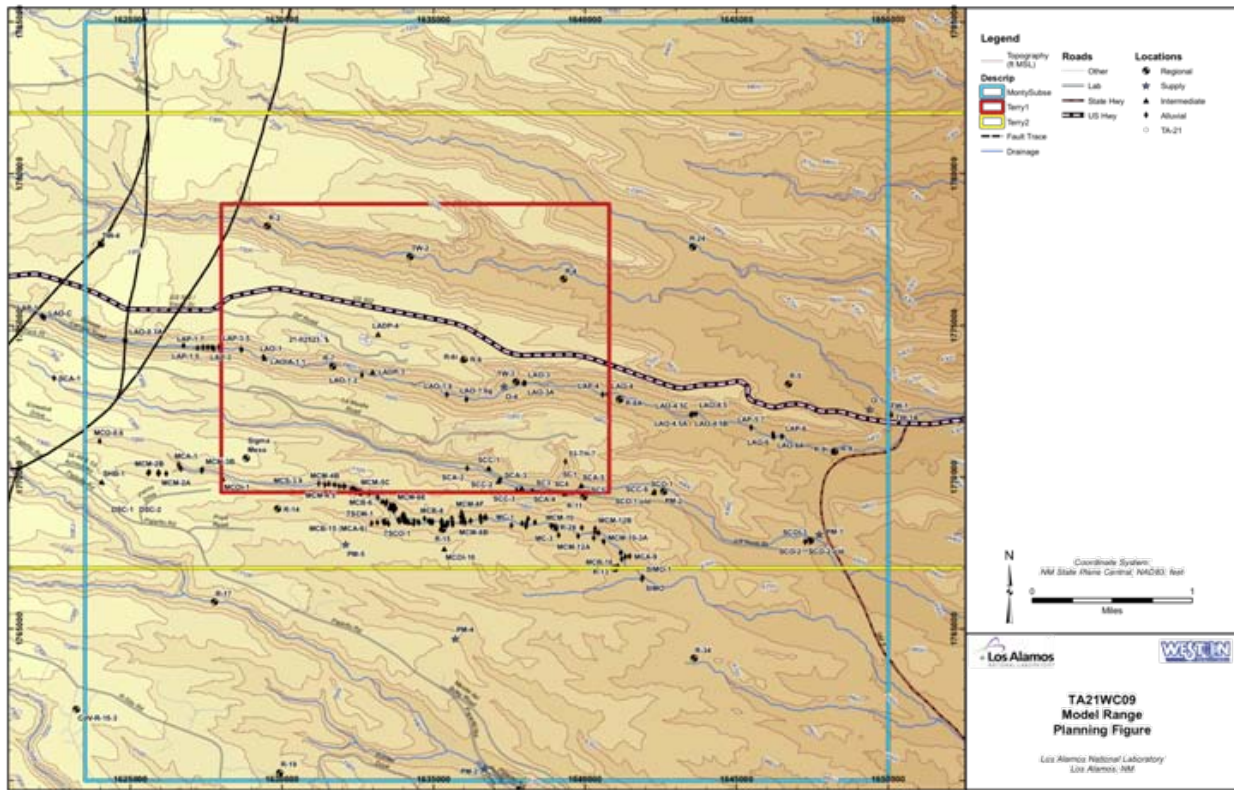


Figure 19
MDA T Model Domain within the WC09 GFM

Section 3.1.1 discusses the development of the two 3-D model meshes, Section 3.1.2 explains how the model was configured to simulate site conditions, and Section 3.1.3 presents the hydrogeologic input data used to populate the model. Descriptions of the simulations that were conducted in support of the groundwater modeling effort are presented in Section 3.1.4.

3.1.1 Development

The two 3-D meshes used to conduct the groundwater modeling are designed to meet several conditions. The first mesh built was a mesa-scale mesh (Figures 21 and 22a), and the second is a high-resolution, local-scale mesh around MDA T that maintains 1-m vertical spacing to the regional aquifer (Figure 22b).

- The mesa-scale mesh created includes the entire TA-21 footprint and was developed to allow long-term modeling such as contaminant migration to the regional aquifer from all waste sites at TA-21.
- Both meshes includes high resolution regions adequate to accurately locate features such as absorption beds
- Both meshes incorporates a recent 3-D GFM (WC09) to define the hydrogeologic layers
- The high resolution local-scale mesh captures hydrogeologic layer resolution on the meter scale to provide accurate solutions of unsaturated flow and streamline-particle-tracking

The ground surface for both meshes is based on the DEM shown in Figure 20. Figure 21 shows the extent of the mesa-scale mesh. Figure 22 shows the high-resolution, local-scale mesh embedded in the mesa-scale mesh to show how the high resolution mesh more accurately captures the stratigraphy in the deeper parts of the mesa. This resolution is vital for the simulations of transport because the larger mesh blocks in the mesa-scale model create numerical diffusion of the wetting front leading to less vertical penetration than seen in the high resolution local-scale mesh. More details on the two meshes can be found in *Attachment II*.

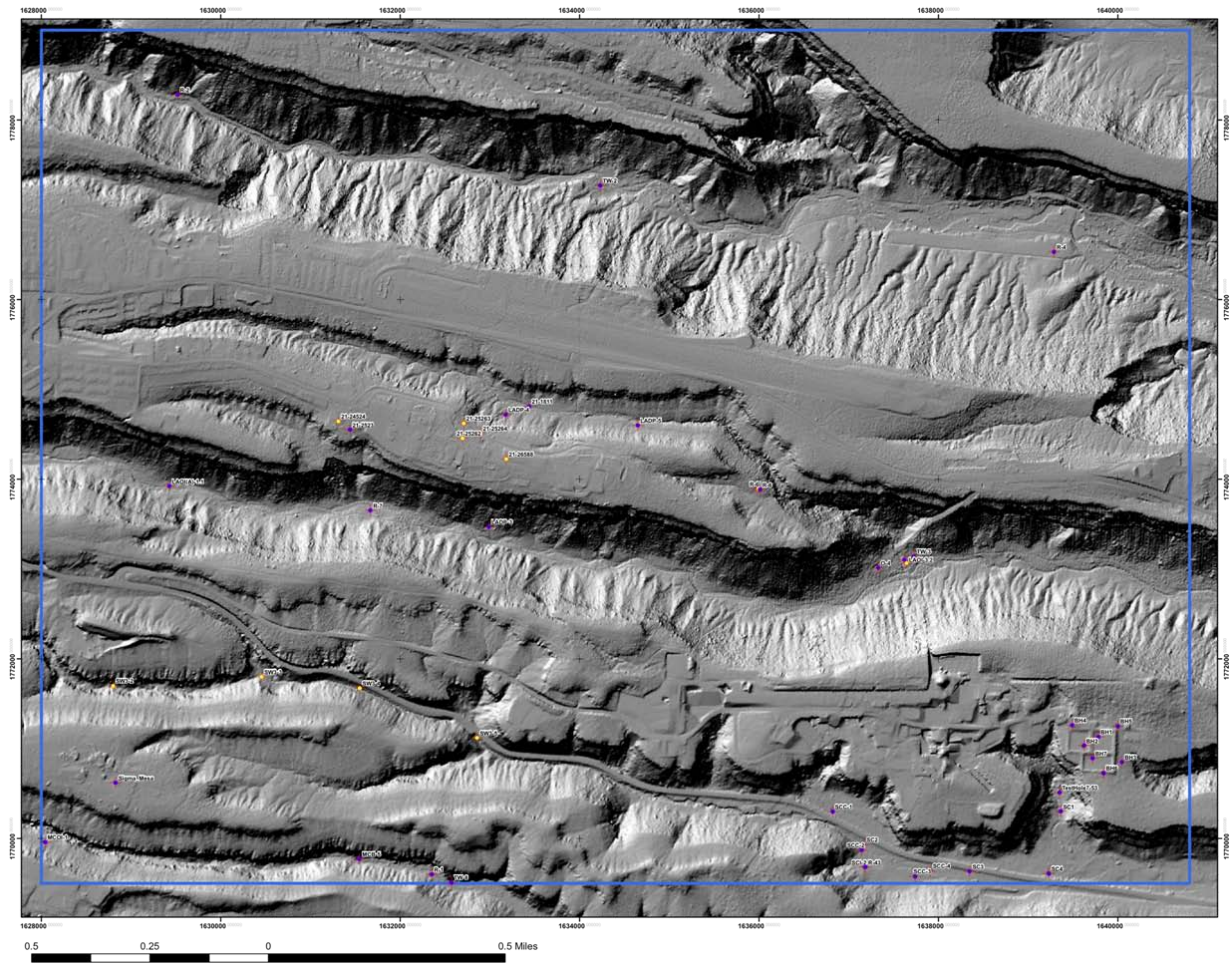


Figure 20
Digital Elevation Model and drillhole locations used for the MDA T GFM

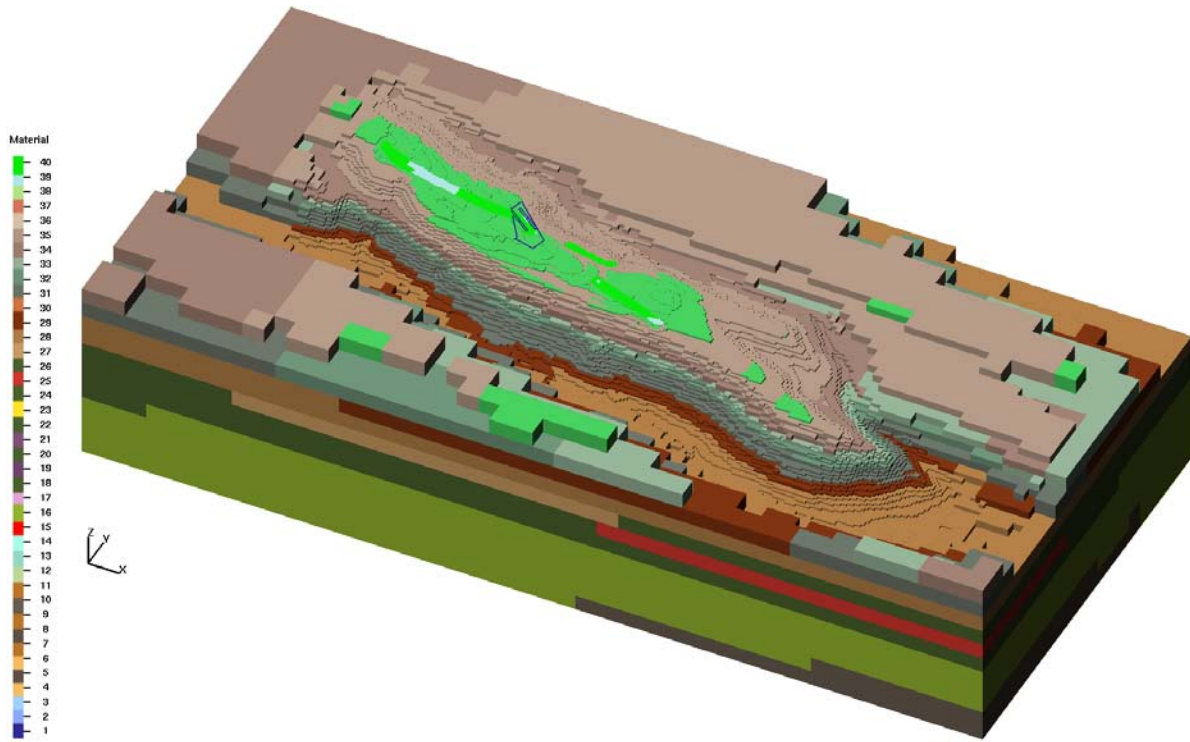


Figure 21
Mesa-scale mesh of TA-21

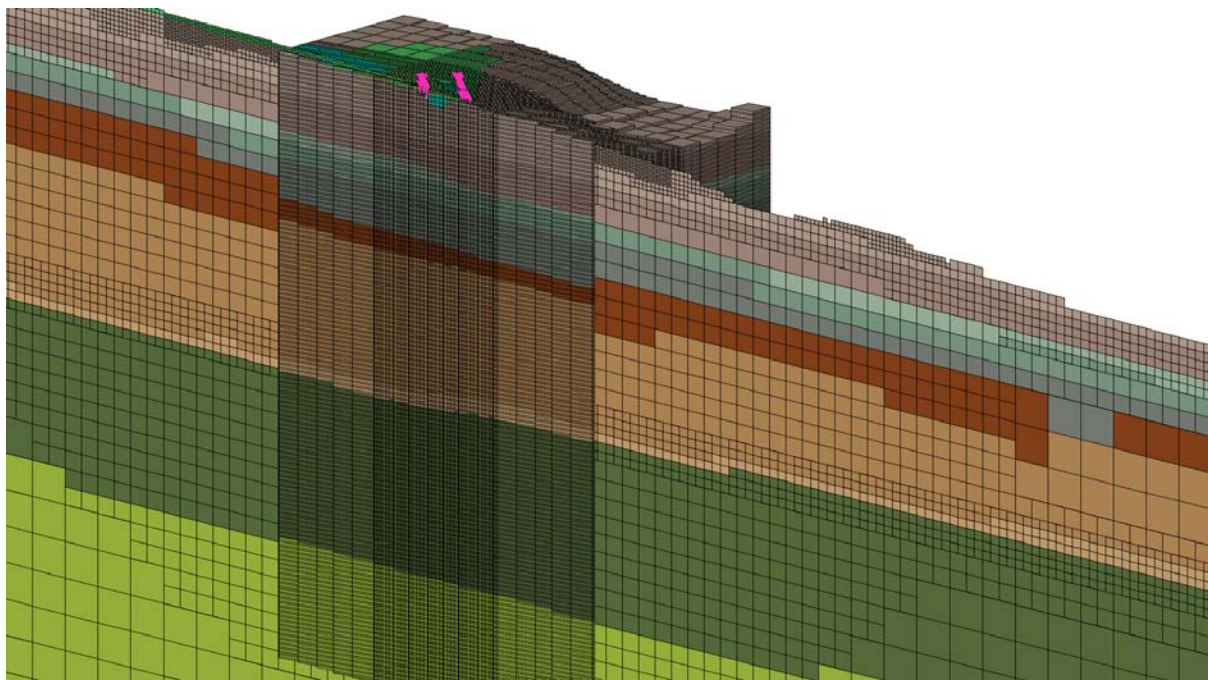


Figure 22a
Slice of the mesa-scale mesh with one half of the high-resolution, local-scale mesh centered on MDA T. Adsorption beds are plotted in bright pink on the surface. The local-scale mesh extrudes behind the slice. The bottom of the local-scale mesh extends to 7 m below the regional aquifer.

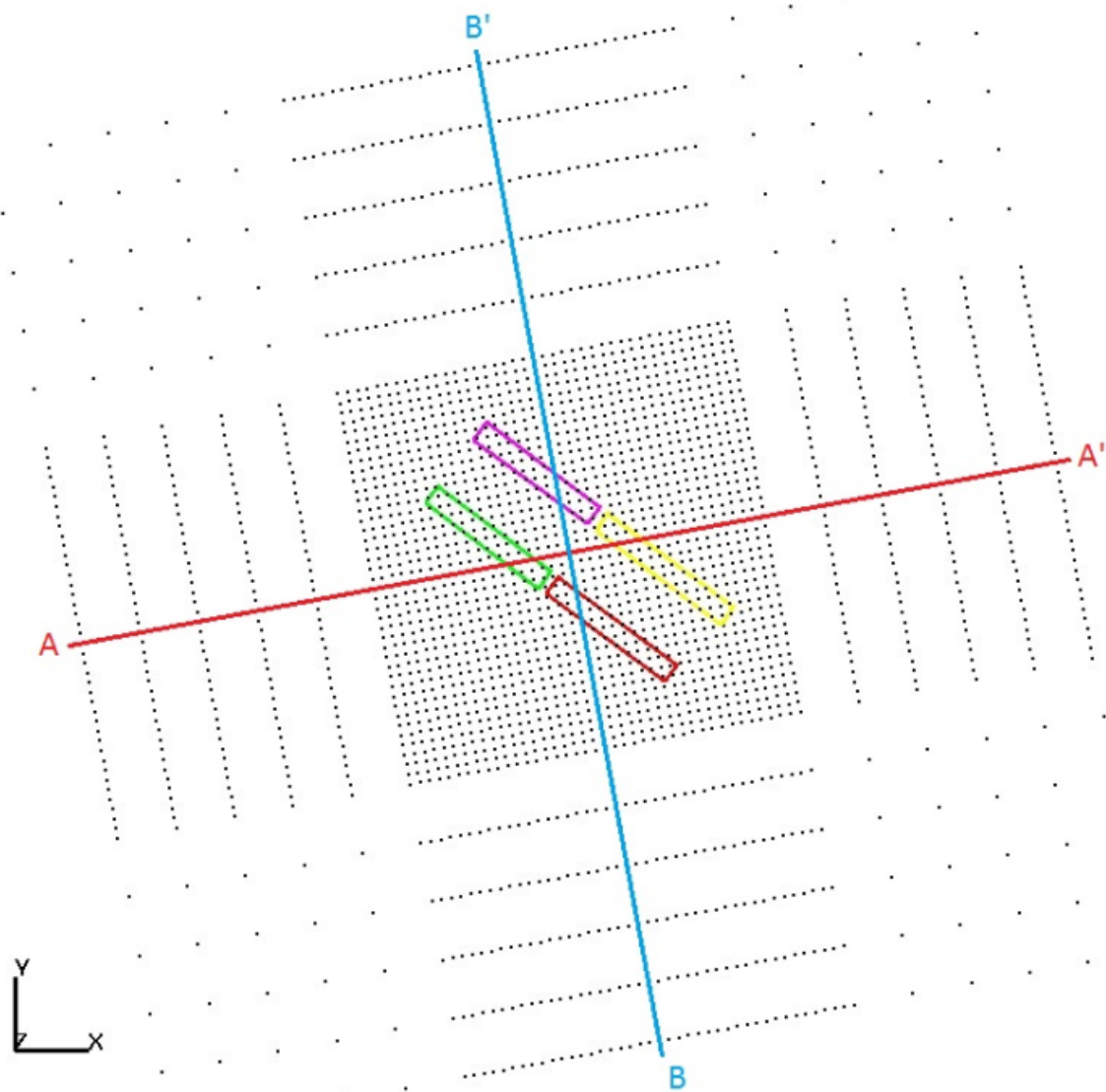


Figure 22b

High-resolution, local-scale mesh. Bed one is green, two red, three purple and four yellow. Mesh spacing is 1 m (3.28 ft) in the z direction from the surface to 7 m below the water table.

3.1.2 Model Configuration and Boundary Conditions

The 3-D mesa-scale model was used for initial calculations that advanced the understanding of this unique system. However, as more was learned about the behavior of the wetting front, it was determined that a higher vertical resolution mesh was needed to accurately capture the propagation of the wetting front to depth. Thus, the high resolution local-scale 3-D mesh is used to trace the travel times of particles released from MDA T and to generate conservative breakthrough curves, otherwise known as residence time distribution functions (RTDs). Because the RTDs vary with release location and infiltration rate, the complexity of the model is reduced by adopting a number of assumptions and boundary conditions that constrain the groundwater transport model and simplify the modeling task.

3.1.2.1 Particle Release Locations

Particle release locations were defined based on the distribution of water and subsurface contaminants found beneath MDA T. Seven regions located beneath the absorption beds were defined as release locations. Each region has a vertical thickness of 35 m (115 ft) and each region is stacked to encompass a total depth from ground surface to 245 m (804 ft) bgs. Within each region, particle release points are located at the areas having the highest simulated saturations (Figure 23). One additional region is located in the middle of the shaft field at a depth of 19 m (62.3 ft) bgs, located in map view on Figure 22b at the intersection of A-A' with B-B'. This scheme implies that contaminants released during the GoldSim step of the modeling will collapse all mass between two release locations onto the lower location, thus ensuring that the simulations do not under-predict travel times for contaminants to the regional aquifer based on the conceptualized mass distribution. This is a necessary step to reduce the complexity of the 3-D model for use in the 1-D abstractions needed in GoldSim.

Particle breakthrough was specified relative to the water table which was defined as a horizontal plane located 392 m (1286 ft) beneath the ground surface of bed 1 at MDA T. Table 3 provides the model coordinates of the particle release locations for each of the eight regions. Although MDA G analysis included a compliance boundary 100 m from the site boundary, travel times in the regional aquifer are short compared to transport in the unsaturated zone, and the water table breakthrough will be nearly identical.

Table 3
Particle Release Locations at MDA T

| Particle Set | Infiltration Rate (mm/yr) | Easting (m) | Northing (m) | Depth (m, ft) |
|-----------------------------|------------------------------|----------------|-----------------|------------------|
| Absorption Beds Depth #1 | 10 | 497661 | 540870 | 35, 115 |
| | 5 | 497661 | 540870 | |
| | 1 | 497661 | 540870 | |
| | 0.1 | 497654 | 540868 | |
| Absorption Beds Depth #2 | 10 | 497645 | 540881 | 70, 230 |
| | 5 | 497643 | 540883 | |
| | 1 | 497656 | 540884 | |
| | 0.1 | 497649 | 540873 | |
| Absorption Beds Depth #3 | 10 | 497657 | 540877 | 105, 334 |
| | 5 | 497657 | 540871 | |
| | 1 | 497650 | 540872 | |
| | 0.1 | 497650 | 540867 | |
| Absorption Beds Depth #4 | 10 | 497655 | 540869 | 140, 459 |
| | 5 | 497651 | 540867 | |
| | 1 | 497650 | 540867 | |
| | 0.1 | 497646 | 540869 | |
| Absorption Beds Depth #5 | 10 | 497654 | 540865 | 175, 574 |
| | 5 | 497653 | 540867 | |
| | 1 | 497647 | 540868 | |
| | 0.1 | 497647 | 540868 | |
| Absorption Beds Depth #6 | 10 | 497644 | 540849 | 210, 689 |
| | 5 | 497650 | 540854 | |
| | 1 | 497650 | 540854 | |
| | 0.1 | 497650 | 540854 | |
| Absorption Beds Depth #7 | 10 | 497638 | 540841 | 245, 804 |
| | 5 | | | |
| | 1 | | | |
| | 0.1 | | | |
| Shafts | 10 | 497657 | 540869 | 19, 62 |
| | 5 | | | |
| | 1 | | | |
| | 0.1 | | | |

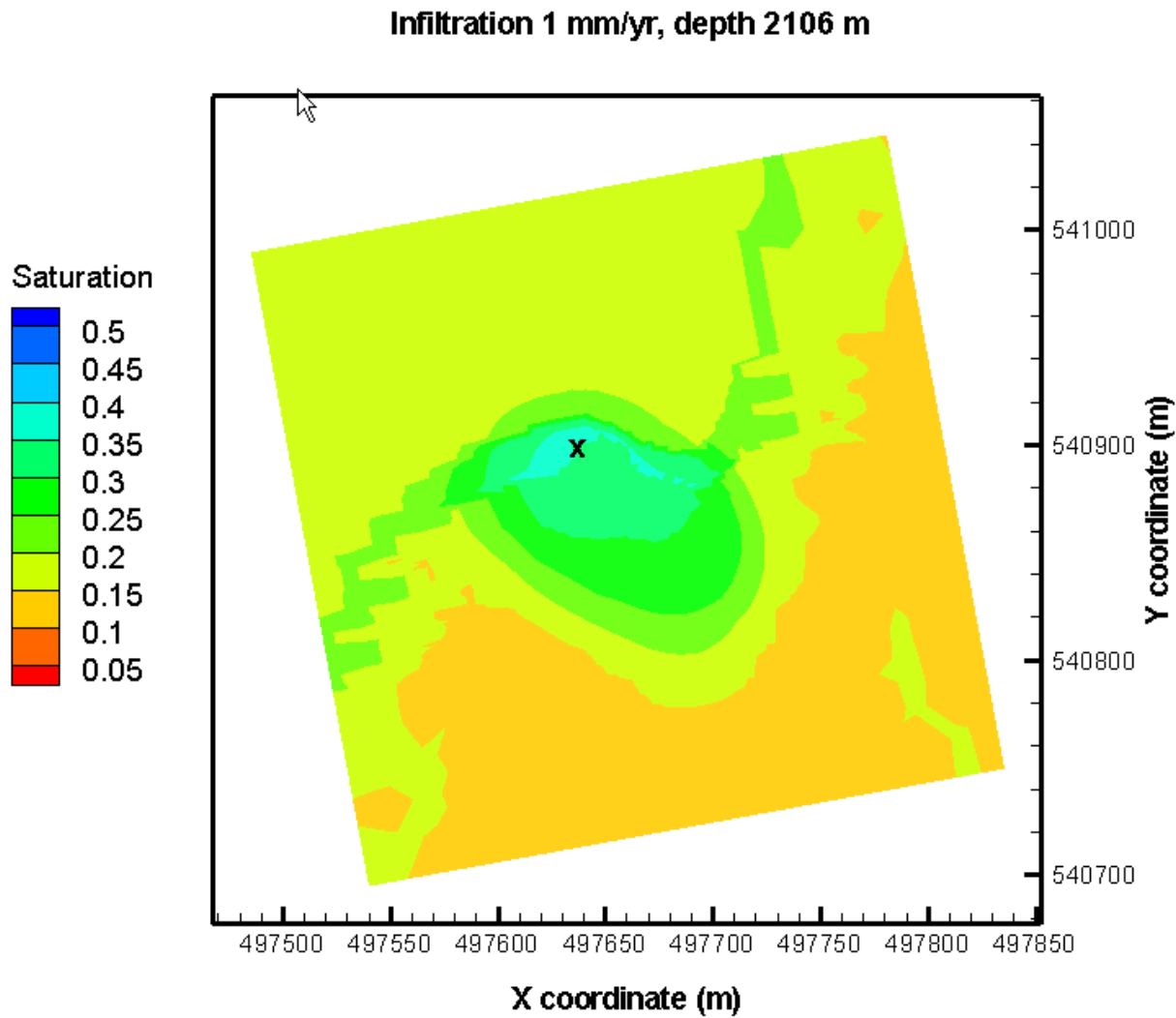


Figure 23
Particle release location and saturation distribution for 1 mm/yr infiltration scenario at elevation 2106 m (230 ft bgs)

Figure 24 shows the particle release locations for four infiltration scenarios (from left to right: 10, 5, 1 and 0.1 mm/yr) at seven elevation levels with intervals of 35 meters (from top to bottom: 2141 m (115 ft bgs), 2106 m (230 ft bgs), 2071 m (344 ft bgs), 2036 m (457 ft bgs), 2001 m (574 ft bgs), 1966 m (689 ft bgs) and 1931 m (804 ft bgs) above mean sea level). Note the release location for the 10 mm/yr infiltration scenario at an elevation of 1931 m was used for the 5, 1 and 0.1 mm/yr infiltration scenarios because the saturations are too evenly distributed at that elevation to choose a location. This also applies for the 5 mm/yr infiltration scenario at an elevation of 1966 m that was used for the 1 and 0.1 mm/yr infiltration scenarios; the 1 mm/yr infiltration scenario at an elevation of 2001 m was used for the 0.1 mm/yr infiltration scenarios; and the 1 mm/yr infiltration scenario at an elevation of 2141 m was used for the 10 and 5 mm/yr infiltration scenarios.

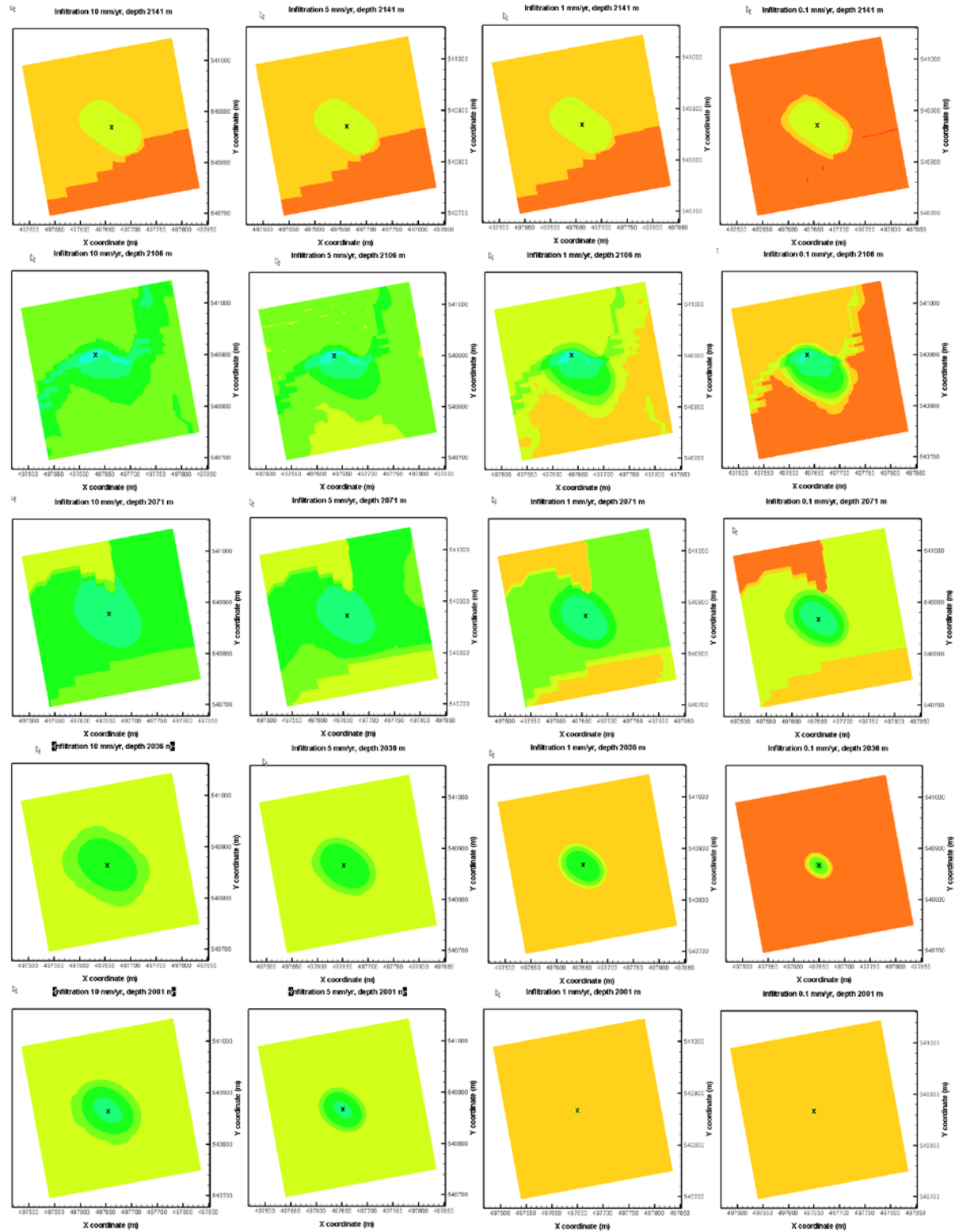


Figure 24a
Particle release locations and saturation distributions for various infiltration scenarios and elevations (from left to right: 10, 5, 1 and 0.1 mm/yr) and from top to bottom in 35 m depth intervals. Color bar for saturation is shown in Figure 23.

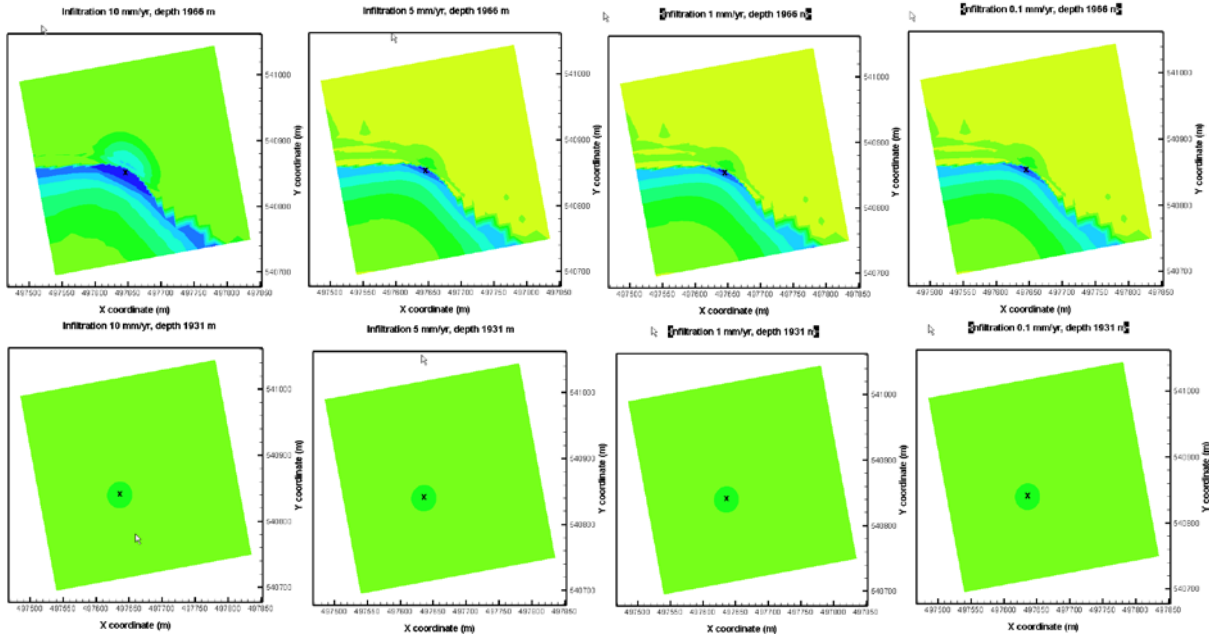


Figure 24b

Particle release locations and saturation distributions for various infiltration scenarios and elevations (from left to right: 10, 5, 1 and 0.1 mm/yr) and from top to bottom in 35 m depth intervals. Color bar for saturation is shown in Figure 23.

3.1.2.2 Infiltration

Long-term infiltration on the mesa is one of the primary uncertainties in simulations of contaminant transport from MDA T to the water table. For this study, it was assumed that the hydrology at MDA T will return to conditions similar to an undisturbed mesa-top site, especially after final closure. To capture the uncertainty in transport travel times through the unsaturated zone, a probability distribution that spans a reasonable range of infiltration rates was used. This distribution was based on data compiled from almost 200 mesa-top infiltration estimates from various modeling, field experiment, and chloride mass balance studies to estimate rates of infiltration (Springer and Schofield, 2004). A statistical analysis shows that the infiltration data are trimodal, with modal values around 0, 15, and 60 mm/yr (0, 0.59, and 2.4 in./yr) (Springer and Schofield, 2004, Fig. 4). In their analysis, Springer and Schofield indicated that infiltration rates greater than 10 mm/yr (0.39 in./yr) were typically associated with disturbed sites.

Infiltration rates adopted for the groundwater transport modeling are 10 mm/yr or less. Four long term infiltration rates were identified as bounding values for MDA T (0.1, 1, 5, and 10 mm/yr), and were used to create a series of 3-D RTD breakthrough curves for releases from the seven waste locations under the absorption beds depths, and one waste location under the disposal shaft region. This resulted in the creation of 32 unique breakthrough curves that can be sampled within GoldSim and used to generate the 1-D pipe pathways needed for calculating contaminant migration to the compliance boundary. In this approach, GoldSim samples the actual, continuous

infiltration rate distribution during model simulations and selects the breakthrough curve that most closely corresponds to this rate within the waste location under consideration. The discretization of the infiltration distribution in the manner described above provides a mechanism for considering the effects of variable infiltration rates on facility performance while maintaining model complexity at a reasonable level.

Potential groundwater-pathway risks are expected to be small at low rates of infiltration. However, at infiltration rates of 5 and 10 mm/yr (0.079 to 0.39 in./yr), the possibility for particle breakthrough to the water table increases substantially.

Each infiltration, or mass flow, value (kg/yr) was assigned to every surface node within the numerical model. This value represents the product of the desired infiltration rate (mm/yr), the surface area over which infiltration occurs (m^2), and the density of water ($1,000 \text{ kg/m}^3$ [62 lb/ft 3]). For example, if a node has a surface area of 1.0 m^2 (11 ft 2) and the desired infiltration rate is 1.0 mm/yr (0.039 in./yr), the infiltration value would be 1.0 kg/yr or $3.2 \times 10^{-8} \text{ kg/s}$.

3.1.2.3 Wastewater Application to Beds

The time series of wastewater discharge to the four absorption beds was taken from Table B-3 of LANL (2004). This time series is shown in Figure 25. No information is available on the distribution of relative amounts of wastewater among the four beds. Based on the configuration of the pipelines, it is known that bed #1 received the most wastewater, following by bed #2, and then about equal amounts to beds #3 and #4. The split among the beds was estimated as follows: 45%, 35%, 10%, and 10% for beds #1, #2, #3, and #4, respectively. The total volume of water disposed at MDA T and the distribution of that water between the beds is uncertain, but those uncertainties were not considered in the simulations. In addition to the documented amounts of wastewater disposed into the absorption beds, Christensen and Thomas (1962) describe infiltration tests that were conducted at bed #1 in the summers of 1960 and 1961. The additional water amount of about 900,000 gallons was included in the FEHM simulations, bringing the total water disposed in the absorption beds to 19.2 million gallons. The time series of water application to all absorption beds is shown in Figure 26.

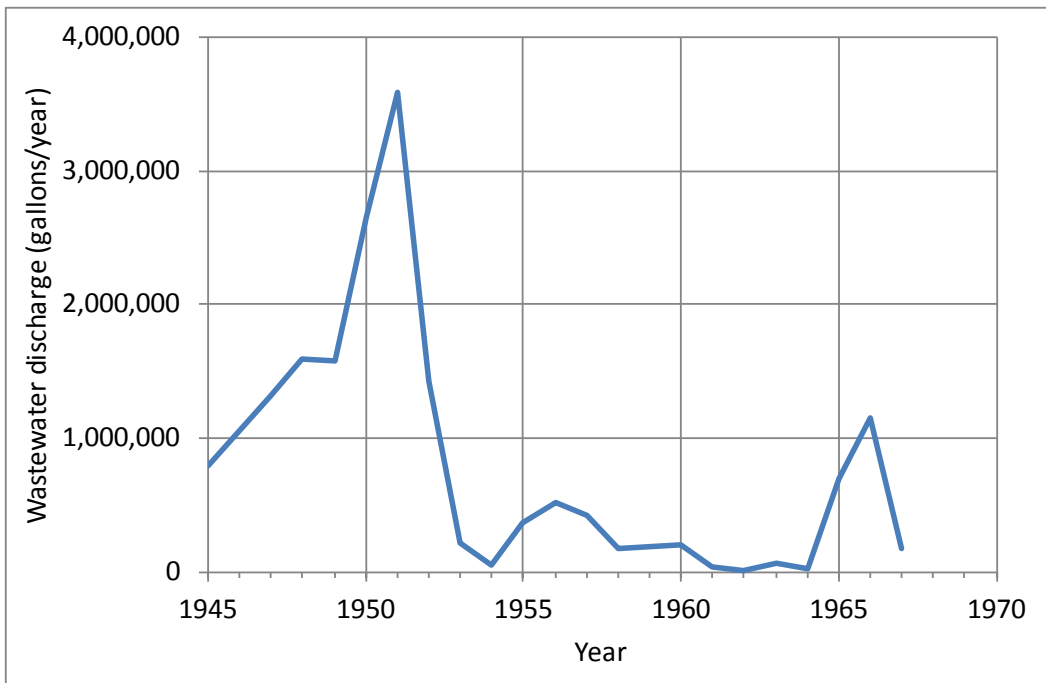


Figure 25
MDA T wastewater disposal history (adapted from LANL, 2004, Table B-3)

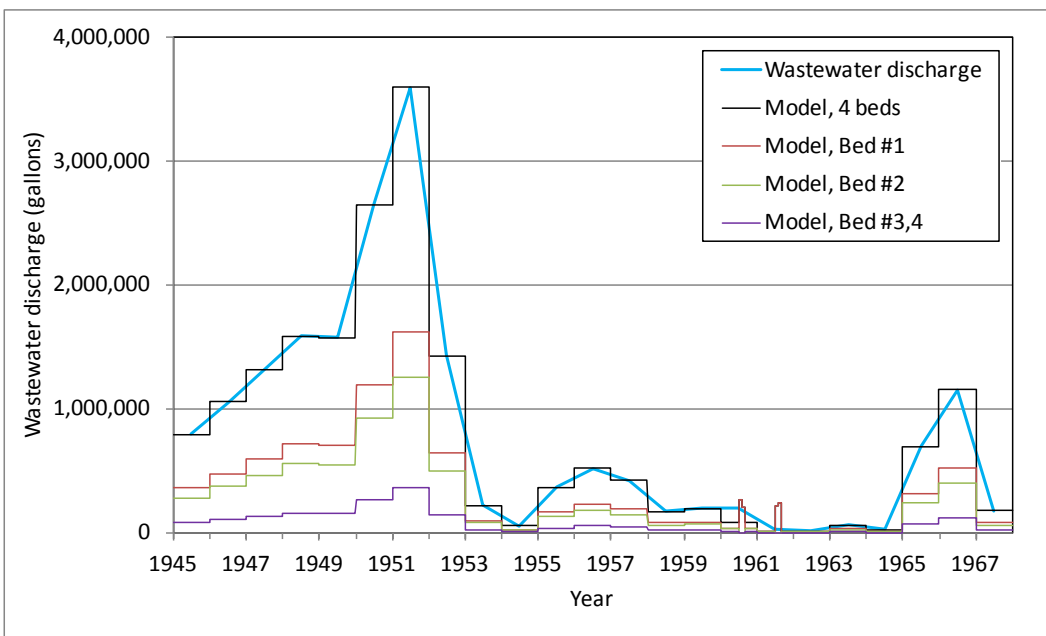


Figure 26
MDA T wastewater disposal history and application to absorption beds in FEHM.

3.1.2.4 Boundary Conditions

All lateral boundaries in the vadose zone were assumed to be no-flow boundaries, that is, no mass could enter or leave the system via these boundaries. Lateral gradients on these boundaries were not considered. Although the water applied to the beds remains mostly well away from the lateral boundary, in some of the higher background infiltration cases, water does reach the boundary during the initial 65 yrs of simulation time. This leads to slightly less spreading than if the mesh had a larger lateral extent. Water reaching the lateral boundary will tend to cause slightly more downward migration than would be seen if the mesh were more laterally extensive, thus this boundary condition does not cause under-prediction of particle arrival times.

3.1.3 Hydrogeologic Input Data

The hydrogeologic properties used in the modeling are presented in Table 4 and described in detail in *Attachment III*. Properties were compiled from all available sources including core from recently-drilled boreholes. Permeabilities measured during soil vapor extraction tests at Area G and MDA L were used for fracture properties.

Table 4
Hydrogeologic Properties Used for the Three-Dimensional Model

| Geologic Unit | Bulk Density (kg/m ³) | Permeability (m ²) | | Porosity | van Genuchten Parameters | | |
|-----------------------|--------------------------------------|-----------------------------------|---------|-----------|--------------------------|----------------|----------|
| | | Horiz. | Vert. | | <i>Sat_{res}</i> | α (1/m) | <i>n</i> |
| Tshirege Qbt3 | 1.3E+03 | 2.0E-13 | 2.0E-13 | 5.1E-01 | 2.0E-02 | 6.4E-01 | 2.1E+00 |
| Tshirege Qbt2 | 1.6E+03 | 1.2E-13 | 1.2E-13 | 4.0E-01 | 1.7E-02 | 3.0E-01 | 2.2E+00 |
| Tshirege Qbt1v | 1.3E+03 | 5.1E-13 | 5.1E-13 | 5.1E-01 | 4.0E-03 | 5.4E-01 | 1.7E+00 |
| Vapor Phase Notch | 1.1E+03 | 3.0E-14 | 3.0E-14 | 5.9E-01 | 0.0E+00 | 7.0E-01 | 1.5E+00 |
| Tshirege Qbt1g | 1.2E+03 | 6.8E-13 | 6.8E-13 | 5.6E-01 | 0.0E+00 | 6.3E-01 | 1.6E+00 |
| Tsankawi Pumice | ND | 2.2E-12 | 2.2E-12 | 5.9E-01 | 0.0E+00 | 4.3E-01 | 1.9E+00 |
| Cerro Toledo interval | 1.2E+03 | 7.1E-13 | 7.1E-13 | 5.1E-01 | 0.0E+00 | 5.3E-01 | 1.4E+00 |
| Otowi | 1.2E+03 | 9.8E-14 | 9.8E-14 | 5.3E-01 | 8.0E-03 | 3.0E-01 | 2.0E+00 |
| Guaje Pumice | 8.4E+02 | 1.6E-13 | 1.6E-13 | 6.6E-01 | 0.0E+00 | 2.8E-01 | 2.5E+00 |
| Puye Formation | 2.6E+03 | 8.7E-13 | 4.1E-14 | 0.21/0.40 | 1.2E-03 | 8.5E-01 | 2.3E+00 |

Numbers are rounded to two significant digits

NA = Not applicable

ND = No data

The longitudinal dispersivity considered in the evaluation was selected on the basis of work conducted by Neuman (1990) and Gelhar et al. (1992) that shows longitudinal dispersivity increasing with the length of the flow path. Gelhar et al. found that the maximum expected longitudinal dispersivity is approximately one-tenth the total flow path length. Although the Gelhar et al. results pertained to saturated systems, they were applied to this study because there are no similar vadose-zone dispersion studies. The flow path length at MDA T is about 387 m (1269 ft) from the ground surface to the water table. A longitudinal dispersivity of 30 m was used throughout the model domain which is less than one tenth of the flow path length from ground surface to the water table. However, many particles were located beneath ground surface where the path length is less than 387 m. The large chosen dispersivity will lead to earlier breakthrough than a shorter dispersivity, thus this model parameter was chosen to ensure that we do not under-predict breakthrough with respect to dispersivity. Transverse dispersivity was not considered in this evaluation.

3.1.4 Model Simulation Initial Steady State Set-up

To generate a steady-state flow field, simulations were run at each of the four selected infiltration rates (0.1, 1, 5, and 10 mm/yr) with constant boundary conditions using the FEHM steady macro until there were no temporal changes in water content, pressure field, or bulk flow at any point in the model domain. Gravimetric water contents for steady-state flow fields calculated using mean values of bulk density data are shown in Figure 27.

As seen in Figure 27, an increase in the rate of infiltration yields higher in-situ water content. As infiltration increases to 10 mm/yr (0.39 in./yr), there is more water accumulated as infiltration increases in the vapor phase notch and at other contacts. The behavior seen in these simulations spans the range of in-situ saturations reported in Birdsell et al. (1999), who also report that no single infiltration rate can reproduce moisture content data from individual boreholes. Birdsell et al. (1999) also suggest that mesa-top infiltration has changed over time, perhaps in response to climate and rainfall changes. This complexity has not been explored in the current model and would require many of the same modeling techniques developed for analysis of the transient effects caused by water in the beds. The current work assumes steady state infiltration after 1967, thus for the low infiltration cases, the model under-predicts saturations in the deeper parts of the Bandelier Tuff and Puye formation, while for the higher infiltration cases, the model over-predicts the saturations in the upper portions of the Bandelier Tuff.

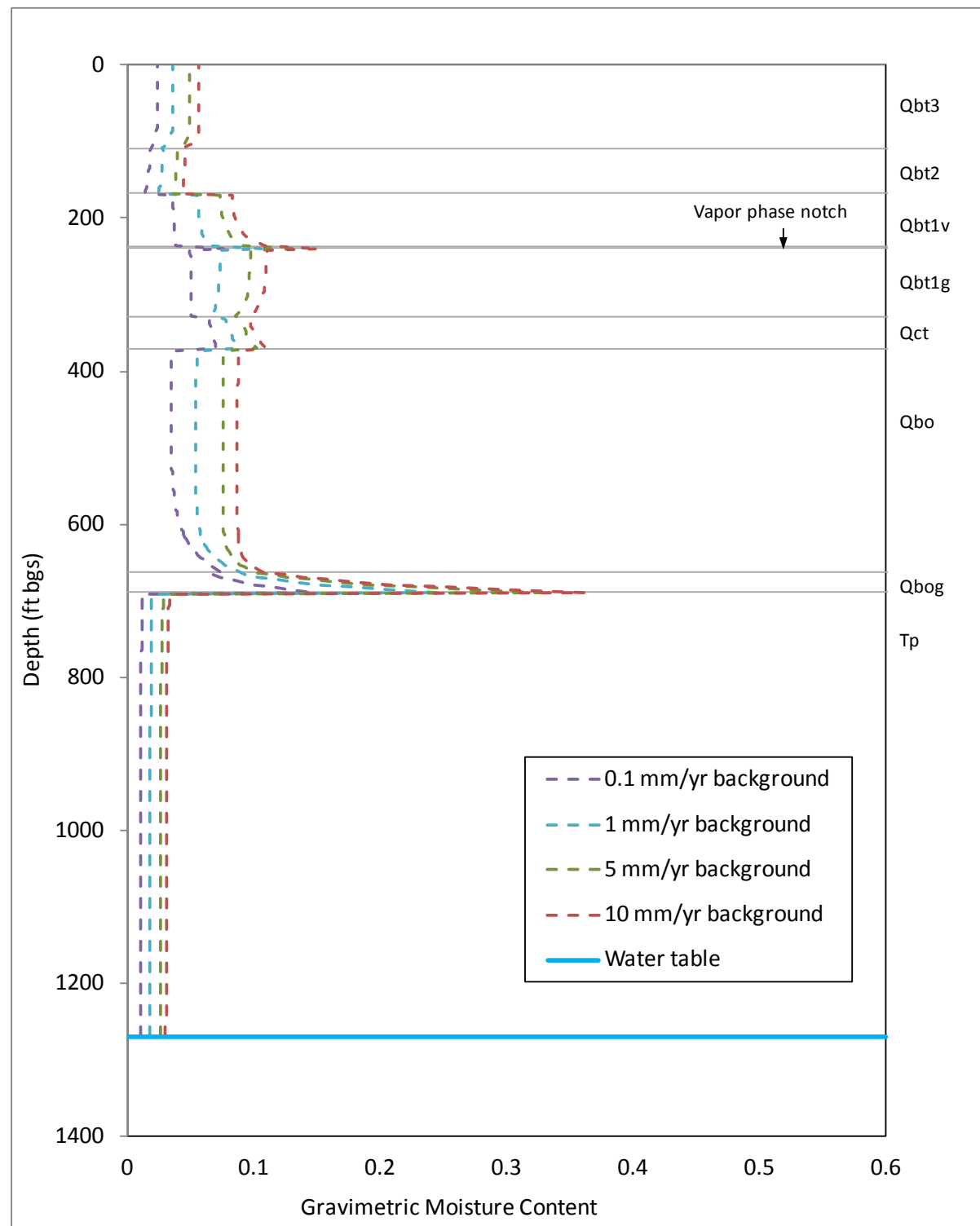


Figure 27
Steady-state water content profiles at four infiltration rates

3.1.4.1 *Conservative Breakthrough Curves*

The 3-D site-scale model is used to trace the travel times of particles (PTRK) released from MDA T and to generate conservative breakthrough curves. Because particles starting from slightly different points may travel different paths through the numerical mesh, thousands of particles must be released at the same time to create an RTD (see Section 3.1.2 for a discussion of the selected release points). The RTD shows the probability that a given particle will arrive at the water table in a given amount of time. All simulations of contaminant transport are started from the flow field calculated for the year 2010.

Because the Area G PA/CA used S PTR in FEHM to simulate particle breakthrough, some scoping calculations for transport simulations were conducted to compare the particle tracking codes PTRK and S PTR. Details of these scoping calculations are included in *Attachment IV*. These calculations were performed on a flow system using an equivalent continuum model as opposed to a single continuum model; however, these two models yield virtually the same results. Transport calculations were performed using both cell based (PTRK macro) and streamline (S PTR macro) particle tracking models. The other difference of note between the dispersion models used by the particle tracking schemes is that for PTRK, the dispersion is applied as a correction to the time a particle spends in each cell it travels through. For S PTR, the particle takes a random step in the direction of dispersion and can actually jump between cells along the flow path.

4.0 Results

This section presents the results of the groundwater modeling efforts. Section 4.1 summarizes results from penetration of the water applied to the beds during 1945–1967, and Section 4.2 describes the results of conservative particle breakthrough at the water table.

4.1 Penetration of Bed Water: 1945 - 2010

The 2010 flow field for each long term background infiltration case with particles was constructed in two steps. First a steady state background flow field was created. Then the 65 years from 1945–2010 were simulated during which time the water added to the beds was simulated.

Using the steady-state flow fields (shown in Figure 27) as initial conditions, GWC profiles were calculated for 2010, after 19.2 million gallons of water was applied to the absorption beds beginning in 1945. These profiles are shown, with measured GWC data (from 2005-2009) in Figure 28a. The figure shows min, mean, and max GWC based on uncertainty in reported bulk density for the different geologic units. Results of this simulation demonstrate that the model reasonably matches observed GWC data. Observed GWC are generally higher than simulated results within the Otowi member and Puye formation. As noted by Birdsell et al. (1999), it is possible that there are higher background water contents within these units than calculated due to residual elevated water contents as a result of higher infiltration during the Pleistocene epoch prior to 10,000 years ago. There is some variability in the measured data for GWC at given depths as can be seen in Figures 28a and 28b. This variability is likely due to lateral heterogeneity within hydrogeologic layers, and perhaps influenced by infiltration from canyons.

Uncertainty in porosity in the Puye formation also can explain some of the data. Based on Bussod et al. (2011), the model uses a porosity of 0.2 for the Puye formation; however the data from borehole 21-607955 show an average of 0.4 for porosity. Figure 28b shows that using 0.4 for the Puye porosity raises the model estimates of GWC closer to the data within the Puye formation. This figure shows that the deep data (below 800 ft bgs) are consistent with a background infiltration of 5–10 mm/yr. This is another indication that the Pleistocene epoch prior to 10,000 years ago was likely wetter on the Pajarito Plateau because current dry mesa infiltration is likely 0.1–1 mm/yr. Similar moisture profiles impacted by climate change are seen at the Nevada Test Site (Kwicklis et al., 2006). The data above 800 ft bgs appear to be elevated; however, spot measurements in the Puye formation can be quite heterogeneous because this formation comprises several types of depositional layers that have very different hydrologic properties and related steady state moisture contents (Bussod et al., 2011).

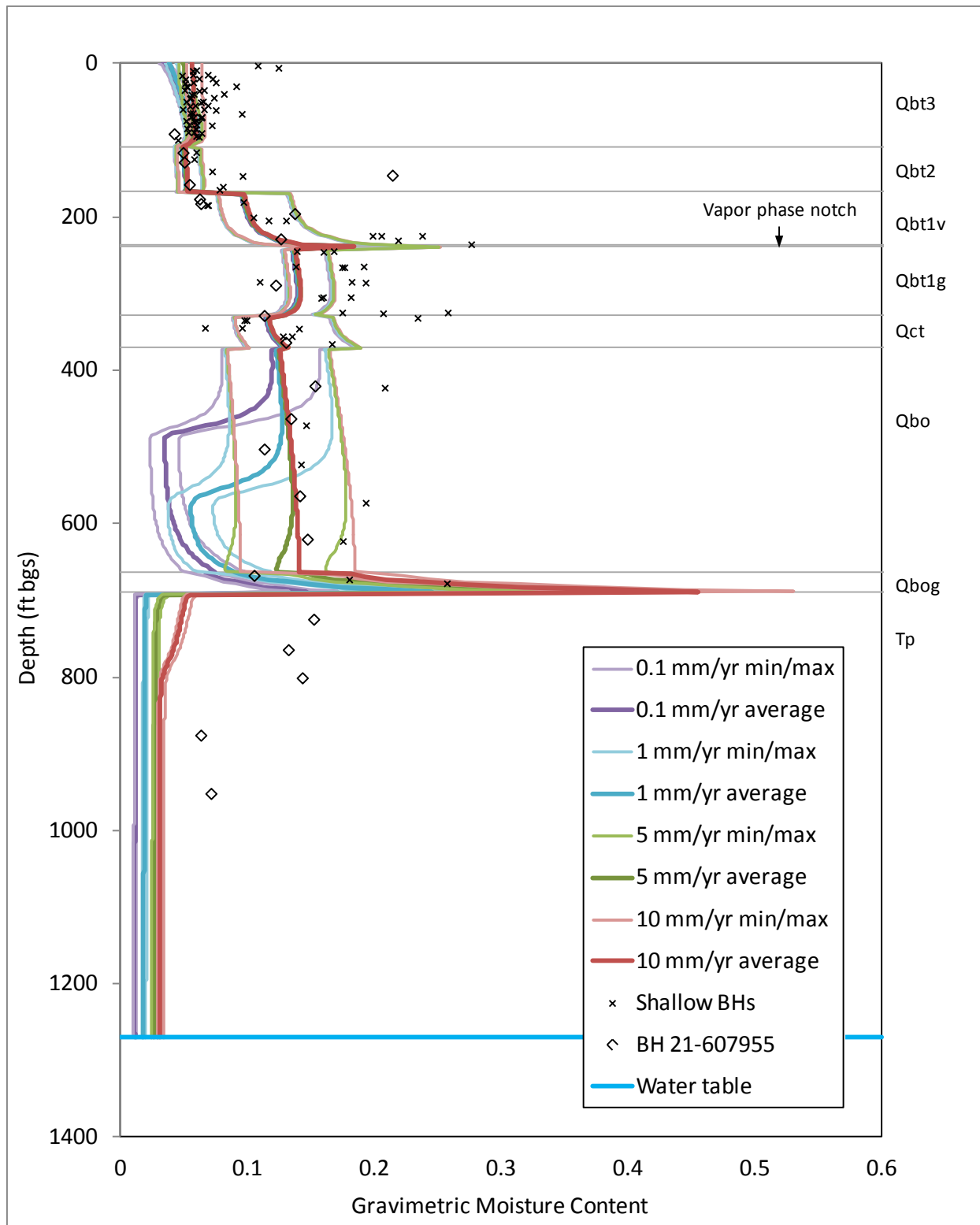


Figure 28a
Simulated gravimetric water content profiles in 2010 at four infiltration rates compared with measured GWC data from 2005-2009.

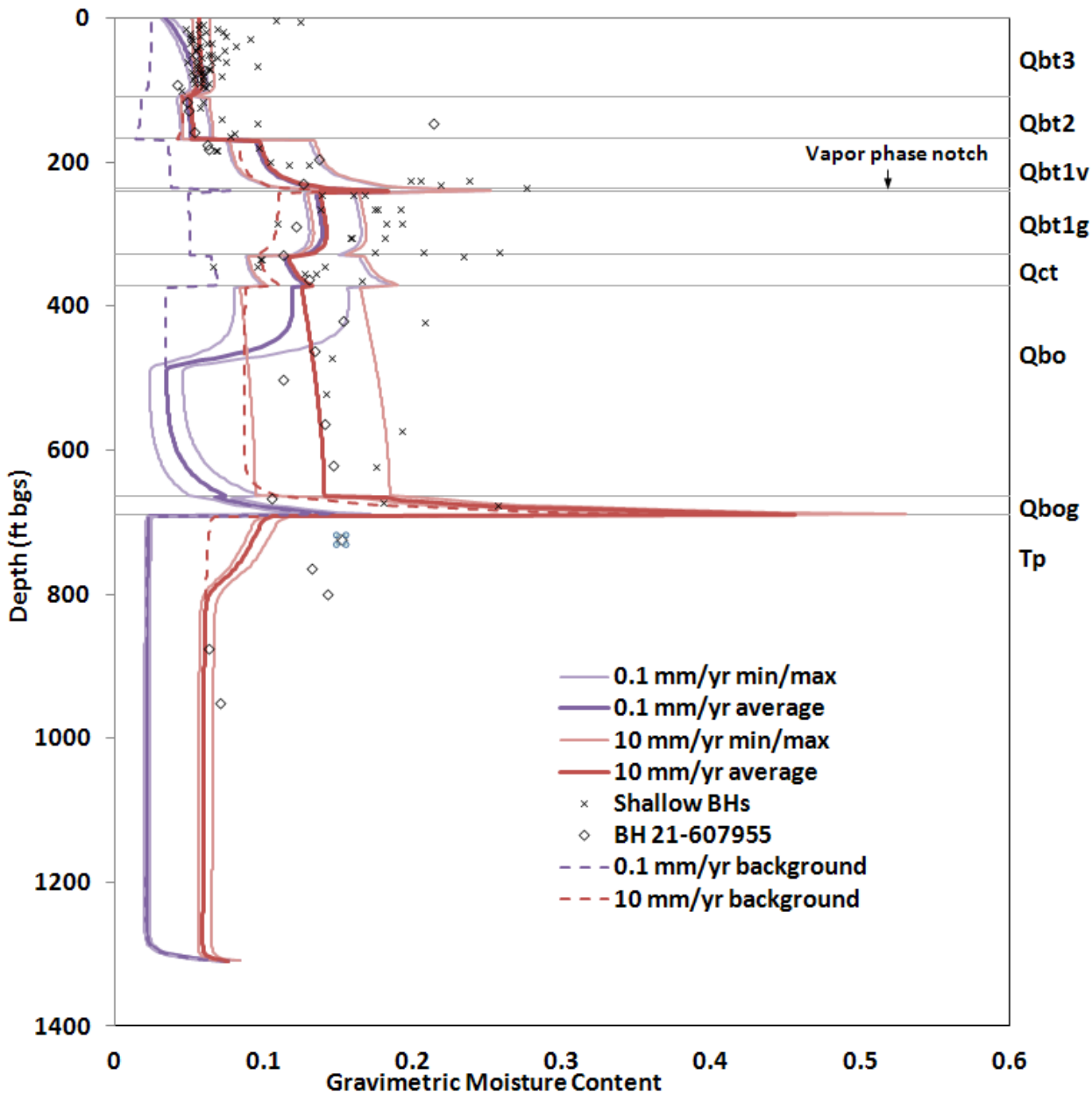


Figure 28b
Simulated gravimetric water content profiles in 2010 at two infiltration rates
compared with measured GWC data from 2005-2009, Puye porosity in this case is 0.4..

Figures 28c and 28d show the saturation on slices A-A' and B-B' at 65 years for the 10 mm/yr case. Elevated saturations are apparent in the vapor phase notch (2100 m elevation), the Cerro Toledo (2060 m elevation), and the Guaje Pumice (1970 m elevation). These figures show the prevailing dip of the geologic units, and also show how water from the beds is just reaching the lateral boundaries of the model domain.

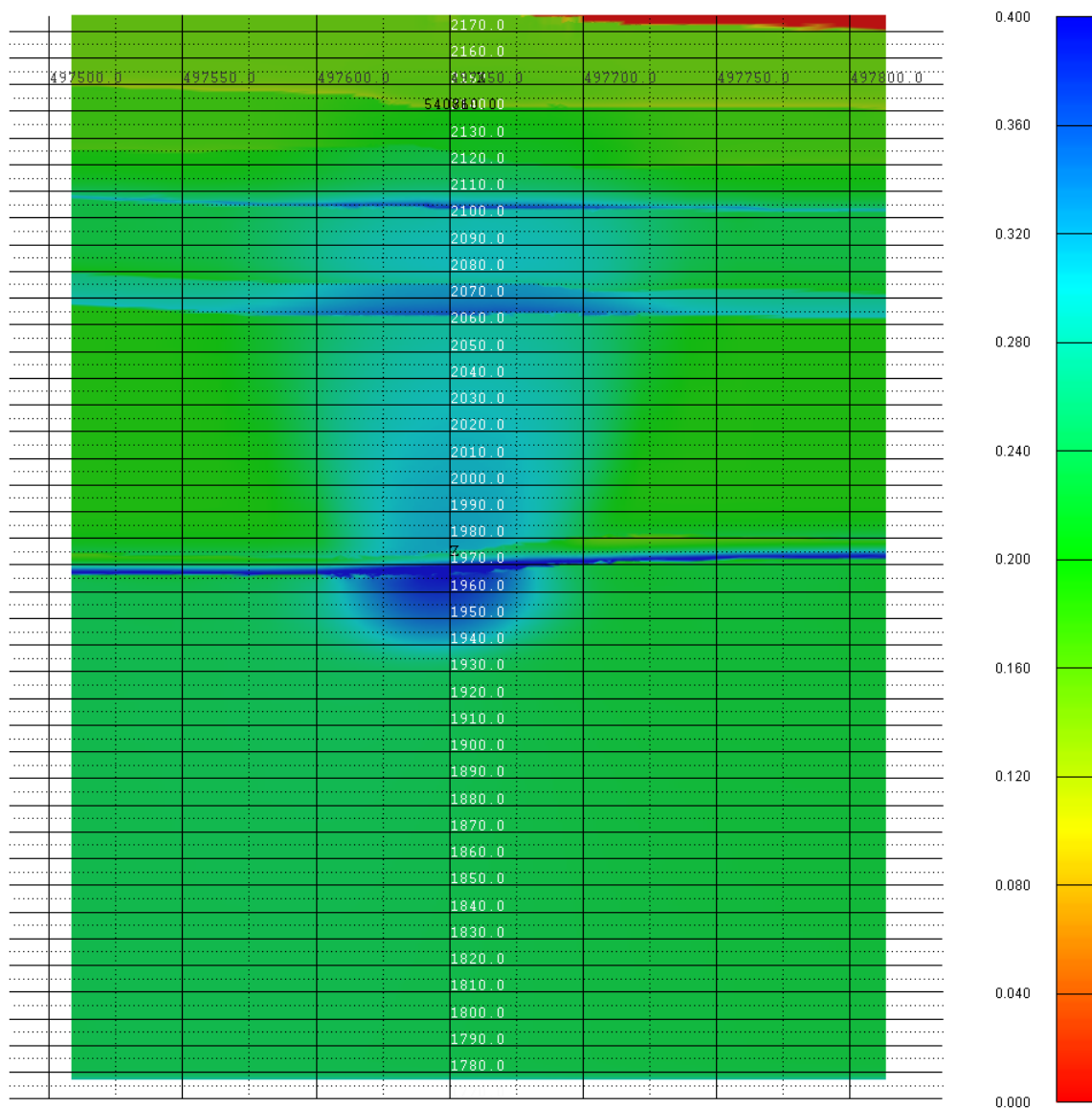


Figure 28c

Simulated saturation distribution at 65 yrs for the 10 mm/yr case in the 3-D high resolution local-scale mesh. The slice is along A-A' of Figure 22b.

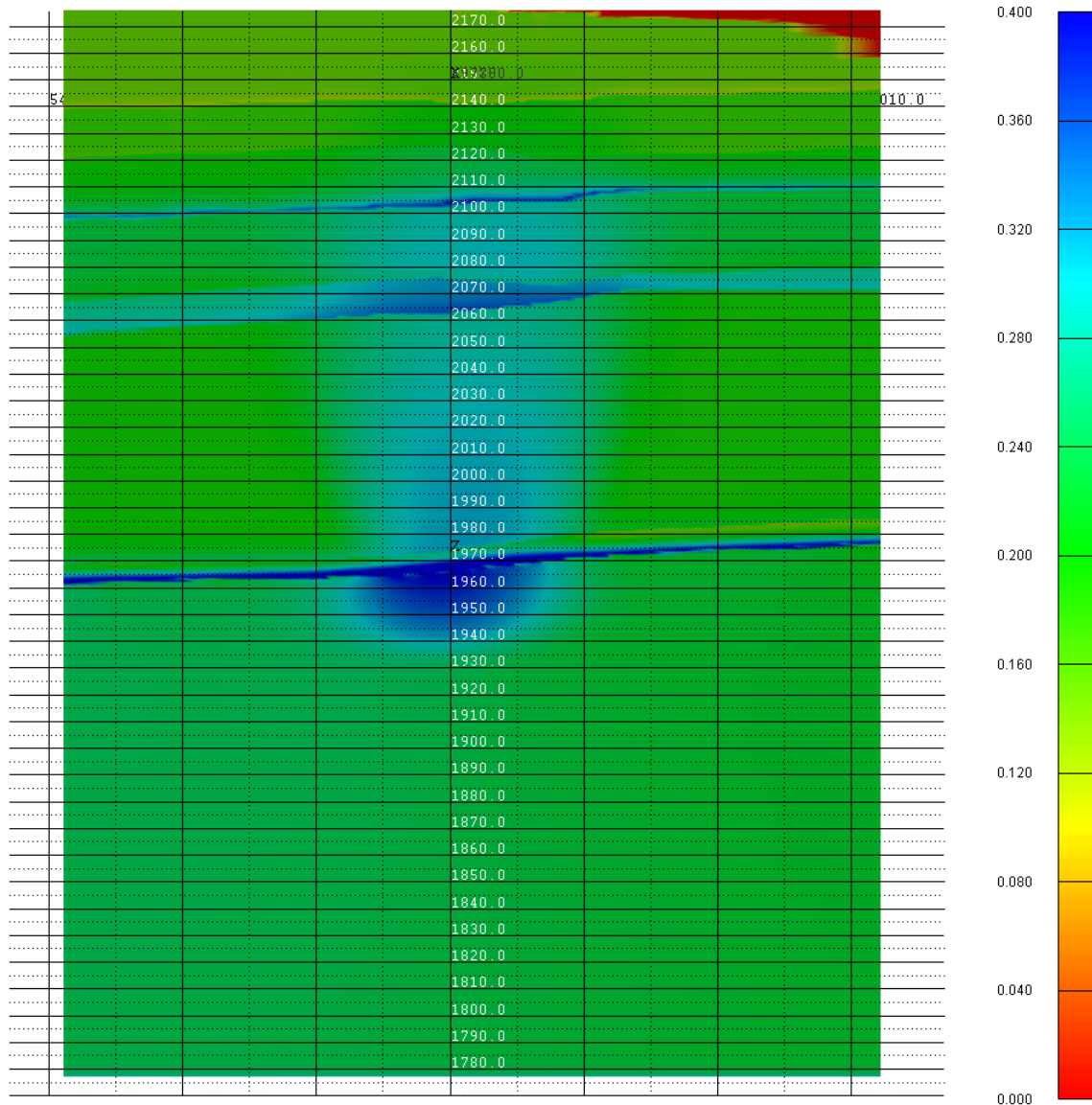


Figure 28d

Simulated saturation distribution at 65 yrs for the 10 mm/yr case in the 3-D high resolution local-scale mesh. The slice is along B-B' of Figure 22b.

4.1.1 *Role of Fractures on Bed Infiltration*

Figures 28e and 28f show the saturation differences calculated for simulations using single-continuum models (scm) for unfractured media and equivalent-continuum models (ecm) for fractured media at 65 years, for the 1 mm/yr background infiltration case. The blue denotes where the scm simulation is wetter, and the red shows where the ecm simulation is wetter. These figures show that although there are differences in the two approaches, the scm leads to greater depth of penetration and less lateral spreading in the vapor phase notch. For this reason, the particle breakthrough described in the next section use only a scm formulation. These results are

in agreement with Robinson et al. (2005) who found that an scm was sufficient to replicate the data from a 1.27×10^6 kg (336,000 gallon) infiltration test. This study cites the ability of high matrix permeability to quickly pull water from fractures as a primary mechanism for the limited role of fracture flow in the Bandelier Tuff. Use of the scm ensures that the fracture/matrix conceptual model does not lead to under-prediction of the penetration of the wetting front under MDA T.

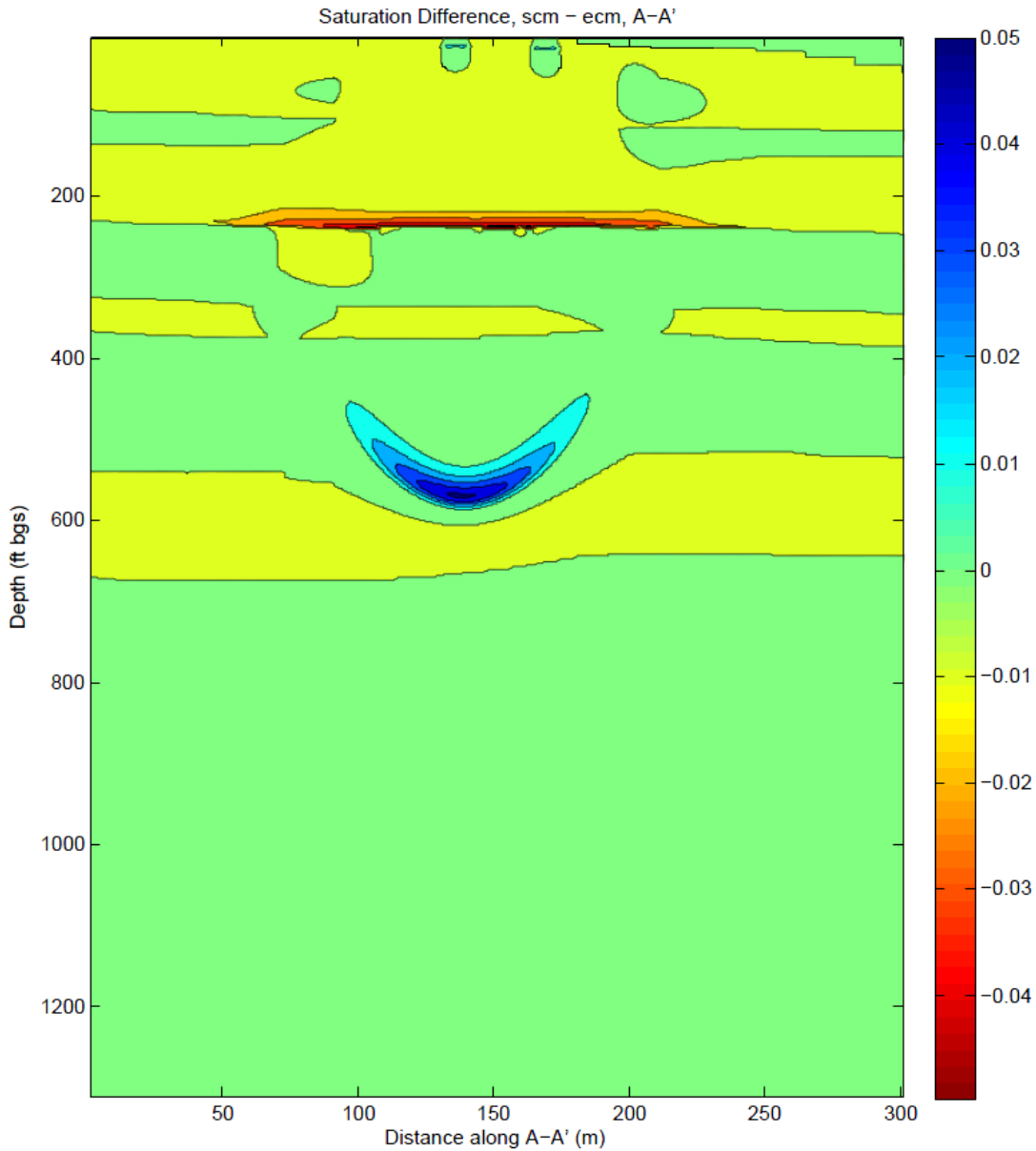


Figure 28
Difference in saturation between the unfractured (scm) and fractured (ecm) simulations for the 10 mm/yr case at 65 years. The slice is along A-A' from Figure 22b.

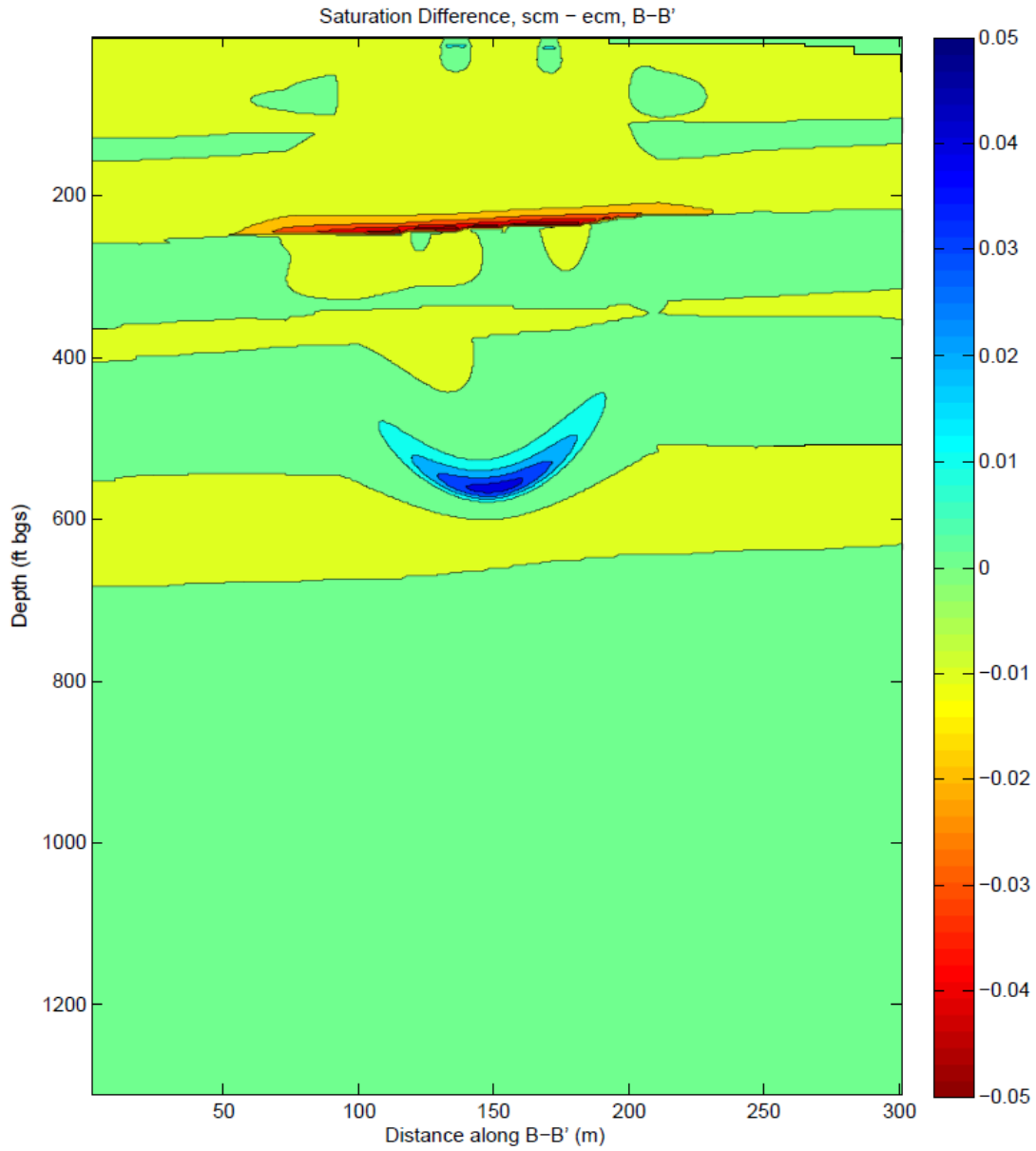


Figure 28f

Difference in saturation between the unfractured (scm) and fractured (ecm) simulations for the 10 mm/yr case at 65 years. The slice is along B-B' from Figure 22b.

4.1.2 Numerical diffusion of the wetting front: Mesa-Scale Versus Local-Scale Meshes

Figure 28g shows results in the year 2010 comparing wetting front penetration in the high resolution local-scale and mesa-scale meshes. The saturation profiles are taken near the center of bed #1, and both simulations were run for the 10 mm/yr case with identical material properties. The figure shows that the wetting front does not penetrate as deeply when using the mesa-scale mesh. This is likely due to numerical diffusion of the wetting front into the large mesh blocks at

depth. This figure demonstrates that by using a high resolution local-scale mesh, the penetration of the wetting front at MDA T is not under-predicted due to mesh block size effects.

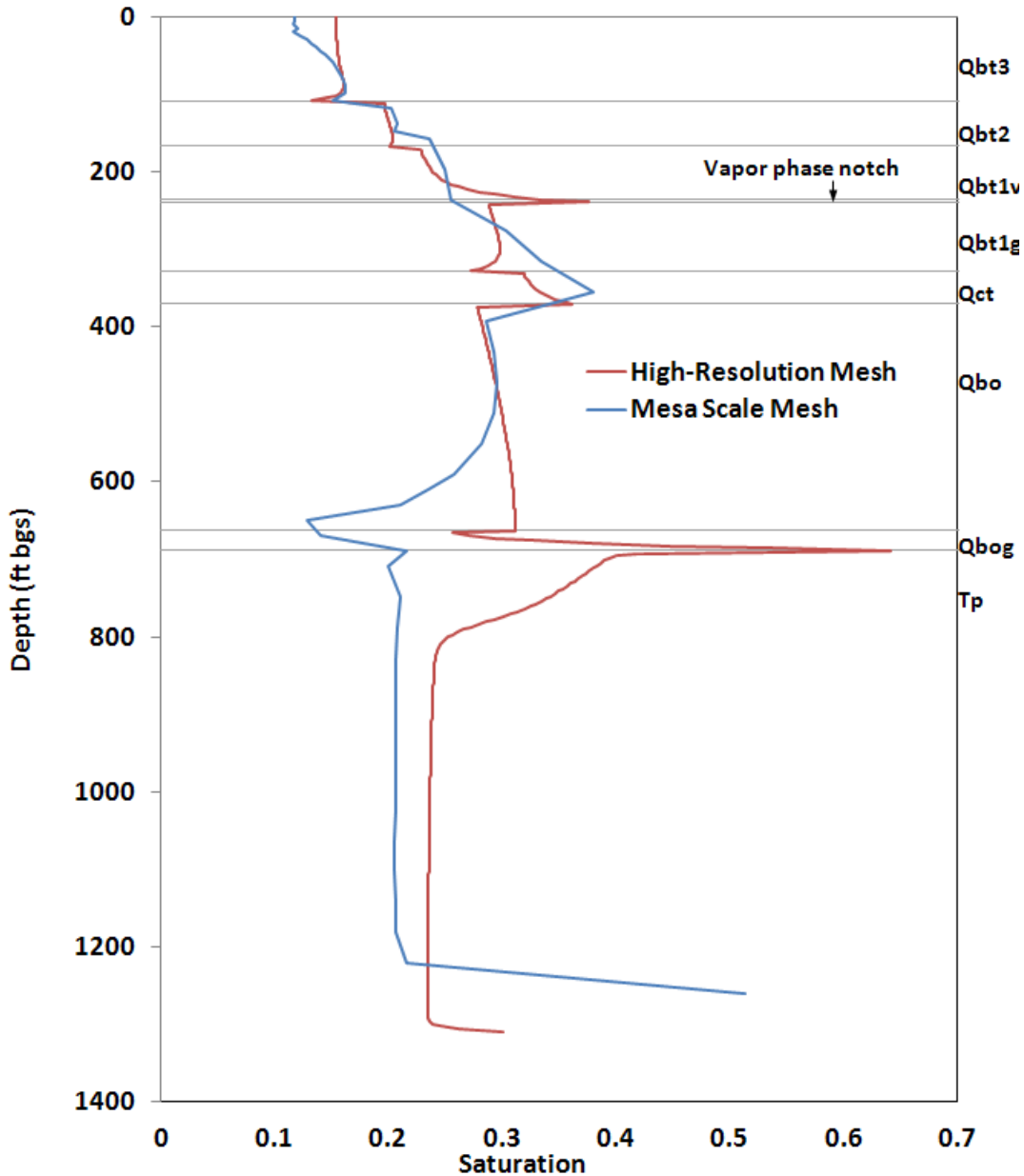


Figure 28g
Saturation front penetration depth for both the high resolution local-scale mesh and the mesa-scale mesh.

4.2 Particle Breakthrough at the Water Table

Conservative RTDs of particle breakthrough at the water table were generated for each particle release depth by releasing over 10,000 particles instantaneously from cells located at 8 distinct depths (Table 3). Particles were released in the year 2010 in the saturation fields shown in Figures 24a and 24b. Simulations were run to a maximum time of 100,000 years. The Goldsim simulations will release part of the MDA T inventory according to the environmental distribution of contaminants measured at the site (Figures 11 through 16). These figures show that the majority of the mass for the RCRA constituents is located within the upper 500 ft, and for the radiological constituents, it is in the upper 100 ft. Only a few detections of potential contaminants are present near the leading edge of the wetting front that is simulated with the bottom three release locations; the Goldsim model will release only a very small inventory from those locations. In addition, the shaft waste accounts for >99% of the MDA T radiological inventory (Figure 6), so the RTDs for that portion of the inventory is represented by the 62 ft bgs curves shown in the following figures.

Figure 29 shows that for the 10 mm/yr background flow field, breakthrough at the water table ranges from 250 yrs for the deepest release location to more than 2000 yrs for particles released at the bottom of the shafts.

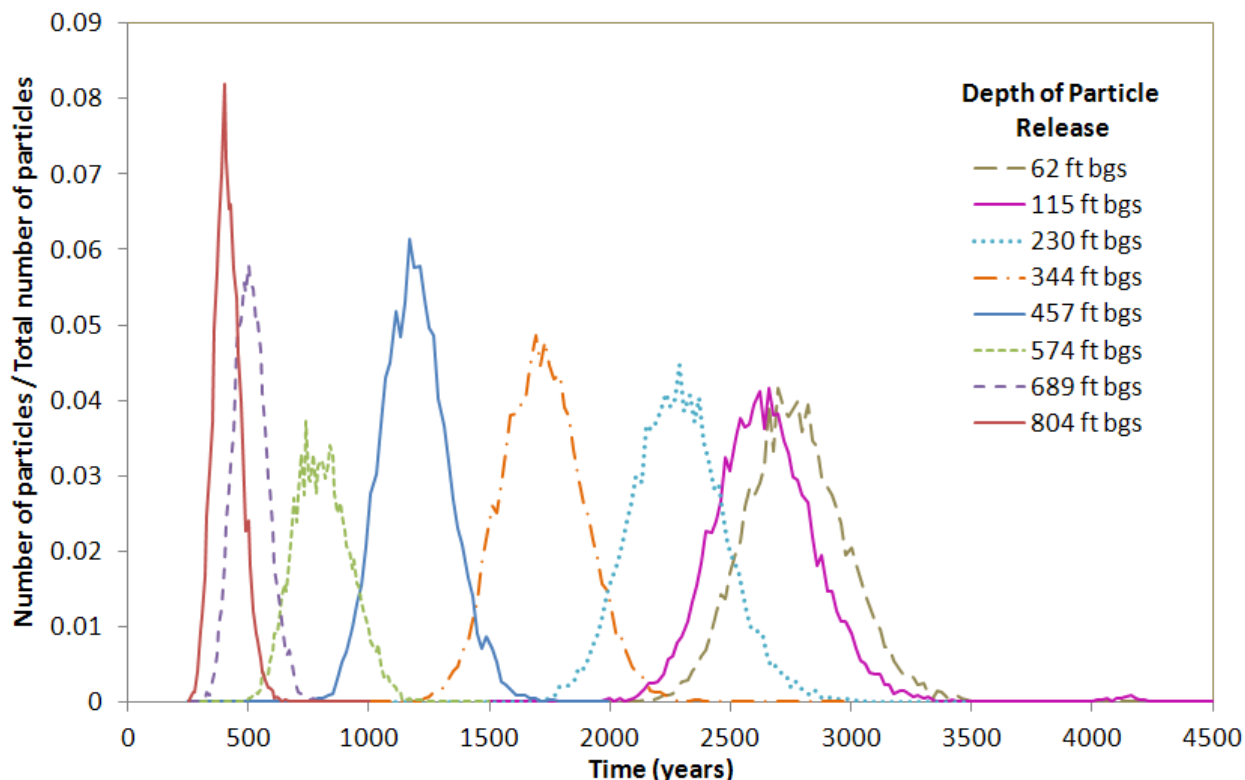


Figure 29
Particle breakthrough for the 10 mm/yr background flow field.

Figure 30 shows that for the 5 mm/yr background flow field, breakthrough at the water table ranges from 470 yrs for the deepest release location to more than 3500 yrs for particles released at the bottom of the shafts. Figure 31 shows that for the 1 mm/yr background flow field, breakthrough at the water table ranges from 1800 yrs for the deepest release location to more than 10,000 yrs for particles released at the bottom of the shafts. Because the flow rate is very low, some particles become stranded in parts of the mesh that have near-zero velocity, and Figure 32 shows that for this case, only 80% of the total initial particles arrive at the water table for shallower release locations. Finally, Figure 33 shows that for the 0.1 mm/yr background flow field, breakthrough at the water table ranges from 10,000 yrs for the deepest release location to more than 80,000 yrs for particles released at the bottom of the shafts. Figure 34 shows the fraction of particles reaching the water table for this minimum infiltration case.

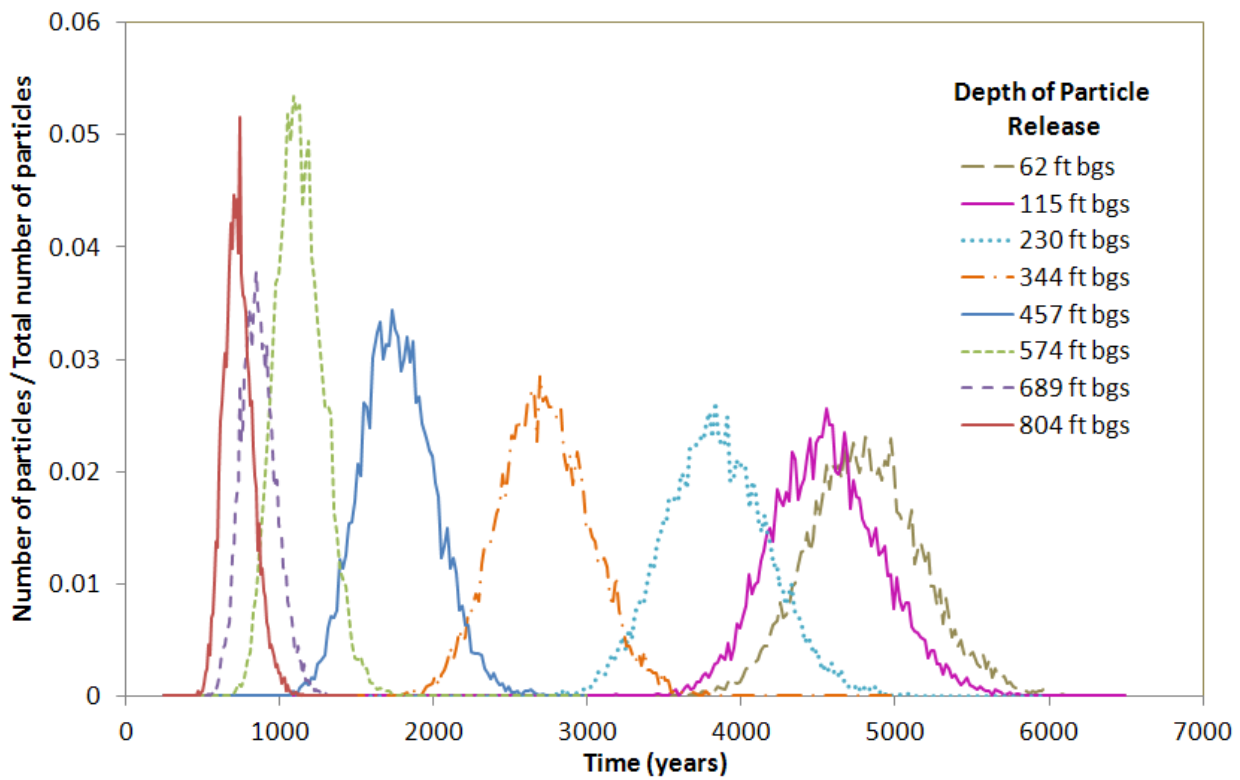


Figure 30
Particle breakthrough for the 5 mm/yr background flow field.

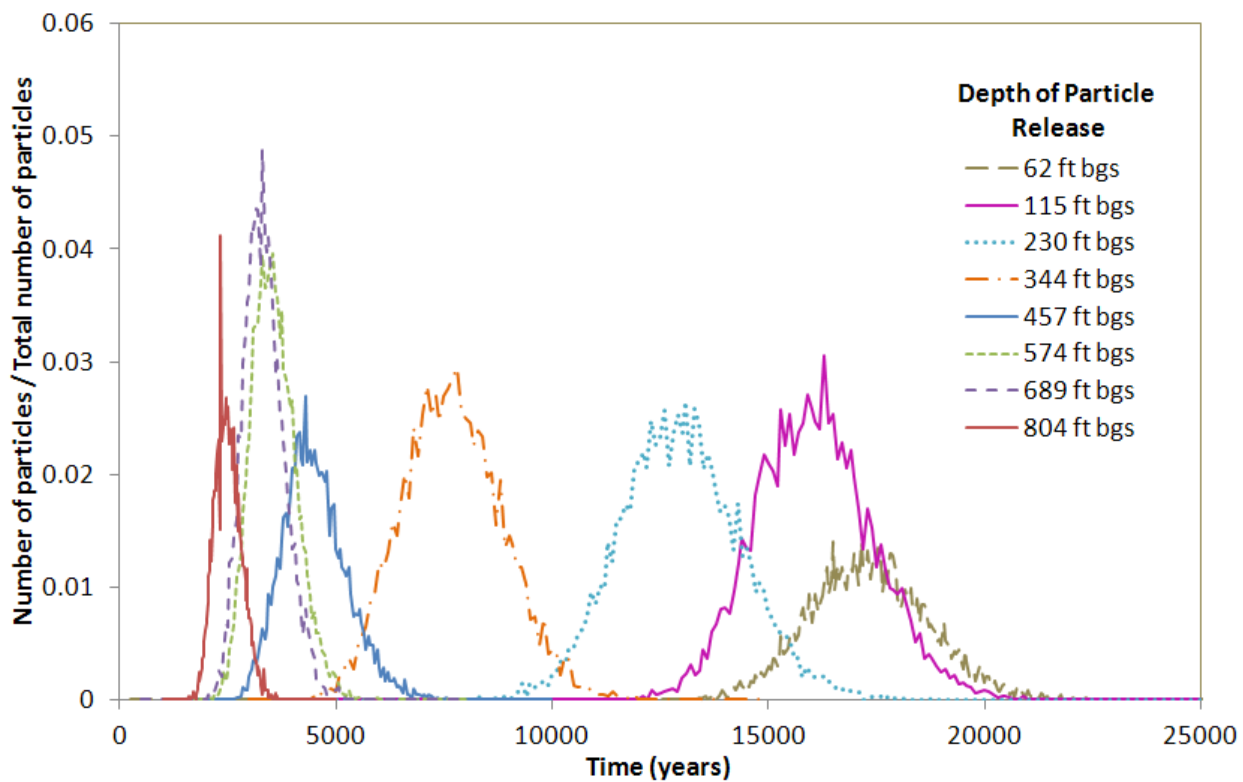


Figure 31
Particle breakthrough for the 1 mm/yr background flow field. Curves are normalized to 10,000 particles due to particle attrition in the low flow background area.

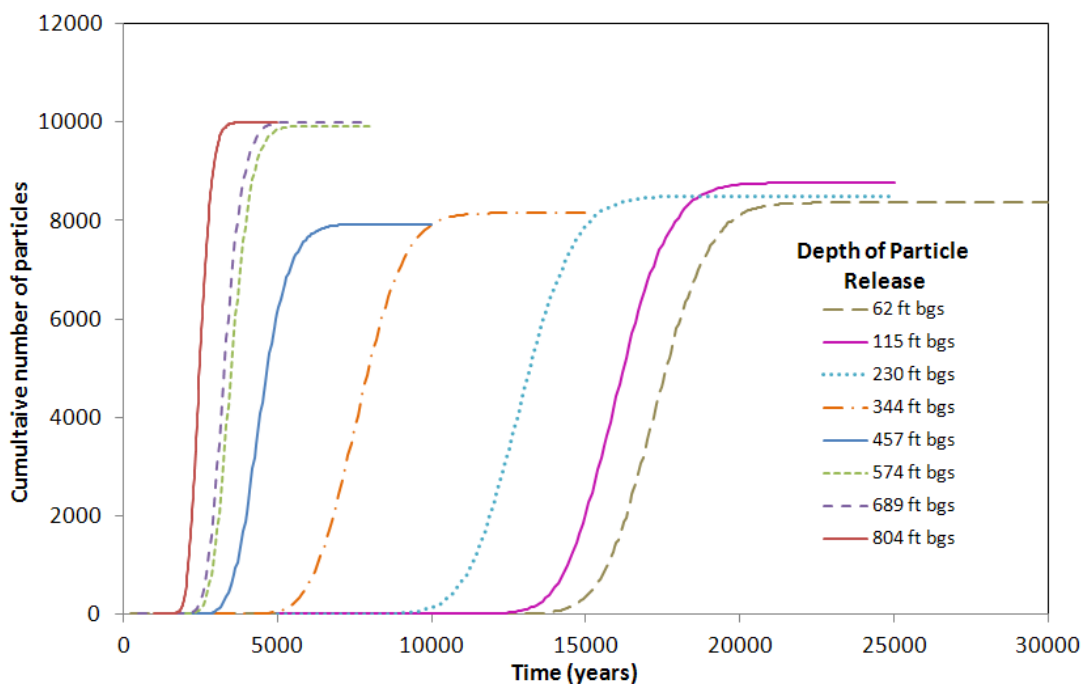


Figure 32
Number of particles reaching the water table for the 1 mm/yr background flow field.

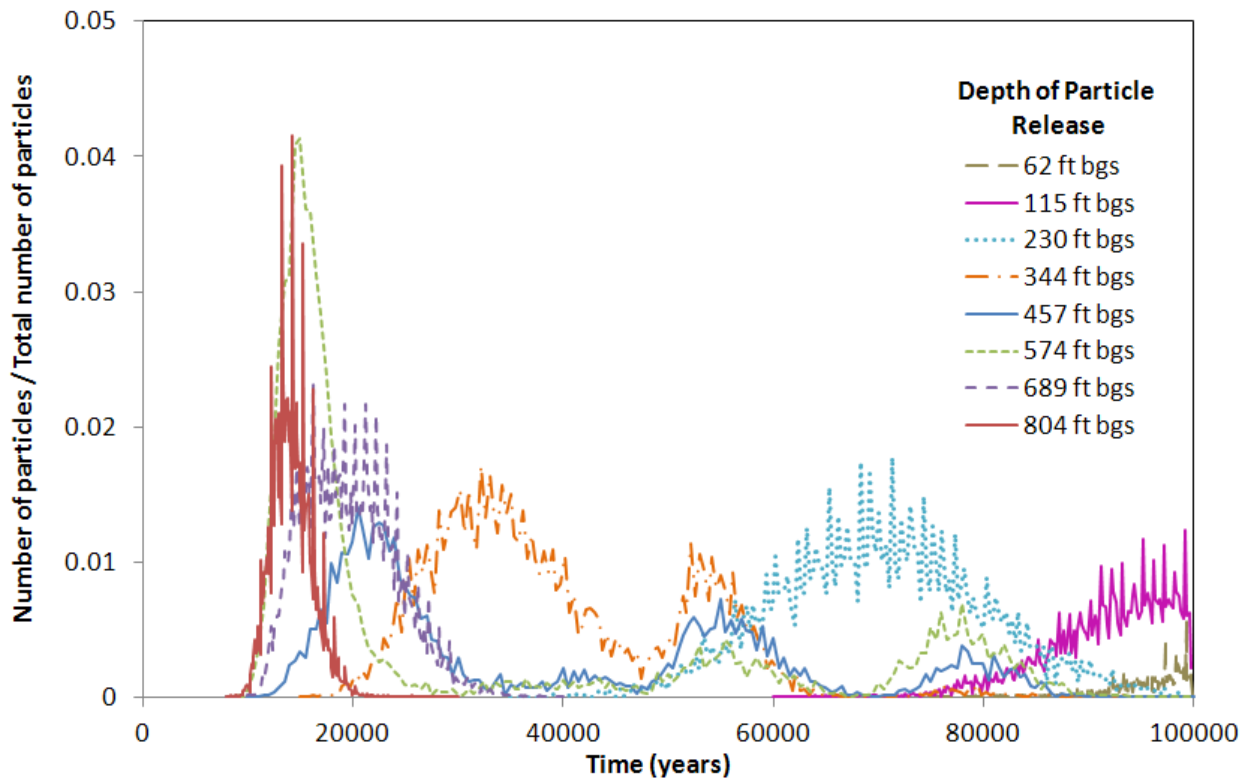


Figure 33
Particle breakthrough for the 0.1 mm/yr background flow field. Curves are normalized to 10,000 particles due to particle attrition in the low flow background area.

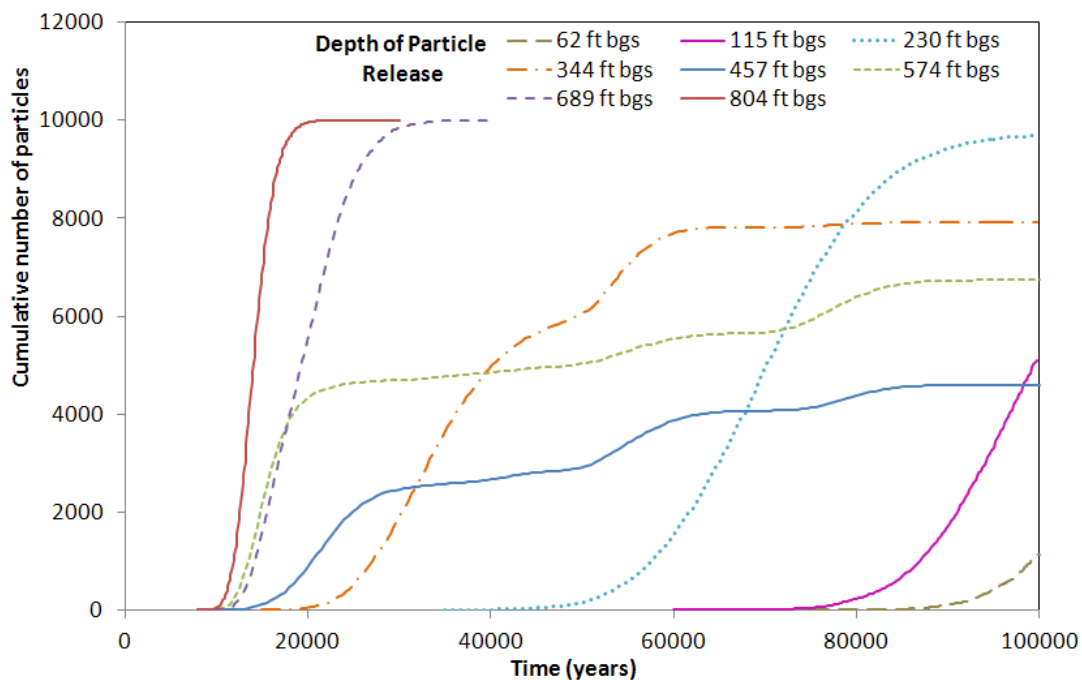


Figure 34
Number of particles reaching the water table for the 0.1 mm/yr background flow field.

5.0 Discussion

The fact that early particle breakthrough requires significant initial depth means that the bulk of the radiological waste at MDA T is in a good location with respect to ground water protection. The results also show that to reduce the likelihood of transport to the regional aquifer from the shallow waste source regions, infiltration at this site should be controlled and limited to low values. The present-day detections of VOCs and other conservative species to depths of 600-800 ft bgs is consistent with the simulated wetting front depth seen in some of the model realizations.

Numerical diffusion of the wetting front in the mesa-scale mesh led to under-prediction of penetration depth. This was remedied by the creation of a high resolution local-scale mesh with 1 m (3.28 ft) spacing from the surface to the water table (Figure 22a). Water penetration in the high resolution mesh reaches the upper 100 ft of the Puye formation in the year 2010, consistent with data in well 21-607955, where the upper Puye formation to 800 ft bgs appears to be wetter than at LADP-4 (Figure 7); however true background moisture at these depths in the Puye formation is poorly constrained. Because of the uncertainty and heterogeneity in the Puye formation, it is possible to conceive of a low-porosity, high-permeability pathway that would cause simulated initial (leading-edge) breakthrough to the water table faster than modeled. An initial estimate of the probability of this result could be tested using simulations based on the Bussod et al. (2011) geostatistical analysis of the Puye formation.

Another useful feature of the high resolution mesh is that it also allows the capture of geologic features such as the vapor phase notch that can lead to increased spreading and lateral diversion along local bedding dip (Figures 28c-d). Results from the increased resolution mesh more closely match the observed data, especially the moisture spikes seen in the vapor phase notch, the base of the Cerro Toledo (Qct), and the Guaje Pumice (Qbo) (Figure 7). Because the high resolution mesh is only 300 m in lateral extent, some realizations of the simulated wetting front have limited interaction with the lateral boundaries of the model. This impact causes less lateral spreading than would occur in a mesh with larger lateral extents. This effect is limited to higher background infiltration cases, and the net impact is to predict slightly faster particle arrival times at the water table.

Comparison of fractured rock simulations to those with only a matrix component shows that the wetting front spreads laterally in the fractured case leading to shallower penetration (Figure 28g). Using the non-fractured scm formulation in simulations of particle breakthrough ensures that the simulations do not under-predict breakthrough times based on the conceptual model for fracture/matrix interactions. Longitudinal dispersivity in the simulations was also set to a value of 30 m for all cases to ensure that particle breakthrough is not under-predicted by the use of a low dispersivity. However, the particle tracking employed in this version of the model does not

include random walk which could lead to earlier breakthrough than reported. Future versions of this work should include a random walk component of particle movement.

The particle release scheme, with release at seven equally spaced depths beneath the beds and one depth beneath the shafts (Table 3), implies that contaminants released during the GoldSim step of the PA modeling will collapse all mass between two release locations onto the lower location, thus ensuring that travel times for contaminants to the regional aquifer are not underpredicted based on their conceptualized mass distribution. This is a necessary step to reduce the complexity of the 3-D model for use in the 1-D abstractions needed in GoldSim. Finally, although particle breakthrough for these simulations is at the water table, the total travel time to a 100 m compliance boundary will be virtually the same due to much higher flow rates along the water table gradient than are likely to be found in the vadose zone.

6.0 References

Birdsell, K.H., W.E. Soll, N.D. Rosenberg, and B.A. Robinson, 1995, Numerical Modeling of Unsaturated Groundwater Flow and Radionuclide Transport at MDA G, Los Alamos National Laboratory Report LA-UR-95-2735.

Birdsell, K., K. Bower, A. Wolfsberg, W. Soll, T. Cherry, and T. Orr, 1999, Simulations of Groundwater Flow and Radionuclide Transport in the Vadose and Saturated Zones beneath Area G, Los Alamos National Laboratory, Los Alamos National Laboratory Report LA-13299-MS.

Birdsell, K.H., A.V. Wolfsberg, D.H. Hollis, T.A. Cherry, K.M. Bower, 2000, Groundwater Flow And Radionuclide Transport Calculations for a Performance Assessment of a Low-Level Waste Site, *J. Contaminant Hydrology*, 46, pp. 99-129.

Birdsell, K.H., B.D. Newman, D.E. Broxton, and B.A. Robinson, 2005. Conceptual Models of Vadose Zone Flow and Transport beneath the Pajarito Plateau, Los Alamos, New Mexico, *Vadose Zone Journal*, Vol. 4, pp. 620–636.

Broxton, D.E. and S.L. Reneau, 1995, Stratigraphic Nomenclature of the Bandelier Tuff for the Environmental Restoration Project at Los Alamos National Laboratory, Los Alamos National Laboratory Report, LA-13010-MS.

Broxton, D.E., and D.T. Vaniman, 2005. Geologic Framework of a Groundwater System on the Margin of a Rift Basin, Pajarito Plateau, North-Central New Mexico. *Vadose Zone Journal* 4:522-550.

Bussod et al., G.Y., 2011. “A New High-Resolution Method for the Characterization of Heterogeneous Subsurface Environments: Providing Flow and Transport Parameters via the Integration of Multiscale HydroGeophysical Data.” New England Research, Inc. DOE-SBIR Grant DE-FG02-07ER84898.

Carey, J.W. and Cole, G., 2002, Description of the Cerro Grande Fire Laser-Altimetry (LIDAR) Data Set, Los Alamos National Laboratory, Report LA-13892-MS, 57pp. plus appendices.

Christensen, C.W. and R.G. Thomas, 1962. Movement of Plutonium through Los Alamos Tuff. Los Alamos Scientific Laboratory Report. ERID-001025.

Dash, Z.V., 2003, Software Users Manual (UM) for the FEHM Application Version 2.22, Los Alamos National Laboratory Document 10086-UM-2.22-00.

U.S. Dept. of Energy (DOE), 2000. Buried Transuranic-Contaminated Waste Information for U.S. Department of Energy Facilities, Office of Environmental Management.

Fetter, C.W., 1999, *Contaminant Hydrogeology*, Prentice-Hall: NJ, USA.

French, S., R. Shuman, G.L. Cole, K.J. Crowell, M.S. Day, C.W. Gable, M.O. Gard, J.J. Whicker, D.G. Levitt, B.D. Newman, B.A. Robinson, E.P. Springer, and P.H. Stauffer, October

2008. Performance Assessment and Composite Analysis for Los Alamos National Laboratory Material Disposal, Area G, Revision 4, Los Alamos National Laboratory document LA-UR-08-06764, Los Alamos, New Mexico.

Gelhar, LW; C. Welty, and K.R. Rehfeldt, 1992, A Critical-Review of Data on Field-Scale Dispersion in Aquifers, *Water Resources Research*, Vol. 28, No. 7.

Golder, 2005a, User's Guide – GoldSim – Probabilistic Simulation Environment, Version 8.02.3, GoldSim Technology Group, January.

Golder, 2005b, User's Guide – GoldSim Contaminant Transport Module, Version 2.22.2, GoldSim Technology Group, January.

Golder, 2007a, User's Guide – GoldSim – Probabilistic Simulation Environment, Version 9.60.3, GoldSim Technology Group, March.

Golder, 2007b, User's Guide – GoldSim Contaminant Transport Module, Version 4.20.3, GoldSim Technology Group, March.

Hollis, D., E. Vold, R. Shuman, K. Birdsall, K. Bower, W. Hansen, D. Krier, P. Longmire, B. Newman, D. Rogers, E. Springer, 1997, Performance Assessment and Composite Analysis for the Los Alamos National Laboratory Disposal Area G, Los Alamos National Laboratory Report LA-UR-97-85, Report-54G-013, March.

Keating, E.H., V.V. Vesselinov, E. Kwicklis, and Z. Lu, 2003, Coupling Basin- and Local-Scale Inverse Models of the Española Basin, *Ground Water*, Vol. 41, No. 2, pp. 200-211.

Krier, D., R. Longmire, and H.J. Turin, 1996, Geologic, Geohydrologic and Geochemical Data Summary of MDA G, TA-54, Los Alamos National Laboratory, Los Alamos National Laboratory Report LA-UR-95-2696.

Krier, D., P. Longmire, R. Gilkeson, and H. Turin, February 1997. Geologic, Geohydrologic, and Geochemical Data Summary of Material Disposal Area G, Technical Area 54, Los Alamos National Laboratory, Revised Edition, Los Alamos National Laboratory document LA-UR-95-2696, Los Alamos, New Mexico.

2006 Kwicklis, E.M., A.V. Wolfsberg, P.H. Stauffer, M.A. Walvoord, and M.J. Sully, Multiphase Multicomponent Parameter Estimation for Liquid and Vapor Fluxes in Deep Arid Systems Using Hydrologic Data and Natural Environmental Traces, *Vadose Zone Journal*, 2006 5:934-950

Kwicklis, E., M. Witkowski, K. Birdsall, B. Newman, and D. Walther, August 2005. Development of an Infiltration Map for the Los Alamos Area, New Mexico, *Vadose Zone Journal*, Vol. 4, pp. 672–693.

Los Alamos National Laboratory (LANL), 2004. Investigation Work Plan for Material Disposal Area T at Technical Area 21, Solid Waste Management Unit 21-016(a)-99, Los Alamos National Laboratory document LA-UR-04-0559, Los Alamos, New Mexico.

LANL, 2005. Investigation Report for Material Disposal Area G, Consolidated Unit 54-013(b)-99, at Technical Area 54, Los Alamos National Laboratory Report LA-UR-05-6398 (ER2005-0626), Los Alamos, New Mexico.

LANL, 2006a. Investigation Report for Material Disposal Area T, Consolidated Unit 21-016(a)-99, at Technical Area 21, Los Alamos National Laboratory document LA-UR-06-6506, Los Alamos, New Mexico.

LANL, 2006b. Investigation Report for Material Disposal Area U, Consolidated Unit 21-017(a)-99, at Technical Area 21, Los Alamos National Laboratory document LA-UR-05-9564, Los Alamos, New Mexico.

LANL, 2006c. Investigation Report for Consolidated Unit 21-018(a)-99, Material Disposal Area V, at Technical Area 21, Los Alamos National Laboratory document LA-UR-06-6609, Los Alamos, New Mexico.

LANL, 2007. Phase II Investigation Report for Material Disposal Area T at Technical Area 21, Los Alamos National Laboratory document LA-UR-07-7692, Los Alamos, New Mexico.

LANL, 2009. Phase III Investigation Report for Material Disposal Area T at Technical Area 21, Revision 1, Los Alamos National Laboratory document LA-UR-09-8109, Los Alamos, New Mexico.

LANL, 2010a. Documented Safety Analysis for the Nuclear Environmental Sites at Los Alamos National Laboratory, Los Alamos National Laboratory Report NES-ABD-0101, R.4.0.

LANL, 2010b. Submittal of the Replacement Pages for the Approval with Modifications Phase III Investigation Report for Material Disposal Area T, at Technical Area 21, Revision 1, Los Alamos National Laboratory letter (EP2010-0100) to J.P. Bearzi (NMED-HWB) from M.J. Graham (LANL) and D.R. Gregory (DOE-LASO), Los Alamos, New Mexico.

LANL, 2010c. Technical Area 21 Groundwater and Vadose-Zone Monitoring Well Network Evaluation and Recommendations, Los Alamos National Laboratory document LA-UR-10-3960, Los Alamos, New Mexico.

LANL, 2011a. R64 Fact Sheet, Los Alamos National Laboratory document LA-UR-11-4247, Los Alamos, New Mexico. ERID-204895.

LANL, 2011b. Periodic Monitoring Report for Vapor-Sampling Activities at Material Disposal Area T, Consolidated Unit 21-016(a)-99, at Technical Area 21, Second Quarter Fiscal Year 2011, Los Alamos National Laboratory document LA-UR-11-3839, Los Alamos, New Mexico. ERID-204633.

LANL, 2011c. Work Plan for Vadose Zone Moisture Monitoring at Material Disposal Area T at Technical Area 21, Los Alamos National Laboratory document LA-UR-11-4247, Los Alamos, New Mexico. ERID-204895.

Levitt, D.G., 2011, Modeling the Movement of Transient Moisture Through Disposal Units at Los Alamos National Laboratory Technical Area 54, Area G, Los Alamos National Laboratory document LA-UR-11-05424, Los Alamos, New Mexico.

Lichtner P.C., S. Kelkar, and B.A. Robinson, 2002, New Form of Dispersion Tensor for Axisymmetric Porous Media with Implementation in Particle Tracking, *Water Resour. Res.*, Vol. 38, No. 8.

Neuman, S.P., 1990, Universal Scaling of Hydraulic Conductivities and Dispersivities in Geologic Media, *Water Resources Research*, Vol. 26, No. 8.

Nyhan, J.W., B.J. Drennon, W.V. Abeele, G. Trujillo, W.J. Herrera, M.L. Wheeler, W.D. Purtymun, and J.W. Booth, July 1984. Distribution of Radionuclides and Water in Bandelier Tuff Beneath a Former Los Alamos Liquid Waste Disposal Site After 33 Years, Los Alamos National Laboratory report LA-10159-LLWM, Los Alamos, New Mexico.

Nylander, C.L, K. A. Bitner, G. Cole, E. H. Keating, S. Kinkead, P. Longmire, B. Robinson, D. B. Rogers, and D. Vaniman, 2003, Groundwater Annual Status Report for Fiscal Year 2002, Los Alamos National Laboratory Report LA-UR-03-0244.

Purtymun, W.D., R. Garde, and R. Peters, June 1978. Movement of Fluids and Plutonium from Shafts at Los Alamos, New Mexico, Los Alamos Scientific Laboratory report LA-7379-MS, Los Alamos, New Mexico.

Robinson, B. A., Stephen G. McLin, and Hari S. Viswanathan, "Hydrologic Behavior of Unsaturated, Fractured Tuff: Interpretation and Modeling of a Wellbore Injection Test", *Vadose Zone Journal* 4:694–707 (2005).

Robinson, B.A. and H. Viswanathan, 2003 Application of the Theory of Micromixing to Groundwater Reactive Transport Models, *Water Resources Res.*, Vol. 39, No. 11.

Rogers, M.A., June 1977. History and Environmental Setting of LASL Near-Surface Land Disposal Facilities for Radioactive Wastes (Areas A, B, C, D, E, F, G, and T), Vol. I, Los Alamos Scientific Laboratory report LA-6848-MS, Los Alamos, New Mexico.

Rogers, D.B. and B.M. Gallaher, 1995, The Unsaturated Hydraulic Characteristics of the Bandelier Tuff, Los Alamos National Laboratory Report LA-12968-MS, September.

Soll, W.E., 1995, Influence of Fracture Fills and Fracture Coatings on Flow in Bandelier Tuff, Los Alamos National Laboratory Report LA-UR-95-2695.

Soll, W. and K. Birdsell, 1998, The Influence of Coatings and Fills on Flow in Fractured, Unsaturated Tuff Porous Media System, *Water Resources Research* Vol. 34, pp. 193 –202.

Springer, E.P., 2005. Statistical Exploration of Matrix Hydrologic Properties for the Bandelier Tuff, Los Alamos, New Mexico, *Vadose Zone Journal* 4: 505-521.

Springer, E.P and T.G. Schofield, 2004, Statistical Analyses of Mesa-Top Percolation Rates at Los Alamos National Laboratory, New Mexico, Los Alamos National Laboratory Report LA-UR-04-7801.

Stauffer P.H. et al., 2005, Groundwater Pathway Model for the Los Alamos National Laboratory Technical Area 54, Material Disposal Area G, LA-UR-05-7393

Stauffer P.H. et al., 2013, Groundwater Pathway Model for the Los Alamos National Laboratory Technical Area 54, Material Disposal Area G, LA-UR-13-24014

Stauffer, P.H., B.A. Robinson, and K.H. Birdsall, 2000, Modeling Transport in Los Alamos Canyon: Effects of Hypothetical Increased Infiltration after the Cerro Grande Fire, Los Alamos National Laboratory Report LA-UR-00-5923.

Stimac, J.A., D.E. Broxton, E.C. Kluk, S.J. Chipera, and J.R. Budahn, July 2002. Stratigraphy of the Tuffs from Borehole 49-2-700-1 at Technical Area 49, Los Alamos National Laboratory, New Mexico, Los Alamos National Laboratory report LA-13969, Los Alamos, New Mexico.

Vaniman, D., G. Cole, J. Gardner, J. Conaway, D. Broxton, S. Reneau, M. Rice, G. WoldeGabriel, J. Blossom, and F. Goff, 1996, Development of a Site-Wide Geologic Model for Los Alamos National Laboratory, Los Alamos National Laboratory Report LA-UR-96-2059.

Zyvoloski, A. George (2007) FEHM: A control volume finite element code for simulating subsurface multi-phase multi-fluid heat and mass transfer. Los Alamos Unclassified Report LA-UR-07-3359. (Report).

Zyvoloski, G. A., B. A. Robinson, Z. V. Dash, and L. L. Trease, 1995a, Models and Methods Summary for the FEHMN Application, Los Alamos National Laboratory Report LA-UR-94-3787, Rev. 1.

Zyvoloski, G. A., B. A. Robinson, Z. V. Dash, and L. L. Trease, 1995b, User's Manual for the FEHMN Application, Los Alamos National Laboratory Report LA-UR-94-3788, Rev. 1.

Attachment I
Geologic Framework Models
for the
Los Alamos National Laboratory Technical Area 21,
Material Disposal Area T

Author:

Terry A. Miller

Introduction

The geometry of the GFM is defined with a three-dimensional (3D) Geocellular model of the Pajarito study area that encompasses MDA T mesa, DP canyon, and Los Alamo Canyon. The framework stratigraphy is formed through a process that creates a 3D model from disparate input data. The process simplifies the available data near the model area and extrapolates from widely spaced data in other areas of the model domain. The WC09 GFM used for these studies is updated with information not previously available and includes 2009 updates that incorporate the geologic information contained in 330 wells and 25 cross sections that are available for the Pajarito Plateau and described in Cole et al. (2009). The WC09 series of the GFM is constructed using Earthvision by Dynamics Graphics Inc. Table 1 gives a correlation of the GFM input surfaces to the materials as they are used for modeling the MDA T area.

The MDA T GFM begins with the full LANL Site domain which includes material units to a depth near bedrock and the Tesuque Fm units. A subset domain is selected around MDA T that is large enough to tie down surfaces at the edges, but small enough to enable the use of higher resolution work near the top soils of the mesa, mesa edges, and canyon bottoms. Figure 1 shows the domain for the MDA T modeling efforts. The topography within the area of interest was downsampled or clipped by using the 4-ft LIDAR data resulting in a 4-ft resolution grid that covers the modeling domain (red). The final extents of the Earthvision WC09 GFM used for modeling are 1,626,000 to 1,641,000 east-west, 1,769,000 to 1,779,000 north-south, 4000 to 7500 elevation (State Plane, zone: 3002, GRS 1980/NAD83).

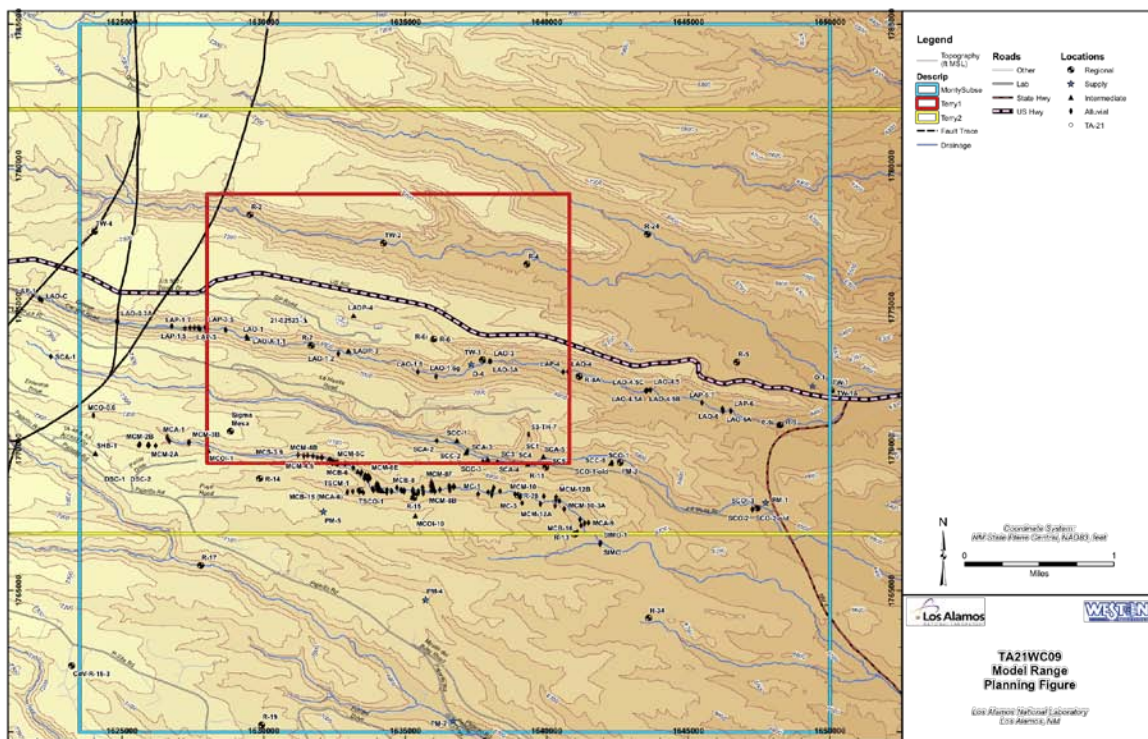


Figure 1. Areas of interest for modeling projects. The WC09 GFM was created for the MDA T domain as shown in red.

The WC09 GFM is evolving as new data are acquired and geologists view and evaluate the resulting GFM. The version used for the MDA T model is the December 2009 WC09 model and a Paleochannel subset that gives special attention to the paleochannel and overburden around the MDA T site. Both these models were built by Weston and delivered December 2009. Since the release of that version, there have been more updates, and the latest version for the full Pajarito study area is now version WC11. Updates to the new version include additional data and improved interpretation of the deeper units near and below the water table. Figure 2 shows an example of additional information being evaluated for update from the WC09 GFM to WC11. New interpretations of the material extents, faulting, and topology are evaluated by geologists and adjusted as needed to be consistent with current and accepted conceptual models.

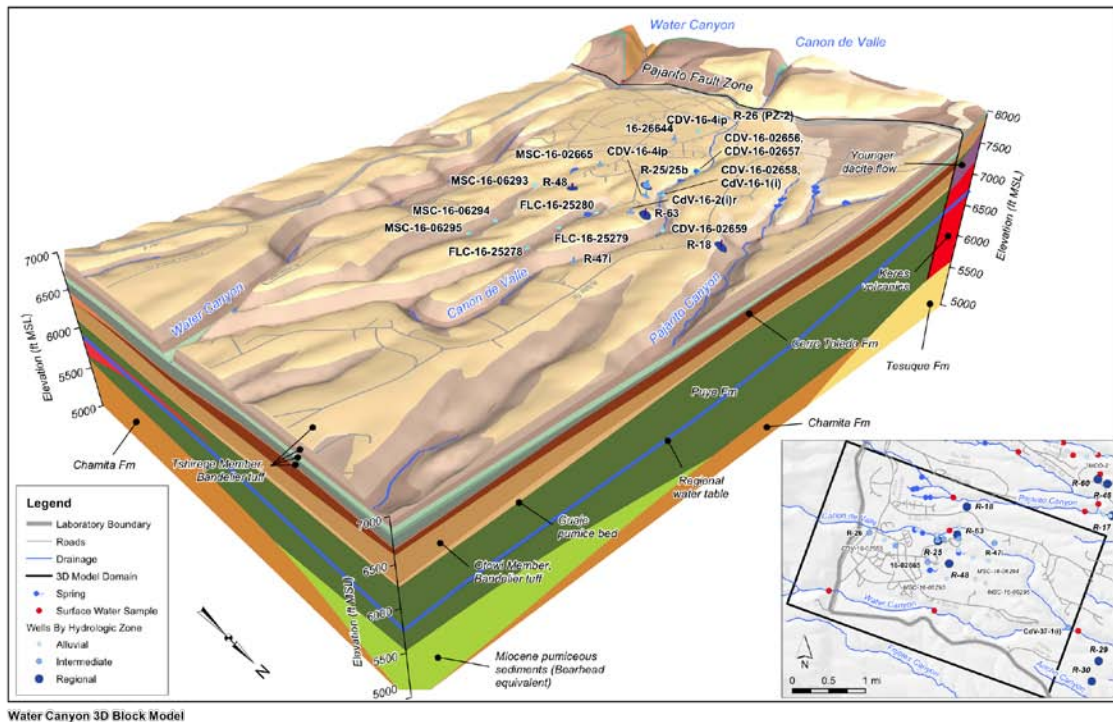


Figure 2. Cut out from WC11 version GFM showing updated information from the WC09 version GFM.

Material Zones WC09 Earthvision
As of December 2009

| MESH | WC09 EV | Name | Geologic Description | RGB |
|------|-------------------------|--------|--|-------------|
| 101 | -1 | | Air | 240 240 240 |
| 40 | 40 | OB2 | Overburden above Paleochannel | 10 235 13 |
| 39 | 39 | | Paleochannel | 178 229 224 |
| 38 | 38 | OB | Overburden Fill/Soil (replaces Qbt3t and Qbt4) | 178 229 128 |
| 37 | 37 | Qbt4 | Tshirege Unit 4 | 214 184 140 |
| 36 | 36 | Qbt3t | Tshirege Unit 3, transition zone | 214 194 170 |
| 35 | 35 | Qbt3 | Tshirege Unit 3 | 176 150 132 |
| 34 | 34 | Qbt2 | Tshirege Unit 2 | 156 126 112 |
| 33 | 33 | Qbt1vu | Tshirege Unit 1 - vitric | 146 176 148 |
| 32 | 32 | Qbt1vc | Tshirege Unit 1 - colanne | 108 144 118 |
| 31 | 31 | Qbt1g | Tshirege Unit 1 - glassy | 106 114 104 |
| 30 | 30 | Qbtt | Tshirege Unit 1, tsankawi pumice | 208 116 68 |
| 29 | 29 | Qct | Cerro Toledo | 124 50 16 |
| 28 | 28 | Qbof | Otowi Member, ash flow | 174 124 70 |
| 27 | 27 | Qbog | Otowi Member, Guaje Pumice | 200 154 100 |
| 25 | 25 | Tb4 | Cerro del Rio Basalts | 210 52 46 |
| 23 | 23 | Qta | Ancha Formation | 255 227 40 |
| 21 | 21 | Tvt2 | Younger Tschicoma Dacites | 126 82 118 |
| 20 | 26,24, 22, 20, 18 | Tpf | fanglomerates | 74 96 46 |
| 19 | 19 | Tvt1 | Older Tschicoma Dacites | 112 68 110 |
| 17 | 17 | Tpt | Totavi Lentil, axial gravels | 228 164 218 |
| 16 | 16 | Tjfp | Bearhead Rhyolite (pumiceous puye-Tpp), Peralta tuff | 146 180 46 |
| 15 | 15 | Tvk | Keres Volcanic flows | 255 0 0 |
| 14 | 14 | Tcac | Chamita Fm, Lithosome A | 167 255 230 |
| 13 | 13 | Ttca | Tesuque Fm. Chamita, Lithosome A | 150 215 199 |
| 12 | 12 | Tcara | Transitional zone: Ttca-Tcar | 194 214 155 |
| 11 | 11,9, 7 | Tcar | axial river deposits and western sandy, tributary fluvial deposits | 188 116 40 |
| 10 | 10 | Tb2 | 8.4 to 9.3 Ma Basalts | 104 92 80 |
| 8 | 5, 8 | Tb1 | 11.6 to 13.1 Ma Basalts | 92 80 72 |
| 6 | 4, 6 | Ttc | Upper Santa Fe Group, includes Tesuque Fm and Chama-El Rito | 246 188 98 |
| 3 | 3 | Ttsf | Tesuque Fm. (Lithosome S - fine) | 160 210 250 |
| 2 | 2 | Ttb | Tesuque Fm. (Lithosome B) | 142 169 249 |
| 1 | 1 | Bedr | Bedrock, Gaisteo Fm and older units | 48 40 150 |

Table 1. Correlation of geologic surfaces used to create WC09 GFM to materials used in meshing for the full site and MDA T GFM modeling.

Drill hole data used for the WC09 GFM are used to define material units in the model. These include data at the mesa site and beyond that help to constrain interpolation at the boundaries (Figure 3).

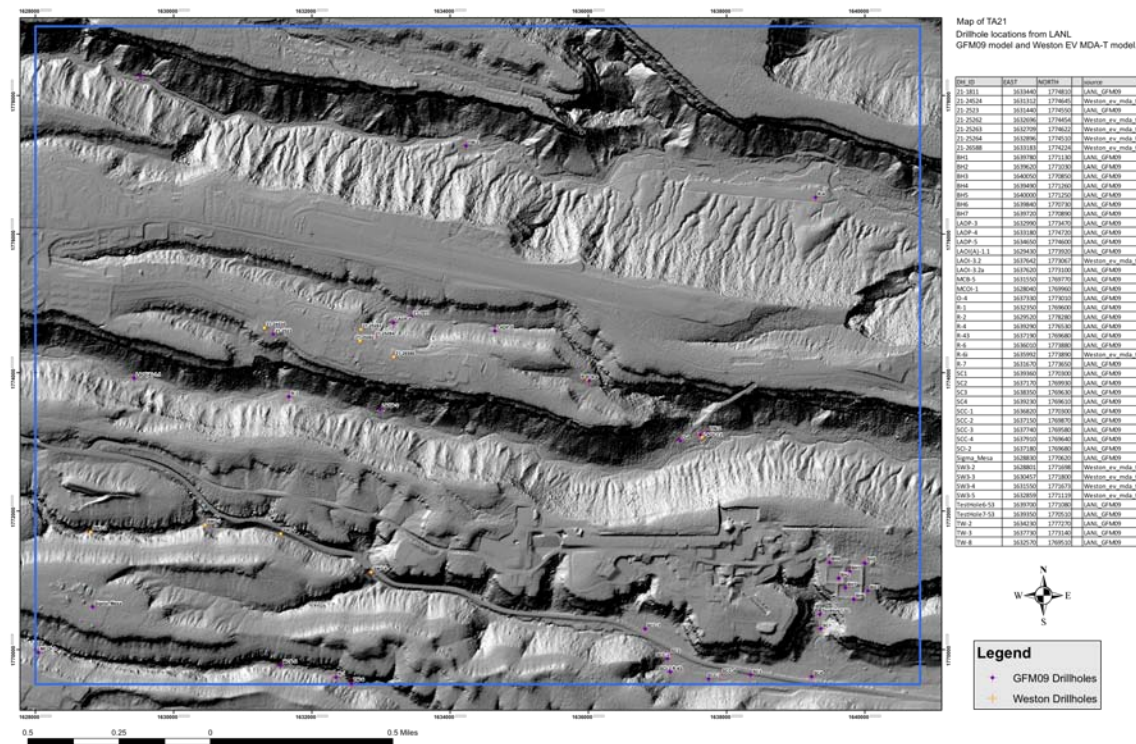


Figure 3. Example of borehole data used to create the WC09 GFM.

Input Data for Absorption Beds and Shafts

The WC09 GFM includes estimated fill depth over the sites and includes geometry of adsorption beds and waste disposal shafts. As written in LANL (2006, page 3), SWMU 21-016(a) is comprised of four inactive absorption beds: the beds measured approximately 120 ft long x 20 ft wide x 6 feet deep (1.82 meters deep). Data on the location of the absorption beds and disposal shafts were provided by Weston. The MDA T disposal shafts were provided as x,y State Feet locations with radius and depth for each. The four absorption beds were provided as polygon shapes at ground surface.

Input Data for Paleochannel

A subset of the WC09 Earthvision model was built with special attention to the paleochannel and soils at the top of the mesa from MDA V, located west of MDA T, to MDA U to the east. The paleochannel feature is observed in soil borings that include the MDA T site. The paleochannel is only partially exposed and is otherwise covered with up to four feet of soils. It is channel-shaped with the bottom ranging from 8 to 35 feet below ground surface. The x,y extents for the paleochannel feature are from a minimum of (1631000, 1774750 ft) to a maximum of (1634700, 1774250 ft). Data for the paleochannel are taken from soil borings and resistivity profiling as shown in Figure 4.



Figure 4. Location of paleochannel feature included in WC09 for MDA T.

Attachment I-6

GFM Unit Material Extents and Elevations for Quality Assurance Checks

The following figures are used to plan the mesh design and model setup. Figures are also used for quality assurance (QA). Each figure is examined and accepted by geologists for modeling needs. The mesh is designed to best capture resolution in important areas such as the mesa top, canyon bottoms, and immediately under the MDA T site. The resulting mesh is then compared against these figures to check for consistency between the GFM and the mesh.

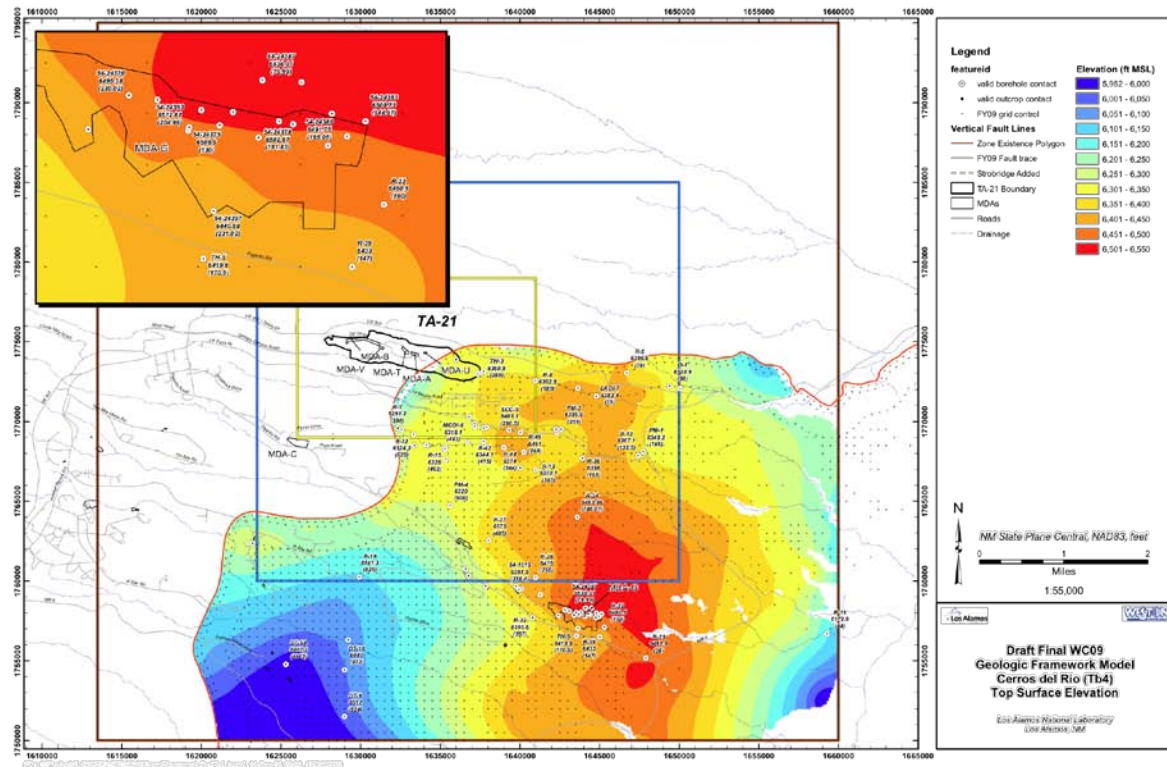


Figure 5. Extents and elevations of basalts below MDA T domain. Example figure shows type of analysis used for examination and QA review of the GFM model and the input data used.

The following figures show the WC09 material units by elevation and extent over the MDA T domain. The top elevation for each material is shown. Additionally, the flow body basalts are shown with both their top and bottom elevations separately. The flow bodies are embedded in the layer –cake stratigraphic structures of the model.

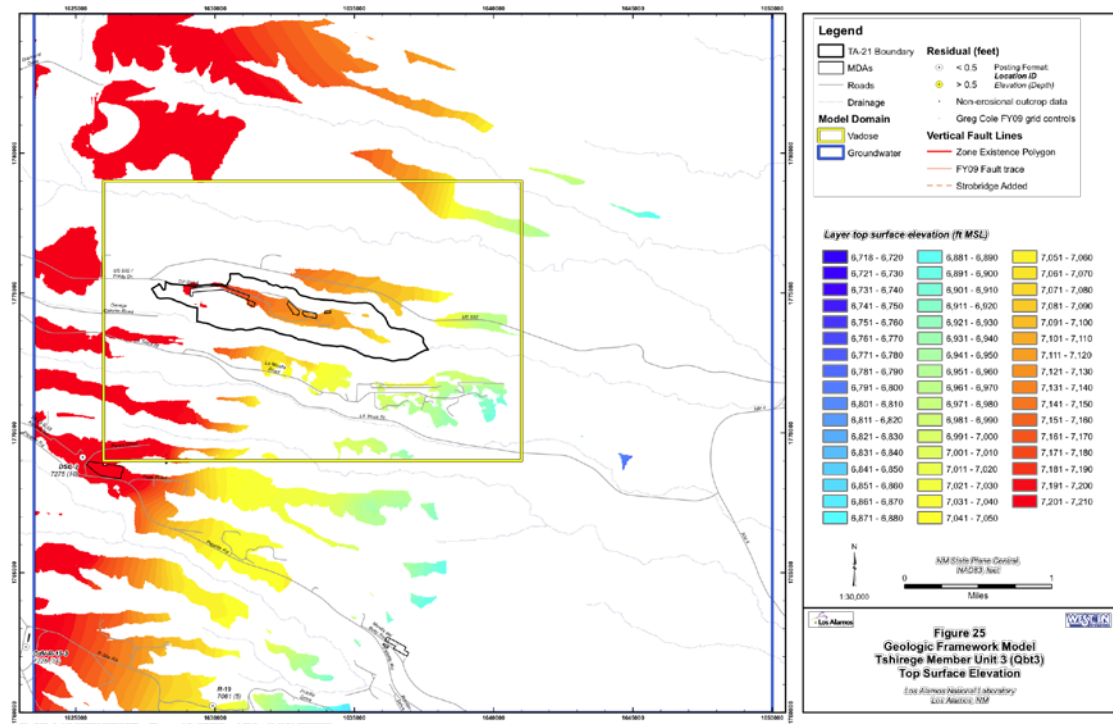


Figure 6a. Top surface elevation of Qbt3

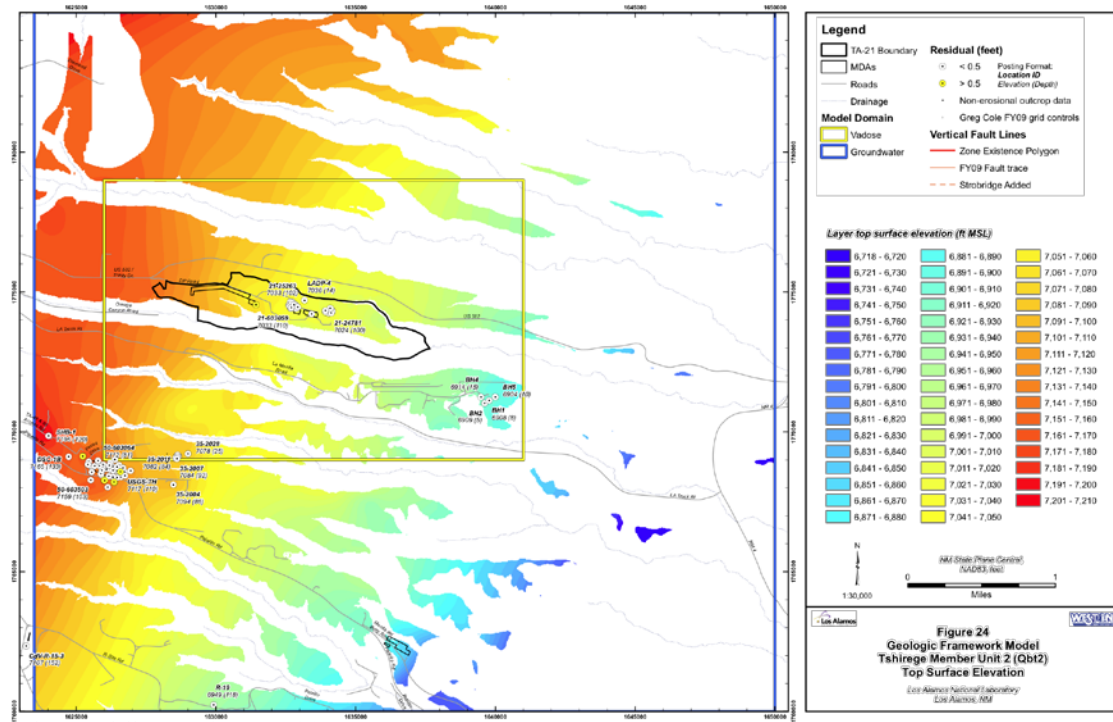


Figure 6b. Top surface elevation of Qbt2

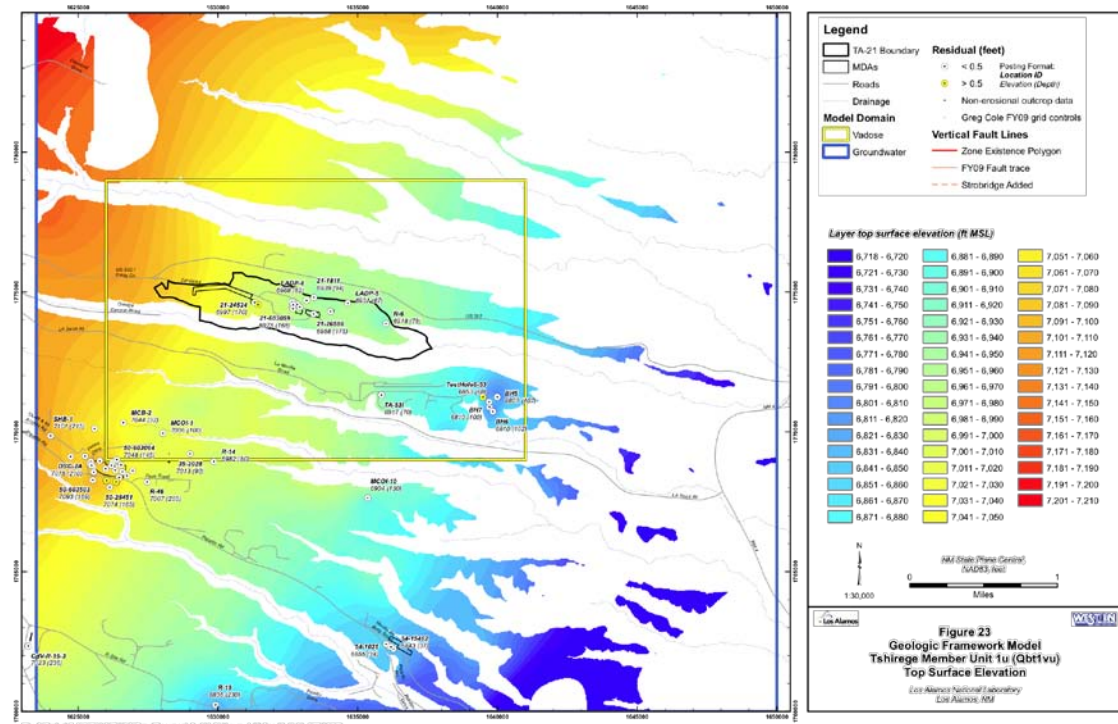


Figure 6c. Top surface elevation of Qbt1vu

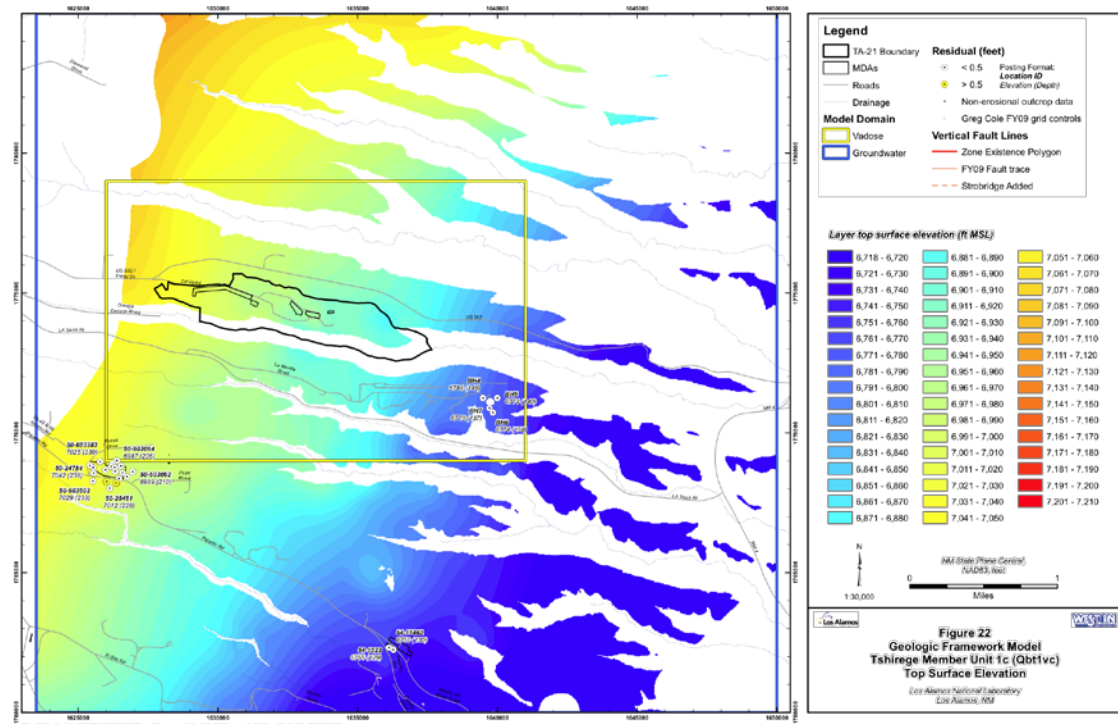


Figure 6d. Top surface elevation of Qbt1vc

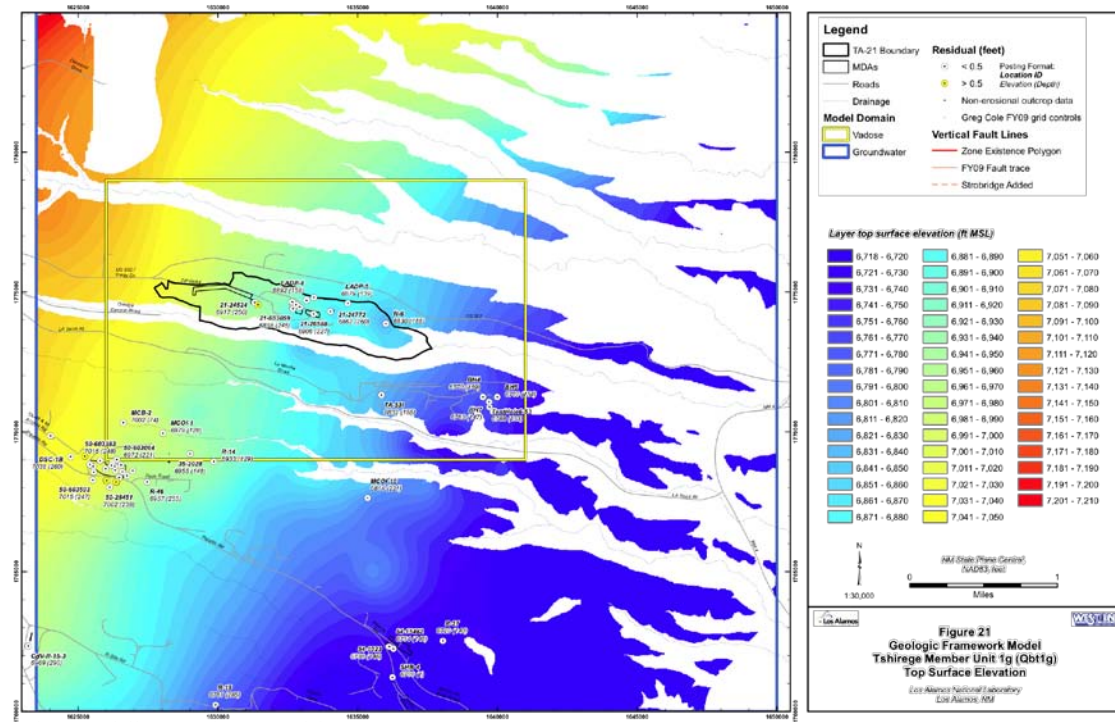


Figure 6e. Top surface elevation of Qbt1g

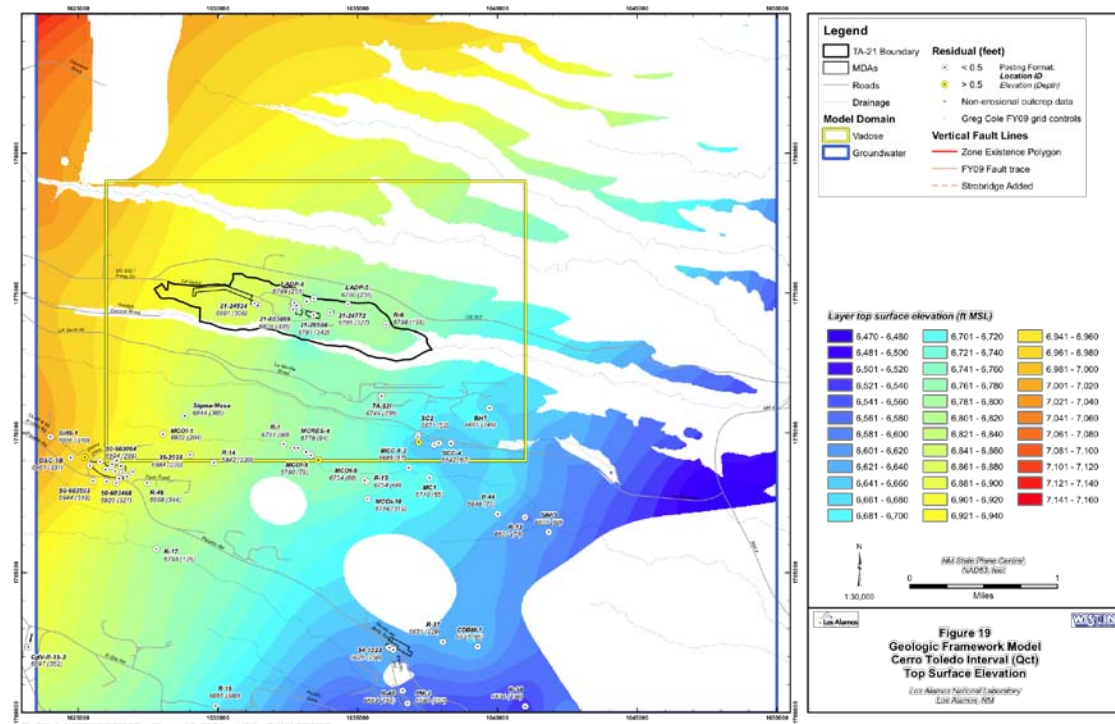


Figure 6f. Top surface elevation of Qct

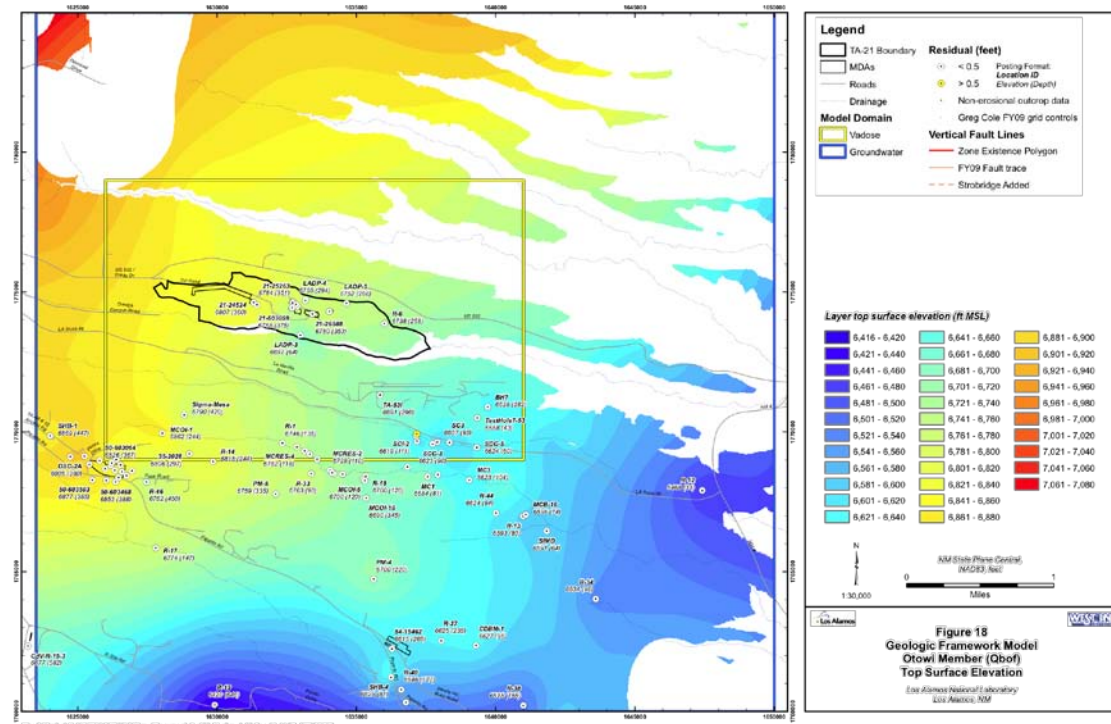


Figure 6g. Top surface elevation of Qbof

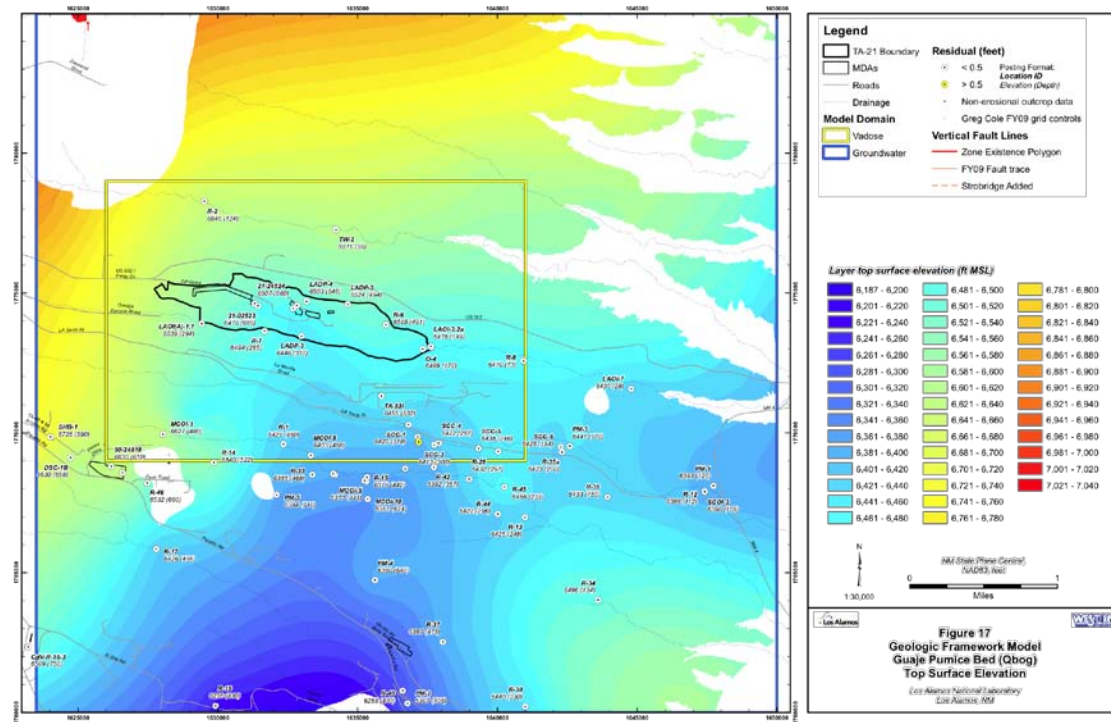


Figure 6h. Top surface elevation of Qbog

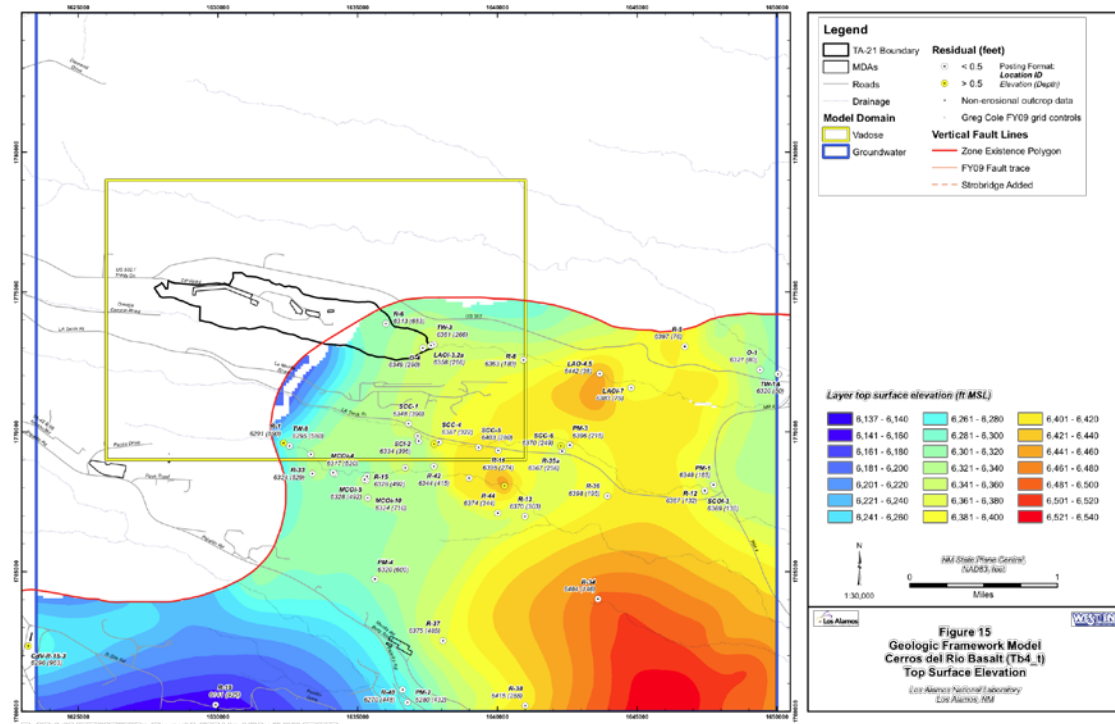


Figure 6i. Top surface elevation of Tb4

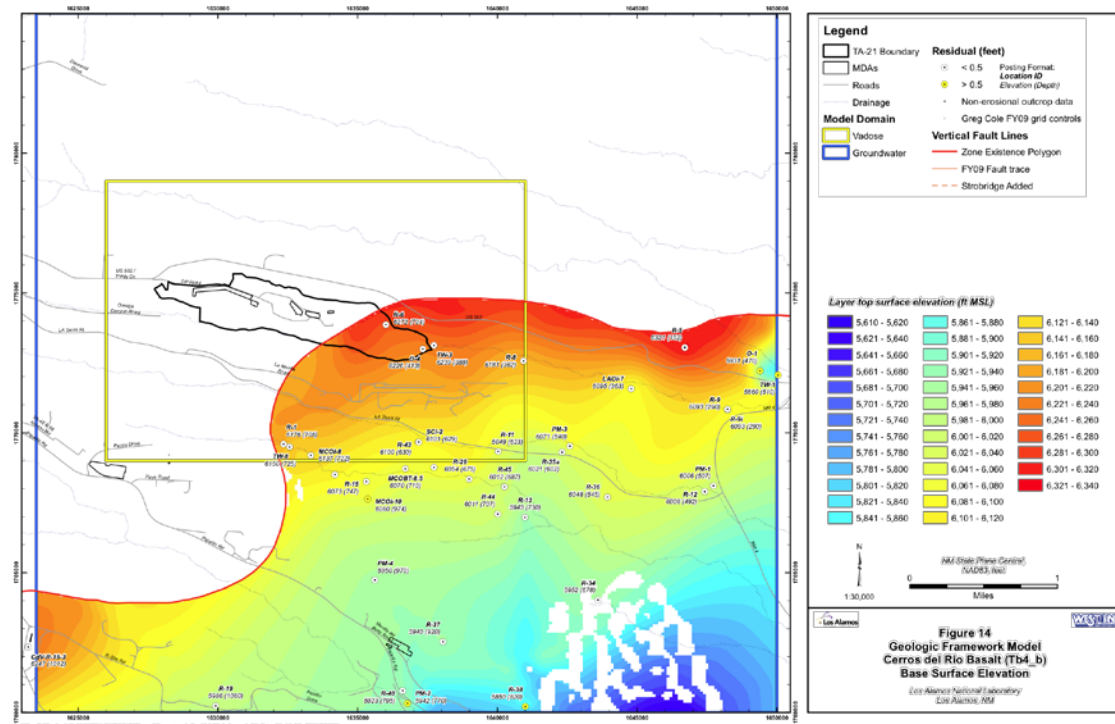


Figure 6j. Bottom surface elevation of Tb4

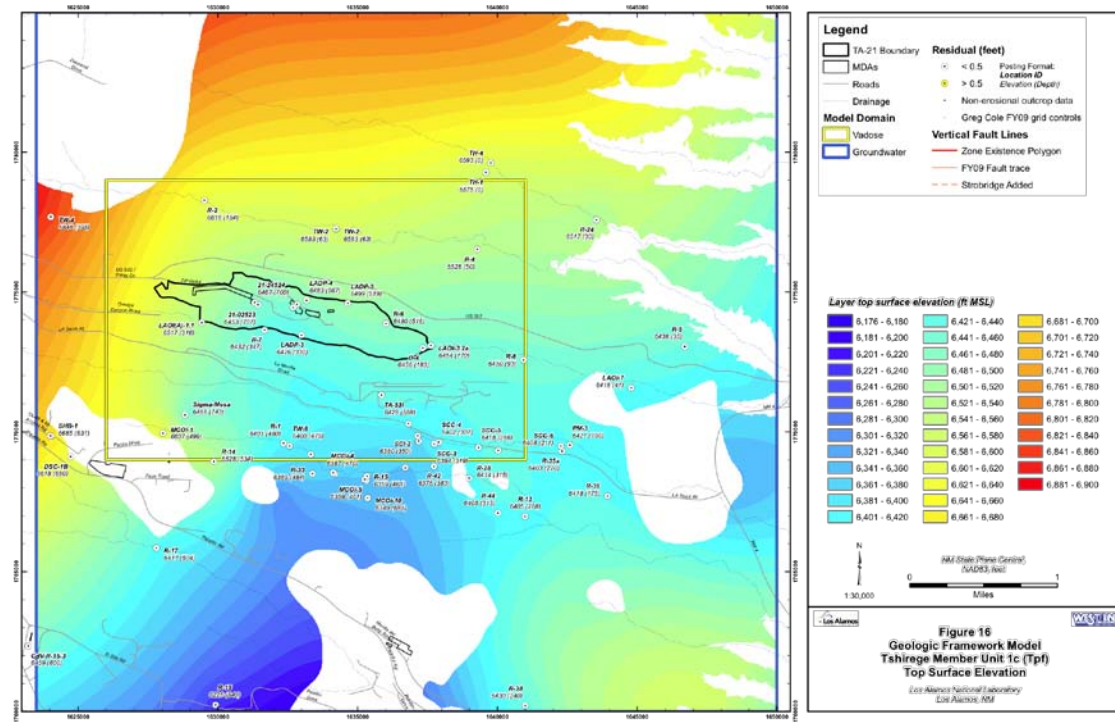


Figure 6k. Top surface elevation of Tp1

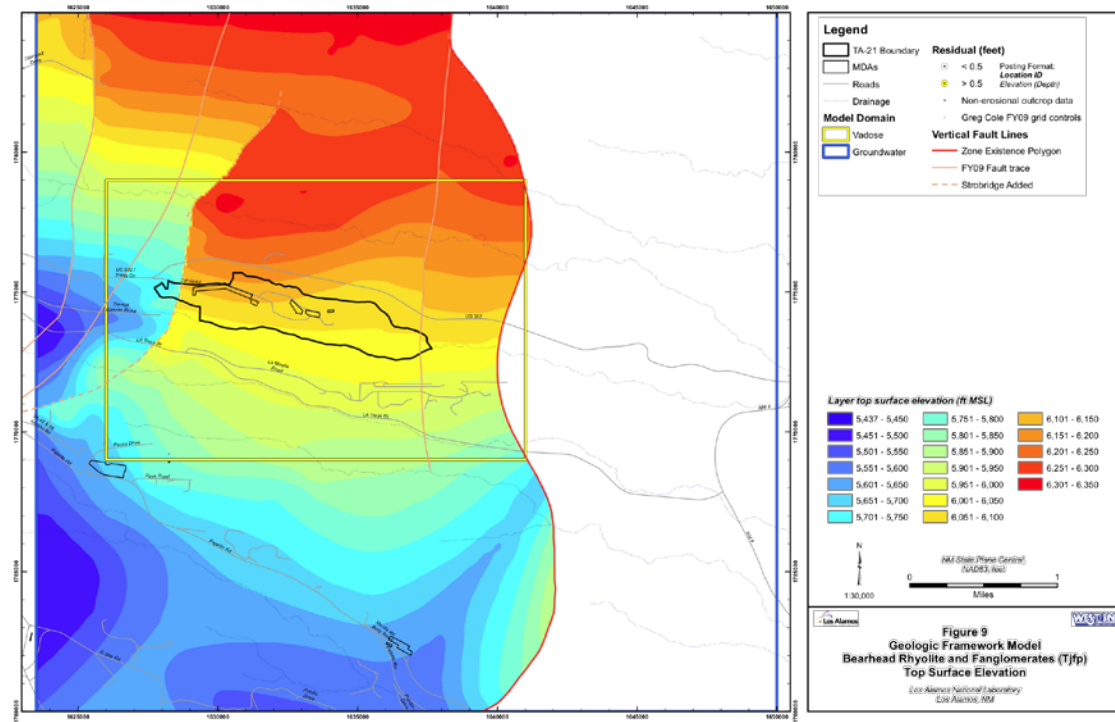


Figure 6l. Top surface elevation of Tjfp

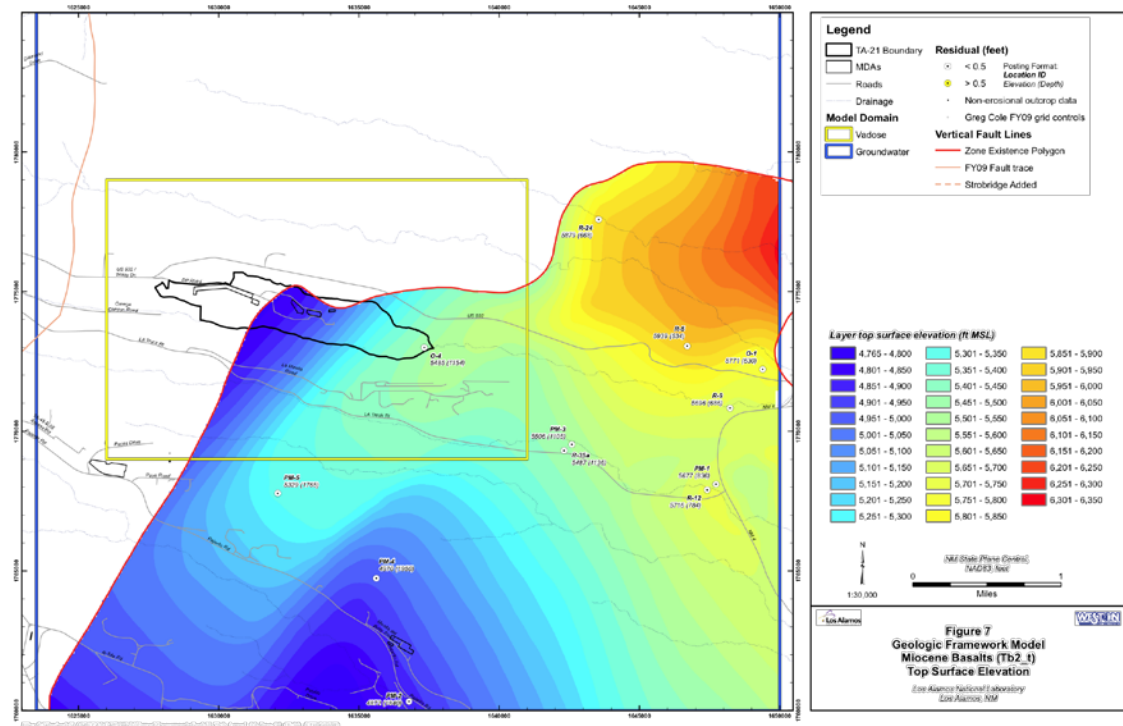


Figure 6m. Top surface elevation of Tb2

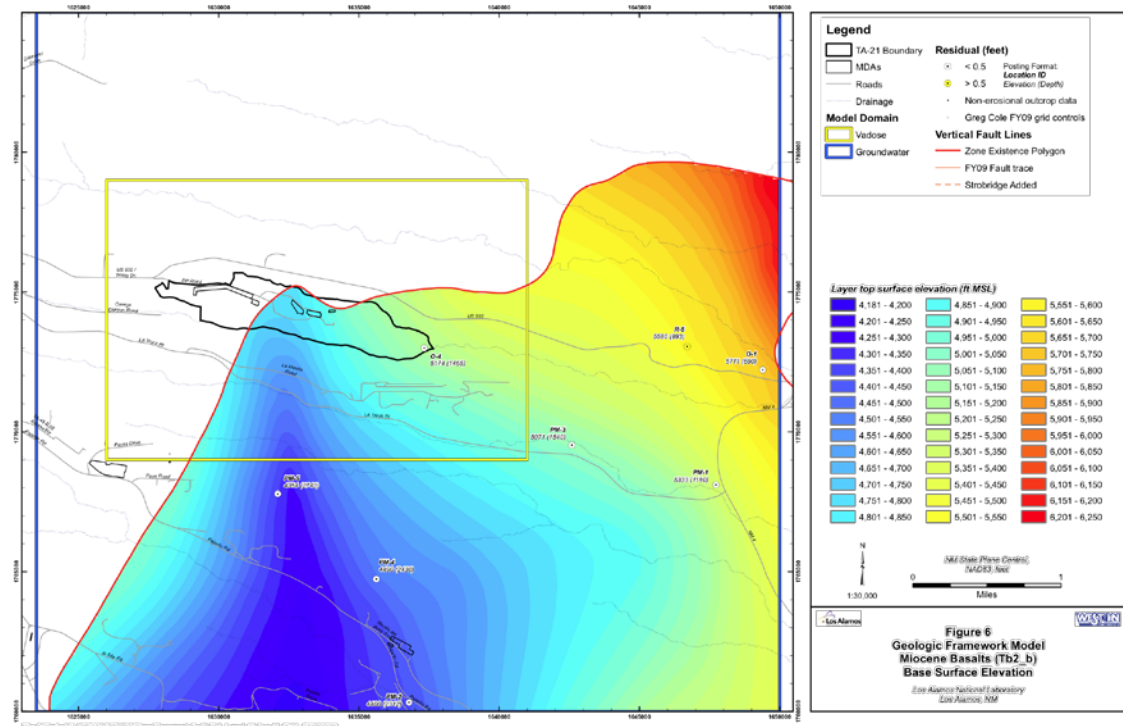


Figure 6n. Bottom surface elevation of Tb2

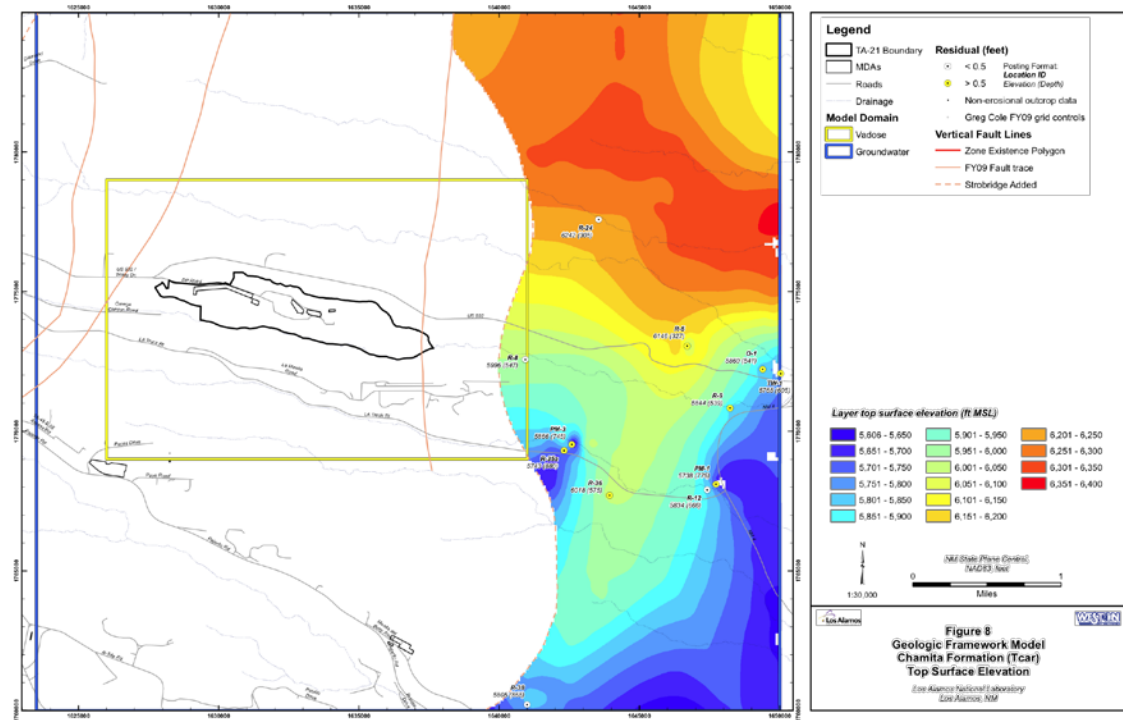


Figure 6o. Top surface elevation of Tear

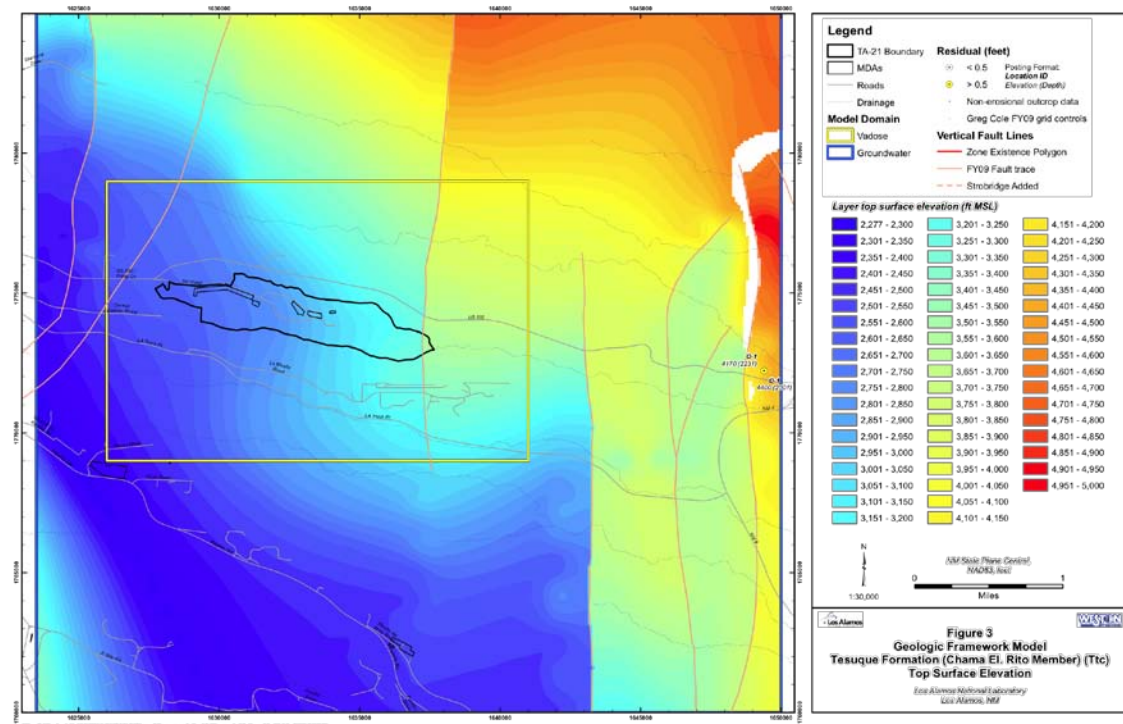


Figure 6p. Top surface elevation of Ttc

References

Cole, D., D. Coblenz, E. Jacobs, D. Koning, D. Broxton, D. Vaniman, F. Goff and G. WoldeGabriel, 2009. The 2009 Three-Dimensional, Geologic Models of the Los Alamos National Laboratory Site, Southern Española Basin, and Española Basin. Los Alamos National Laboratory Report LA-UR-09-03701.

Attachment II
Mesh Generation
for the
Los Alamos National Laboratory Technical Area 21,
Material Disposal Area T

Author:

Terry A. Miller

Contents

| | |
|--|----|
| Introduction..... | 3 |
| Mesh Criteria (Mesh Design) for Mesa Mesh | 6 |
| Mesh Criteria (Mesh Design) for Beds Mesh | 6 |
| Input Data..... | 8 |
| Mesh Generation Process..... | 8 |
| Mesh Generation Process for Beds Mesh | 8 |
| Mesh Generation Process for Mesa Mesh | 10 |
| Mesh Hydrogeologic Properties | 13 |
| Mesh Properties for Absorption Beds and Concrete Shafts..... | 16 |
| Mesh Properties for LA and DP Canyon Bottoms..... | 18 |
| Output | 19 |
| Grid Quality | 21 |
| References..... | 26 |

Introduction

The groundwater pathway model presented in this report represents Material Disposal Area (MDA) T at technical area (TA)-21 and includes important features such as the paleochannel, absorption beds, and concrete shafts. Two meshes were constructed: 1) a mesa-scale mesh that includes all of DP Mesa and TA-21; and 2) a high-resolution local-scale mesh around MDA T. Both meshes have materials defined by the Weston Earthvision model WC09 (Attachment I). This updated geologic model estimates fill depth over sites and includes the geometries of absorption beds and waste disposal shafts. Special attention was given to the location of the top soil and the paleochannel at 50 foot depth, and the interface between Qbog and Tpf materials below the MDA T site.

Two meshes were created; a large-domain mesh that incorporates the full mesa and adjacent canyons (mesa-scale “Mesa” mesh), and a smaller-domain, high-resolution, box shaped mesh that captures the area around the MDA T absorption beds (local-scale “Beds” mesh). In general, the Mesa mesh allows exploration of various modeling scenarios over the full domain while the Beds mesh is used for focused and more accurate modeling immediately around and beneath MDA T. The Mesa mesh is deeper with a top surface in air at 2272 meters (7454.07 feet) and a flat bottom located more than 100 meters below the water table at 1600 meters (5249.34 feet) elevation. The Beds mesh has a flat top at 2176 (highest elevation of beds), and a flat bottom located at an elevation of 1777 meters.

The Mesa mesh was developed for area studies needing the full domain but not high resolution at depth and away from MDA T site. The Beds mesh was needed to capture thin material units and their slope. By reducing the size of the domain to an area around the absorption beds and less depth, the density of mesh nodes for the area was increased. Although both meshes have approximately one-meter resolution near the ground surface, at 15 meters depth, the Beds mesh spacing of 1 meter captures geologic features much better than the 3 to 6 meter vertical spacing of the Mesa mesh. The Mesa and Beds meshes are shown in Figures 1a and 1b, respectively. Coordinate and spacing information for the Mesa and Beds meshes are included in Tables 1a and 1b, respectively.

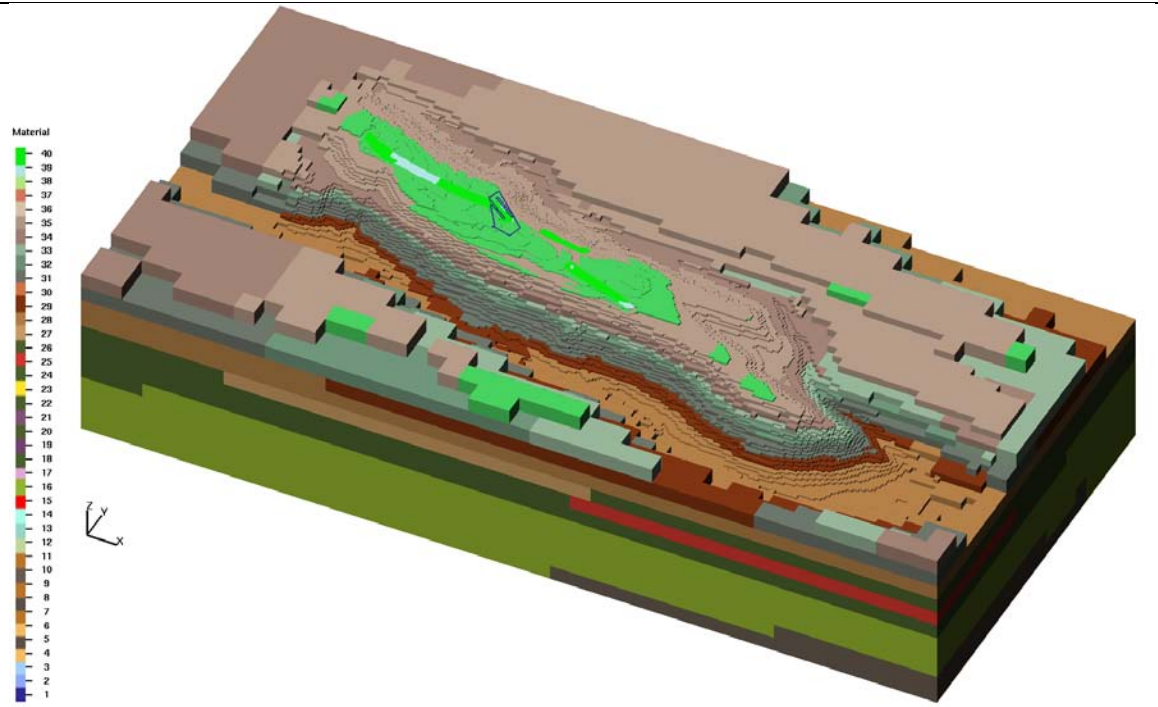


Figure 1a Full Mesa Mesh

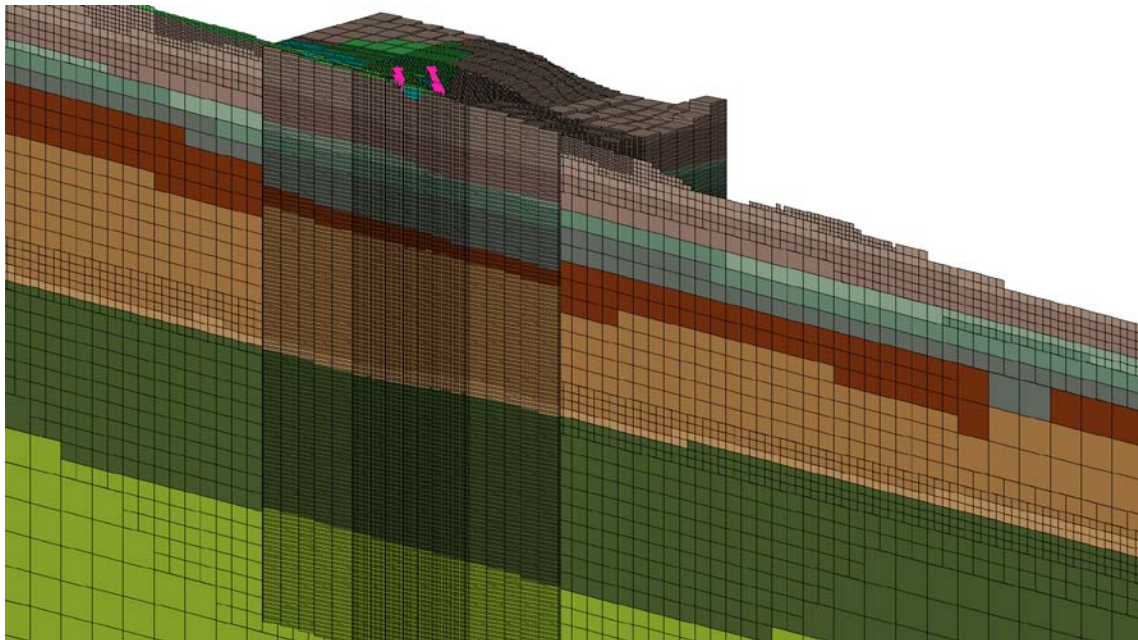


Figure 1b High Resolution Beds Mesh (cut at middle) and Slice from Full Mesa Mesh

Figures 1a and 1b. MDA T Computational meshes colored by the WC09 GFM materials (Table 1) and truncated at ground surface. The Full Mesa mesh has variable octree spacing with high resolution located in the top soils, the mesa sides and both canyon bottoms. The high resolution Beds mesh has a constant 1 meter vertical spacing. The polygon in Figure 1a shows the location of MDA T beds and shafts, the absorption beds for the high resolution Beds mesh are shown as pink in Figure 1b.

Table 1a. MDA T Mesa Mesh Coordinates and Spacing

| MDA T Full Mesa Mesh | | | |
|-------------------------------------|--|----------------------------|--|
| Number of Mesh Nodes: | | 1,041,642 | |
| Number of Tetrahedral Cells: | | 6,189,770 | |
| Vertical spacing: | | 1.5 to 48 meters | |
| Horizontal spacing: | | 2 to 64 meters | |
| Total Computational Volume of mesh: | | 2,312,110,100 cubic meters | |

| Boundary Coordinates State Plane Meters NAD 83 | | | |
|---|------------|------------|------------|
| | Minimum | Maximum | Difference |
| East-West (x) | 496,720.00 | 499,408.00 | 2688.00 |
| North-South (y) | 540,100.00 | 541,380.00 | 1280.00 |
| Vertical (z) | 1600.00 | 2272.00 | 672.00 |

| Boundary Coordinates State Plane Feet NAD 83 | | | |
|---|--------------|--------------|------------|
| | Minimum | Maximum | Difference |
| East-West (x) | 1,629,658.79 | 1,638,477.69 | 8818.89 |
| North-South (y) | 1,771,981.63 | 1,776,181.10 | 4199.48 |
| Vertical (z) | 5249.34 | 7454.07 | 2204.72 |

Table 1b. MDA T Beds Mesh Coordinates and Spacing

| MDA T High Resolution Beds Mesh | | | |
|--|--|-------------------------|--|
| Number of Mesh Nodes: | | 1,040,400 | |
| Number of Tetrahedral Cells: | | 5,985,000 | |
| Vertical spacing: | | 1 meter | |
| Horizontal spacing: | | 3 to 18 meters | |
| Total Computational Volume of mesh: | | 35,910,000 cubic meters | |

| Boundary Coordinates State Plane Meters NAD 83 | | | |
|---|------------|------------|------------|
| | Minimum | Maximum | Difference |
| East-West (x) | 497,485.17 | 497,834.82 | 349.65 |
| North-South (y) | 540,695.17 | 541,044.82 | 349.65 |
| Vertical (z) | 1777.00 | 2176.00 | 399.00 |

| Boundary Coordinates State Plane Feet NAD 83 | | | |
|---|---------|---------|------------|
| | Minimum | Maximum | Difference |
| East-West (x) | | | |
| North-South (y) | | | |
| Vertical (z) | | | |

Mesh Criteria (Mesh Design) for Mesa Mesh

The Mesa mesh is designed to be used for both unsaturated zone and saturated zone calculations using the FEHM flow and transport code. The volume being modeled is the subsurface area of MDA T and regions beneath the mesa and the surrounding Los Alamos and DP canyons. Within the MDA T area, the primary features of interest are the top soils, a paleochannel, and shafts with concrete caps in tuff, and absorption beds in large cobbles. The mesh was designed with spacing to capture fine resolution to represent the absorption beds, shafts, top soils, and paleochannel, but also able to spread mesh spacing large enough to capture the full domain of the mesa to O-4 groundwater monitoring well, both LA and DP canyons and to a depth that includes the Tpf Puye and basalt materials under the mesa and nearby canyons.

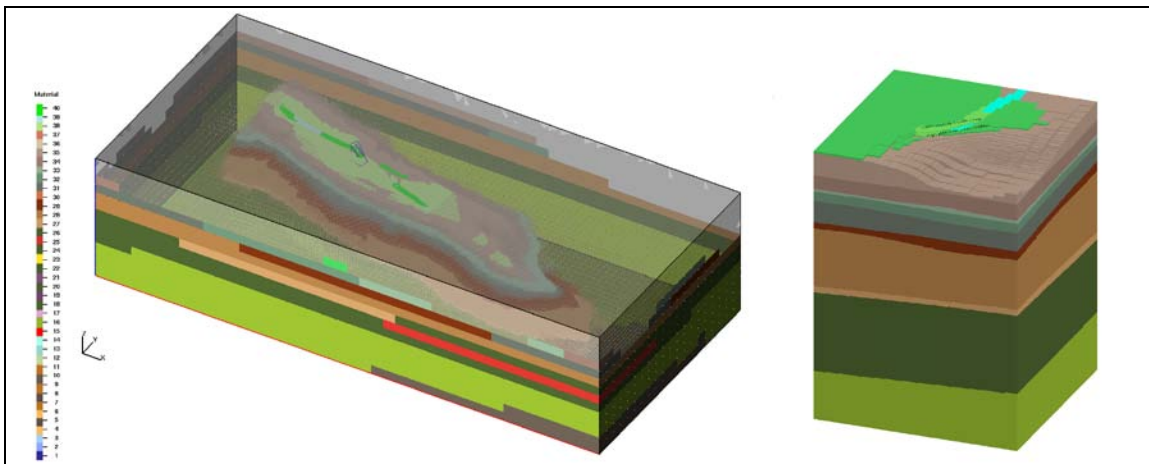
An octree refined mesh using orthogonal hexahedral elements was chosen for the MDA T flow and transport model. The principal reason structured grids are used for this work is to allow for the use of the streamline particle-tracking transport capability of FEHM. Although the structured grids are not as flexible as unstructured grids in fitting complex geometry, tests have shown that they provide accurate solutions as long as there is adequate resolution to represent the geometry of the different materials in each hydrogeologic layer. Moreover, there must be enough resolution to account for any large gradients present in the flow or transport model. Therefore the grid will need appropriate resolution along the expected particle paths. Accuracy and higher resolution at the ground surface is needed to correctly locate features such as the paleochannel, absorption beds, and the shafts.

The Mesa mesh is a balanced octree grid with resolution added to capture the ground topography and target features. Mesh spacing is designed to telescope out from fine resolution at MDA T and coarser as distance from MDA T and ground surface increases. A mesh spacing of 2 x 1.5 meters was chosen for the MDA T area. Vertical resolution in the thick Qbof and Tpf units are thick enough to be represented with 12 and 24 meter spacing. The Qbog layer was deemed important enough to use 6 meter spacing and ensure this thin unit has enough refinement to be continuous and to capture the south and east slope contours. Node information for the Mesa mesh is included in Table 2.

Mesh Criteria (Mesh Design) for Beds Mesh

The Beds Mesh has a constant 1 meter vertical spacing and was created after modeling with the Mesa mesh determined that higher resolution was needed for modeling water flow under the absorption beds. It was decided that each of the materials under the beds and to the water table needed to be represented more accurately. The total mesh nodes needed to stay near approximately one million for time and computational constraints. The Beds mesh is near the same number of nodes as the Mesa mesh, but with a Beds domain located immediately around the MDA T beds and with 400 meter depth. Vertical resolution under the beds is a constant 1 meter vertical and 2 meter horizontal. This resolution is able to capture the slope and thickness of the Qbt Tshirege and Qct Cerro Toledo units. This resolution also allowed the inclusion of ~~a~~ a layer to represent the Vapor Phase Notch by tagging the bottom nodes of the Qbt1vc (colonade) unit. Node information for the Beds mesh is included in Table 2.

Table 2. Node information for Mesa and Beds meshes



Mesa and Beds Mesh Materials from WC09 GFM

| Beds Mesh Nodes | Mesa Mesh Nodes | Name | Geologic Description | Mesh ID |
|------------------------|------------------------|----------------------------------|---------------------------------|----------------|
| 7511 | 312618 | | Air | 101 |
| 1425 | 17080 | OB2 | Overburden above Paleochannel | 39 |
| 1584 | 14205 | PC | Paleochannel | 40 |
| 4435 | 82684 | OB | Overburden Fill/Soil | 38 |
| 71034 | 315111 | Qbt3 | Tshirege Unit 3 | 35 |
| 53853 | 35970 | Qbt2 | Tshirege Unit 2 | 34 |
| 14553 | 20542 | Qbt1vu | Tshirege Unit 1 - vitric | 33 |
| 34145 | 7602 | Qbt1vc | Tshirege Unit 1 - colannde | 32 |
| 74881 | 14688 | Qbt1g | Tshirege Unit 1 - glassy | 31 |
| 27952 | 17511 | Qct | Cerro Toledo | 29 |
| 227196 | 89999 | Qbof | Otowi Member, ash flow | 28 |
| 21255 | 39961 | Qbog | Otowi Member, Guaje Pumice | 27 |
| 0 | 517 | Tb4 | Cerros del Rio Basalts | 25 |
| 293996 | 51369 | Tpf | Fanglomerates | 20 |
| 206580 | 21394 | Tjfp | Bearhead Rhyolite, Peralta tuff | 16 |
| 0 | 391 | Tb2 | 8.4 to 9.3 Ma Basalts | 10 |
| 1,040,400 | 1,041,642 | Total Mesh Nodes | | |
| 3591.0E+04 | 231211.0E+04 | Total Mesh Volume (cubic meters) | | |

Input Data

The input data for building the Mesa and Beds meshes include a geologic framework model (GFM) and data to represent features such as the paleochannel, absorption beds, and concrete shafts.

The geology of both meshes are defined with the WC09 Geologic Framework Model (GFM) as described in Attachment I. The WC09 GFM is a three-dimensional (3D) Geocellular model of the Pajarito study area and encompassing MDA T. The framework stratigraphy is formed through a process that creates a 3D model from disparate input data that incorporate the geologic information contained in wells and cross sections. The resulting 3D model is then evaluated for consistency with the input data and accepted conceptual models for the area.

The GFM includes a small but fine resolution Earthvision model used to capture shallow features at the top of the mesa. The subset model is a high resolution representation of the paleochannel and soils within 50 feet depth from MDA V in the West to MDA U in the East. The WC09 geologic model includes estimated fill depth over the sites and includes geometry of absorption beds and waste disposal shafts. The four absorption beds were provided as polygon shapes at ground surface and extended to depth.

Mesh Generation Process

The meshes were developed using the Los Alamos Grid Generation software package (LaGriT)(George 1997). LaGriT contains a comprehensive set of software macros that uses hydrogeologic, GIS, and geometry data to build and optimize computational grids. LaGriT is used to write model setup files for FEHM and is also used for grid analysis and visualization work. The mesh generation methods and images for both Mesa and Beds meshes can be found at http://meshing.lanl.gov/proj/ER_LANL_TA-21_2009/catalog.html

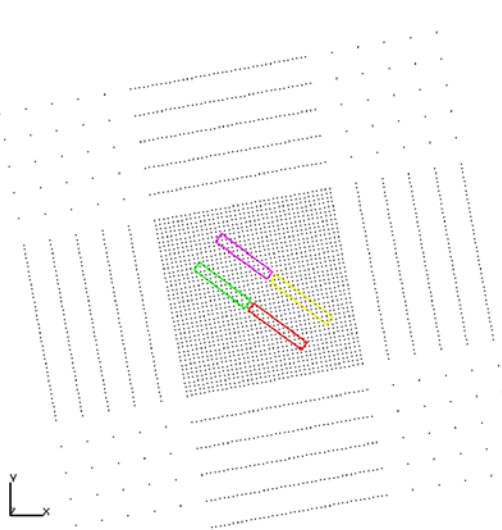
Mesh Generation Process for Beds Mesh

The high resolution Beds mesh was created with a constant vertical spacing of 1 meter and 399 meters height. It has a 2 meter horizontal spacing in a 120 x 120 meter area around the absorption beds. Mesh cells are added to the outer zone of the Beds mesh to act as a boundary, the outside middle cells have 18 x 3 meter spacing and outside corners have 18 x 18 meter spacing. The mesh was translated and rotated so the Beds center was located at the center between the four absorption beds as shown in Figure 3. The Beds mesh is rotated 45 degrees to keep the beds in the middle of the high resolution rectangular shape.

The corner point coordinates of the translated and rotated mesh are:

SW 497539.8477542 540695.1756772
SE 497834.8242265 540749.8463349
NE 497780.1535688 541044.8228071
NW 497485.1770966 540990.1521495

The mesh nodes were tagged with the WC09 GFM and absorption bed locations the same as was done for the Mesa mesh described below. The result is a high density computational mesh representing the hydrogeologic layers around and below the absorption beds.



Distribution of High Resolution Beds Mesh showing locations of the absorption beds.

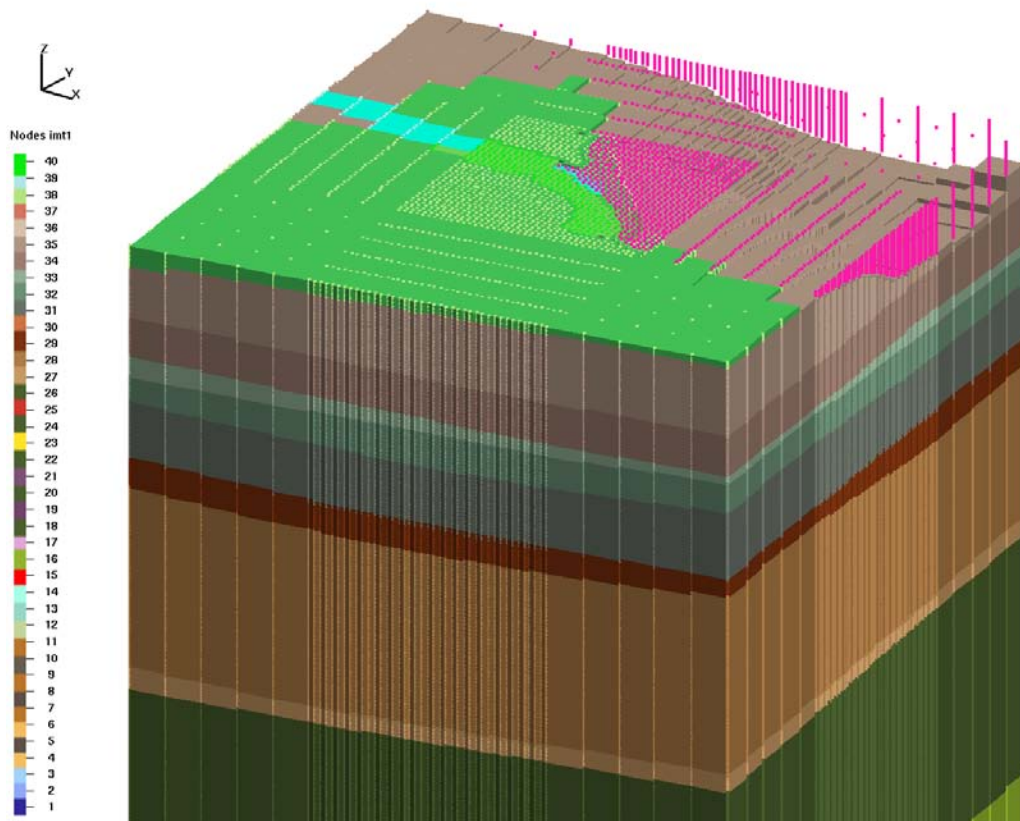


Figure 2. High Resolution Beds Mesh showing GFM colors as described in Table 1. Pink nodes are identified as air above the mesa ground.

Mesh Generation Process for Mesa Mesh

This section details the steps to build the Mesa Mesh. These steps include: building the base grid within area extents, refinement of grid blocks in areas requiring further resolution, grid optimization, assignment of node properties, and the output of FEHM grid and property files. Although the GFM is in units of feet, the grid is written in meters for input into the FEHM modeling program. This is a simple conversion and does not introduce any inaccuracies.

The geologic framework for the model region is the first consideration for constructing a grid for a model area. The grid resolution in the vertical dimension must be chosen to adequately represent groundwater flow and transport in the model. Each layer in a structured grid is horizontal, but the layers of the physical hydrogeologic units are gently sloping. The grid layers will have a stair-step shape, but increasing vertical resolution can capture the shape of the slope (as shown in the Beds mesh). A grid with finer resolution and more nodes can more accurately represent the geologic structure, but will require increased computational demands. Careful design of grid node distribution will result in a balance between grid size and a grid resolution that captures the geologic framework (Miller et al., 2007).

Computational meshes generally evolve from relatively simple large regions, to smaller focus areas with added detail and resolution. Each generation of refinement is considered a new “level”. The Mesa mesh is a 5-level octree refined mesh. The spacing is selected to provide the resolution for accurately representing flow and transport along critical flow and transport path ways in model area and with special attention to the area around and under MDA T. A much finer resolution is used at shallower portions of the model, and a progressively coarser resolution is used for deeper portions. Each element is slightly shorter in the vertical to optimize resolution in the vertical direction. The mesh spacing ranges from 2 x 1.5 meters (approximately 6 x 4 feet) at the mesa top to 64 x 48 meters (approximately 210 x 157 feet) at the bottom and outside edges of the model domain. The structure of the grid’s vertical layering is summarized in Table 3 and illustrated in Figure 3.

For the horizontal resolution, the general criteria used for grid refinement is geometric. A polygon which outlines the mesa bottom at the canyons and mesa top are used with the ground surface to refine along the mesa walls. Refinement directly under the absorption beds and shafts is selected radially with MDA T at the center. A box shape fitting the paleochannel is used to select the final high resolution representing this shallow feature.

Table 3 summarizes the spacing and selection criteria. Figure 4 shows the mesh for each of the five refinement levels starting with the level 0 background mesh. Refinement telescopes in toward the smallest resolution located at top of mesa and along the paleochannel where the high resolution captures features needed for modeling MDA T and surrounding area.

Table 3. Spacing Used in the MDA T Computational Mesh

| Level | Vertical Spacing (m) | Horizontal Spacing (m) | Area Selected for additional Resolution – each level divides spacing by half such that spacing telescopes inward toward smallest edge lengths. |
|-------|----------------------|------------------------|--|
| 0 | 64 | 48 | Entire Mesh (this is the starting mesh) |
| 1 | 32 | 24 | Rotated region around MDA mesa and canyons. |
| 2 | 16 | 12 | Inner region immediately around mesa and canyons |
| 3 | 8 | 6 | Mesa surface top and canyon. Elevations containing Qbog. |
| 4 | 4 | 3 | Mesa top including the MDA T site and immediately below. |
| 5 | 2 | 1.5 | Beds around paleochannel and radial distance encompassing the MDA T site. |

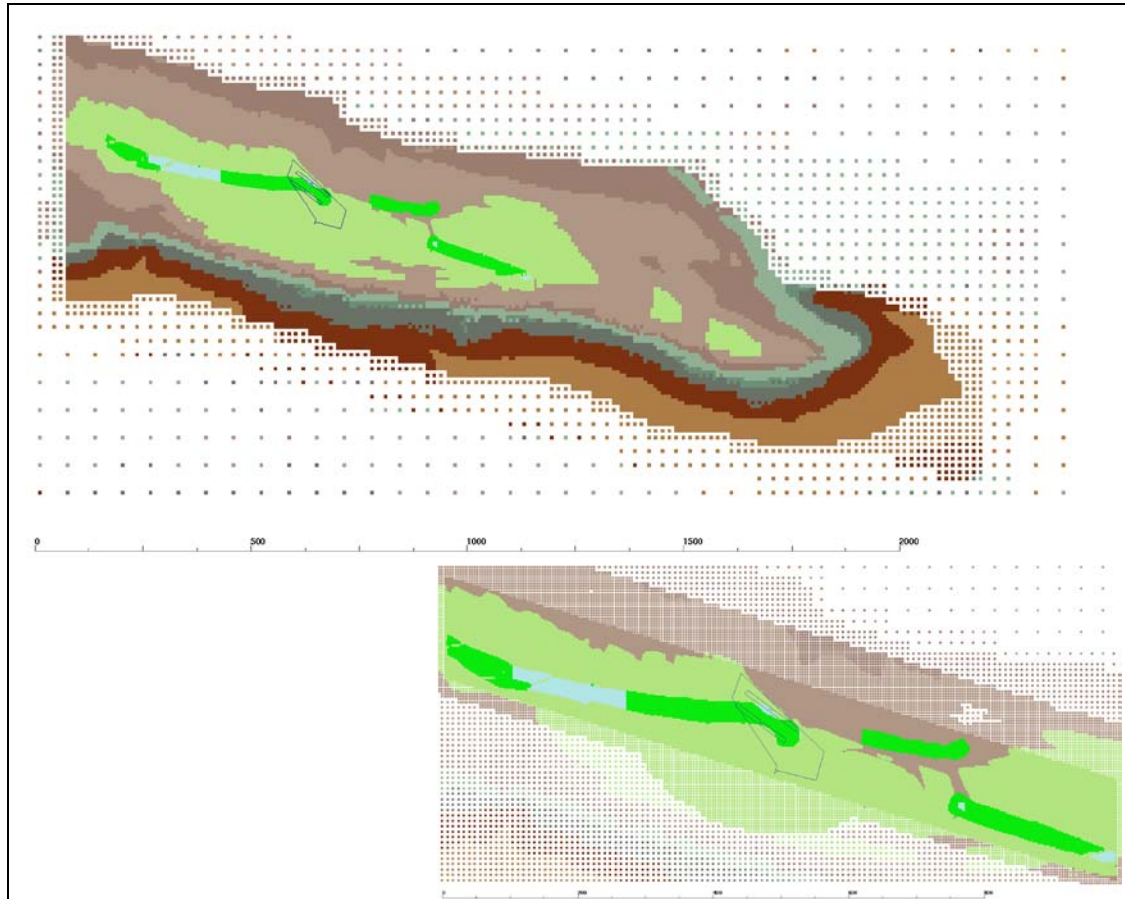
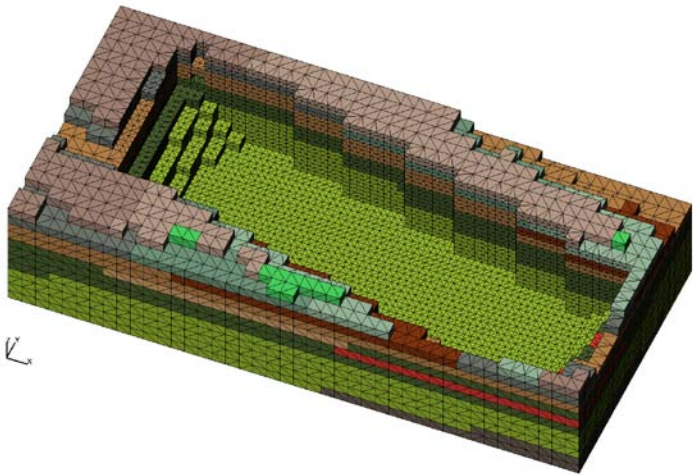


Figure 3. MDA T Mesa mesh top views showing full mesh and MDA T area refinement. Highest resolution spacing is in the immediate vicinity around MDA T and at mesa top soils to represent the thin paleochannel and capture mesa walls. Hydrogeologic units are colored with WC09 GFM color map as shown in Table 2.

Level 0 Background mesh with coarse resolution 64 x 48 meter edges. Outside elements rotated around mesa and canyons.



Level 1 resolution around includes full mesa, canyon bottoms, and canyon confluence on east edge 32 x 24 meter edges.



Level 2 bottom goes through fanglomerates and includes mesa and canyon edges 16 x 12 meter edges.



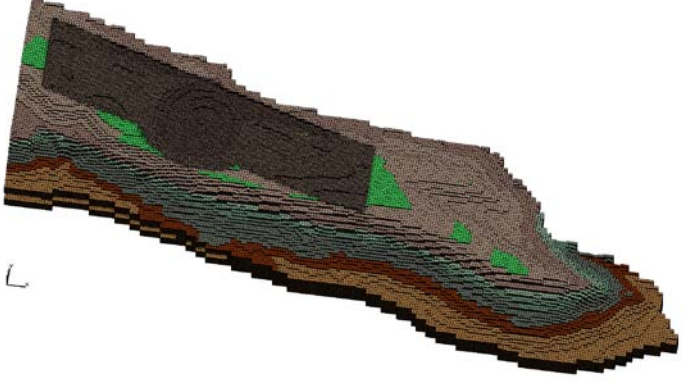
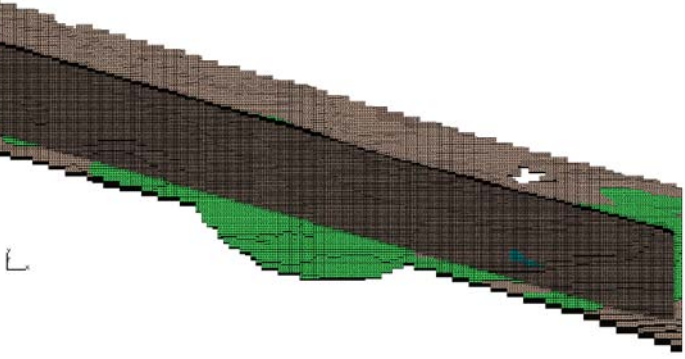
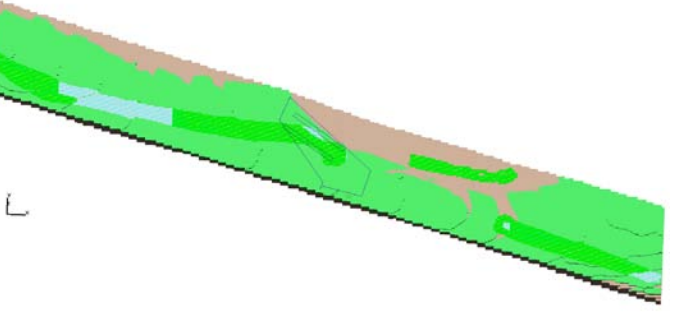
| | |
|--|--|
| <p>Level 3</p> <p>includes Qbog elevations, full mesa surface to 35 meter depth, and east to Well O-4 8 x 6 meter edges.</p> |  |
| <p>Level 4</p> <p>includes 12 meter top of mesa and 400 meter radius around and below MDA T site 4 x 3 meter edges.</p> |  |
| <p>Level 5</p> <p>is a 4 meter deep Beds shape containing the paleochannel and boundary of MDA T site 2 x 1.5 meter edges.</p> |  |

Figure 4. Model mesh development for each of the 5 refinement levels.

Mesh Hydrogeologic Properties

After constructing the mesh, the physical hydrogeologic unit present at each node in the computational grid is assigned. The WC09 GFM Earthvision model is used for this step. The volumes of the GFM represent the shape of each hydrogeologic layer. The mesh nodes and the hydrogeologic features are both imported into LaGriT and are used to identify the hydrogeologic layer designation for each node and cell of the computational mesh nodes are also identified as

above and below the ground surface, and for each of the absorption beds and shafts. Figures 5 and 6 illustrate the variable mesh spacing with associated hydrogeologic units for the Mesa mes. Figure 7 illustrates the mesh spacing and associated hydrogeologic units for the Beds mesh.

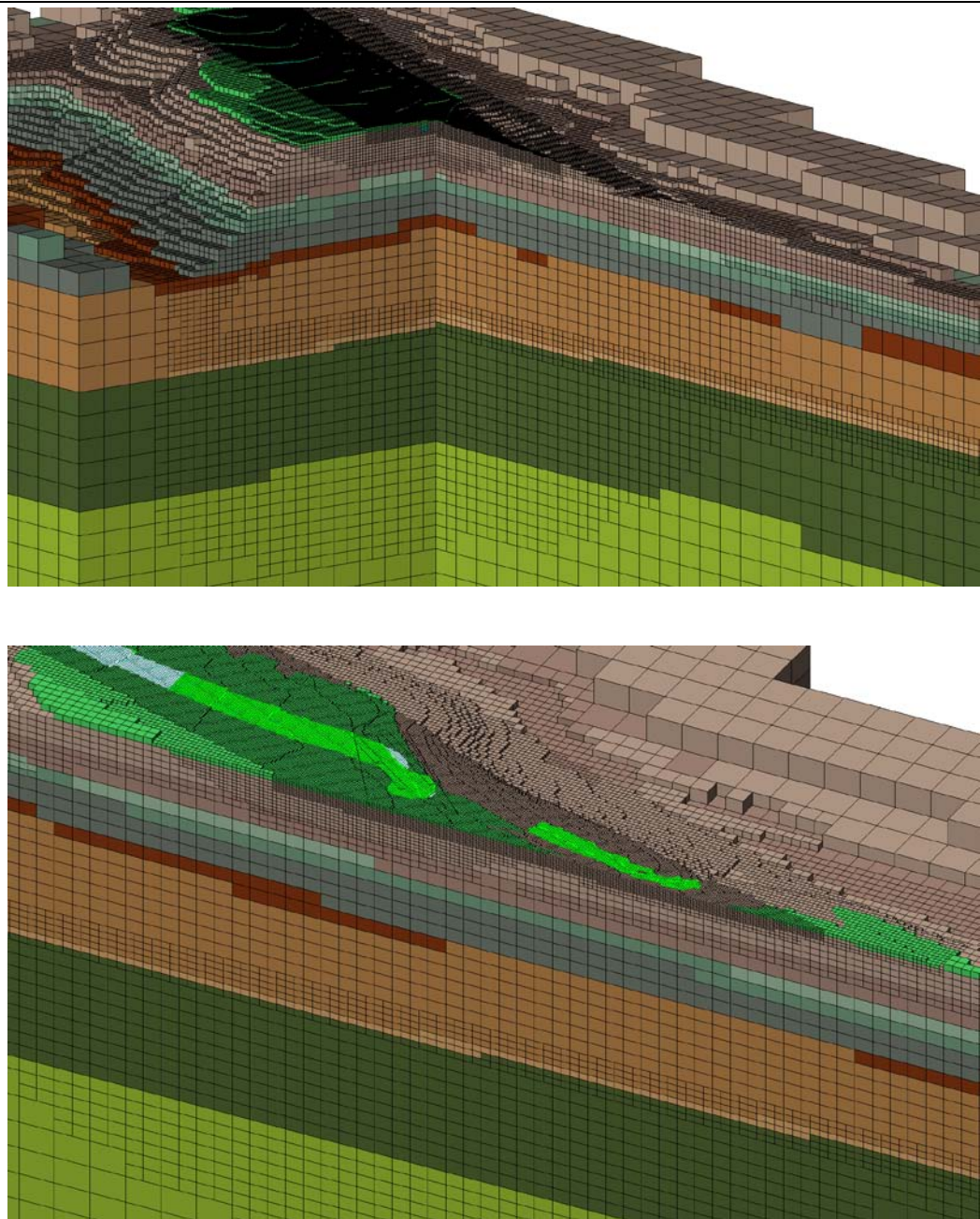


Figure 5 Cutaway showing a close up of the refined area of the MDA T mesh where vertical spacing reduces from 37.5 meters (123.03 feet) down to 6.25 meters (20.5 feet). The cut out is the north east section of the mesa and shows the Cerros Del Rio Tb4 red) and layers up to surface with the Otowi layers in tan. Soil, or overburden shows here as bright green. Vertical lines show shaft locations 1, 7, 4, 5 (left to right).

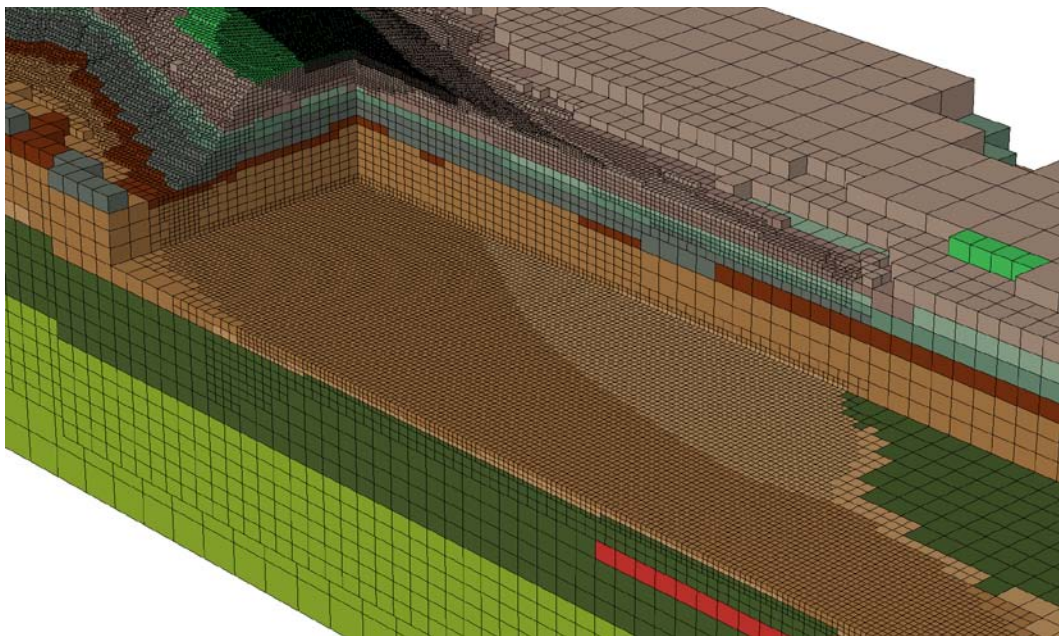


Figure 6. Full Mesa Mesh colored by WC09 and cutout to show the Otowi members in brown and Fanglomerates in greens. The highest resolution is along the mesa top and beneath.

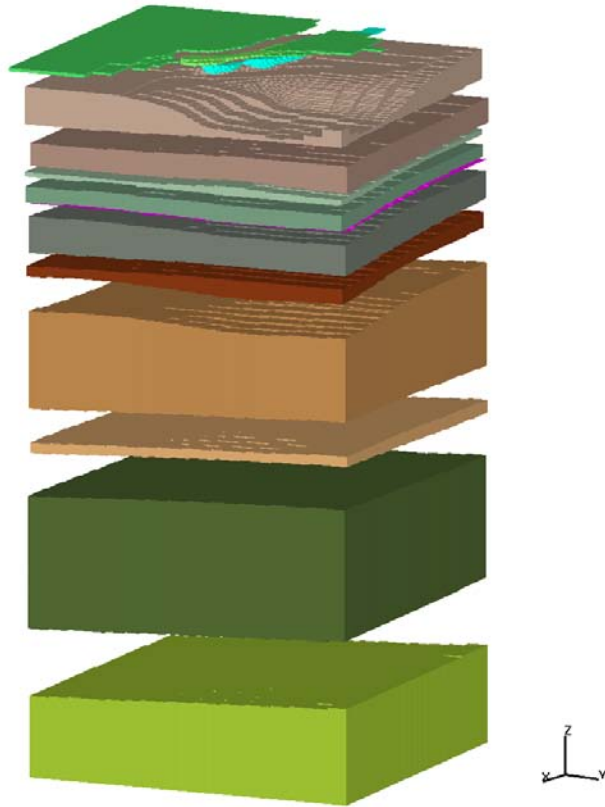


Figure 7. Beds Mesh colored with WC09 GFM. Materials have been separated at the interfaces. An additional material to represent the Vapor phase notch was created from the bottom nodes of Qbt1vc and is shown here as the pink layer.

Mesh Properties for Absorption Beds and Concrete Shafts

The absorption bed zones are identified using polygons for each bed 1 through 4 with beds 1 and 2 further south and at higher elevation (2176 meters) than Beds 3 and 4 located toward the DP canyon side at elevations from 2130 to 2175 meters. Each polygon is defined as parallel bed shapes defined by 3 points, one each in the SW, SE, and NW corner (Table 4).

Table 4. Absorption bed coordinates.

| Bed Points | X (meters) | Y (meters) |
|------------|------------|------------|
| Bed 1 SW | 497616.88 | 540885.25 |
| Bed 1 SE | 497651.22 | 540859.38 |
| Bed 1 NW | 497620.31 | 540890.12 |
| Bed 2 SW | 497653.25 | 540857.81 |
| Bed 2 SE | 497689.28 | 540831.25 |
| Bed 2 NW | 497656.69 | 540862.62 |
| Bed 3 SW | 497668.38 | 540877.00 |
| Bed 3 SE | 497706.44 | 540848.44 |
| Bed 3 NW | 497671.50 | 540882.21 |
| Bed 4 SW | 497631.09 | 540904.44 |
| Bed 4 SE | 497666.03 | 540879. |
| Bed 4 NW | 497633.28 | 540909.44 |

Each horizontal layer of mesh nodes are labeled from top down to 3 layers deep with each layer 1.5 meters apart. The top nodes of beds 1 and 2 (south) are at elevation 2176.0 meters. The top nodes of beds 3 and 4 (north) are at elevation 2174.5 meters. This is consistent with the ground elevations in this area which slope generally downwards toward the north and east from 2177 meters to 2174 meters.

There are 100 shaft zones located between the four absorption beds located at various depths. The shaft nodes are selected by constructing a 1 meter cylinder around actual shaft line locations and tagging the mesh nodes within this cylinder. Mesh resolution at top is 2 meters horizontal and 1.5 meter vertical so actual shaft locations will vary from the nearest node selected to represent the shaft. The representative shaft nodes are written with elevations and associated material so the modeler can choose mesh nodes to best simulate actual conditions.

The absorption beds are for the Mesa and Beds meshes are shown in Figures 8 and 9, respectively. Figure 10 shows the absorption beds, shafts, and paleochannel.

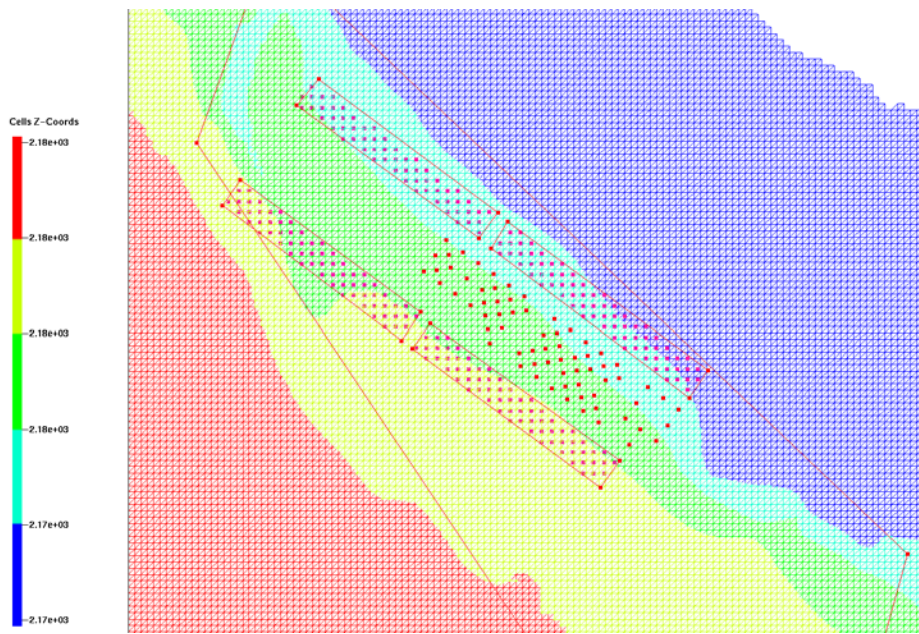


Figure 8. Mesa mesh detail showing mesh nodes used to represent the four absorption beds and concrete shafts. The MDA T site polygon is included for reference only.

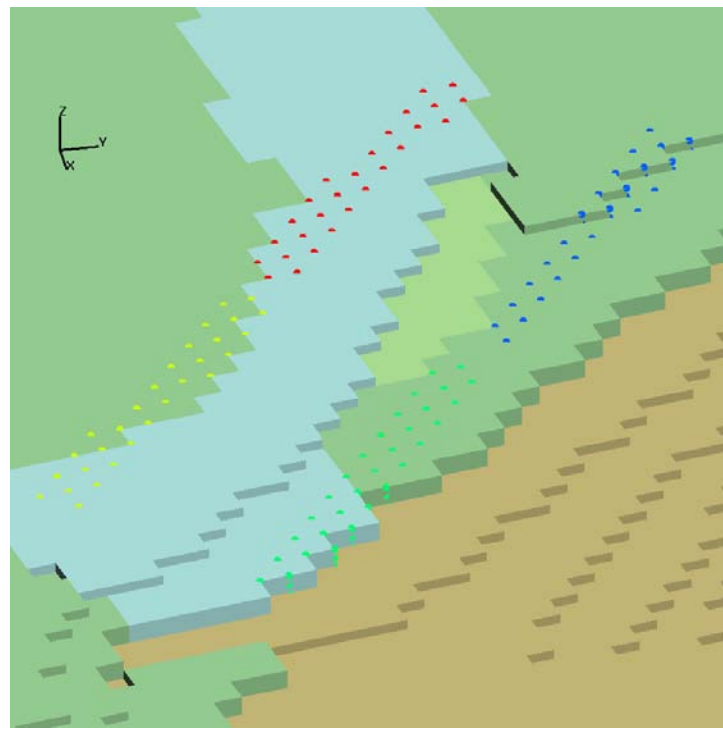
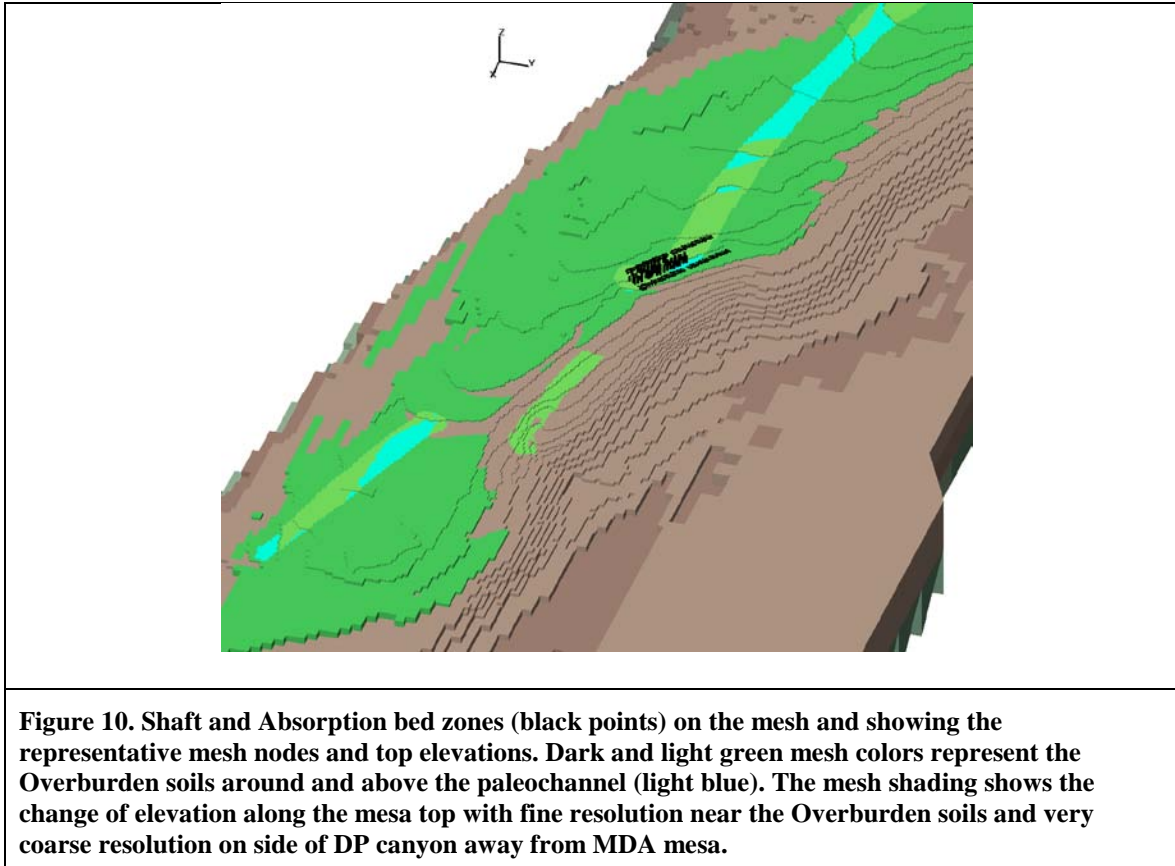


Figure 9. Beds mesh showing the mesh nodes representing the top layer of each of the four beds. Stair stepping can be seen as the mesh changes to represent the slope of elevation toward DP canyon direction.



Mesh Properties for LA and DP Canyon Bottoms

These files represent LA canyon, DP canyon, and all nodes at the top ground surface and connected to the air mesh nodes above. The surface representing the top ground (and below air) has 58542 mesh nodes with a total Voronoi area of 3440640 square meters. LA Canyon has 2272 nodes and a total Voronoi area of 404445 square meters. DP Canyon has 1791 mesh nodes and a Voronoi area of 83858 square meters. LA and DP canyons can be seen in Figure 11.

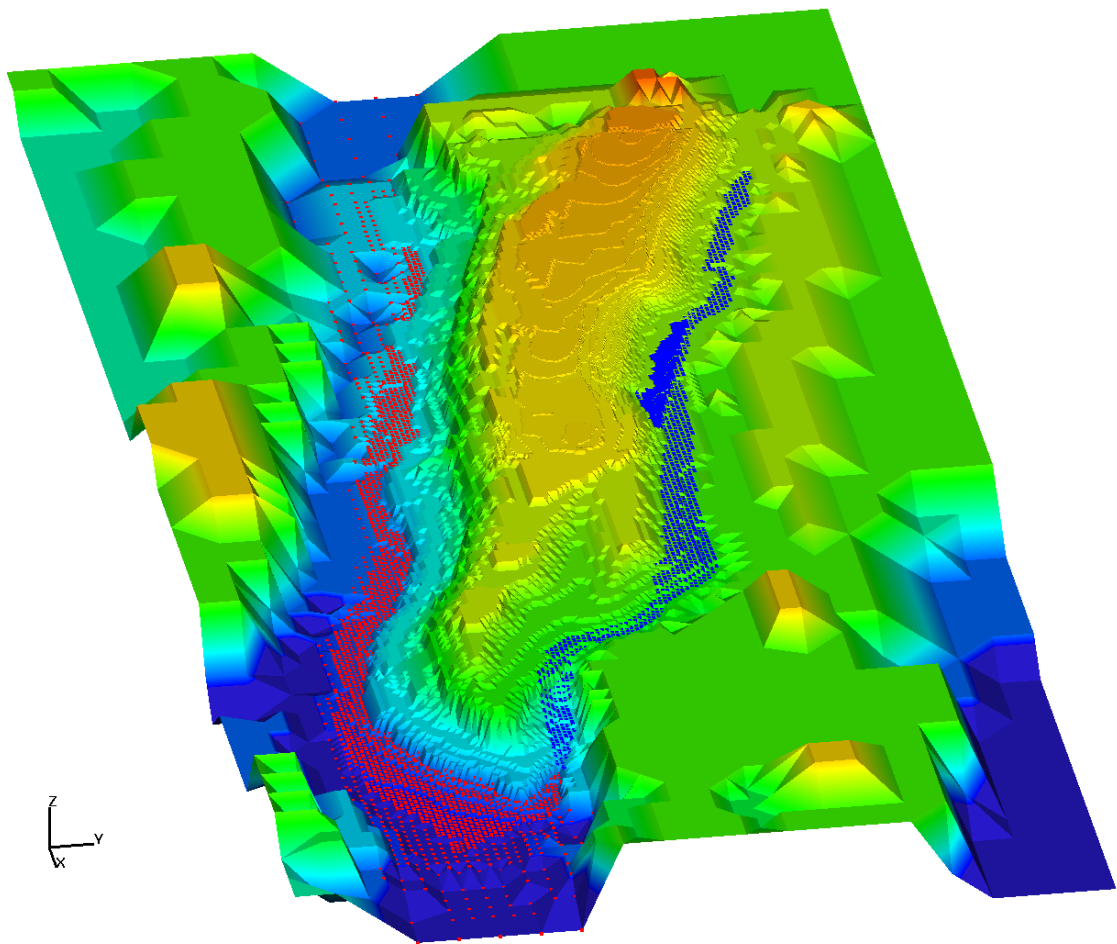


Figure 11. Ground surface extracted from the Mesa mesh and colored by elevation. Points on the surface represent selected canyon points. These represent the mesh nodes below at top ground surface and connected to air nodes. The red points are Los Alamos Canyon and the blue are DP Canyon mesh nodes.

Output

Once the grid quality is checked and the geometry conforms to the GFM, FEHM input files are generated. The FEHM software code is used in modeling to obtain numerical solutions describing groundwater flow and transport. The control-volume finite element (CVFE) method is used in FEHM to obtain a numerical solution to the groundwater flow equation over the model domain. Grid tetrahedral are divided into volumes associated with grid blocks and areas associated with interblock distances. The grid block volumes are the Voronoi volumes associated with each grid block. LaGriT is designed to produce these CVFE grids by translating the coordinate and grid attribute information into a form that is valid for finite-element heat and mass compilations.

LaGriT is used to write FEHM files listed in Table 5. The files include the grid geometry, lists of nodes on external boundaries, and node lists sorted by hydrogeologic unit. The number of nodes assigned to each hydrogeologic unit is presented in Table 1.

Table 5. Mesh generation output files for FEHM.

| | |
|--|--|
| tet_WC09_material.zone | FEHM zone list format for each hydrostratigraphic unit as defined from WC09 and Paleochannel GFMs. Materials 10 to 40 and 101 assigned to mesh nodes. Air is material zone 101 |
| tet_WC09_outside.zone | FEHM zone list format for each face of the model (top, bottom, N, S, E, W). These are median areas. |
| tet_WC09_outside.area | FEHM area format file with the vector area associated with each exterior node. These are median areas. |
| tet_WC09.fehmn | FEHM 'coor' and 'elem' information for node coordinates and element connectivity. State Plane Meters NAD 83. |
| tet_ascii.stor tet_bin_linux.stor | FEHM sparse matrix coefficients in ASCII and binary format for linux OS.. |
| DP_canyon.zone DP_canyon_area.dat LA_canyon.zone LA_canyon_area.dat top_surf.zone top_surf_area.dat | The top ground surface has highest nodes with materials 1-40 and connected to air. The .dat files are Voronoi areas of nodes at top ground surface. |
| MDAT_shaft_nodes.dat shafts_material.zone | |
| MDAT_bed_nodes.dat bed1_top_material.zone bed1_layer1_material.zone bed1_layer2_material.zone bed1_layer3_material.zone bed2_top_material.zone bed2_layer1_material.zone bed2_layer2_material.zone bed2_layer3_material.zone bed3_top_material.zone bed3_layer1_material.zone bed3_layer2_material.zone bed3_layer3_material.zone bed4_top_material.zone bed4_layer1_material.zone bed4_layer2_material.zone bed4_layer3_material.zone | |

Grid Quality

The final step of mesh generation is to convert the colored hex mesh to a tetrahedral mesh that satisfies the Delaunay criteria. This is required because FEHM does not support direct import of an octree refined hexahedral grid.

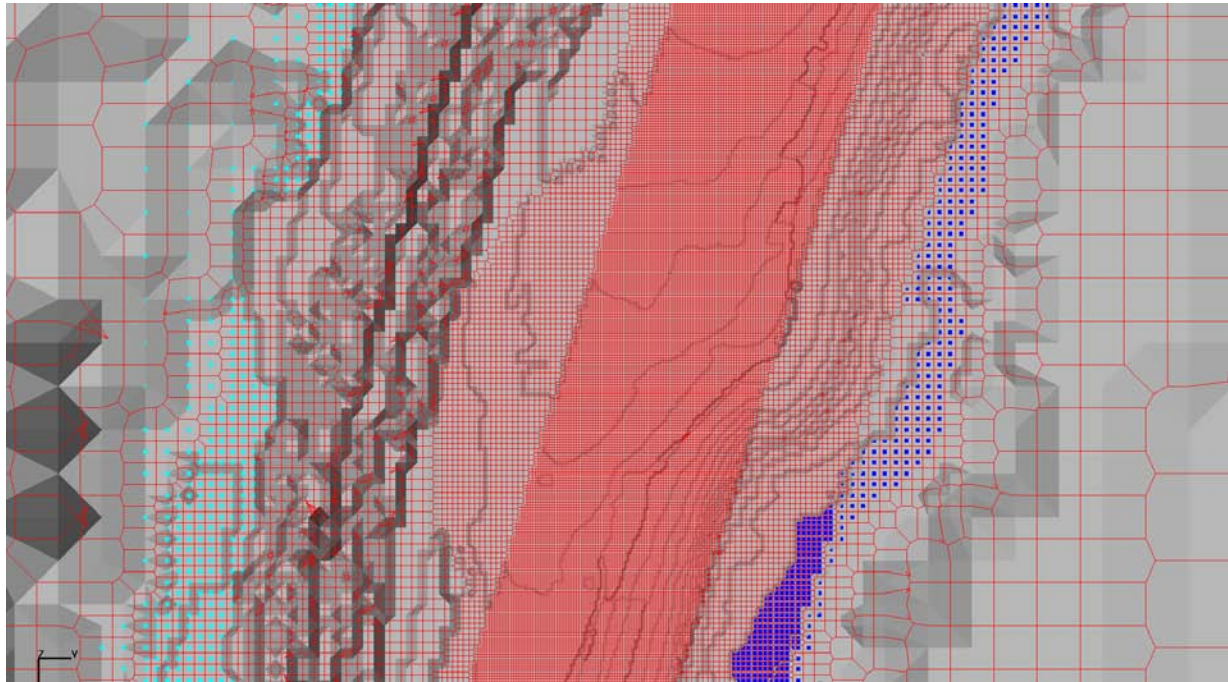


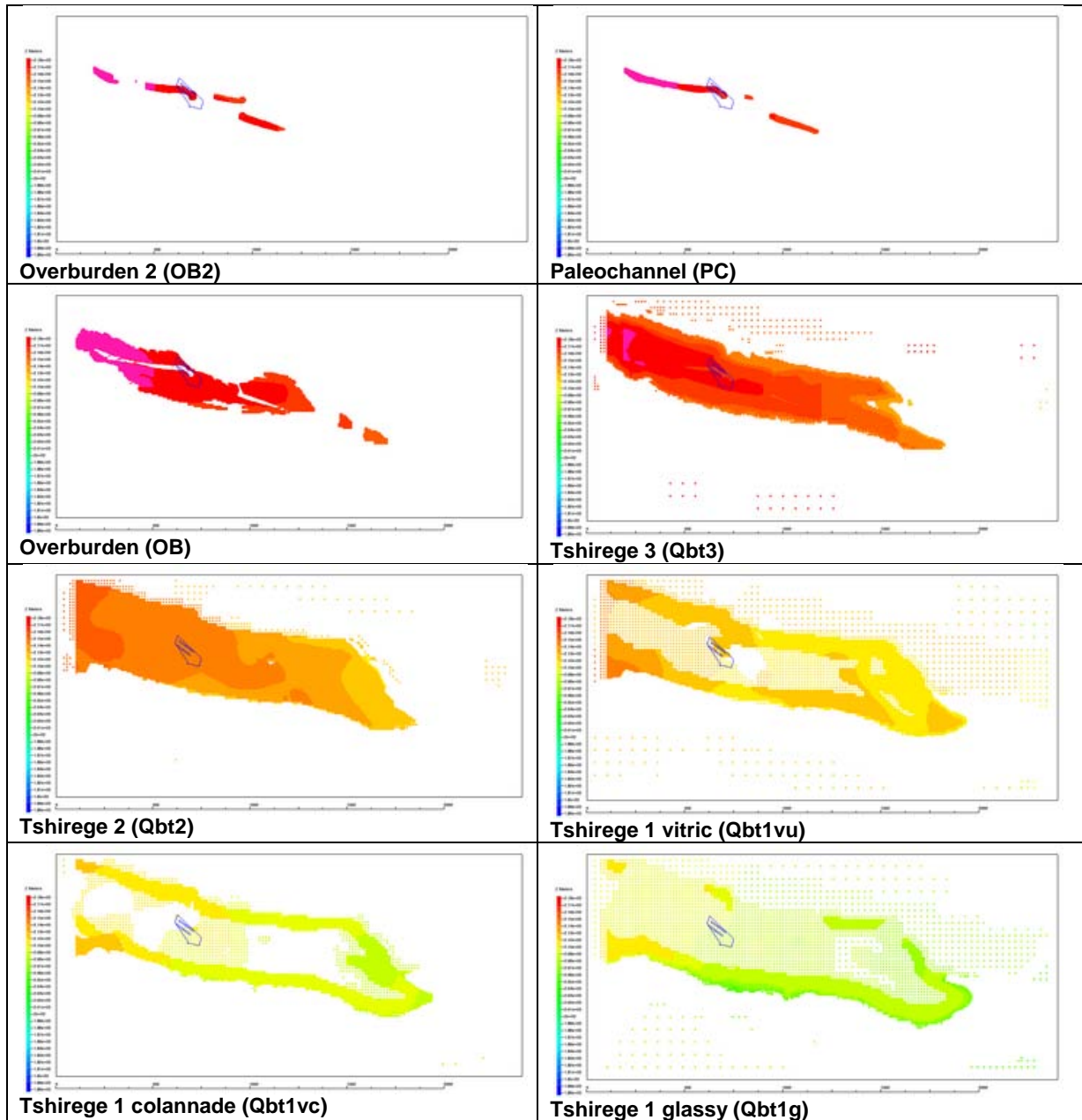
Figure 12. Top view of Mesa mesh showing the Voronoi volumes formed from the Delaunay connected mesh. Voronoi volumes are formed around each mesh node.

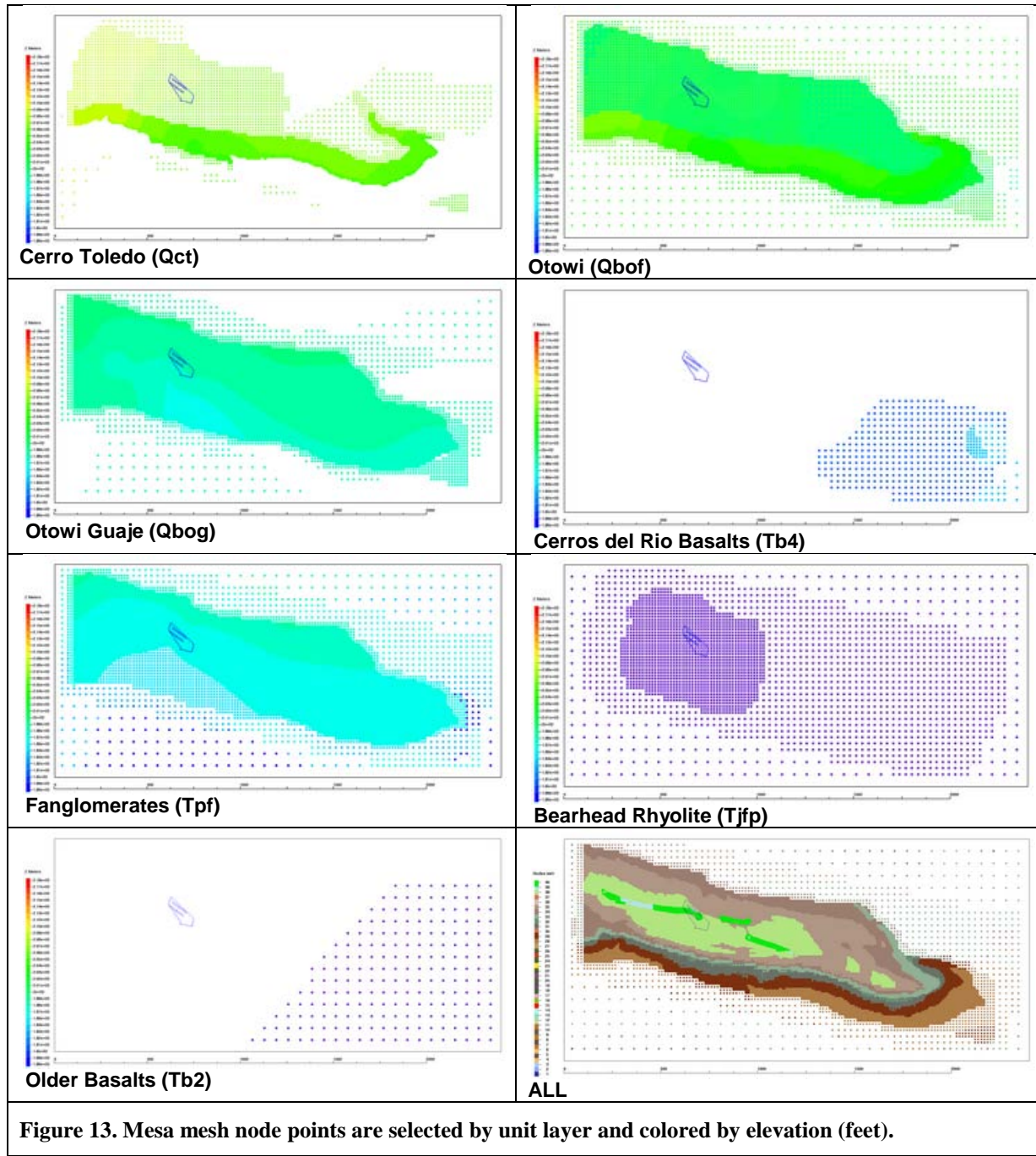
Quality checks are performed to ensure that the final grid is correct. These include isopach thickness checks of the hydrogeologic surfaces. All nodes are automatically and visually checked to ensure that they are assigned the correct material identification corresponding to the input WC09 GFM. Lists of the number of nodes associated with each material are compared to confirm that the hydrogeologic units are identified correctly. Feature locations are checked against WC09 GFM and area maps as shown in Figures in Attachment I. Slices are compared to the WC09 GFM slices.

As expected, the accuracy of represented hydrogeologic units are related to the grid spacing. The amount of error within the refined area is less than the grid block size of 1.5 meters. Thin but important units such as Qbog are given enough resolution to capture a thickness of at least one mesh node, and a continuous connectivity where it exists. Away from the refined area and beyond the influence on particle pathways, the grid blocks are large and represent the units only coarsely. The extents and resolution of each material unit are shown by the top views in the set of Figures below. The Beds mesh has more than the needed resolution to capture all including the deeper thin units such as Cerro Toledo.

The following set of figures (Figure 13) from the Mesa mesh are used to compare unit layer extents of the grid nodes when comparing to the WC09 GFM or map contours (see Attachment I

figures). They provide the modeler with information on how well the grid captures the layers and how layer extents may influence the modeling setup. Note where node spacing is wide, the material units may appear sparse. This is because mesh spacing for that region is larger than the thickness of the corresponding material layer in the GFM. These are compared against the Figures in Attachment I to check that the elevations and extents are reasonable within the grid resolution. Where the grid has spacing greater than 6 meters (20 feet), the thin layers are only coarsely captured and the layer becomes discontinuous. This was expected and the Beds mesh is used where this may affect modeling results. Most the coarse mesh is outside of the mesh and used mainly for setting boundary conditions.





Comparisons to the WC09 GFM and the mesh are also done with cut views and slices. From these comparisons we can see the shapes of the top of the Tb4 layer (red), the Otowi members Qbog and Qbof (tan) and TpF(green). As seen in Attachment I, two of the thickest layers in the GFM are Tb4 and Qbof and they exert control over the shapes of overlaying layers. Figure 14 shows cutouts that show the Mesa mesh is a good representation of the WC09 GFM.

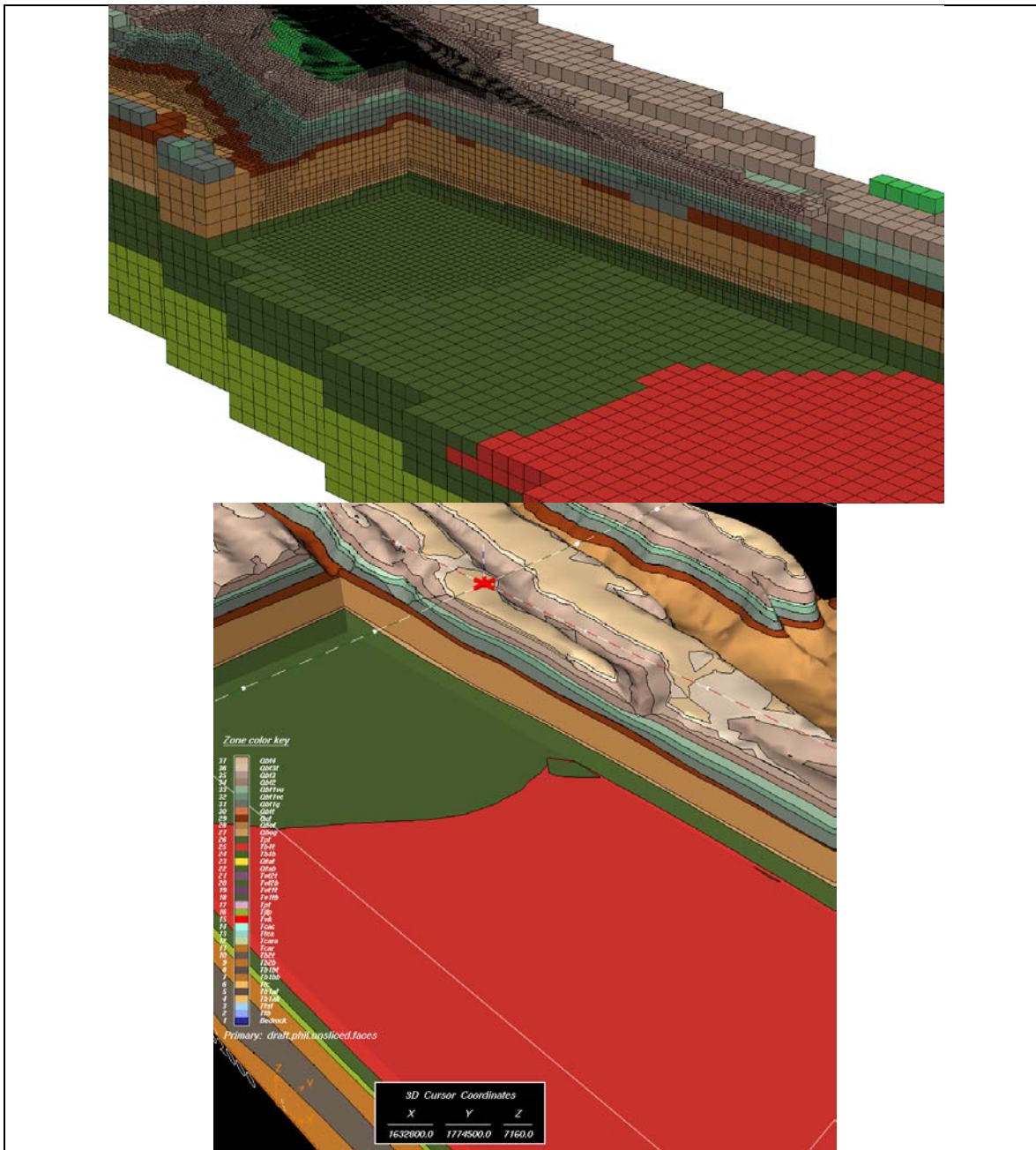


Figure 14. Cut away showing the Mesa mesh (top) and the WC09 GFM (bottom).

For intentions used in these studies, the Full Mesa computational mesh is adequate for coarse scoping work and the High Resolution Beds mesh is preferred for accurate modeling results. Increased vertical resolution of the High Resolution Beds mesh captures the very thin layers such as Cerro Toledo (QCT) to ensure it is continuous through the model area. Resolving details of the locations of groundwater pathways are improved by using the High Resolution Beds mesh, which captures the interfaces within the important layers. Figures 15 and 16 illustrate the difference in resolution between the Mesa and Beds meshes.

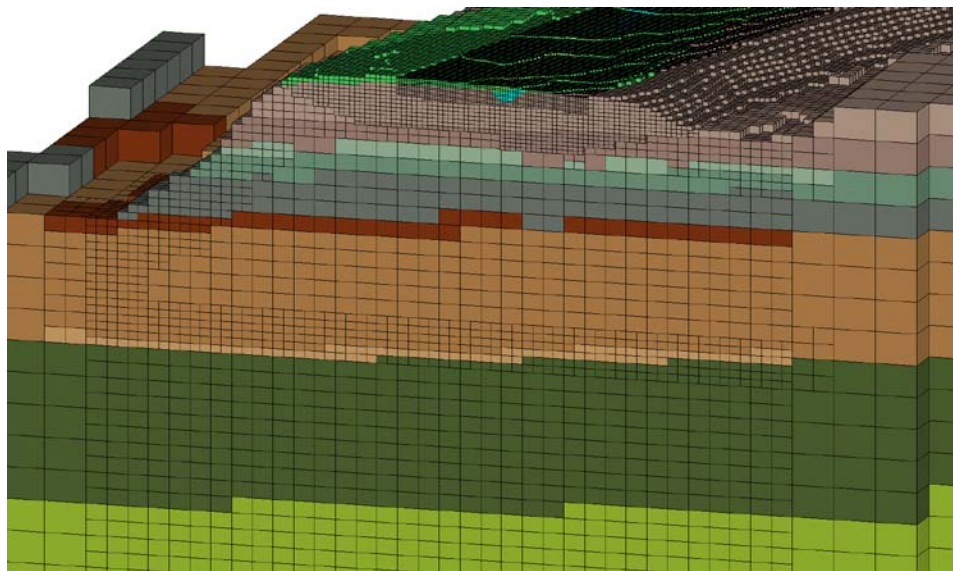


Figure 15. Slice of Mesa mesh shows good resolution in top soils, but lacking in the Qbt(olive) and Qct(rust) layers.



Figure 16. Slice of Beds mesh shows good resolution from ground to bottom.

References

George, Denise "Unstructured 3D Grid ToolBeds for Modeling and Simulation", LA-UR-97-3052, presented at the 1997 Workshop on Computational Electronics and Nanoelectronics, Urbana, Illinois, October 20-22, 1997

Miller, T., Vesselinov, V., Stauffer, P., Birdsall, K., and Gable, C., 2007, Integration of Geologic Frameworks in Meshing and Setup of Computational Hydrogeologic Models, Pajarito Plateau, New Mexico: New Mexico Geologic Society Guidebook, LA-UR-07-1721

Attachment III
Summary of Hydraulic Properties
for the
Los Alamos National Laboratory Technical Area 21,
Material Disposal Area T

Authors:

Daniel G. Levitt
Philip H. Stauffer

Summary

This attachment summarizes the sources of vadose zone hydraulic properties used for numerical modeling of flow and transport for studies related to Material Disposal Area (MDA) T at Technical Area (TA) 21 (TA-21) at the Los Alamos National Laboratory (LANL). Hydraulic properties were acquired from published sources and recent TA-21 Investigation Reports summarizing measured hydraulic properties from specific boreholes at TA-21. Measured and calibrated bulk permeabilities from TA-54, and fracture properties from various sources are also summarized. In addition, the recent findings by Bussod et al. (2011) regarding hydraulic properties of the Puye Formation are summarized. Finally, FEHM (Zyvoloski et al. 1997) macro files using “nominal” settings based on average hydraulic properties are built.

Table of Contents

| | |
|--|----|
| Summary | 2 |
| Table of Contents | 2 |
| Table of Figures | 3 |
| Table of Tables | 3 |
| Abbreviations | 3 |
| Technical Area 21 | 4 |
| Stratigraphy at MDA T | 7 |
| Hydraulic Properties | 8 |
| Springer et al. (2000) | 8 |
| Springer (2005) | 8 |
| MDA U Borehole 21-24772 (BH-4) | 9 |
| MDA A Borehole 21-26588 | 9 |
| MDA T Investigation Reports | 10 |
| MDA V Borehole 21-24524 | 10 |
| Bulk Permeability Data | 17 |
| Fracture Properties | 19 |
| Puye Formation: Upscaled Hydraulic Properties from Fine-scale Measurements | 19 |
| FEHM Input File Setup for MDA T | 20 |
| References | 24 |

Table of Figures

| | |
|---|----|
| Figure 1. Map of TA-21 showing MDAs A, B, T, U, and V (adapted from LANL, 2011, Figure 1)..... | 4 |
| Figure 2. Map of MDA A showing location of borehole 21-26588. | 5 |
| Figure 3. Map of MDA T showing locations of boreholes with measured hydraulic properties. .. | 5 |
| Figure 4. Map of MDA U showing location of borehole 21-24772. | 6 |
| Figure 5. Map of MDA V showing locations of boreholes 21-24524 and 21-02523..... | 6 |
| Figure 6. Generalized stratigraphy of bedrock units at MDA T (LANL, 2009, EP2006-0779, Figure 4.2-1). | 7 |
| Figure 7. Comparison of Qbt 3 Ksats from Springer et al. (2000) and Nyhan (1979). | 9 |
| Figure 8. Depth profiles of porosity, bulk density, and Ksat from all TA-21 boreholes..... | 14 |
| Figure 9. Depth profiles of van Genuchten values of alpha and n from all TA-21 boreholes..... | 15 |
| Figure 10. Depth profiles of measured and calibrated bulk permeability values from Area G and MDA L boreholes at TA-54..... | 18 |

Table of Tables

| | |
|--|----|
| Table 1. Comparison of Qbt 3 Ksats from Springer et al. (2000) and Nyhan (1979)..... | 9 |
| Table 2. Hydraulic properties measured on core from MDA T boreholes. | 11 |
| Table 3. Hydraulic properties (vG) measured on core from MDA T borehole 21-607955..... | 12 |
| Table 4. Hydraulic properties measured at MDA V boreholes 21-24524W, S. | 13 |
| Table 5. Compiled hydraulic property statistics from all TA-21 boreholes. | 16 |
| Table 6. Hydraulic properties for the vapor phase notch..... | 17 |
| Table 7. Compilation of fracture properties..... | 19 |
| Table 8. Upscaled hydraulic properties of five subunits of the Puye Formation..... | 20 |
| Table 9. FEHM RLP Macro..... | 21 |
| Table 10. FEHM Rock Macro | 22 |
| Table 11. FEHM Perm Macro | 23 |

Abbreviations

| | |
|----------|------------------------------------|
| bgs | below ground surface |
| ft | feet |
| IR | Investigation Report |
| Ksat | saturated hydraulic conductivity |
| LANL | Los Alamos National Laboratory |
| MDA | Material Disposal Area |
| SVE | soil vapor extraction |
| SSVE | supplemental soil vapor extraction |
| TA | Technical Area |
| ThetaRes | residual water content |
| ThetaSat | saturated water content |
| vG | van Genuchten |
| VPN | vapor phase notch |

Technical Area 21

Figure 1 shows a map of TA-21 located on DP Mesa with locations of MDAs A, B, T, U, and V, and locations of monitoring wells. DP Mesa is bounded by DP Canyon to the north and Los Alamos Canyon to the south.

Figures 2, 3, 4, and 5 are maps of MDA A, T, U, and V, respectively, showing the locations of boreholes (in red ovals) with measured hydraulic properties.

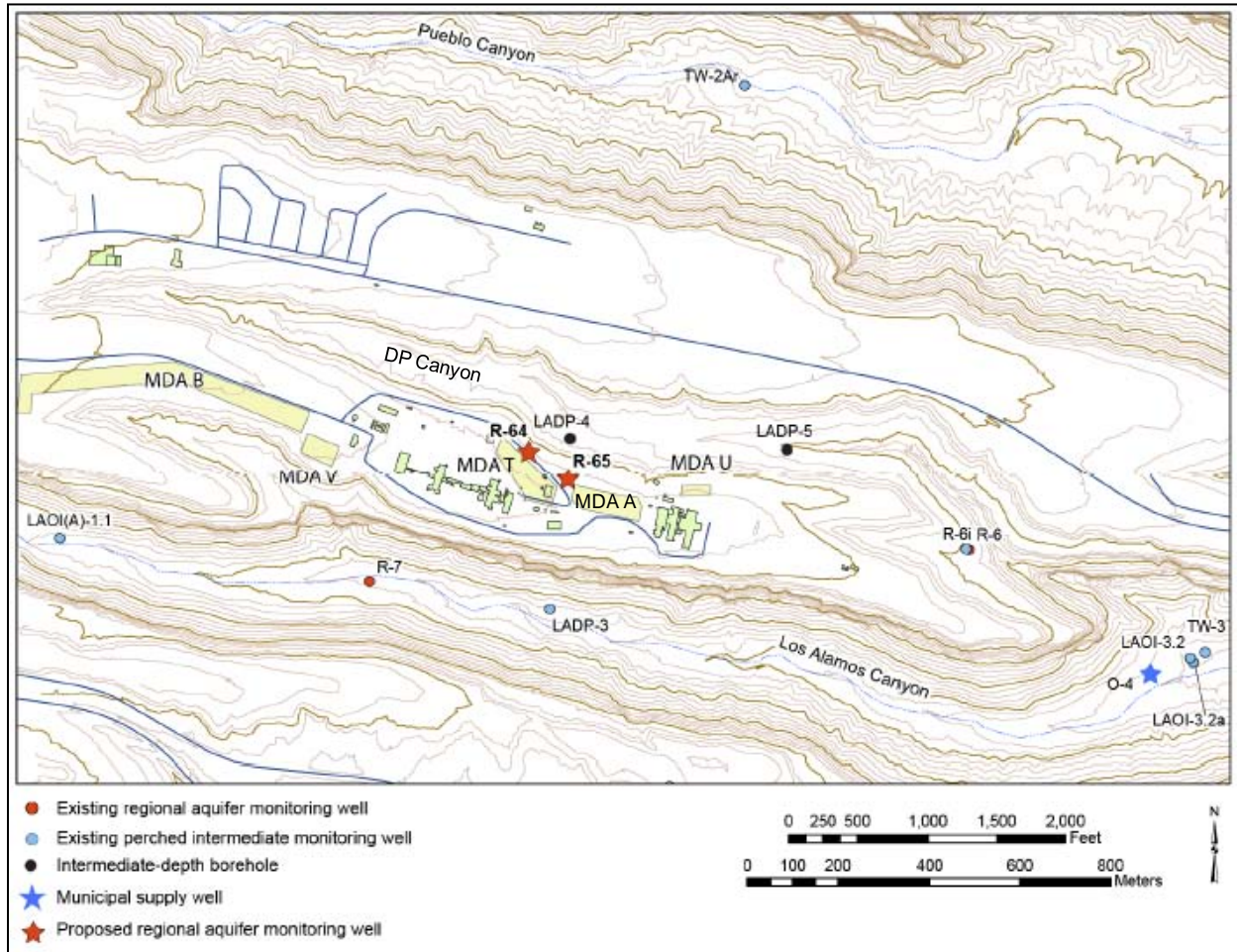


Figure 1. Map of TA-21 showing MDAs A, B, T, U, and V (adapted from LANL, 2011, Figure 1).

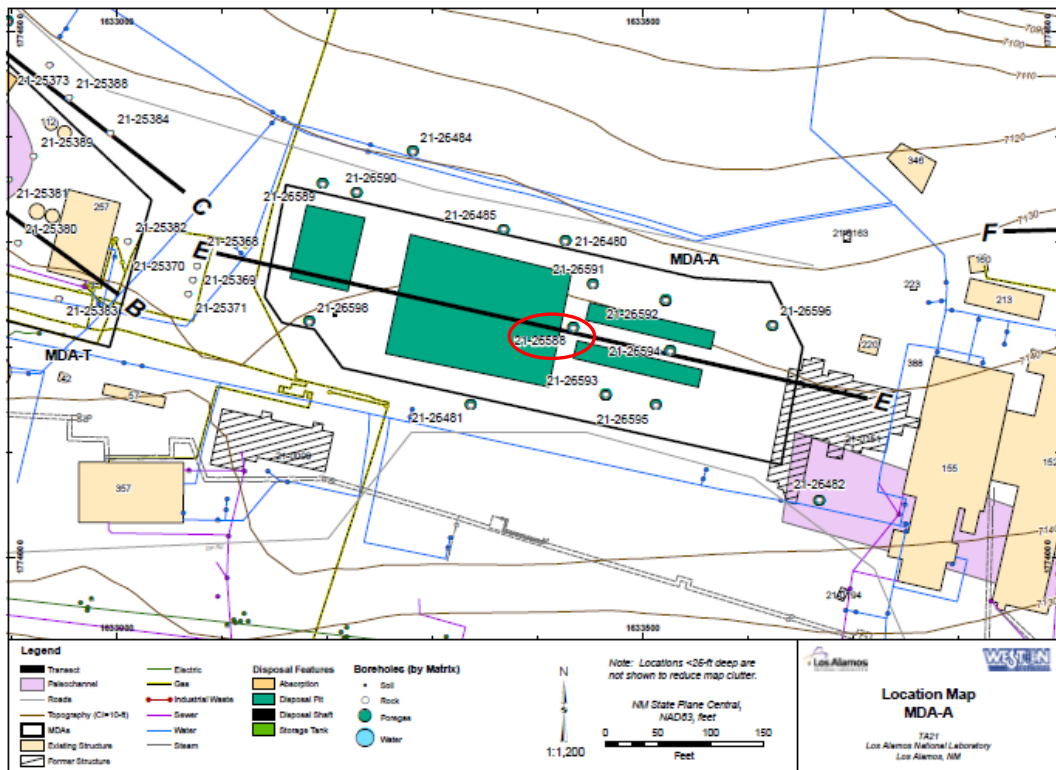


Figure 2. Map of MDA A showing location of borehole 21-26588.

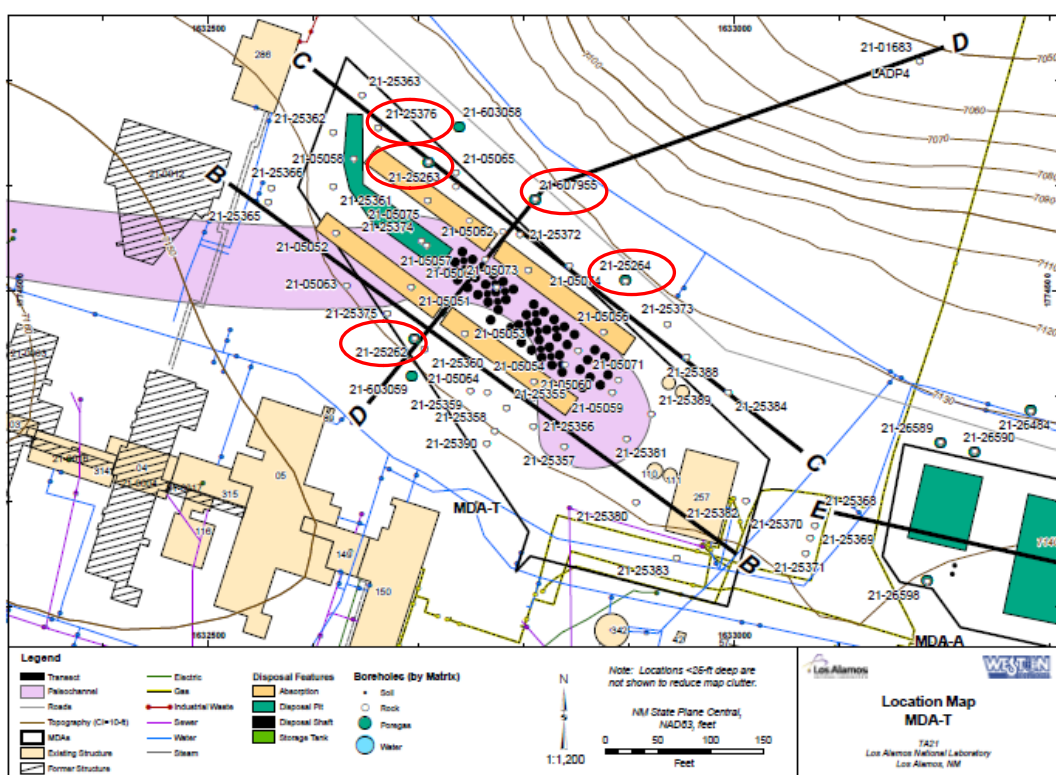


Figure 3. Map of MDA T showing locations of boreholes with measured hydraulic properties.

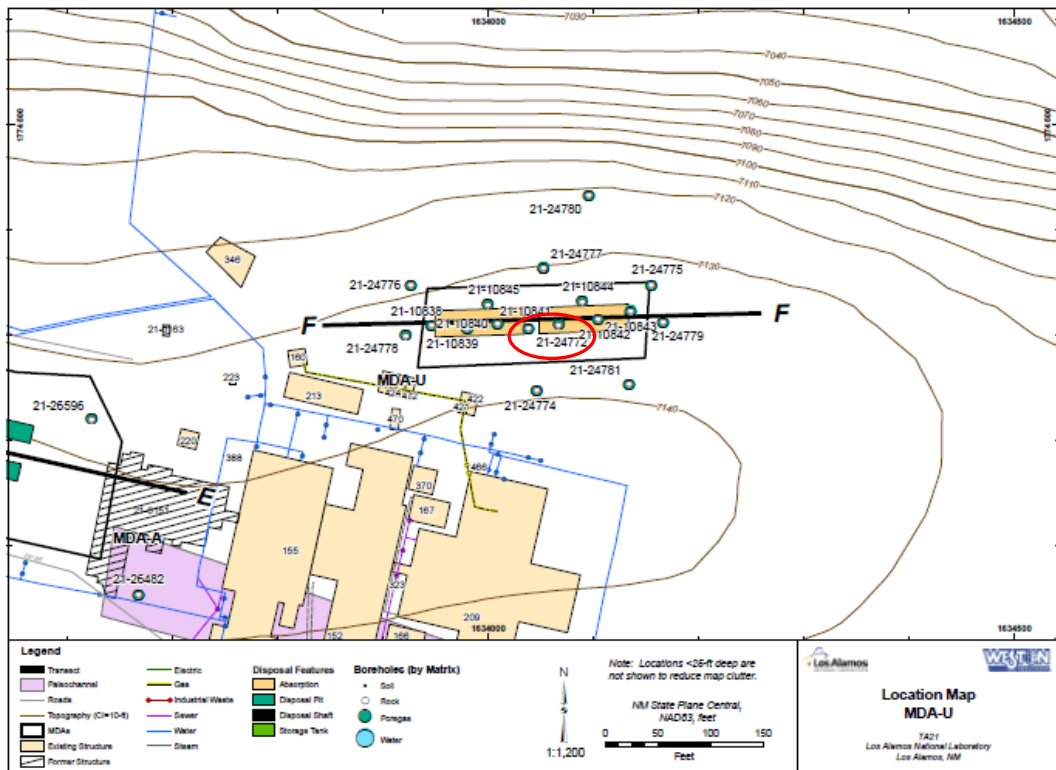


Figure 4. Map of MDA U showing location of borehole 21-24772.

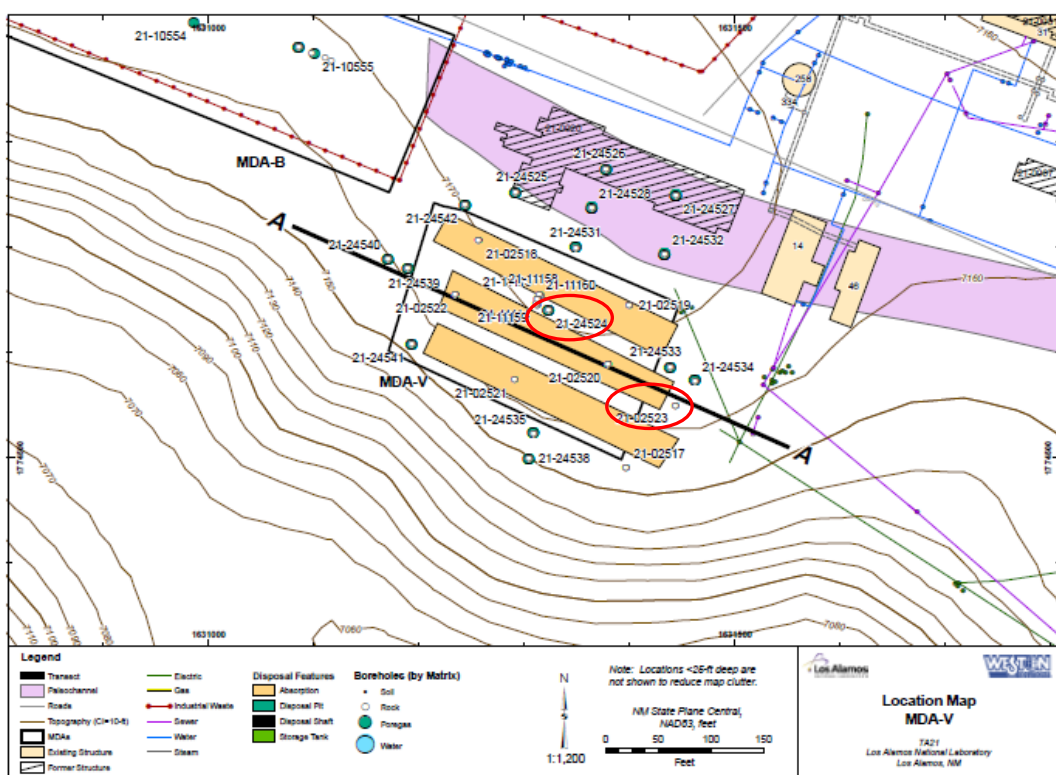


Figure 5. Map of MDA V showing locations of boreholes 21-24524 and 21-02523.

Stratigraphy at MDA T

The generalized stratigraphy of bedrock units at MDA T is shown in Figure 6. This stratigraphy was encountered during drilling of borehole 21-607955 at MDA T. The vapor phase notch (VPN) located between units Qbt 1v and Qbt 1g is also shown in Figure 6.

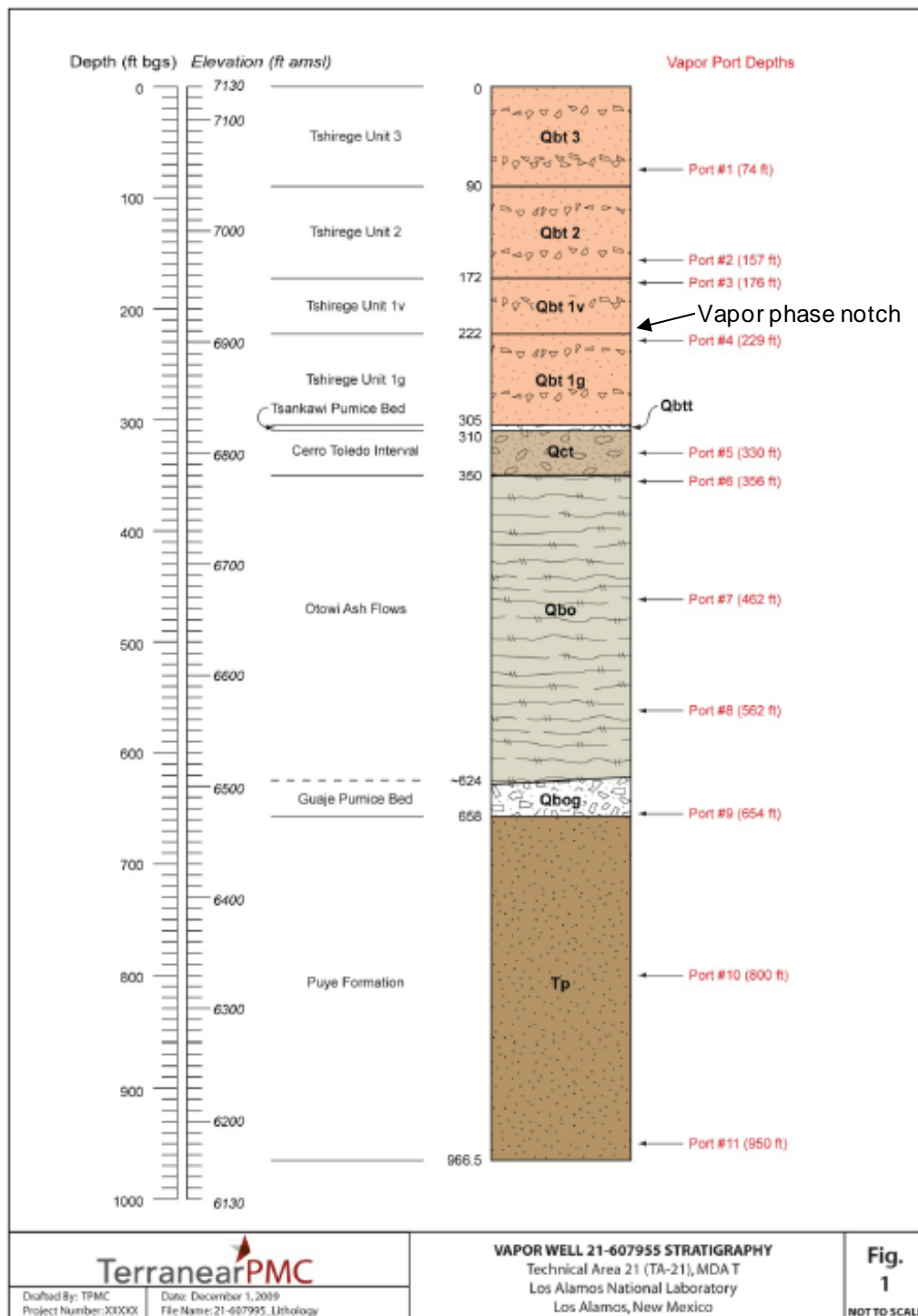


Figure 6. Generalized stratigraphy of bedrock units at MDA T (LANL, 2009, EP2006-0779, Figure 4.2-1).

Hydraulic Properties

Springer et al. (2000)

Springer et al. (2000) provide the earliest summary of TA-21 hydraulic properties. Their report includes tables of hydraulic properties of each of the Tshirege units, and the Otowi member of the Bandelier tuff shown in Figure 6. Springer et al. (2000) provide hydraulic properties from core samples collected from three boreholes near TA-21: LADP-3; LADP-4; and MDAVDH. Borehole LADP-3 is located in Los Alamos Canyon while LADP-4 is located on a sideslope of DP canyon (see Figure 1). Borehole MDAVDH is located on the east side of MDA V, and is renamed 21-02523 in Springer (2005, Table A1). The location of borehole 21-02523 is shown in Figure 5. Springer et al. (2000) also provide hydraulic properties for the VPN and the Guaje pumice bed.

Springer et al. (2000) provide hydraulic properties for cases when saturated water content (ThetaSat) is calculated (and equal to porosity), and measured (at a water potential of zero). Hydraulic properties using measured ThetaSat are summarized in this report.

Springer (2005)

Springer (2005) summarizes hydraulic properties for many technical areas at LANL. The properties listed for TA-21 are nearly identical to those in Springer et al. (2000). The one exception is the summary of saturated hydraulic conductivity (Ksat) listed in Table 6 of Springer (2005) which has 36 core samples for TA-21, compared to 12 samples used in Table 1 of Springer et al. (2000). Springer (2005) includes 24 samples listed as originating from borehole “MDAT” in Table A1. These 24 core samples are from Nyhan (1979, Table III) who does not report sample depth with Ksat.

Figure 7 shows Ksat values measured from samples from unit Qbt 3 from Springer et al. (2000) and Springer (2005). Clearly, the Ksat values from Springer et al. (2000) are significantly higher than those from Nyhan (1979). Minimum, maximum, mean, and geometric mean values are shown for the Springer et al. (2000) and Nyhan (1979) samples in Table 1. The mean and geometric mean values from the Springer et al. (2000) samples are factors of 10 and 6 larger than the Nyhan (1979) samples, respectively.

Hydraulic properties were collected on additional core samples after Springer’s 2005 summary and are described below.

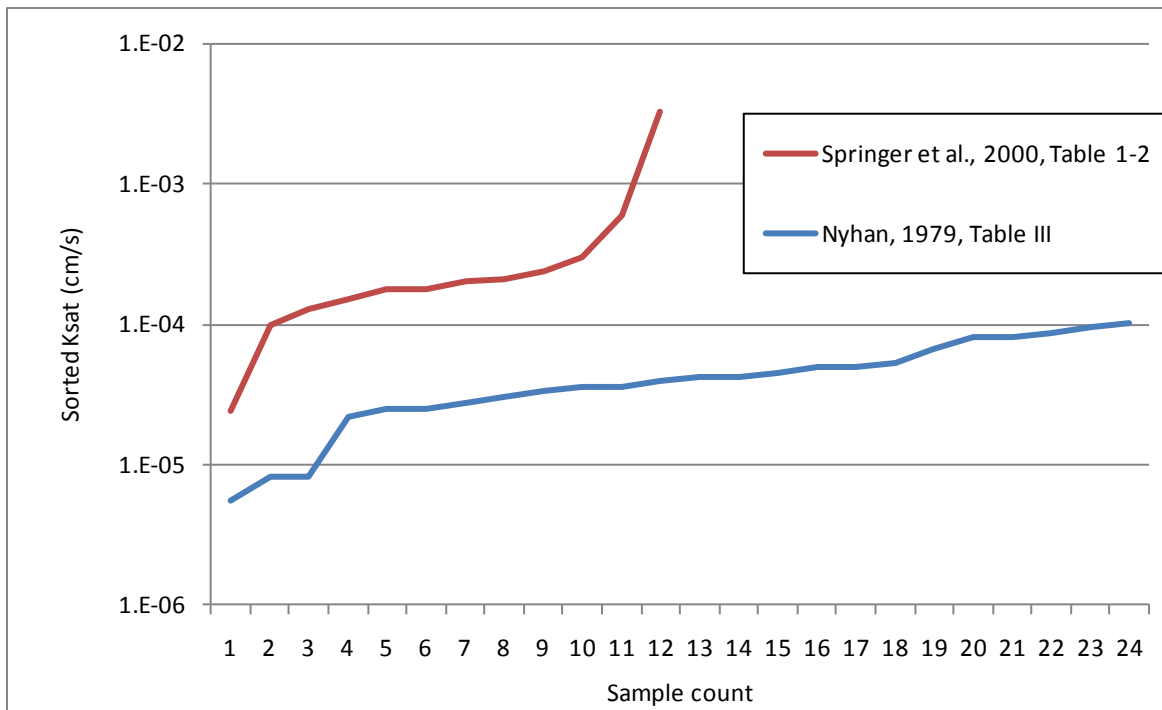


Figure 7. Comparison of Qbt 3 Ksats from Springer et al. (2000) and Nyhan (1979).

Table 1. Comparison of Qbt 3 Ksats from Springer et al. (2000) and Nyhan (1979).

| | Nyhan 1979, Table III | Springer et al., 2000, Table 1-2 |
|----------------|--------------------------|-------------------------------------|
| | Ksat (cm/s) | Ksat (cm/s) |
| Minimum | 5.556E-06 | 2.400E-05 |
| Maximum | 1.028E-04 | 3.300E-03 |
| Mean | 4.537E-05 | 4.668E-04 |
| Geometric Mean | 3.635E-05 | 2.131E-04 |

MDA U Borehole 21-24772 (BH-4)

Borehole 21-24772 (also known as BH-4) was drilled at MDA U in September 2005 to a depth of 360 ft below ground surface (bgs). Fourteen core samples were collected and analyzed for geotechnical properties: water content, bulk density, Ksat, and porosity. Hydraulic properties from samples collected in this borehole are summarized in Table 4.9-1 of the MDA U Investigation Report (IR) (LANL, 2006, ER2005-0923).

MDA A Borehole 21-26588

Borehole 21-26588 was drilled at MDA A in 2006 to a depth of 360 ft bgs. One sample was collected from between 337 and 339 ft bgs and analyzed for water content, bulk density, porosity and Ksat (LANL, 2006, EP2006-0835, p. 24-25). The one sample was collected from the Cerro Toledo interval.

MDA T Investigation Reports

Table 4.3-5 of the MDA T IR (LANL, 2006, EP2006-0779) reports hydraulic properties from five MDA T boreholes. One of the five boreholes (21-25375) only has properties from the soil (“fill”) layer. Hydraulic properties from four boreholes (excluding 21-25375) are shown in Table 2. These four boreholes are 21-25262, 21-25263, 21-25264, and 21-25376, which were drilled to total depths of 380, 354, 354, and 283 ft bgs, respectively, in 2006 (LANL, 2006, Table 4.3-1).

In 2009, borehole 21-607955 was drilled to a total depth of 966 ft bgs, and borehole 21-25262 was re-drilled and extended to a total depth of 695 ft bgs. Samples were collected from both these boreholes for analysis of hydraulic properties (LANL, 2009, EP2009-0676). Seven samples were collected from the extended borehole 21-25262 from depths of 420 to 680 ft bgs and analyzed for water content, porosity, bulk density, and Ksat (LANL, 2009, Table 4.1-2). Twenty-four samples were collected from borehole 21-607955 between depths of 75 and 953 ft bgs which were analyzed for water content, porosity, bulk density, and Ksat, as well as for van Genuchten (vG) properties alpha, n, ThetaSat, and ThetaRes. The properties from borehole 21-607955 are reported in LANL (2010, EP2010-0100).

Hydraulic properties from the 2006 MDA T IR (LANL, 2006, EP2006-0079), the 2009 Phase III IR, Revision 1 (LANL, 2009, EP2009-0676), and the 2010 Phase III IR, Revision 1 Replacement Pages (LANL, 2010, EP2010-0100) are shown in Tables 2 and 3.

MDA V Borehole 21-24524

Two vapor monitoring wells were drilled at MDA V in 2009. These wells retained the location identification number of 21-24524, but with an additional designation of west (21-24524W) and south (21-24524S) to indicate their locations relative to former location 21-24524. Borehole 21-24524W was drilled to 400 ft bgs and 21-24524S was drilled to 721 ft bgs (LANL 2009, EP2009-0649). Samples were collected from both boreholes for hydraulic property analysis including water content, bulk density, porosity, Ksat, and van Genuchten alpha and n (but not ThetaSat or ThetaRes). These properties are summarized from three tables in LANL (2009, EP2009-0649) and presented here in Table 4.

Table 2. Hydraulic properties measured on core from MDA T boreholes.

| | Depth | | Bulk Density | Ksat | | |
|-----------|-------------|--------|--------------|----------|----------|------------------------------------|
| Borehole | (ft bgs) | Unit | (g/cm3) | (cm/s) | Porosity | Source |
| 21-25262 | 26–27 | Qbt 3 | 1.48 | 3.40E-04 | 0.442 | 2006 PhI IR, Table 4.3-5 |
| 21-25262 | 124.6–125 | Qbt 2 | 1.77 | 3.50E-04 | 0.333 | 2006 PhI IR, Table 4.3-5 |
| 21-25262 | 172–172.8 | Qbt 1v | 1.10 | 6.50E-02 | 0.586 | 2006 PhI IR, Table 4.3-5 |
| 21-25262 | 238–238.9 | Qbt 1v | 1.18 | 3.90E-05 | 0.553 | 2006 PhI IR, Table 4.3-5 |
| 21-25262 | 335–336 | Qct | 1.03 | 1.80E-02 | 0.612 | 2006 PhI IR, Table 4.3-5 |
| 21-25262 | 352–353 | Qct | 1.42 | 7.50E-04 | 0.465 | 2006 PhI IR, Table 4.3-5 |
| 21-25262 | 420–425 | Qbo | 1.11 | 9.20E-05 | 0.581 | 2009 PhIII IR, Rev1, Table 4.1-2 |
| 21-25262 | 470–473 | Qbo | 1.13 | 1.90E-03 | 0.575 | 2009 PhIII IR, Rev1, Table 4.1-2 |
| 21-25262 | 520–525 | Qbo | 1.07 | 1.70E-03 | 0.595 | 2009 PhIII IR, Rev1, Table 4.1-2 |
| 21-25262 | 570–575 | Qbo | 1.12 | 2.90E-05 | 0.579 | 2009 PhIII IR, Rev1, Table 4.1-2 |
| 21-25262 | 620–625 | Qbo | 1.13 | 1.90E-04 | 0.572 | 2009 PhIII IR, Rev1, Table 4.1-2 |
| 21-25262 | 670–675 | Qbog | 0.91 | 7.60E-05 | 0.656 | 2009 PhIII IR, Rev1, Table 4.1-2 |
| 21-25262 | 675–680 | Qbog | 0.79 | 1.60E-04 | 0.704 | 2009 PhIII IR, Rev1, Table 4.1-2 |
| 21-25263 | 0.3–0.9 | Fill | 1.47 | 2.40E-04 | 0.445 | 2006 PhI IR, Table 4.3-5 |
| 21-25263 | 50–51 | Qbt 3 | 1.23 | 6.20E-03 | 0.537 | 2006 PhI IR, Table 4.3-5 |
| 21-25263 | 186–187 | Qbt 1v | 1.08 | 3.10E-03 | 0.591 | 2006 PhI IR, Table 4.3-5 |
| 21-25263 | 251.5–252.5 | Qbt 1g | 1.11 | 1.60E-03 | 0.581 | 2006 PhI IR, Table 4.3-5 |
| 21-25263 | 336–337 | Qct | 1.53 | 7.00E-05 | 0.423 | 2006 PhI IR, Table 4.3-5 |
| 21-25264 | 0–1 | Fill | 1.37 | 7.10E-04 | 0.482 | 2006 PhI IR, Table 4.3-5 |
| 21-25264 | 75.5–76.5 | Qbt 3 | 1.49 | 1.10E-03 | 0.438 | 2006 PhI IR, Table 4.3-5 |
| 21-25264 | 159–160 | Qbt 2 | 1.46 | 9.00E-04 | 0.448 | 2006 PhI IR, Table 4.3-5 |
| 21-25264 | 241–242 | Qbt 1g | 1.24 | 4.60E-04 | 0.532 | 2006 PhI IR, Table 4.3-5 |
| 21-25264 | 329–330 | Qct | 1.48 | 1.50E-03 | 0.441 | 2006 PhI IR, Table 4.3-5 |
| 21-25376 | 33.2–34 | Qbt 3 | 1.35 | 3.70E-02 | 0.489 | 2006 PhI IR, Table 4.3-5 |
| 21-25376 | 126.3–127 | Qbt 2 | 1.59 | 1.40E-02 | 0.400 | 2006 PhI IR, Table 4.3-5 |
| 21-607955 | 70–75 | Qbt 3 | 1.27 | 5.70E-03 | 0.520 | 2010 PhIII IR, Rev1, Table G-2.0-1 |
| 21-607955 | 89–94 | Qbt 3 | 1.23 | 1.80E-03 | 0.535 | 2010 PhIII IR, Rev1, Table G-2.0-1 |
| 21-607955 | 114–118 | Qbt 2 | 1.66 | 1.10E-04 | 0.374 | 2010 PhIII IR, Rev1, Table G-2.0-1 |
| 21-607955 | 126–131 | Qbt 2 | 1.66 | 1.10E-04 | 0.372 | 2010 PhIII IR, Rev1, Table G-2.0-1 |
| 21-607955 | 143–148 | Qbt 2 | 1.38 | 2.80E-03 | 0.478 | 2010 PhIII IR, Rev1, Table G-2.0-1 |
| 21-607955 | 155–160 | Qbt 2 | 1.45 | 1.10E-04 | 0.453 | 2010 PhIII IR, Rev1, Table G-2.0-1 |
| 21-607955 | 174–179 | Qbt 1v | 1.44 | 1.10E-03 | 0.455 | 2010 PhIII IR, Rev1, Table G-2.0-1 |
| 21-607955 | 180–185 | Qbt 1v | 1.30 | 1.80E-04 | 0.508 | 2010 PhIII IR, Rev1, Table G-2.0-1 |
| 21-607955 | 194–197 | Qbt 1v | 1.39 | 4.10E-03 | 0.474 | 2010 PhIII IR, Rev1, Table G-2.0-1 |
| 21-607955 | 227–230 | Qbt 1g | 1.21 | 8.20E-04 | 0.544 | 2010 PhIII IR, Rev1, Table G-2.0-1 |
| 21-607955 | 287–290.5 | Qbt 1g | 1.06 | 5.20E-04 | 0.600 | 2010 PhIII IR, Rev1, Table G-2.0-1 |
| 21-607955 | 327–329.8 | Qct | 1.53 | 4.30E-04 | 0.423 | 2010 PhIII IR, Rev1, Table G-2.0-1 |
| 21-607955 | 362–364.8 | Qbo | 1.16 | 3.80E-04 | 0.560 | 2010 PhIII IR, Rev1, Table G-2.0-1 |
| 21-607955 | 418.6–421.7 | Qbo | 1.24 | 1.30E-04 | 0.533 | 2010 PhIII IR, Rev1, Table G-2.0-1 |
| 21-607955 | 461–464.6 | Qbo | 1.36 | 6.00E-04 | 0.488 | 2010 PhIII IR, Rev1, Table G-2.0-1 |
| 21-607955 | 500–505 | Qbo | 1.23 | 1.30E-03 | 0.534 | 2010 PhIII IR, Rev1, Table G-2.0-1 |
| 21-607955 | 562–565 | Qbo | 1.30 | 6.80E-04 | 0.510 | 2010 PhIII IR, Rev1, Table G-2.0-1 |
| 21-607955 | 618.3–621.7 | Qbo | 1.26 | 5.30E-04 | 0.525 | 2010 PhIII IR, Rev1, Table G-2.0-1 |
| 21-607955 | 666–668.4 | Tp | 1.74 | 2.70E-04 | 0.345 | 2010 PhIII IR, Rev1, Table G-2.0-1 |
| 21-607955 | 722.7–726 | Tp | 1.43 | 3.70E-03 | 0.460 | 2010 PhIII IR, Rev1, Table G-2.0-1 |
| 21-607955 | 762–766.2 | Tp | 1.54 | 3.70E-03 | 0.418 | 2010 PhIII IR, Rev1, Table G-2.0-1 |
| 21-607955 | 799.6–801.9 | Tp | 1.67 | 5.50E-04 | 0.370 | 2010 PhIII IR, Rev1, Table G-2.0-1 |
| 21-607955 | 874–877 | Tp | 1.63 | 4.60E-03 | 0.384 | 2010 PhIII IR, Rev1, Table G-2.0-1 |
| 21-607955 | 950–953 | Tp | 1.65 | 1.10E-02 | 0.376 | 2010 PhIII IR, Rev1, Table G-2.0-1 |

Table 3. Hydraulic properties (vG) measured on core from MDA T borehole 21-607955.

| Depth (ft bgs) | | alpha (1/cm) | n | ThetaRes | ThetaSat | Source |
|-------------------|--------|-----------------|-------|----------|----------|------------------------------------|
| 70–75 | Qbt 3 | 0.0087 | 2.171 | 0.0019 | 0.458 | 2010 PhIII IR, Rev1, Table G-2.0-2 |
| 89–94 | Qbt 3 | 0.0104 | 1.858 | 0.0024 | 0.427 | 2010 PhIII IR, Rev1, Table G-2.0-2 |
| 114–118 | Qbt 2 | 0.0012 | 2.476 | 0.0000 | 0.339 | 2010 PhIII IR, Rev1, Table G-2.0-2 |
| 126–131 | Qbt 2 | 0.0012 | 2.531 | 0.0000 | 0.325 | 2010 PhIII IR, Rev1, Table G-2.0-2 |
| 143–148 | Qbt 2 | 0.0057 | 2.131 | 0.0053 | 0.395 | 2010 PhIII IR, Rev1, Table G-2.0-2 |
| 155–160 | Qbt 2 | 0.0033 | 1.621 | 0.0000 | 0.342 | 2010 PhIII IR, Rev1, Table G-2.0-2 |
| 174–179 | Qbt 1v | 0.0020 | 1.790 | 0.0000 | 0.290 | 2010 PhIII IR, Rev1, Table G-2.0-2 |
| 180–185 | Qbt 1v | 0.0024 | 1.715 | 0.0000 | 0.333 | 2010 PhIII IR, Rev1, Table G-2.0-2 |
| 194–197 | Qbt 1v | 0.0025 | 1.667 | 0.0000 | 0.339 | 2010 PhIII IR, Rev1, Table G-2.0-2 |
| 227–230 | Qbt 1g | 0.0021 | 1.682 | 0.0000 | 0.408 | 2010 PhIII IR, Rev1, Table G-2.0-2 |
| 287–290.5 | Qbt 1g | 0.0048 | 1.660 | 0.0000 | 0.475 | 2010 PhIII IR, Rev1, Table G-2.0-2 |
| 327–329.8 | Qct | 0.0041 | 1.512 | 0.0000 | 0.351 | 2010 PhIII IR, Rev1, Table G-2.0-2 |
| 362–364.8 | Qbo | 0.0042 | 1.566 | 0.0000 | 0.484 | 2010 PhIII IR, Rev1, Table G-2.0-2 |
| 418.6–421.7 | Qbo | 0.0038 | 1.649 | 0.0088 | 0.473 | 2010 PhIII IR, Rev1, Table G-2.0-2 |
| 461–464.6 | Qbo | 0.0037 | 1.556 | 0.0092 | 0.426 | 2010 PhIII IR, Rev1, Table G-2.0-2 |
| 500–505 | Qbo | 0.0084 | 1.472 | 0.0000 | 0.416 | 2010 PhIII IR, Rev1, Table G-2.0-2 |
| 562–565 | Qbo | 0.0056 | 1.650 | 0.0106 | 0.446 | 2010 PhIII IR, Rev1, Table G-2.0-2 |
| 618.3–621.7 | Qbo | 0.0110 | 1.422 | 0.0000 | 0.454 | 2010 PhIII IR, Rev1, Table G-2.0-2 |
| 666–668.4 | Tp | 0.0111 | 1.316 | 0.0000 | 0.357 | 2010 PhIII IR, Rev1, Table G-2.0-2 |
| 722.7–726 | Tp | 0.4991 | 1.190 | 0.0000 | 0.461 | 2010 PhIII IR, Rev1, Table G-2.0-2 |
| 762–766.2 | Tp | 0.0079 | 1.386 | 0.0297 | 0.403 | 2010 PhIII IR, Rev1, Table G-2.0-2 |
| 799.6–801.9 | Tp | 0.0125 | 1.304 | 0.0000 | 0.393 | 2010 PhIII IR, Rev1, Table G-2.0-2 |
| 874–877 | Tp | 0.0192 | 1.393 | 0.0000 | 0.316 | 2010 PhIII IR, Rev1, Table G-2.0-2 |
| 950–953 | Tp | 0.0560 | 1.337 | 0.0000 | 0.350 | 2010 PhIII IR, Rev1, Table G-2.0-2 |

Table 4. Hydraulic properties measured at MDA V boreholes 21-24524W, S.

| Source: LANL, 2009, EP2009-0649 | | | | | | |
|---------------------------------|--------|-------------|-------------|-------------|--------------|-------|
| Table 2.0-1 | | | Table 5.1-2 | Table 5.1-3 | | |
| Borehole | Media | Depth (ft) | Porosity | Ksat (cm/s) | alpha (1/cm) | n |
| 21-24524W | Qbt 3 | 20–21 | 0.460 | 2.60E-04 | 0.0078 | 1.664 |
| 21-24524W | Qbt 3 | 44–45 | 0.478 | 1.50E-03 | 0.0089 | 1.940 |
| 21-24524W | Qbt 3 | 60–61 | 0.533 | 1.40E-04 | 0.0061 | 1.603 |
| 21-24524W | Qbt 3 | 80–81 | 0.513 | 5.00E-04 | 0.0059 | 2.560 |
| 21-24524W | Qbt 2 | 100–101 | 0.509 | 9.20E-05 | 0.0075 | 1.845 |
| 21-24524W | Qbt 2 | 125–126 | 0.362 | 1.70E-04 | 0.0023 | 1.781 |
| 21-24524W | Qbt 2 | 140–141 | 0.366 | 8.40E-05 | 0.0033 | 2.862 |
| 21-24524W | Qbt 1v | 160–161 | 0.429 | 8.20E-04 | 0.0018 | 1.887 |
| 21-24524W | Qbt 1v | 175–176 | 0.547 | 6.60E-04 | 0.0205 | 1.492 |
| 21-24524W | Qbt 1v | 200–201 | 0.584 | 1.20E-03 | 0.0142 | 1.562 |
| 21-24524W | Qbt 1g | 259.5–260.5 | 0.610 | 7.80E-04 | 0.0048 | 1.882 |
| 21-24524W | Gbtt | 302–303 | 0.617 | 2.30E-03 | 0.0038 | 1.843 |
| 21-24524W | Gbtt | 303–304 | 0.567 | 2.00E-03 | 0.0049 | 2.013 |
| 21-24524W | Qct | 330–331 | 0.324 | 7.70E-05 | 0.0068 | 1.312 |
| 21-24524W | Qbo | 380–381 | 0.665 | 7.00E-04 | 0.0039 | 1.720 |
| 21-24524W | Qbo | 381–382 | 0.642 | 1.80E-03 | 0.0030 | 1.714 |
| 21-24524W | Qbo | 399–400 | 0.547 | 3.60E-04 | 0.0037 | 1.693 |
| 21-24524S | Qbo | 449–450 | 0.616 | 1.40E-04 | 0.0053 | 1.586 |
| 21-24524S | Qbo | 479–480 | 0.599 | 7.70E-04 | 0.0103 | 1.436 |
| 21-24524S | Qbo | 549–550 | 0.617 | 2.30E-05 | 0.0062 | 1.620 |
| 21-24524S | Qbo | 579–580 | 0.620 | 6.93E-03 | 0.0063 | 1.657 |
| 21-24524S | Qbo | 649–650 | 0.625 | 1.60E-04 | 0.0062 | 1.596 |
| 21-24524S | Qbog | 669–670 | 0.617 | 5.50E-05 | 0.0047 | 1.733 |
| 21-24524S | Qbog | 679–680 | 0.636 | 1.00E-03 | 0.0058 | 1.637 |
| 21-24524S | Tpf | 714–715 | 0.431 | 4.50E-03 | 0.1738 | 1.230 |
| 21-24524S | Tpf | 715–716 | 0.429 | 3.00E-03 | 0.0085 | 1.454 |

Depth profiles of hydraulic properties from all the TA-21 borehole datasets are shown plotted in Figures 8 and 9. The stratigraphy shown in Figures 8 and 9 is taken from borehole 21-607955 (shown in Figure 6), and may not be exactly correct for all boreholes shown in these two figures. The depths for boreholes LADP-3 and LADP-4 were adjusted to account for the ground surface elevation differences between these boreholes and the TA-21 mesa top. Depths were adjusted by adding 310 ft and 80 ft to all LADP-3 and LADP-4 depths, respectively. The Ksat data identified as “Nyhan” (Nyhan 1979) do not have depths associated with Ksat values but are plotted from depths of 1 to 93 ft within the Qbt 3 unit to help illustrate their relatively low values compared to other Qbt 3 Ksat values.

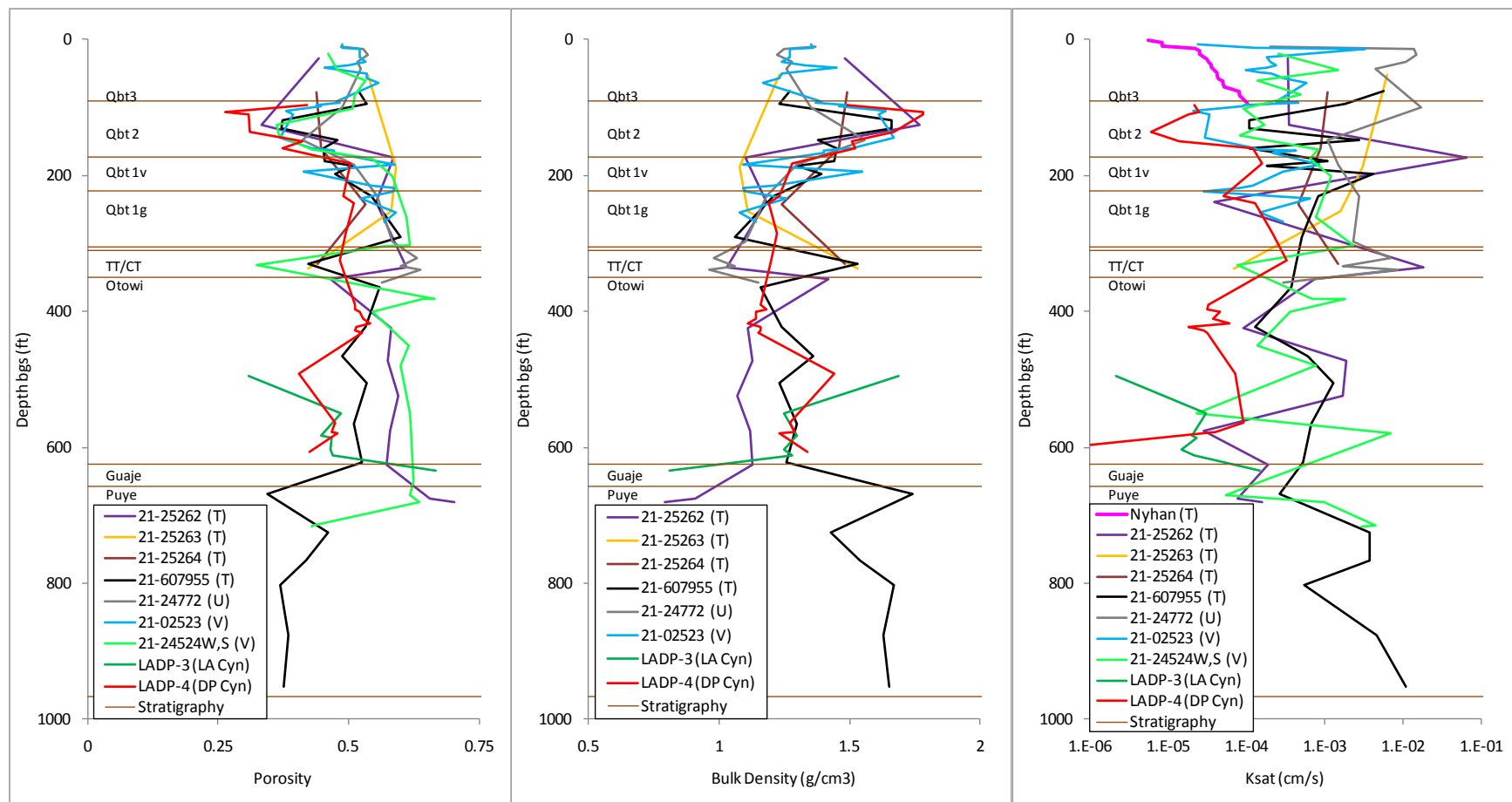


Figure 8. Depth profiles of porosity, bulk density, and Ksat from all TA-21 boreholes.

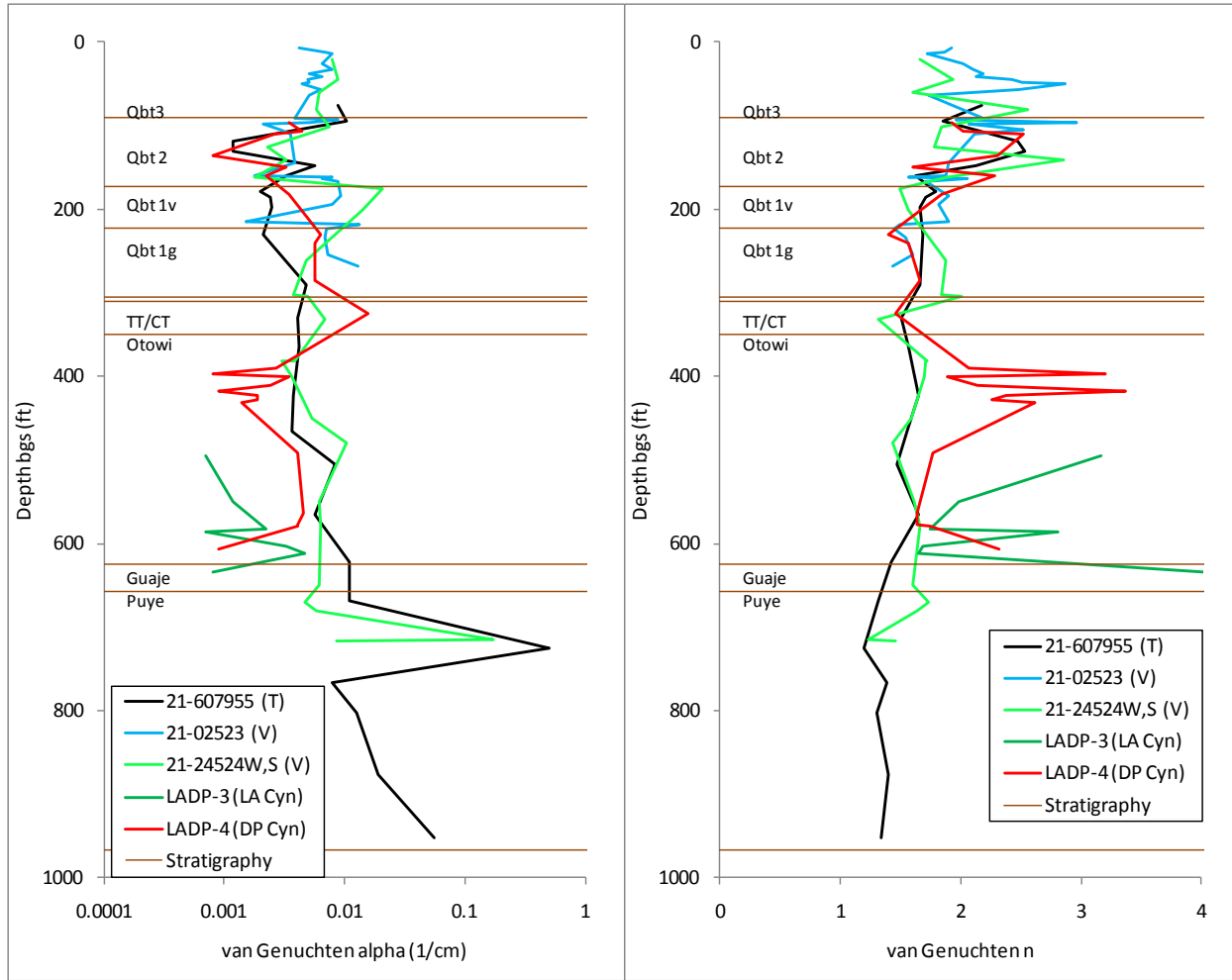


Figure 9. Depth profiles of van Genuchten values of alpha and n from all TA-21 boreholes.

Hydraulic properties from all TA-21 borehole datasets described above are compiled into one table (Table 5) with statistical values (sample count, minimum, maximum, mean, geometric mean, and standard deviation) calculated for each stratigraphic unit.

There is only one sample from the VPN, but hydraulic properties for this sample are summarized in Table 6. Table 6 also includes VPN properties from TA-54 (Vold 1997). The VPN properties from Vold (1997) were used in a recent modeling study for LANL Area G (Levitt, 2011), and modeled water content profiles reasonably matched measured profiles.

Table 5. Compiled hydraulic property statistics from all TA-21 boreholes.

| Unit | Metric | Bulk Density (g/cm3) | Ksat (cm/s) | Porosity | ThetaSat | ThetaRes | vG n | vG alpha (1/cm) |
|--------|-----------|-------------------------|----------------|----------|----------|----------|-------|--------------------|
| Qbt 3 | Count | 24 | 52 | 28 | 13 | 14 | 18 | 18 |
| Qbt 3 | Min | 1.170 | 5.56E-06 | 0.438 | 0.320 | 0.000 | 1.603 | 4.20E-03 |
| Qbt 3 | Max | 1.490 | 3.70E-02 | 0.558 | 0.458 | 0.023 | 2.864 | 1.04E-02 |
| Qbt 3 | Mean | 1.305 | 2.36E-03 | 0.506 | 0.378 | 0.010 | 2.098 | 6.60E-03 |
| Qbt 3 | Geo. Mean | | 1.97E-04 | | | | | 6.40E-03 |
| Qbt 3 | Std Dev | 0.084 | 6.29E-03 | 0.032 | 0.040 | 0.007 | 0.354 | 1.72E-03 |
| Qbt 2 | Count | 22 | 25 | 25 | 18 | 18 | 21 | 21 |
| Qbt 2 | Min | 1.370 | 6.00E-06 | 0.264 | 0.264 | 0.000 | 1.608 | 8.00E-04 |
| Qbt 2 | Max | 1.780 | 1.40E-02 | 0.509 | 0.406 | 0.024 | 2.967 | 8.90E-03 |
| Qbt 2 | Mean | 1.565 | 8.45E-04 | 0.401 | 0.332 | 0.007 | 2.167 | 3.50E-03 |
| Qbt 2 | Geo. Mean | | 1.18E-04 | | | | | 2.99E-03 |
| Qbt 2 | Std Dev | 0.127 | 2.80E-03 | 0.060 | 0.047 | 0.008 | 0.374 | 2.01E-03 |
| Qbt 1v | Count | 16 | 19 | 19 | 12 | 12 | 15 | 15 |
| Qbt 1v | Min | 1.080 | 6.00E-06 | 0.413 | 0.290 | 0.000 | 1.394 | 8.00E-04 |
| Qbt 1v | Max | 1.550 | 1.40E-02 | 0.591 | 0.628 | 0.015 | 2.058 | 7.90E-03 |
| Qbt 1v | Mean | 1.280 | 9.71E-04 | 0.514 | 0.432 | 0.002 | 1.721 | 4.08E-03 |
| Qbt 1v | Geo. Mean | | 4.98E-04 | | | | | 5.40E-03 |
| Qbt 1v | Std Dev | 0.148 | 2.84E-03 | 0.058 | 0.098 | 0.005 | 0.188 | 2.26E-03 |
| Qbt 1g | Count | 13 | 14 | 14 | 8 | 8 | 9 | 9 |
| Qbt 1g | Min | 0.980 | 1.30E-04 | 0.484 | 0.408 | 0.000 | 1.430 | 2.10E-03 |
| Qbt 1g | Max | 1.260 | 6.90E-03 | 0.631 | 0.620 | 0.000 | 1.882 | 1.56E-02 |
| Qbt 1g | Mean | 1.152 | 1.28E-03 | 0.558 | 0.501 | 0.000 | 1.610 | 7.30E-03 |
| Qbt 1g | Geo. Mean | | 6.60E-04 | | | | | 6.29E-03 |
| Qbt 1g | Std Dev | 0.082 | 1.81E-03 | 0.045 | 0.067 | 0.000 | 0.134 | 4.28E-03 |
| Qbtt | Count | 0 | 2 | 2 | 0 | 0 | 2 | 2 |
| Qbtt | Min | | 1.20E-04 | 0.567 | | | 1.843 | 1.50E-03 |
| Qbtt | Max | | 6.90E-03 | 0.617 | | | 2.013 | 9.20E-03 |
| Qbtt | Mean | | 1.30E-03 | 0.592 | | | 1.928 | 5.98E-03 |
| Qbtt | Geo. Mean | | 2.14E-03 | | | | | 4.32E-03 |
| Qbtt | Std Dev | | 1.81E-03 | 0.035 | | | 0.120 | 2.86E-03 |
| Qct | Count | 8 | 9 | 9 | 1 | 1 | 2 | 2 |
| Qct | Min | 0.960 | 3.90E-05 | 0.324 | 0.351 | 0.000 | 1.312 | 1.50E-03 |
| Qct | Max | 1.530 | 6.50E-02 | 0.639 | 0.351 | 0.000 | 1.512 | 1.35E-02 |
| Qct | Mean | 1.248 | 5.69E-03 | 0.507 | 0.351 | 0.000 | 1.412 | 7.27E-03 |
| Qct | Geo. Mean | | 6.91E-04 | | | | | 5.28E-03 |
| Qct | Std Dev | 0.263 | 1.72E-02 | 0.116 | | | 0.141 | 3.45E-03 |
| Qbo | Count | 31 | 39 | 39 | 25 | 25 | 33 | 33 |
| Qbo | Min | 1.070 | 3.90E-05 | 0.309 | 0.257 | 0.000 | 1.422 | 1.50E-03 |
| Qbo | Max | 1.690 | 6.50E-02 | 0.665 | 0.484 | 0.042 | 3.376 | 2.05E-02 |
| Qbo | Mean | 1.229 | 5.49E-03 | 0.529 | 0.402 | 0.004 | 1.952 | 6.93E-03 |
| Qbo | Geo. Mean | | 9.56E-05 | | | | | 3.03E-03 |
| Qbo | Std Dev | 0.122 | 1.72E-02 | 0.071 | 0.049 | 0.009 | 0.533 | 6.43E-03 |
| Qbog | Count | 3 | 5 | 5 | 1 | 1 | 3 | 3 |
| Qbog | Min | 0.790 | 2.10E-05 | 0.617 | 0.557 | 0.000 | 1.637 | 1.80E-03 |
| Qbog | Max | 0.910 | 4.10E-03 | 0.704 | 0.557 | 0.000 | 4.026 | 2.05E-02 |
| Qbog | Mean | 0.837 | 9.72E-04 | 0.656 | 0.557 | 0.000 | 2.465 | 6.03E-03 |
| Qbog | Geo. Mean | | 1.59E-04 | | | | | 2.79E-03 |
| Qbog | Std Dev | 0.064 | 1.23E-03 | 0.033 | | | 1.352 | 6.12E-03 |
| Tp | Count | 6 | 8 | 8 | 6 | 6 | 8 | 8 |
| Tp | Min | 1.430 | 1.80E-05 | 0.345 | 0.316 | 0.000 | 1.190 | 1.80E-03 |
| Tp | Max | 1.740 | 1.50E-03 | 0.460 | 0.461 | 0.030 | 1.454 | 2.05E-02 |
| Tp | Mean | 1.610 | 3.23E-04 | 0.402 | 0.380 | 0.005 | 1.326 | 5.95E-03 |
| Tp | Geo. Mean | | 2.47E-03 | | | | | 3.11E-02 |
| Tp | Std Dev | 0.109 | 4.78E-04 | 0.039 | 0.051 | 0.012 | 0.087 | 5.51E-03 |

Table 6. Hydraulic properties for the vapor phase notch.

| | | Bulk Den (g/cm3) | Ksat (cm/s) | Porosity | ThetaSat | ThetaRes | vG n | vG alpha (1/cm) | Source |
|---------------------------|----------|---------------------|----------------|----------|----------|----------|--------|--------------------|------------------------------------|
| Borehole | Location | | | | | | | | |
| 21-02523 | MDA V | 1.1 | 2.90E-05 | 0.586 | 0.464 | 0.0000 | 1.4519 | 0.007 | Springer et al. 2000, Table 1-2 |
| Average of 5 samples | TA-54 | | 6.89E-05 | | 0.503 | 0.0048 | 1.427 | 0.0044 | Vold (1997, Table II) |
| Std. dev. of 5 samples | TA-54 | | 8.86E-06 | | 0.041 | 0.0030 | 0.026 | 0.0025 | Vold (1997, Table II) |

Bulk Permeability Data

Permeability data described in this section refer to bulk permeability values, including the effects of fractures and matrix permeabilities, whereas the Ksat values described above are for matrix properties only and were measured on core samples. The bulk permeability values are based on air-phase flow data. Several datasets of bulk permeability for the Bandelier tuff at Area G and MDA L in TA-54 are presented here. Some permeability datasets are calculated from suction and air flow rates measured in the field. Other datasets are calibrated to match subsurface vapor-phase contaminant concentrations.

In the 1990s, bulk permeabilities of each unit of the Bandelier tuff were measured in seven boreholes at MDA L using a trailer-mounted packer system (SEA 1996, 1997, 1998). The mean, min, and max permeabilities for each unit and from all seven boreholes are shown in Figure 10 (red lines). The mean measured permeabilities were used as a starting point for calibrating a 2D radial model of a soil vapor extraction (SVE) experiment at Area G (LANL 2009, EP2009-0117). The final calibrated values for the Area G SVE test are also shown in Figure 10 (black line). The trends between the solid red (mean values) and black lines are the same, but there is a shift to higher permeabilities for the calibrated model.

LANL 2010 (EP2010-0235) describes the 2010 supplemental SVE (SSVE) pilot test activities conducted at Area G. Appendix H of LANL 2010 (EP2010-0235) presents permeability test results based on the 2D radial model described above. The calibrated permeabilities from the SSVE are shown in Figure 10 (blue line) and are generally lower than those from the first SVE test (LANL 2009, EP2009-0117).

Permeabilities were also calculated for two sites at MDA L where SVE tests were conducted. Stauffer et al. (2011) describe the methods used to calculate permeability in the x-y and z directions at these two sites. The calibrated permeabilities from the Stauffer et al. (2011) are also shown in Figure 10 (orange, pink, light green, and dark green lines). The orange and pink lines are not directly comparable to the other data series in this figure because they are for horizontal permeabilities, but the green lines are comparable, and they bound some of the other permeabilities within a given unit. The exception to this is for the Otowi member where the Stauffer et al. (2011) values are lower than any other Otowi member permeabilities.

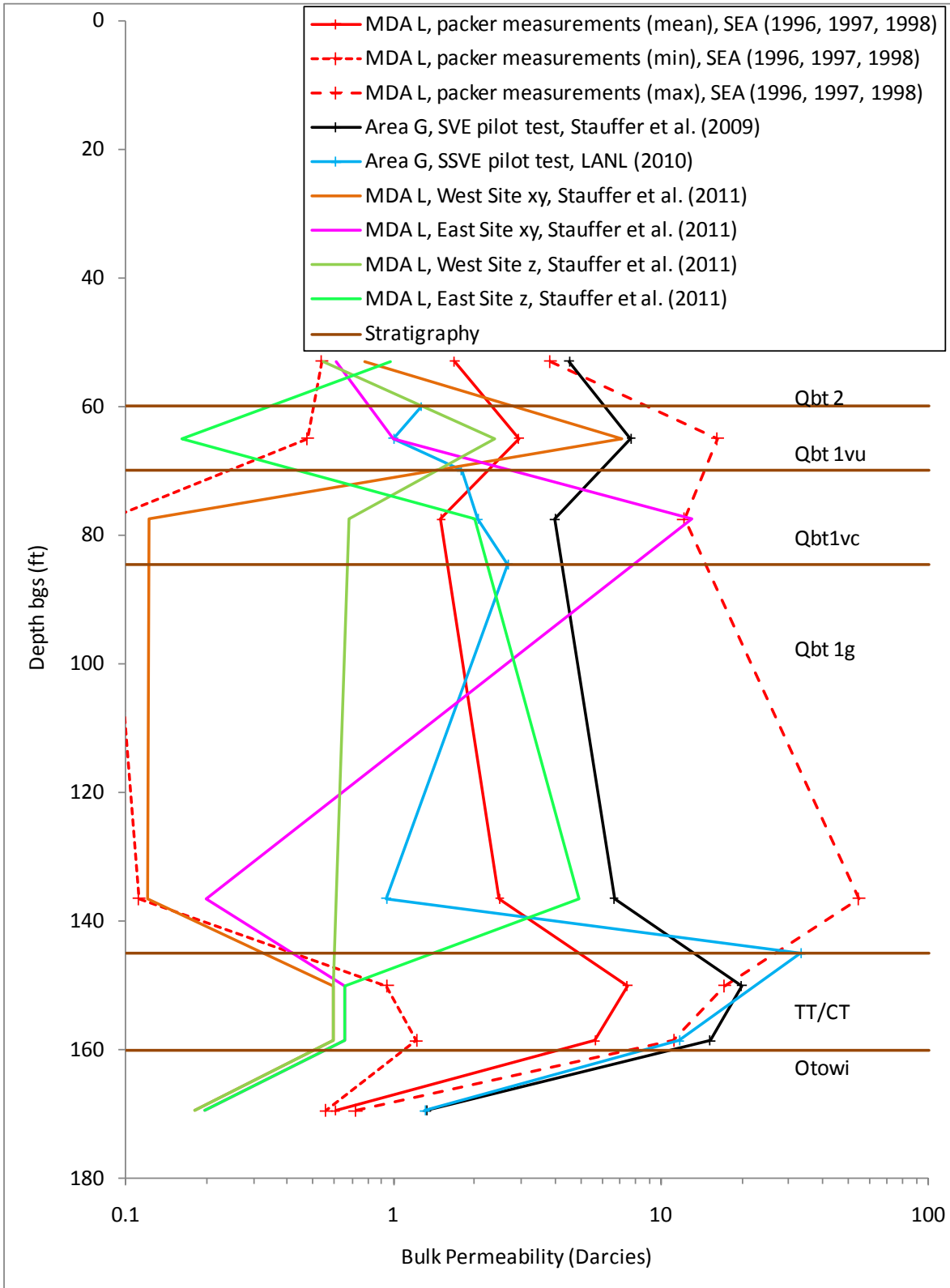


Figure 10. Depth profiles of measured and calibrated bulk permeability values from Area G and MDA L boreholes at TA-54.

Fracture Properties

The importance of fracture properties in a flow and transport model such as FEHM depends on the type of model employed. For example, Robinson et al. (2005) describe the use of a single continuum model, an equivalent continuum model, a dual permeability model, and a discrete fracture model used with the flow and transport code FEHM. All of these models require inputs of fracture properties, either as discrete fracture properties, or as a bulk property that combines matrix and fracture properties.

Some published fracture properties have been compiled in Table 7. This table includes fracture properties reported by Robinson et al. (2005) for the Pajarito Plateau at LANL, fracture properties of the Cerros del Rio basalts at LANL (Stauffer et al., 2005), fracture properties of the nonwelded Paintbrush tuff (PTn) at Yucca Mountain (DOE 2008), and the Ksat for a coarse silica sand (Schroth et al., 1996). Fracture properties are also included for specific units that were calculated during calibration of the SVE tests at Area G.

Table 7. Compilation of fracture properties.

| Media | Permeability (m ²) | Ksat (cm/s) | vG alpha (1/cm) | vG n | Porosity | ThetaRes | Source |
|-----------------------------------|-----------------------------------|--------------------|--------------------|-------|---------------|-------------|----------------------------------|
| Pajarito Plateau | 1.00E-12 | 9.78E-04 | 0.050 | 1.500 | 1.00E-03 | 3.00E-05 | Robinson et al. (2005, Table 1) |
| Cerros del Rio Basalts | 1E-11 to 1E-12 | 9.8E-03 to 9.8E-04 | | | 0.001 to 0.01 | | Stauffer, Stone (2005, Table 5) |
| Yucca Mtn PTn unit | 3.00E-13 | 2.93E-04 | 0.140 | 2.725 | 1.00E-02 | | DOE (2008, Table 2.3.2-4, ptn22) |
| Silica sand 12/20 grade | 5.15E-10 | 5.03E-01 | | | | | Schroth et al. (1996, Table 4) |
| | | | | | Max. Sat. | Resid. Sat. | |
| Tshirege Member of Bandelier tuff | 1.0E-10 to 3.3E-09 | 3.23 to 9.78E-02 | 0.14 | 2 | 0.999 | 0.001 | Based on Area G SVE tests |

Puye Formation: Upscaled Hydraulic Properties from Fine-scale Measurements

A recent report has been published on a methodology for upscaling fine-scale measurements of hydraulic properties (Bussod et al. 2011). Bussod et al. (2011) has developed high-resolution geophysical laboratory methods to characterize the hydrogeologic properties that control the transport and dispersion of contaminants in the subsurface. Using millimeter-scale hydrogeophysical measurements on porous rock and unconsolidated sediment cores, Bussod et al. has devised (and tested) a new upscaling method that captures the effects of fine-scale heterogeneities in measured properties and has produced model parameters that permit the predictive modeling of heterogeneous, anisotropic hydrologic properties at the site- and regional scales. Bussod et al. (2011) applied these methods to several sites including Mortandad Canyon at LANL, and for all geologic units from the ground surface to the lower Puye Formation for the Mortandad Canyon site. Hydraulic properties for the Puye Formation are of particular interest to the modeling needs at TA-21 due to the highly heterogeneous nature of the Puye Formation,

whose facies represent the deposits of the ancestral Rio Grande River that experienced periods of damming and diversions caused by eruptions of lavas (Broxton and Vaniman, 2005).

Bussod et al. (2011) calculated upscaled parameters from five cluster subunits of the Puye Formation. These parameters, from Bussod et al. (2011, Tables 3.1 and 4.1) are shown in Table 8. This parameterization of subunits can be employed with FEHM as part of an uncertainty analysis, or the average of the units can be used as a single parameter set.

Table 8. Upscaled hydraulic properties of five subunits of the Puye Formation.

| Subunit | Kh (cm/s) | Kv (cm/s) | Porosity | ThetaRes | vG n | vG alpha |
|-----------|-----------|-----------|----------|----------|-------|----------|
| Subunit 1 | 6.40E-04 | 1.29E-04 | 0.207 | 0.11 | 2.747 | 0.797 |
| Subunit 2 | 2.69E-03 | 4.16E-05 | 0.207 | 0.116 | 2.016 | 1.534 |
| Subunit 3 | 9.58E-04 | 2.07E-05 | 0.207 | 0.077 | 2 | 0.83 |
| Subunit 4 | 3.59E-04 | 4.13E-05 | 0.207 | 0.044 | 2.217 | 0.528 |
| Subunit 5 | 7.35E-04 | 2.31E-05 | 0.207 | 0.136 | 2.421 | 0.837 |
| Average | 1.08E-03 | 5.12E-05 | | 0.097 | 2.280 | 0.905 |
| Geomean | 8.46E-04 | 4.03E-05 | | | | 0.852 |

FEHM Input File Setup for MDA T

Hydraulic properties are included in three macros within FEHM: the rlp, rock, and perm macros. The rlp macro includes data for the relative permeability and capillary pressure model. The rock macro includes rock density and porosity data. The perm macro includes permeabilities (in m^2) in the x, y, and z directions.

FEHM requires inputs of permeability in m^2 rather than as K_{sat} , and residual and maximum saturation rather than as residual and saturated water content. Residual saturation is equal to ThetaRes/porosity and max saturation is equal to ThetaSat/porosity. The cutoff saturation is generally equal to ThetaRes + 0.001.

The following rlp, rock, and perm macros are nominal settings based on the average hydraulic properties compiled in this report. The values in black are the prior values used in the preliminary simulations of MDA T. The values in red are the new averages (or geometric mean values for K_{sat} [converted into permeabilities] and vG alpha) described in this report. The matrix permeability and porosity values for the Puye Formation are from Table 8 above.

The perm macro represents bulk permeabilities, and this macro is not used if model 4 is selected in the rlp macro (which includes both fracture and rock permeability values). The perm macro shown below includes values in red that are the mean values measured at MDA L and shown as the solid red line in Figure 10. These values are about an order of magnitude higher than the prior permeabilities used for the preliminary MDA T simulations.

Table 9. FEHM RLP Macro

| Model 3,4: | RP1 | RP2 | RP3 | FP4 | RP5 | RP6 | | | | | cmt Flag | Unit | Comment | | | |
|------------|----------|----------|----------|--------|-----------|----------|-----------|-----------|------------|----------|-------------|---------------------------------------|---------|--|--|--|
| | | | vG alpha | | | Cutoff | | | | | | | | | | |
| | Res_sat | Max_sat | (1/m) | vG n | Fit param | sat | | | | | | | | | | |
| Model 4: | RP7 | RP8 | RP9 | RP10 | RP11 | RP12 | RP13 | RP14 | RP15 | | | | | | | |
| | | | vG alpha | | | Low sat | Cutoff | Fracture | Matrix | Fracture | cmt | | | | | |
| | Res_sat | Max_sat | (1/m) | vG n | Fit param | sat | perm (m2) | perm (m2) | vol. frac. | Flag | Unit | Comment | | | | |
| 3 | 0.001 | 1 | 3.84 | 1.474 | 2 | 0.011 | | | | # | Tb2 | (10) Same as Cerros del Rio Basalt | | | | |
| 3 | 0.01 | 1 | 5 | 2.68 | 2 | 0.011 | | | | # | Tcar | (11) | | | | |
| 3 | 0.01 | 1 | 5 | 2.68 | 2 | 0.011 | | | | # | Tjfp | (16) Pumiceous Puye and Tpp | | | | |
| 3 | 1.23E-02 | 0.946613 | 0.851813 | 2.2802 | 2 | 0.013325 | | 4.12E-14 | | # | Tpf | (20) Puye Formation, fanglomerates | | | | |
| 3 | 0.001 | 1 | 3.84 | 1.474 | 2 | 0.011 | | | | # | Tb4 | (25) Cerros del Rio Basalt | | | | |
| 3 | 0.000 | 0.849 | 0.279 | 2.465 | 2 | 0.001 | | 1.62E-13 | | # | Qbog | (27) Otowi Member, Guaje Pumice | | | | |
| 4 | 0.008 | 0.761 | 0.303 | 1.952 | 2 | 0.009 | | | | | | | | | | |
| | 0.001 | 0.999 | 14 | 2 | 2 | 0.01 | 6.10E-11 | 9.77E-14 | 0.01 | # | Qbof | (28) Otowi Member, ash flow | | | | |
| 4 | 0.000 | 0.691 | 0.528 | 1.412 | 2 | 0.001 | | | | | | | | | | |
| | 0.001 | 0.999 | 14 | 2 | 2 | 0.01 | 5.70E-10 | 7.07E-13 | 0.01 | # | Qct | (29) Cerro Toledo | | | | |
| 4 | 0.000 | 0.000 | 0.432 | 1.928 | 2 | 0.001 | | | | | | | | | | |
| | 0.001 | 0.999 | 14 | 2 | 2 | 0.01 | 7.50E-10 | 2.19E-12 | 0.01 | # | Qbtt | (30) Tshirege Unit 1, tsankawi pumice | | | | |
| 4 | 0.000 | 0.898 | 0.629 | 1.610 | 2 | 0.001 | | | | | | | | | | |
| | 0.001 | 0.999 | 14 | 2 | 2 | 0.01 | 2.50E-10 | 6.75E-13 | 0.01 | # | Qbt1g | (31) Tshirege Unit 1-glassy | | | | |
| 4 | 0.004 | 0.841 | 0.540 | 1.721 | 2 | 0.005 | | | | | | | | | | |
| | 0.001 | 0.999 | 14 | 2 | 2 | 0.01 | 1.50E-10 | 5.09E-13 | 0.01 | # | Qbt1vc | (32) Tshirege Unit 1-colanne | | | | |
| 4 | 0.004 | 0.841 | 0.540 | 1.721 | 2 | 0.005 | | | | | | | | | | |
| | 0.001 | 0.999 | 14 | 2 | 2 | 0.01 | 2.90E-10 | 5.09E-13 | 0.01 | # | Qbt1vu | (33) Tshirege Unit 1-vitric | | | | |
| 4 | 0.017 | 0.830 | 0.299 | 2.167 | 2 | 0.018 | | | | | | | | | | |
| | 0.001 | 0.999 | 14 | 2 | 2 | 0.01 | 1.70E-10 | 1.21E-13 | 0.01 | # | Qbt2 | (34) Tshirege Unit 2 | | | | |
| 4 | 0.020 | 0.747 | 0.640 | 2.098 | 2 | 0.021 | | | | | | | | | | |
| | 0.001 | 0.999 | 14 | 2 | 2 | 0.01 | 3.00E-10 | 2.01E-13 | 0.01 | # | Qbt3 | (35) Tshirege Unit 3 | | | | |
| 3 | 0.020 | 0.747 | 0.640 | 2.098 | 2 | 0.021 | | 2.01E-13 | | # | Qbt3t | (36) Tshirege Unit 3, transition zone | | | | |
| 3 | 0.026 | 0.974 | 0.621 | 2.143 | 2 | 0.027 | | | | # | Qbt4 | (37) Tshirege Unit 4 | | | | |
| 4 | 0.020 | 0.747 | 0.640 | 2.098 | 2 | 0.021 | | | | | | | | | | |
| | 0.001 | 0.999 | 14 | 2 | 2 | 0.01 | 3.00E-10 | 2.01E-13 | 0.01 | # | OB | (38) Tshirege Unit 3 | | | | |
| 4 | 0.020 | 0.747 | 0.640 | 2.098 | 2 | 0.021 | | | | | | | | | | |
| | 0.001 | 0.999 | 14 | 2 | 2 | 0.01 | 3.00E-10 | 2.01E-13 | 0.01 | # | OB2 | (39) Tshirege Unit 3 | | | | |
| 3 | 0.196 | 0.847 | 6.756 | 1.472 | 2 | 0.1966 | | | | # | PC | (40) Paleochannel | | | | |
| 1 | 1.00E-05 | 0 | 1.0 | 1.0 | 0.001 | 1.00 | | | | # | AIR | (101) Same as NTS Crater Air | | | | |

Table 10. FEHM Rock Macro

| JA | JB | JC | DENRD | DPRD | | | | | |
|------|----|----|------------------------|-------------------------|-------------------|-----------------|-------------|-------|---------------------------------------|
| | | | Rock dens. (Kg/m^3) | Rock sp. ht (J/kg/K) | Prior Porosity | New Porosity | cmt Flag | Unit | Comment |
| 1 | 0 | 0 | 2580 | 488 | 0.001 | 0.001 | # | Tb2 | (10) Same as Cerros del Rio Basalt |
| -10 | 0 | 0 | 2580 | 488 | 0.001 | 0.001 | # | Tb2 | (10) Same as Cerros del Rio Basalt |
| -11 | 0 | 0 | 1200 | 1000 | 0.35 | 0.35 | # | Tcar | (11) |
| -16 | 0 | 0 | 1200 | 1000 | 0.35 | 0.35 | # | Tjfp | (16) Pumiceous Puye and Tpp |
| -20 | 0 | 0 | 1610 | 1000 | 0.392 | 0.207 | # | Tpf | (20) Puye Formation, fanglomerates |
| -25 | 0 | 0 | 2580 | 488 | 0.001 | 0.001 | # | Tb4 | (25) Cerros del Rio Basalt |
| -27 | 0 | 0 | 990 | 1000 | 0.627 | 0.656 | # | Qbog | (27) Otowi Member, Guaje Pumice |
| -28 | 0 | 0 | 1252 | 1000 | 0.422 | 0.529 | # | Qbof | (28) Otowi Member, ash flow |
| -29 | 0 | 0 | 1365 | 1000 | 0.437 | 0.507 | # | Qct | (29) Cerro Toledo |
| -30 | 0 | 0 | 1120 | 1000 | 0.473 | 0.592 | # | Qbtt | (30) Tshirege Unit 1, tsankawi pumice |
| -31 | 0 | 0 | 1169 | 1000 | 0.533 | 0.558 | # | Qbt1g | (31) Tshirege Unit 1 - glassy |
| -32 | 0 | 0 | 1319 | 1000 | 0.472 | 0.514 | # | Qbt1v | (32) Tshirege Unit 1 - colannde |
| -33 | 0 | 0 | 1319 | 1000 | 0.472 | 0.514 | # | Qbt1v | (33) Tshirege Unit 1 - vitric |
| -34 | 0 | 0 | 1555 | 1000 | 0.35 | 0.401 | # | Qbt2 | (34) Tshirege Unit 2 |
| -35 | 0 | 0 | 1293 | 1000 | 0.384 | 0.506 | # | Qbt3 | (35) Tshirege Unit 3 |
| -36 | 0 | 0 | 1293 | 1000 | 0.384 | 0.506 | # | Qbt3t | (36) Tshirege Unit 3, transition zone |
| -37 | 0 | 0 | 1293 | 1000 | 0.384 | 0.384 | # | Qbt4 | (37) Tshirege Unit 4 |
| -38 | 0 | 0 | 1293 | 1000 | 0.384 | 0.506 | # | OB | (38) Tshirege Unit 3 |
| -39 | 0 | 0 | 1293 | 1000 | 0.384 | 0.506 | # | OB2 | (39) Tshirege Unit 3 |
| -40 | 0 | 0 | 1276 | 1000 | 0.518 | 0.518 | # | PC | (40) Paleochannel |
| -101 | 0 | 0 | 1200 | 1000 | 0.999 | 0.999 | # | AIR | (101) Same as NTS Crater Air |

Table 11. FEHM Perm Macro

| JA | JB | JC | PNXD, PNYD, PNZD | X,Y,Z-dir | | cmt | |
|------|----|----|------------------|------------------------|------|-------|---------------------------------------|
| | | | | Perm (m ²) | Flag | | |
| 1 | 0 | 0 | | 1.00E-12 | # | Tb2 | (10) Same as Cerros del Rio Basalt |
| -10 | 0 | 0 | | 1.00E-12 | # | Tb2 | (10) Same as Cerros del Rio Basalt |
| -11 | 0 | 0 | | 1.14E-12 | # | Tcar | (11) |
| -16 | 0 | 0 | | 3.88E-12 | # | Tjfp | (16) Pumiceous Puye and Tpp |
| -20 | 0 | 0 | | 4.12E-14 | # | Tpf | (20) Puye Formation, fanglomerates |
| -25 | 0 | 0 | | 1.00E-12 | # | Tb4 | (25) Cerros del Rio Basalt |
| -27 | 0 | 0 | | 1.62E-13 | # | Qbog | (27) Otowi Member, Guaje Pumice |
| -28 | 0 | 0 | | 9.77E-14 | # | Qbof | (28) Otowi Member, ash flow |
| -29 | 0 | 0 | | 7.07E-13 | # | Qct | (29) Cerro Toledo |
| -30 | 0 | 0 | | 2.19E-12 | # | Qbtt | (30) Tshirege Unit 1, tsankawi pumice |
| -31 | 0 | 0 | | 6.75E-13 | # | Qbt1g | (31) Tshirege Unit 1 - glassy |
| -32 | 0 | 0 | | 5.09E-13 | # | Qbt1v | (32) Tshirege Unit 1 - colannde |
| -33 | 0 | 0 | | 5.09E-13 | # | Qbt1v | (33) Tshirege Unit 1 - vitric |
| -34 | 0 | 0 | | 1.21E-13 | # | Qbt2 | (34) Tshirege Unit 2 |
| -35 | 0 | 0 | | 2.01E-13 | # | Qbt3 | (35) Tshirege Unit 3 |
| -36 | 0 | 0 | | 2.01E-13 | # | Qbt3t | (36) Tshirege Unit 3, transition zone |
| -37 | 0 | 0 | | 8.27E-14 | # | Qbt4 | (37) Tshirege Unit 4 |
| -38 | 0 | 0 | | 2.01E-13 | # | OB | (38) Tshirege Unit 3 |
| -39 | 0 | 0 | | 2.01E-13 | # | OB2 | (39) Tshirege Unit 3 |
| -40 | 0 | 0 | | 1.16E-11 | # | PC | (40) Paleochannel |
| -101 | 0 | 0 | | 1.25E-09 | # | AIR | (101) Same as NTS Crater Air |

References

Broxton, D.E., and D.T. Vaniman, 2005. Geologic Framework of a Groundwater System on the Margin of a Rift Basin, Pajarito Plateau, North-Central New Mexico. *Vadose Zone Journal* 4:522-550.

Bussod et al., G.Y., 2011. "A New High-Resolution Method for the Characterization of Heterogeneous Subsurface Environments: Providing Flow and Transport Parameters via the Integration of Multiscale HydroGeophysical Data." New England Research, Inc. DOE-SBIR Grant DE-FG02-07ER84898.

DOE (U.S. Department of Energy), Office of Civilian Radioactive Waste Management, June 2008. Yucca Mountain Repository License Application, Safety Analysis Report. DOE/RW-0573, Rev. 0.

LANL (Los Alamos National Laboratory), February 2006. "Investigation Report for Material Disposal Area U, Consolidated Unit 21-017(a)-99, at Technical Area 21," Los Alamos National Laboratory document LA-UR-05-9564, Los Alamos, New Mexico. ER2005-0923.

LANL (Los Alamos National Laboratory), September 2006. "Investigation Report for Material Disposal Area T, Consolidated Unit 21-016(a)-99, at Technical Area 21," Los Alamos National Laboratory document LA-UR-06-6506, Los Alamos, New Mexico. EP2006-0779.

LANL (Los Alamos National Laboratory), November 2006. "Investigation Report for Material Disposal Area A, Solid Waste Management Unit 21-014, at Technical Area 21," Los Alamos National Laboratory document LA-UR-06-7902, Los Alamos, New Mexico. EP2006-0835.

LANL (Los Alamos National Laboratory), March 2009. "Numerical Analysis of the Soil-Vapor Extraction Test at Material Disposal Area G, Technical Area 54," Los Alamos National Laboratory document LA-UR-09-0995, Los Alamos, New Mexico. (EP2009-0117).

LANL (Los Alamos National Laboratory), December 2009. "Periodic Monitoring Report for Vapor-Sampling Activities at Material Disposal Area V, Consolidated Unit 21-018(a)-99, at Technical Area 21, June to October 2009," Los Alamos National Laboratory document LA-UR-09-8123, Los Alamos, New Mexico. EP2009-0649.

LANL (Los Alamos National Laboratory), December 2009. "Phase III Investigation Report for Material Disposal Area T at Technical Area 21, Revision 1," Los Alamos National Laboratory document LA-UR-09-8109, Los Alamos, New Mexico. EP2009-0676.

LANL (Los Alamos National Laboratory), March 8, 2010. "Submittal of the Replacement Pages for the Approval with Modifications Phase III Investigation Report for Material Disposal Area T, at Technical Area 21, Revision 1," Los Alamos National Laboratory letter (EP2010-0100) to J.P. Bearzi (NMED-HWB) from M.J. Graham (LANL) and D.R. Gregory (DOE-LASO), Los Alamos, New Mexico. EP2010-0100.

LANL (Los Alamos National Laboratory), May, 2010. "Report for Supplemental Soil-Vapor Extraction Pilot Test at Material Disposal Area G, Technical Area 54," Los Alamos National Laboratory document LA-UR-10-3409, Los Alamos, New Mexico. EP2010-0235.

LANL (Los Alamos National Laboratory), Jan 2011. "Drilling Work Plan for Regional Aquifer Wells MW-14 (R-64) and MW-10 (R-65)," Los Alamos National Laboratory document LA-UR-11-0186, Los Alamos, New Mexico.

Levitt, D.G., 2011. "Modeling the Movement of Transient Moisture through Disposal Units at Los Alamos National Laboratory Technical Area 54, Area G," Los Alamos National Laboratory document LA-UR-11-05424, Los Alamos, New Mexico.

Nyhan, J.W. 1979. Radioactive waste burial in tuff at Los Alamos. p. 53–55. In Nuclear waste management technology development activities. Rep. LA-7921-PR. Los Alamos Natl. Lab., Los Alamos, NM.

Robinson, B.A., S.G. McLin, and H.S. Viswanathan, 2005. Hydrologic Behavior of Unsaturated, Fractured Tuff: Interpretation and Modeling of a Wellbore Injection Test. *Vadose Zone Journal* 4:694-707.

Schroth, M.H., S.J. Ahearn, J.S. Selker, and J.D. Istok, 1996. Characterization of Miller-Similar Silica Sands for Laboratory Hydrologic Studies. *Soil Sci. Soc. Am. J.* 60:1331-1339.

Science and Engineering Associates, Inc. (SEA), January 1996. "Data Report: Open Borehole Anemometry and In-Situ Gas Permeability Measurements in Boreholes 54-1001 through 54-1006, Los Alamos Technical Area 54," SEA Report SEA-SF-TR-94-020 (Revised).

Science and Engineering Associates, Inc. (SEA), November 1997. "Passive Air Flow Tests at Well 54-1001 during 1995 and at Well 54-1017 during 1996," SEA Report SEA-SF-TR-97-172.

Science and Engineering Associates, Inc. (SEA), May 1998. "Passive Vapor Extraction Test at TA-54, Well 54-1006 during 1997," SEA Report SEA-SF-TR-98-195.

Springer, E.P., G.J. Langhorst, and E.S. Hamilton, 2000. "Hydrogeologic Properties of the Bandelier Tuff and Groundwater Occurrence at DP Mesa, TA-21, Los Alamos National Laboratory, Los Alamos, NM," Los Alamos National Laboratory document LA-UR-00-1541, Los Alamos, New Mexico.

Springer, E.P., 2005. Statistical Exploration of Matrix Hydrologic Properties for the Bandelier Tuff, Los Alamos, New Mexico. *Vadose Zone Journal* 4:505-521.

Stauffer, P.H. and W.J. Stone, 2005. Surface water-Groundwater Connection at the Los Alamos Canyon Weir Site: Part 2. Modeling of Tracer Test Results. *Vadose Zone Journal* 4:718-728.

Stauffer, P.H., K.H. Birdsell, and W.J. Rice, 2011. "3-D Model Validation in Support of Site Closure, Material Disposal Area L, Los Alamos, NM," Proceedings of the Waste Management 2011 Conference, Phoenix AZ, March 7-11, 2011.

Vold, E, 1997. "Synopsis of Hydrologic Data Collected by Waste Management for Characterization of Unsaturated Transport at Area G," Los Alamos National Laboratory Report LA-UR-97-5185, Los Alamos, New Mexico.

Zyvoloski, G.A., B.A. Robinson, Z.V. Dash, and L.L. Trease, July 1997. "Summary of the Models and Methods for the HFEM Application – A Finite-Element Heat- and Mass- Transfer Code," Los Alamos National Laboratory Report LA-13307-MS, Los Alamos, New Mexico.

Attachment IV
Scoping Calculations for Transport Simulations
for the
Los Alamos National Laboratory Technical Area 21,
Material Disposal Area T

Authors:

Zora Dash
Philip H. Stauffer

Introduction

This attachment describes scoping calculations for transport simulations that were conducted to compare the particle tracking codes ptrk and sptr. Transport calculations were performed using both cell-based (ptrk macro) and streamline (sptr macro) particle tracking models.

Methods

Scoping calculations for transport simulations were run using the original large MDA T grid and a preliminary parameter set was used that is not the same as the parameters presented in Attachment III. These calculations were also done on a flow system using an equivalent continuum model as apposed to a single continuum model. However, these two models yield virtually the same results. This attachment includes the code that processes the ptrk output and parses it into a binned breakthrough curve.

The flow simulation started with a steady-state flow field run with a uniform infiltration rate of 10 mm/yr across the domain and assumed that this average background infiltration rate continued. Additional water was introduced into the system to represent the 19 million gallons of water that was disposed of in the MDA T adsorption beds between 1945 and 1967, as described in detail in the main report. At the end of this transient condition, the simulation returned to the 10 mm/yr background infiltration rate.

Transport calculations were performed using both cell based (ptrk macro) and streamline (sptr macro) particle tracking models. Three cases were run for each particle tracking model: no dispersion, 2 m dispersion, and 30 m dispersion. For the ptrk model dispersion was only applied in the primary flow direction (Z), for the sptr model longitudinal dispersion with no transverse dispersion was used. The other difference of note between the dispersion models used by the particle tracking schemes is that for ptrk, the dispersion is applied as a correction to the time a particle spends in each cell it travels through. For sptr, the particle takes a random step in the direction of dispersion and can actually jump between cells along the flow path.

Ten thousand particles were used for the particle tracking models. For ptrk they were entered at a single node (226728) with coordinates $x = 4.97648E+05$, $y = 5.40868E+05$, and $z = 2.068E+03$ m. For sptr, the particles were entered over a 1 m² patch (in x and y) at the same coordinates.

Results

Figure 1 shows the saturation at the beginning of the transport calculations, representing conditions in 2010, 65 years after the start of disposal of 19 million gallons of water and wastewater. The effects of the water added from 1945 through 1967 are present as a bulge of enhanced saturation beneath MDA T. The slice is taken at the x coordinate of the particle input location. Particle breakthrough at the water table for the two particle tracking models and the different dispersion models is illustrated in Figure 2. Simulations with low dispersion yield nearly identical results for either particle tracking model. Differences become apparent when greater values of dispersion are used. Figures 3 through 8 illustrate saturations at 100, 200, 300, 400, 500, and 550 years after 2010. The effect of enhanced infiltration due to wastewater disposal on saturation has almost totally dissipated by 500 years.

To explore the transient effects of the wastewater disposal, the transport simulations were rerun without dispersion assuming transients in the flow system were negligible by 600, 1000, 1500, and 2000 years. The simulations were run with transient flow and then restarted using the flow field existing at the assumed time. Results for these simulations are shown in Figure 9. As can be seen from the illustration, although saturations appear fairly stable by 550 years, transient flow affects the transport results (breakthrough curves) for up to 1500 years for this flow model.

Finally, Figure 10 is included to show how sptr breakthrough on the new high resolution mesh (Attachment II) compares to ptrk breakthrough. As a result of the high dispersivity (30 m) combined with the random walk algorithm in sptr, the sptr results are unreliable, with only 1/3 of sptr particles reaching the water table. The sptr breakthrough shown in Figure 10 (red squares) is normalized to 10,000 particles and does not compare well with the ptrk results (blue diamonds). Well-behaved particle breakthrough is shown in Figure 9 where the 50% breakthrough happens at about the same time regardless of the model chosen. For this reason, we have chosen to use ptrk to create breakthrough curves for the particle release points beneath the beds and shafts that are described in the main report.

In summary, these scoping calculations show that ptrk rather than sptr should be used for the transport calculations and that a transient flow field is required to accurately calculate transport from MDA T.

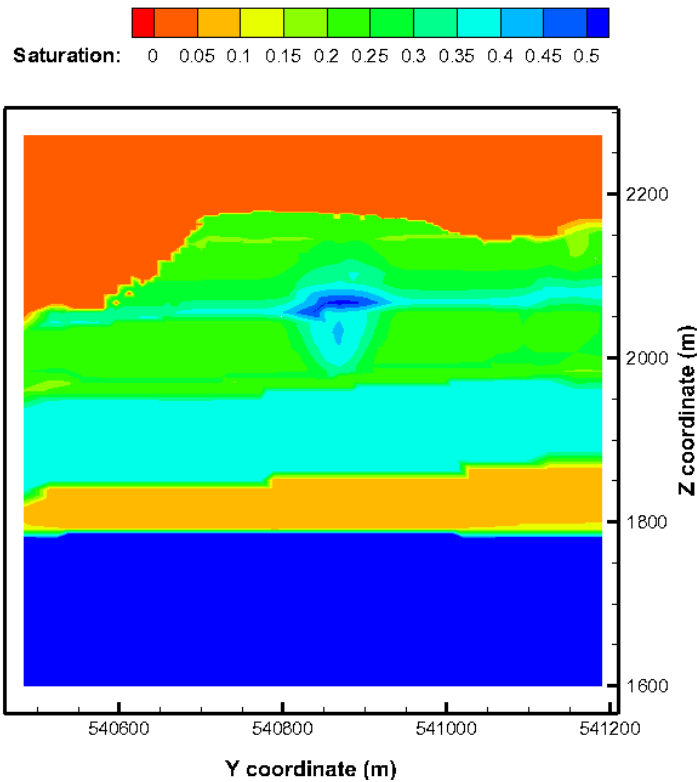


Figure 1. Calculated saturation field at beginning of transport simulation (2010). Note that orange is above ground surface.

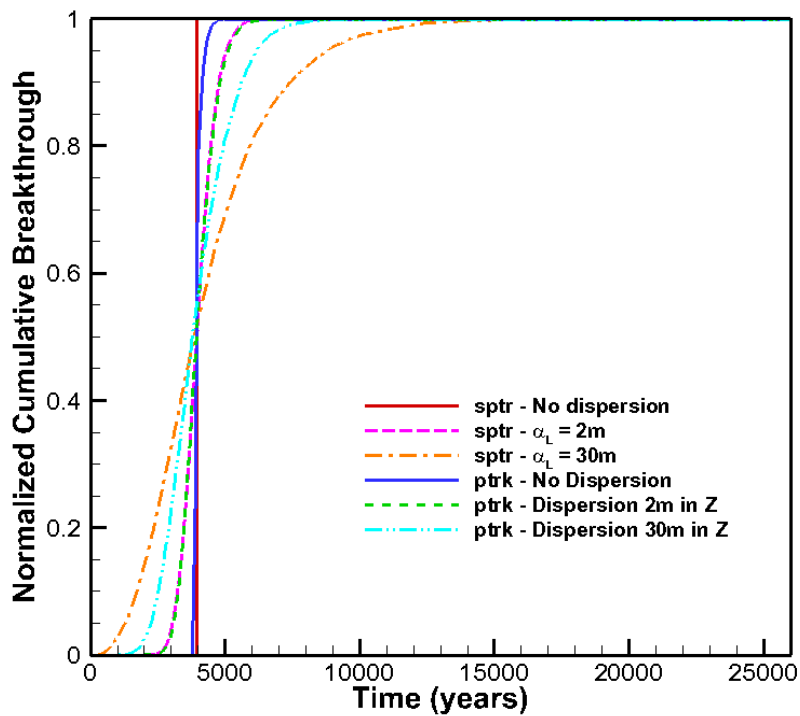


Figure 2. Normalized breakthrough concentration for the cell based and streamline particle tracking models.

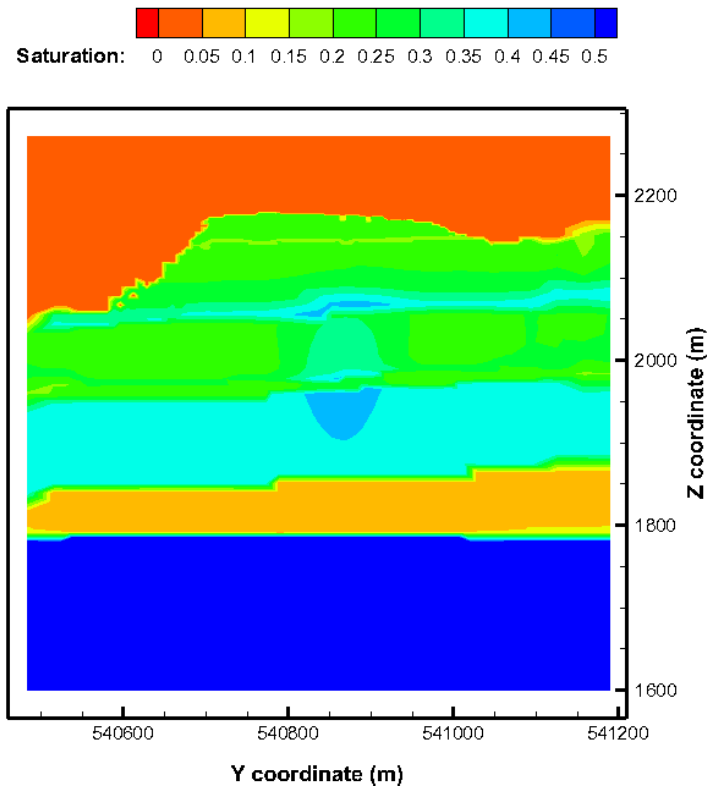


Figure 3. Calculated saturation field in 2110 (with background infiltration rate of 10 mm/yr).

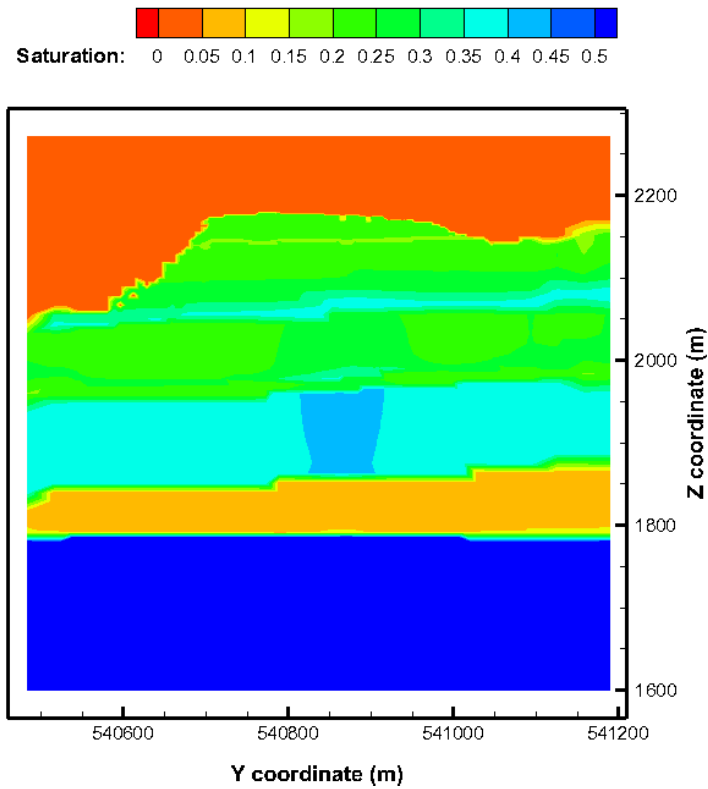


Figure 4. Calculated saturation field in 2210 (with background infiltration rate of 10 mm/yr).

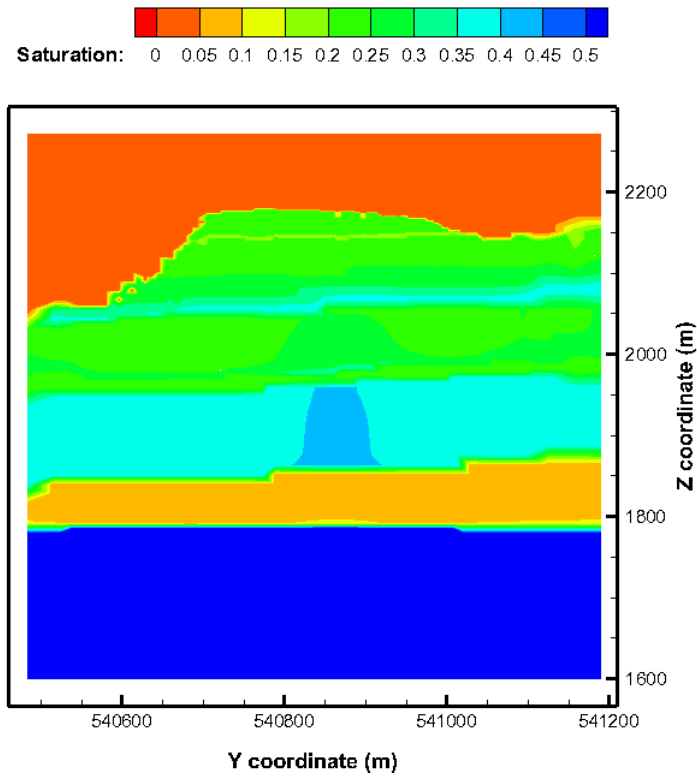


Figure 5. Calculated saturation field in 2310 (with background infiltration rate of 10 mm/yr).

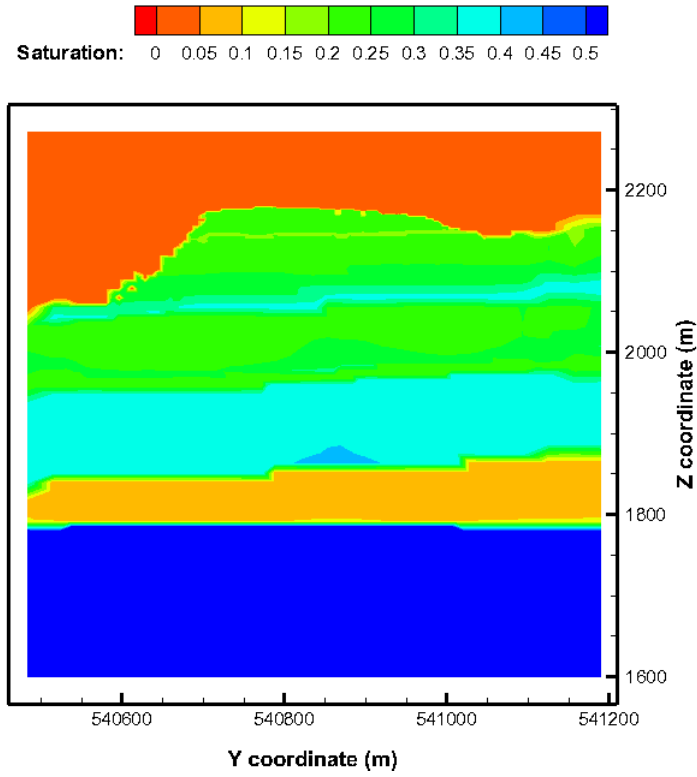


Figure 6. Calculated saturation field in 2410 (with background infiltration rate of 10 mm/yr).

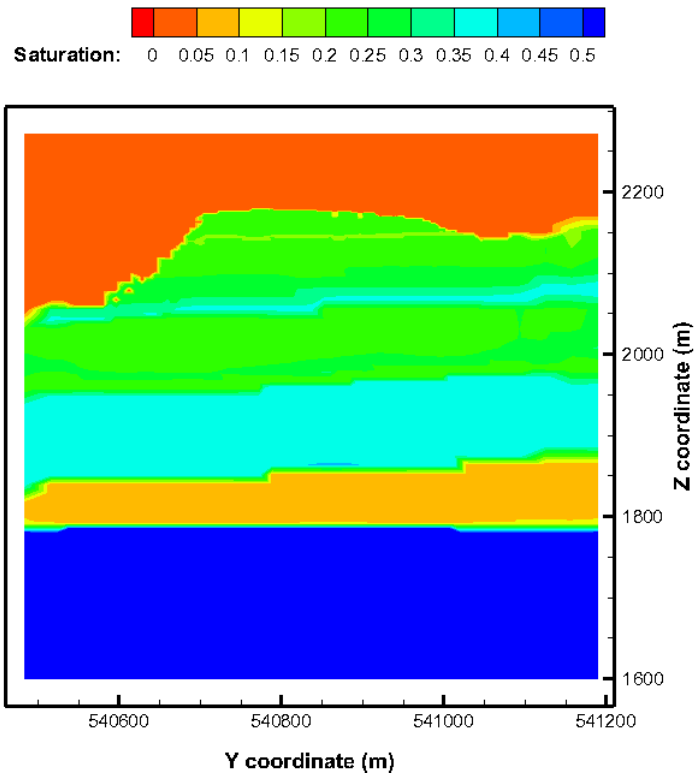


Figure 7. Calculated saturation field in 2510 (with background infiltration rate of 10 mm/yr).

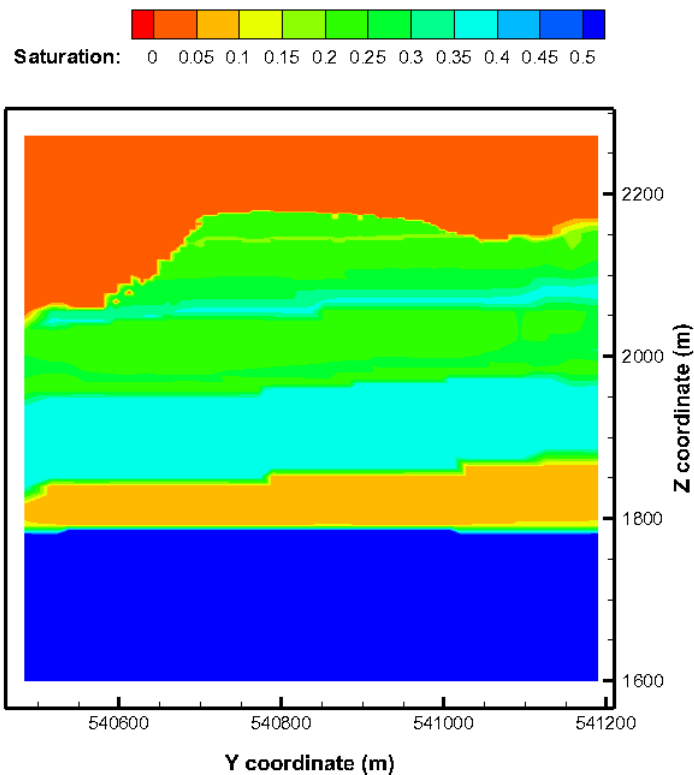


Figure 8. Calculated saturation field in 2560 (with background infiltration rate of 10 mm/yr).

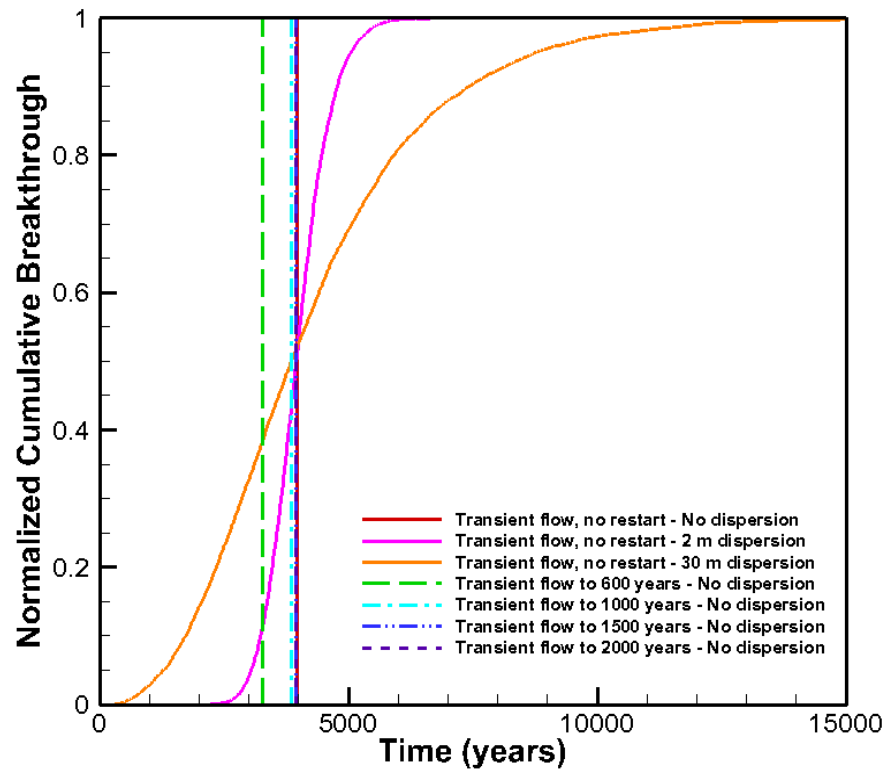


Figure 9. Normalized breakthrough concentration for streamline particle tracking runs with variable transient flow intervals.

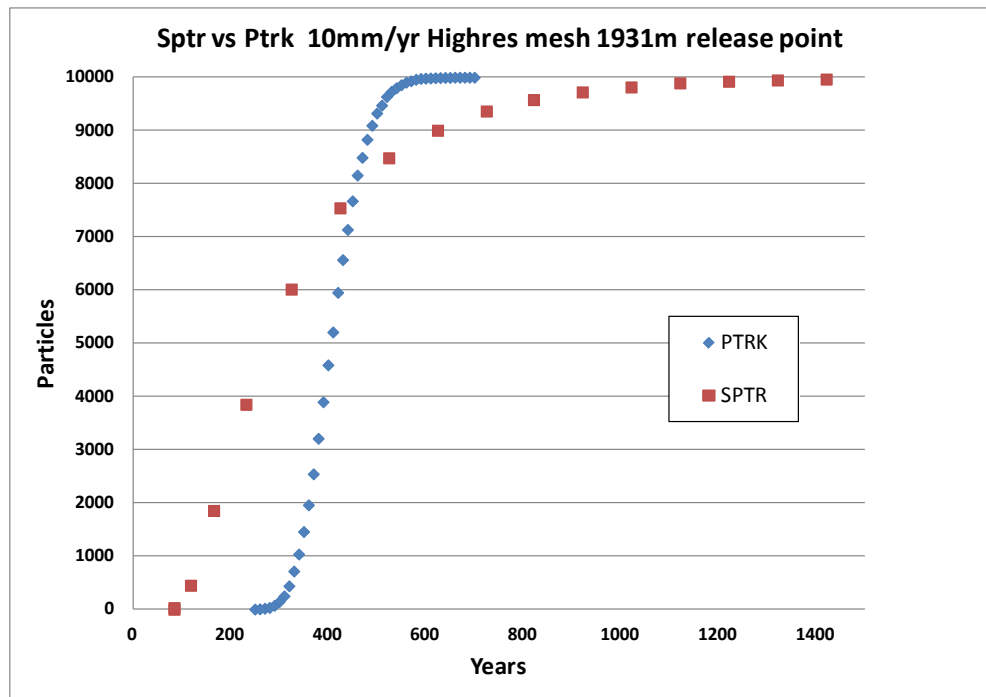


Figure 10. Particle breakthrough for streamline particle tracking runs comparing sptr to ptrk using the high resolution mesh.

COMPUTE_BREAKTHROUGH

A utility for computing zone breakthrough curves from an FEHM ptrk run.

Files

- Control file: compute_breakthrough.ctl

Line 1: Name of the input file (*.trc)
Line 2: Name of the output file
Line 3: Number of particles modeled
Line 4: Breakthrough zone number
Line 5: Flag specifying if breakthrough should be calculated based on the time particles enter or leave the breakthrough zone, iflag > 0 count when a particle enters zone, iflag < 0 count when a particle leaves zone
Line 6: Starting time for binning the data
Line 7: Ending time for binning the data
Line 8: Bin time interval
Line 9: Output time units (seconds, minutes, hours, days, years). All times are input in terms of the output time units.
Line 10: Zone id string

| Example control file |
|---|
| output/example-flow-nodp_zptr.trc output/example-flow-nodp_btc_zptr2.dat 10000 2 -1 0. 200000. 100. years Zone 2 out |

- Input file: .trc file obtained when using ptrk option pout = -7.

When this option is used, following the header lines, output is written every time a particle leaves a cell. This output is particle number, cell number that the particle is leaving, zone number of the cell, time the particle is in the cell, and time the particle leaves the cell. Note times in this file are in seconds.

Example .trc file

```

FEHM V3.00gf 11-08-24 QA:NA      08/25/2011      09:05:13
1D column ER-12-3 saturated flow at Rainier Mesa
  Particle #    Node Number      Zone  Time in node  Current time (sec)
    1            101            0  1.33135626E+10  1.33135626E+10
    1            100            4  2.42488858E+09  1.57384509E+10
    1            99             4  1.64060559E+10  3.21445069E+10
    1            98             4  3.20870789E+10  6.42315878E+10
    1            97             4  5.00964270E+10  1.14328011E+11
    .
    .
    .

```

- Output file

The output file will contain three header lines followed by breakthrough time, number of particles in the zone during the current time interval, and the cumulative number of particles that have been in the zone, for each time bin. The time is recorded as the initial time of the time interval.

Example breakthrough output file

```

TITLE = "1D column ER-12-3 saturated flow at Rainier Mesa"
VARIABLES = "Time (years)" "Number of particles" "Cumulative particles"
ZONE T = "Zone 1 in"
  0.0000000000000000          0          0
  100.00000000000000          0          0
  .
  .
  .
  67900.000000000000          7          489
  68000.000000000000          13         502
  68100.000000000000          7          509
  .
  .
  .
  163500.000000000000          0          9999
  163600.000000000000          1         10000
  163700.000000000000          0         10000
  .
  .
  .
  199900.000000000000          0         10000
  200000.000000000000          0         10000

```

Source code

```
program compute_breakthrough

!*****
! Copyright 2011 Los Alamos National Security, LLC All rights reserved
! Unless otherwise indicated, this information has been authored by an
! employee or employees of the Los Alamos National Security, LLC (LANS),
! operator of the Los Alamos National Laboratory under Contract No.
! DE-AC52-06NA25396 with the U. S. Department of Energy. The U. S.
! Government has rights to use, reproduce, and distribute this
! information. The public may copy and use this information without
! charge, provided that this Notice and any statement of authorship are
! reproduced on all copies. Neither the Government nor LANS makes any
! warranty, express or implied, or assumes any liability or
! responsibility for the use of this information.
!*****
! Compute zone breakthrough from data in .trc file if pout = -7

implicit none

integer :: ctl_unit = 10
integer :: trc_unit = 11
integer :: out_unit = 12
integer :: i, numpart, zone, iflag, tbins, pnum, node, zid, sum
integer, allocatable :: count(:), lastzone(:)
logical, allocatable :: counted(:)
real(8) :: dt, te, ts, tscale, tnode, ptime, ptimes
real(8), allocatable :: time(:)
character(1) :: tunit
character(7) :: tlabel
character(80) :: tstring, zstring
character(200) :: trc_file, out_file

open (unit = ctl_unit, file = 'compute_breakthrough.ctl', status = 'old')
! Read input file name
read (ctl_unit, '(a200)') trc_file
! Read output file name
read (ctl_unit, '(a200)') out_file
! Number of particles modeled
read (ctl_unit, *) numpart
! Breakthrough zone
read (ctl_unit, *) zone
! Flag, iflag > 0 count when particle enters zone, iflag < 0 count when particle leaves zone
read (ctl_unit, *) iflag
! Times should be entered in terms of the selected output units
! Start time
read (ctl_unit, *) ts
! End time
read (ctl_unit, *) te
! Time bin interval
read (ctl_unit, *) dt
! Output time units
read (ctl_unit, '(a1)') tunit
! Zone id string
read (ctl_unit, '(a80)') zstring

close (ctl_unit)

select case (tunit)
case ('s', 'S')
    ! Seconds
    tscale = 1.d0
    tlabel = 'seconds'
case ('m', 'M')
    ! Minutes
    tscale = 60.
    tlabel = 'minutes'
case ('h', 'H')

```

```

! Hours
tscale = 3600.
tlabel = 'hours'
case ('d', 'D')
! Days
tscale = 86400.
tlabel = 'days'
case ('y', 'Y')
! Years
tscale = 31557600.
tlabel = 'years'
case default
! Output in the trc file is in seconds
tscale = 1.d0
tlabel = 'seconds'
end select

tbins = int((te - ts) / dt) + 1

allocate (count(tbins), time(tbins))
allocate (counted(numpart), lastzone(numpart))

counted = .false.
count = 0
lastzone = 0

do i = 1, tbins
  time(i) = ts + (i - 1) * dt
end do

open (unit = trc_unit, file = trc_file, status = 'old')

! Read past version line
read (trc_unit, *)
! Read title line
read (trc_unit, '(80a)') tstring
! Read past variable line
read (trc_unit, *)

! tnode - the time the particle has spent in the current node
! ptime - total time
do
  read (trc_unit, *, end = 9) pnum, node, zid, tnode, ptime
  if (.not. counted(pnum)) then
    if (iflag .gt. 0) then
      ! Have I just entered or started in the breakthrough zone
      if (zid .eq. zone) then
        counted(pnum) = .true.
        ptimes = (ptime - tnode) / tscale
        do i = 1, tbins
          if (ptimes .ge. time(i) .and. ptimes .lt. time(i+1)) then
            count(i) = count(i) + 1
            exit
          end if
        end do
      end if
    else if (iflag .lt. 0) then
      if (zid .ne. zone .and. zone .eq. lastzone(pnum)) then
        counted(pnum) = .true.
        ptimes = (ptime - tnode) / tscale
        do i = 1, tbins
          if (ptimes .ge. time(i) .and. ptimes .lt. time(i+1)) then
            count(i) = count(i) + 1
            exit
          end if
        end do
      end if
    end if
    lastzone(pnum) = zid
  end do
end do

```

```
9 close (trc_unit)

open (unit = out_unit, file = out_file, status = 'unknown')

write (out_unit, 1) trim(tstring)
write (out_unit, 2) trim(tlabel)
write (out_unit, 3) trim(zstring)

do i = 1, tbins
    sum = sum + count(i)
    write (out_unit, *) time(i), count(i), sum
end do

close (out_unit)

1 format ('TITLE = ''', a, '''')
2 format ('VARIABLES = "Time (', a, ')" "Number of particles" "Cumulative particles"')
3 format ('ZONE T = ''', a, '''')

end program compute_breakthrough
```